University of Sheffield

Department of Civil and Structural Engineering

A Study on Transverse Mixing in Shallow Flows within Partially Vegetated Channels

Thesis submitted in fulfilment of the requirements for the degree of Doctor of Philosophy

Santiago Rojas Arques

March 2021

Declaration

Santiago Rojas Arques certifies that all the material contained within this thesis is his own work except where it is clearly referenced to others.

Santiago Rojas Arques

Acknowledgements

First, I would like to thank my supervisors Dr. James Shucksmith and Dr. Andy Nichols, who have been always willing to help and guide me during this hard and amazing process. I am indebted to them for making this possible and support me. In the same way, I am grateful to Dr. Matteo Rubinato, who has helped me since the first day with his advice.

A special thanks goes to my family, to my brother Álvaro and my sister Marian, and especially to my Mum and Dad. They have always been there for me to cheer me up, despite the distance or the mood I was in that day. I could never thank them enough for the efforts they have done for me.

Last, but not least, I would like to thank Paloma, who was always there to listen to me and to have a break for a coffee or a beer. Thanks for supporting me and for making me laugh, for all the good moments together and for those who are yet to come.

Santiago Rojas Arques
Department of Civil and Structural Engineering

Contents

Santiago Rojas Arques

Department of Civil and Structural Engineering

Santiago Rojas Arques
Department of Civil and Structural Engineering

List of Figures

Santiago Rojas Arques
Department of Civil and Structural Engineering

Santiago Rojas Arques
Department of Civil and Structural Engineering

Santiago Rojas Arques
Department of Civil and Structural Engineering

Santiago Rojas Arques
Department of Civil and Structural Engineering

x

Santiago Rojas Arques

Department of Civil and Structural Engineering

List of Tables

Santiago Rojas Arques
Department of Civil and Structural Engineering

Santiago Rojas Arques
Department of Civil and Structural Engineering

List of Symbols

a	Frontal area of vegetation per unit volume	[stems/m]
$a_{Cyclops}$	Variance slope from Cyclops concentration profiles	[m]
a_{PCA}	Variance slope from PCA concentration profiles	[m]
A	Cross sectional area	[m^2]
$A_{\emptyset}$	Empirical coefficient depended on vegetation density	[−]
c_1	Experimental coefficient	[−]
c_2	Experimental coefficient	[−]
C	Time-averaged solute concentration	[L/L]
C_C	Chezy coefficient	[m$^{1/2}$/s]
C_D	Drag coefficient	[−]
C_{D_e}	Effective drag coefficient	[−]
C_e	Experimental concentration	[L/L]
C_{Max}	Maximum concentration	[L/L]
$C_{Max-Spill}$	Maximum concentration at injection	[L/L]
$Coeff$	Empirical coefficient	[−]
C_p	Predicted concentration	[L/L]
$C.V.$	Coefficient of variation	[−]
d	Stem diameter	[m]
D_{sed}	Average grain size	[m]
D_x	Longitudinal mixing coefficient	[m^2/s]
D_y	Transverse mixing coefficient	[m^2/s]
$D_{y_{free}}$	Transverse mixing coefficient within the free open flow	[m^2/s]
$D_{y_{max}}$	Maximum transverse mixing coefficient	[m^2/s]
D_{y_o}	Initial D_y within the optimisation routine	[m^2/s]
$D_{y_{veg}}$	Transverse mixing coefficient within the vegetation	[m^2/s]
D_z	Vertical mixing coefficient	[m^2/s]
e_x	Turbulent diffusion in the longitudinal coordinate	[m^2/s]
e_y	Turbulent diffusion in the transversal coordinate	[m^2/s]
e_z	Turbulent diffusion in the vertical coordinate	[m^2/s]

Santiago Rojas Arques
Department of Civil and Structural Engineering

$f(x)$	Generic function	[−]
$f'(x)$	Generic derived function	[−]
F	Force	[N]
$F_{AdapCorr}$	Adaptive correlation factor	[−]
F_d	Drag force	[N]
F_{MovAv}	Moving average factor	[−]
g	Acceleration due to gravity	[m^2/s]
h	Water depth	[m]
i	Transversal cell position	[−]
j	Longitudinal cell position	[−]
J_x	Mass flux in the longitudinal coordinate	[kg/m^{2}s]
J_y	Mass flux in the transversal coordinate	[kg/m^{2}s]
J_z	Mass flux in the vertical coordinate	[kg/m^{2}s]
k_s	Equivalent roughness height	[m]
K	Constant	[−]
K_y	Non-dimensional transverse mixing coefficient	[−]
l	Length scale	[m]
L	Length	[m]
L_{50}	Distance to reduce a 50 % the maximum concentration	[m]
L_y	Downstream distance for full transverse mixing	[m]
L_z	Downstream distance for full vertical mixing	[m]
$L_{z_{Middle}}$	L_z for a point source located at mid-depth	[m]
$L_{z_{Surface}}$	L_z for a point source located at the water surface	[m]
$L_{z_{Top}}$	L_z for a point source located at the bottom depth	[m]
M	Longitudinal dimension of size area	[−]
M_0	Zero moment	[m]
M_1	First moment	[m^2]
M_2	Second moment	[m^3]
n	Manning's coefficient	[s/m$^{1/3}$]
n_{iter}	Number of iterations	[−]
n_{values}	Number of values	[−]

Santiago Rojas Arques
Department of Civil and Structural Engineering

n_{veg}	Equivalent Manning's coefficient for vegetated flows	$[s/m^{1/3}]$
N	Transversal component of size area	$[-]$
N_d	Stem density	$[stems/m^2]$
N_s	Number of samples	$[-]$
p	F.D.M. coefficient	$[-]$
P	Wetted perimeter	$[m]$
q	F.D.M. coefficient	$[-]$
Q	Flow rate	$[m^3/s]$
Q_{PIV}	Flow rate obtained from PIV data	$[m^3/s]$
$Q_{Solution}$	Flow rate obtained	$[m^3/s]$
r	F.D.M. coefficient	$[-]$
R	Pearson correlation	$[-]$
Re	Reynolds number	$[-]$
Re_{stem}	Stem scale Reynolds number	$[-]$
R_H	Hydraulic radius	$[m]$
$RMSu$	Average longitudinal turbulence intensity	$[m/s]$
$RMSv$	Average transversal turbulence intensity	$[m/s]$
$RMSw$	Average vertical turbulence intensity	$[m/s]$
RD_U	Relative difference between surface and mid-depth velocity	$[\%]$
RD_Q	Relative difference between flow rates	$[\%]$
S_o	Bed slope	$[-]$
S_c	Schmidt number	$[-]$
t	Time	$[s]$
TF_x	Total flux in the longitudinal coordinate	$[kg/s]$
TF_y	Total flux in the transversal coordinate	$[kg/s]$
TF_z	Total flux in the vertical coordinate	$[kg/s]$
U	Main longitudinal velocity	$[m/s]$
U_{free}	Longitudinal velocity within free open flow	$[m/s]$
U_{Inner}	Longitudinal velocity within inner layer	$[m/s]$
$U_{Linear\ Step}$	Dimensionless velocity between both constant velocity layers	$[-]$
U_m	Longitudinal velocity at match position	$[m/s]$

Santiago Rojas Arques
Department of Civil and Structural Engineering

U_{max}	Maximum longitudinal velocity recorded	[m/s]
$U_{Mid-depth}$	Longitudinal velocity at mid-depth	[m/s]
U_{Outer}	Longitudinal velocity within outer layer	[m/s]
U_s	Slip velocity	[m/s]
$U_{Surface}$	Surface longitudinal velocity	[m/s]
U_{veg}	Longitudinal velocity within vegetation	[m/s]
U_{veg0}	Initial velocity within vegetation	[m/s]
$U_{Veg\ Result}$	Velocity within vegetation obtained	[m/s]
$U_{x_{min}}$	Minimum longitudinal velocity range	[m/s]
$U_{x_{max}}$	Maximum longitudinal velocity range	[m/s]
$U_{y_{max}}$	Maximum transversal velocity range	[m/s]
u^*	Shear velocity	[m/s]
u'	Longitudinal velocity deviation	[m/s]
V	Main transversal velocity	[m/s]
v'	Transversal velocity deviation	[m/s]
W	Main vertical velocity	[m/s]
W_d	Channel width	[m]
W_{free}	Free flow region width	[m]
W_{veg}	Vegetated bank width	[m]
w'	Vertical velocity deviation	[m/s]
x	Longitudinal coordinate	[m]
y	Transversal coordinate	[m]
y_{Centre}	Position of the centre of the channel	[m]
y_{Inj}	Position of solute injection	[m]
y_{Inner}	Inner layer starting position	[m]
y_m	Match position between inner and outer layers	[m]
y_{max}	Position of maximum transverse mixing coefficient	[m]
y_o	Inflection point position	[m]
y_{Outer}	Inner layer ending position	[m]
y_{Shear}	Injection position within the shear layer	[m]
z	Vertical coordinate	[m]

Santiago Rojas Arques
Department of Civil and Structural Engineering

Greek Alphabet

α	F.D.M. coefficient	$[-]$
α_{C_D}	Parameter to obtain drag coefficient	$[-]$
β	F.D.M. coefficient	$[-]$
β_{C_D}	Parameter to obtain drag coefficient	$[-]$
γ	F.D.M. coefficient	$[-]$
δ	F.D.M. coefficient	$[-]$
δ_{Inner}	Inner layer length	$[m]$
δ_{Outer}	Outer layer length	$[m]$
$\delta_{V.S.L.}$	Total length of shear layer along submerged vegetated flow	$[m]$
ε	Eddy viscosity	$[Ns/m^2]$
η	Molecular diffusion coefficient	$[m^2/s]$
θ	Angle of the channel slope	$[^\circ]$
κ	von Karman constant	$[-]$
μ	Dynamic viscosity	$[Ns/m^2]$
ρ	Density	$[kg/m^3]$
$\emptyset$	Solid volume fraction	$[-]$
σ_y^2	Variance	$[m^2]$
τ_o	Boundary shear stress	$[N/m^2]$
τ_R	Reynolds stress tensor	$[N/m^2]$
τ_t	Shear stress	$[N/m^2]$
υ	Kinematic viscosity	$[m^2/s]$
φ	Centroid	$[m]$
ΔD	Total distance increment	$[m]$
Δt	Time increment	$[s]$
ΔU	Velocity difference	$[m/s]$
Δx	Longitudinal distance increment	$[m]$
Δy	Transversal distance increment	$[m]$

Santiago Rojas Arques
Department of Civil and Structural Engineering

Abstract

Increasing instances of river pollution and sewer overflows, coupled with more stringent regulatory requirements for ecological status and flood risk management; demand a deeper understanding of mixing processes and natural solutions to reduce peak pollutant concentrations while minimising flow obstruction.

This thesis presents an experimental study of flow surface velocity and transverse mixing processes in open channel shallow flows with partial vegetation. A technique that simultaneously measures mixing processes and surface velocity fields in shallow flows using low cost cameras and lighting is developed and validated.

The technique is used here to record surface velocity fields and depth averaged concentrations of a solute in a rectangular laboratory flume over a recorded length of 4.48 m. Artificial vegetation is installed at different densities at one bank to simulate partial coverage of emergent vegetation under a range of shallow flow conditions. Using the experimental results, a semi-empirical model for transverse mixing based on the velocity gradients across the shear layer is developed to relate the mixing behaviour to the velocity distribution in vegetated shear layers. The proposed model is validated using surface velocity and depth-averaged concentration of a solute recorded during experiments with two vegetated banks with the same vegetation density and flow depth conditions as the previous experiments.

This thesis provides a semi-empirical predictive model that estimates longitudinal surface velocity and variable transverse mixing coefficient in shallow flows with vegetated banks. The model only requires the vegetation parameters and free flow region data such as velocity and water depth, producing an approach without the requirement for extensive data collection or complex hydrodynamic numerical models. Initial scenario testing of the model suggests that vegetation induced mixing may significantly reduce the impacts of acute pollution events, although further work is required to validate these findings in field conditions.

Santiago Rojas Arques
Department of Civil and Structural Engineering

1. Introduction

Water is arguably the most valuable resource for human life (**Oki and Kanae, 2006**) and its use and correct management is indispensable for human activities from irrigation and industry use to supply for consumption. In many areas of the world, the growth of human population and the development and industrialization of nations are producing an increase of clean water demand, whilst an increase of sewage and polluted water discharge, resulting in a large stress on water resources (**Vörösmarty et al., 2000**).

The safe preservation of natural resources is crucial for local ecosystem and habitat. Therefore, a full understanding of pollution dynamics in natural watercourses becomes crucial. Examples regarding water pollution and its negative impacts on water resources are the wash-off nutrients such as phosphates and nitrogen components from farmland as well as sewage from cities, which produce the eutrophication of rivers; or the presence of pesticides, which can produce malformations and the death of species (**Jasim et al., 2006**). As a result, there is an increased need to understand pollutant transport and mixing processes within natural rivers, particularly the movement and spreading of pollution in rivers.

Solute transport in natural rivers is a phenomenon on which several researchers have focused, especially due to its significance in modelling of the fate of contaminant discharge into a river and how its concentration changes across the width, length, depth and time **(Rutherford, 1994)**. The understanding of the mixing of pollutants becomes more relevant for outlet structures in sewage treatment plants or factories where it is necessary to comply with water quality criteria established in the EU Water Framework Directive 2000/60/EC (WFD) (**Tsakiris and Alexakis, 2012**).

There is a large body of work regarding mixing processes in idealised open channel flows in which the complete mathematical description of transport and mixing processes can be simplified using semi-empirical models (**Rutherford, 1994**). However, complex and highly variable flow watercourses can differ from these idealised flows. One of the most influential parameters on mixing in rivers is the presence of vegetation. Riparian vegetation has been recognised as an important valuable resource due to several factors:

- Dissipating flow energy: Vegetation increases the flow resistance, and thus reduces the local stream velocity, reducing the soil erosion (**Nepf, 1999**). However, this reduction of flow velocity produces an increase in the flow depth.
- Sediment trapping: As velocity within vegetation is reduced, a decrease of suspended sediments in the flow is produced (**Lopez and Garcia, 1998**). As a result, there is a decrease of water turbidity and the enhancement of stream banks.
- Providing wildlife habitats: the sediment trapping also results in the retention of nutrients, which improves habitability in rivers and oxygen production (**Kadlec and Knight, 1996**)
- Increase in pollutant filtration: The deposition of sediments because of the velocity reduction improves the absorbance of pollutants by the deposited grains (**Palmer et al., 2004**). Moreover, the increase in oxygen improves the removal and degradation of pollutants by biochemical processes.

Therefore, an understanding of the effects of vegetation in rivers is important. The presence of vegetation in a flow increases the flow resistance by adding extra drag. The increase of resistance slows the flow velocity, increasing the water depth relative to a non-vegetated

Santiago Rojas Arques
Department of Civil and Structural Engineering

channel (**Hoffman 2004; Shucksmith, 2008**). Several previous studies (**Stone and Shen, 2002; James et al, 2004; Lightbody and Nepf, 2006**) have investigated the influence of both artificial and real vegetation in channel flows, showing the dependence of the resistance induced by the vegetation on parameters such as vegetation density, stem diameter, vegetation mass distribution, stem height or stem flexibility. All of these properties vary from one plant species to another, and change for the same species because of seasonal variation or canopy growth (**Green, 2005**). Therefore, most researchers have focused on the use of idealised stems, usually plastic rods or cylinders, to study the influence of vegetation in flows (**Nepf, 1999; Stone and Shen, 2002; White and Nepf, 2008**).

Some previous laboratory studies have investigated the effects of velocity variation induced by vegetation in solute mixing processes. Most of these studies have focused on the study of mixing processes in flows with vegetation over the entire flow width. These researchers include both mixing processes within fully emergent vegetated flows over the entire flow width (**Nepf et al. 1997; Serra et al., 2004; Shucksmith, 2008; Sonnenwald et al. 2017**) and within submerged vegetated flows (**Ghisalberti and Nepf, 2005**). However, there are few publications about mixing processes in rivers with vegetated banks (**Tabatabei et al., 2013; West, 2016; West et al., 2020**) despite this vegetated configuration being present in most natural rivers (**Haslam, 1978**) and having potential to improve mixing processes by the enhancing the large-scale turbulence structures (**West, 2016).**

Mixing processes that affect the spreading of a solute can be divided into vertical, transversal and longitudinal mixing processes, depending on which direction the solute spreading is produced. For the majority of practical problems in open channel systems, the vertical mixing affects the region close to the solute injection, and the longitudinal mixing process is only important if the concentration varies significantly in time. This thesis is focused therefore on the study of the transverse mixing component, as it is arguably more important in terms of water quality management than the other two mixing processes. In reality, most pollutants enter the river from one side and hence the input can be considered as a point rather than a transversally well-mixed injection. Therefore, transverse mixing becomes an important term of water quality management when considering impacts in the locality of the injection (**Rutherford, 1994**).

This thesis will investigate the effects of the vegetation located at the river banks on transverse mixing processes in open channel flows. This will lead to improved knowledge of the impacts produced by this type of vegetated configuration and its possible effect on the spreading of contaminant discharges.

1.1 Aim of Thesis

The aim of this study is to quantify the influence of vegetated banks on transverse mixing processes in open channel flows.

Santiago Rojas Arques
Department of Civil and Structural Engineering

2. Literature Review

The purpose of this section is to present a background of knowledge about flow, turbulence, mixing processes and the effects of vegetation on flow processes. The principles of these concepts are presented as well as results and findings of previous studies in order to define a knowledge framework from which to start the current study and identify the gaps in current understanding.

2.1. Open Channel Flow

Water movement along a sloping channel is subject to gravitational forces acting over the water body with a component acting downstream, and resistance forces produced by channel boundaries and any other obstacle in the channel, such as vegetation acting in the upstream direction. Flow can be classified as:

- Unsteady non-uniform flow if the water depth is variable both in time and in space.
- Steady non-uniform flow if the water depth is constant in time but not in space.
- Steady uniform flow if the water depth is constant both in time and in space.

Steady uniform flow is produced when the gravitational and resistance forces are in equilibrium (**Chow, 1959**). In a free flow with no vegetation or other elements, it is commonly understood that the resistance force comes solely from the frictional effects of the channel boundaries as shown in **Figure 2.1**.
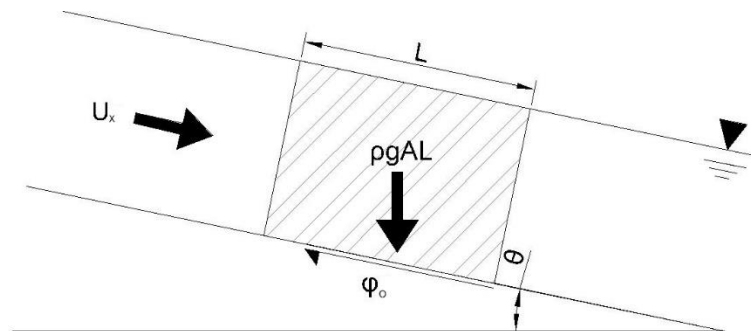
Figure 2.1. Force diagram in uniform flow condition.

In 1769, Antoine de Chezy proposed an expression to obtain the mean longitudinal flow velocity for a uniform open channel flow. **Chezy (1769)** considered that the resistance force is proportional to the square of the mean longitudinal velocity, and the longitudinal component of gravity force that induced the movement of the water body downstream is equal to the flow resistance.

$$F = KU^2 \qquad\qquad eq.\,2.1$$

$$\rho gAL sin\theta = \tau_o PL \qquad\qquad eq.\,2.2$$

Where U is the mean longitudinal flow velocity, K is a constant, ρ is the water density, g is the acceleration due to gravity, A is the cross sectional area, L is the length considered, θ is the angle of the channel slope, τ_o is the boundary shear stress and P is the wetted perimeter.

Santiago Rojas Arques
Department of Civil and Structural Engineering

As channel slope in real rivers usually is quite small, $sin\theta \approx tan\theta \approx S_o$, where S_o is the bed slope. Thus, **eq. 2.2** becomes.

$$\tau_o = \rho g R_H S_o \qquad\qquad eq.\,2.3$$

Where $R_H = A/P$ is the hydraulic radius. Combining **eq. 2.1** and **eq. 2.3**:

$$U = \sqrt{\frac{\rho g R_H S_o}{K}} \qquad\qquad eq.\,2.4$$

Considering the Chezy coefficient as:

$$C_c = \sqrt{\frac{\rho g}{K}} \qquad\qquad eq.\,2.5$$

The mean longitudinal flow velocity can be obtained as:

$$U = C_c\sqrt{R_H S_o} \qquad\qquad eq.\,2.6$$

The coefficient proposed by Chezy ($C_c\,[\mathrm{m}^{1/2}/\mathrm{s}]$) depends on both the bed roughness and the Reynolds number, which is the ratio between the inertia force and the viscous force acting on the flow. The Reynolds number is defined as:

$$Re = \frac{Ul}{v} \qquad\qquad eq.\,2.7$$

Where l is the length scale, $v = \mu/\rho$ is the kinematic viscosity and μ is the dynamic viscosity. For wide open flows the length scale can be considered equal to the flow depth ($l = h$).

In 1889, Robert Manning proposed an expression to obtain the Chezy coefficient based on both experimental observations and previous Chezy coefficient expression (**eq. 2.5**).

$$C_c = \frac{R_H^{1/6}}{n} \qquad\qquad eq.\,2.8$$

Where n is the Manning's coefficient. This is an empirical coefficient related to the bed roughness. Substituting **eq. 2.8** into **eq. 2.6**.

$$U = \frac{R_H^{2/3} S_o^{1/2}}{n} \qquad\qquad eq.\,2.9$$

This equation is frequently used as Manning's coefficient is strongly linked with bed roughness. This equation only is valid for uniform flows with a constant flow depth, cross-sectional area and cross-sectional mean velocity in which the resistance is primarily due to channel boundaries.

Although these equations can be used to obtain average longitudinal flow velocity in open channel flows, the local velocity is not homogeneous within the full cross sectional area of the channel. Usually, in broad, rapid shallow channel flows or flows with a very smooth channel bed, maximum longitudinal velocity can be found at the free surface and in the centreline of the channel (**Chow, 1959**). As the flow resistance is produced by channel boundaries, the roughness of the channel bed produces a decrease of the longitudinal flow velocity in the area close to the boundary, resulting in a logarithmic profile of the longitudinal velocity over the water depth.

Santiago Rojas Arques
Department of Civil and Structural Engineering

For fully developed open channel flows, the vertical profile of longitudinal velocity can be described with Prandtl's logarithmic law modified by **Nikuradse (1933)**.

$$\frac{U(z)}{u^*} = \frac{1}{\kappa} \ln \frac{z}{k_s} \qquad\qquad eq.\,2.10$$

Where u^* is the shear velocity defined as:

$$u^* = \sqrt{\frac{\tau_o}{\rho}} = \sqrt{gR_H S_o} \approx \sqrt{ghS_o} \qquad\qquad eq.\,2.11$$

In addition, h is the water depth from the channel bed, κ is the von Karman constant, z is the vertical coordinate and k_s is the equivalent roughness height. Both von Karman constant and equivalent roughness have been studied experimentally (**Bakhmeteff, 1936; Hinze, 1964; Middleton and Southard, 1978**). The von Karman constant is usually approximated as $\kappa = 0.41$ and the equivalent roughness height, defined as the mean height above the channel bed where the longitudinal velocity value predicted by **eq. 2.10** is zero, depends on the bed roughness. An approximation of the relationship between k_s and mean sediment diameter was suggested by **Robert (2003)** for flows over granulated materials:

$$k_s = \frac{D_{sed}}{30.1} \qquad\qquad eq.\,2.12$$

Where D_{sed} is the average grain size.

2.1.1. Types of Flow Regimes

Osborne Reynolds (1883) was the first person to deeply investigate the existence of different flow regimes. He conducted several experiments with different flows through a glass tube while injecting a filament of dye. He observed that for low flow rates the dye produced a nominally straight line, but as the flow rate was increased some variability in space and time appeared as shown in **Figure 2.2**.
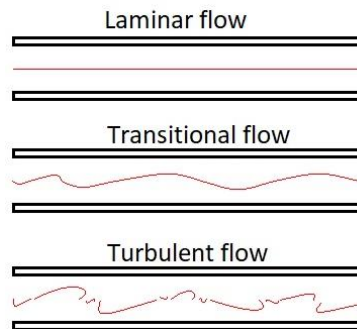
Figure 2.2. Scheme of Reynolds experiment (**Reynolds, 1883**).

He classified the pipe flows based on the Reynolds number introduced previously in **eq. 2.7** by considering the length scale equal to the pipe diameter as shown in **Table 2.1**.

Santiago Rojas Arques
Department of Civil and Structural Engineering

Table 2.1. Flow regimes proposed by Reynolds for open channel flows.

Re	$Flow\ Regime$
$Re < 500$	$Laminar$
$500 < Re < 2000$	$Transitional$
$Re > 2000$	$Turbulent$

Laminar flows can be described as a series of very thin layers of flow sliding over one another subject to the shearing action with the layer below. When the flow velocity increases, this pattern starts to break down and the different layers begin to mix at discrete points in space and time, this is known as the transitional regime. If the velocity increases further, the flow starts to enter into a turbulent behaviour where the different layers from laminar flow disappear and the motion of each fluid particle starts to be chaotic. This regime is dominated by turbulent eddies which increase mass and momentum transport within the flow. These eddies appear to occur randomly in space and time as irregular regions of velocity (**Durbin and Petterson, 2001**). Therefore, in a turbulent flow the velocity field can be considered as:

$$\bar{U} = \bar{U}(x, y, z, t) \qquad\qquad eq.\,2.13$$

Where $\bar{U}$ is the time-averaged longitudinal velocity. However, if the time-averaged velocity of the turbulence regime remains constant with time, the flow can still be classified as steady. **Figure 2.3** shows the longitudinal velocity signal of a flow in which, although the instantaneous velocity varies in time, the time-averaged longitudinal velocity remains constant.
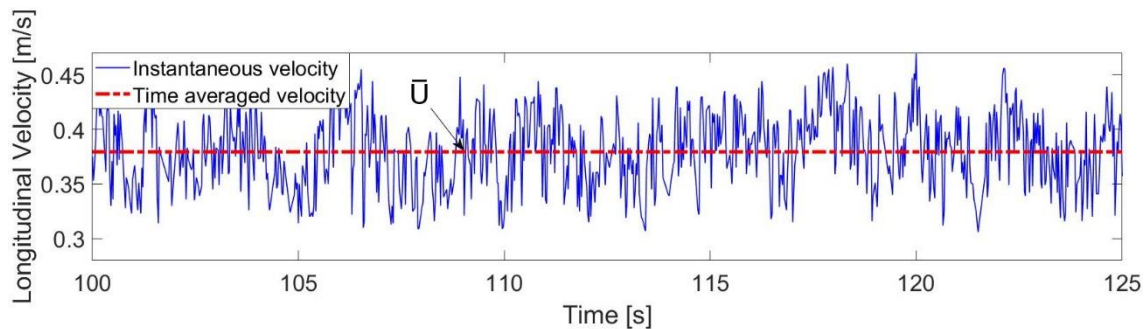
Figure 2.3. Example of longitudinal velocity measurement in turbulent flow.

Thus, turbulent velocity at any point of the flow field can be decomposed into three velocity components: longitudinal velocity U (following downstream flow), transversal velocity V (parallel to the channel bed but normal to the longitudinal component), and vertical W (normal to the bed surface). As shown in **Figure 2.3,** any of these velocity components will not be constant in time although the time-averaged velocity will be constant. Therefore, an instantaneous velocity component can be defined as:

$$U = \bar{U} + u' \qquad\qquad eq.\,2.14$$

$$V = \bar{V} + v' \qquad\qquad eq.\,2.15$$

$$W = \bar{W} + w' \qquad\qquad eq.\,2.16$$

Where u', v' and w' are instantaneous velocity deviations in x, y and z directions respectively. x is the streamwise direction, y is the spanwise direction and z is the vertical

Santiago Rojas Arques
Department of Civil and Structural Engineering

direction. The average turbulence intensity for a specific spatial position of the flow field can be obtained by calculating the variability of the velocity deviation over time.

$$RMSu = \sqrt{\overline{u'^2}} \qquad\qquad eq.\,2.17$$

$$RMSv = \sqrt{\overline{v'^2}} \qquad\qquad eq.\,2.18$$

$$RMSw = \sqrt{\overline{w'^2}} \qquad\qquad eq.\,2.19$$

Turbulence can be classified into different categories (**Durbin and Petterson, 2001**). If statistical values of turbulence intensities are not a function of the spatial position, they are classified as homogeneous turbulence, and non-homogeneous turbulence if statistical values depend on the spatial position. In addition, if this homogeneity of values is conserved in time, turbulence is classified as stationary. Finally, if turbulence is equal in all coordinate directions, it is classified as isotropic. In the same way, if there is a directional preference, turbulence is classified as anisotropic.

In addition, a second order matrix can be considered using the average of the products of the velocity deviation for each component.

$$\tau_R = \begin{bmatrix} \overline{u'u'} & \overline{u'v'} & \overline{u'w'} \\ \overline{v'u'} & \overline{v'v'} & \overline{v'w'} \\ \overline{w'u'} & \overline{w'v'} & \overline{w'w'} \end{bmatrix} \qquad\qquad eq.\,2.20$$

Where τ_R is the Reynolds stress tensor. This is a symmetrical matrix ($\overline{u'v'} = \overline{v'u'}$) and the diagonal components ($\overline{u'^2} = \overline{u'u'}$, $\overline{v'^2} = \overline{v'v'}$ and $\overline{w'^2} = \overline{w'w'}$) are the normal stresses while the off-diagonal components ($\overline{u'v'}$, $\overline{u'w'}$ and $\overline{v'w'}$) are the shear stresses (**Pope, 2000**).

In the case of the vertical profile, assuming the longitudinal velocity follows the logarithmic law introduced in **eq. 2.10** and by considering the maximum shear stress is produced at the bottom and the shear stress is zero on the surface, then:

$$\tau_t = -\rho\overline{u'w'} = \rho\varepsilon\frac{dU}{dz} \approx \rho u^{*2}\left(1 - \frac{z}{h}\right) \qquad\qquad eq.\,2.21$$

Where ε is the eddy viscosity and τ_t is the total shear stress.

2.2. Vegetated Flow

A vegetated flow is one in which some portion of the flow contains vegetation such as reeds. In contrast to conventional open channel flows, in vegetated flows resistance is also produced by vegetation elements. Thus, vegetation reduces the overall channel flow capacity compared with non-vegetated flows and increases water depth for the same flow rate (**Hoffman, 2004, Shucksmith, 2008**).

Newton's third law is commonly used to account for this extra resistance. The force acting on the flow because of the presence of an immersed object is equal to the force on the object due to the flow. This force acting on the object that is moving through the flow is given by the drag equation, which can be described as (**Pope, 2000**).

Santiago Rojas Arques
Department of Civil and Structural Engineering

$$F_d = \frac{1}{2} C_D \rho U^2 A_i \qquad\qquad eq.\,2.22$$

Where F_d is the drag force, C_D is the drag coefficient of the immersed body and A_i is its frontal area. The effect of this drag force has been shown to be significant even for a small amount of vegetation elements (**Nepf, 1999**). To define resistance from vegetation properties (**eq. 2.22**), the main characteristics that must be defined are the drag coefficient C_D, which has been shown to depend strongly on the vegetation morphology (**James et al, 2004**); and the frontal area A_i, which is commonly defined based on vegetation size and density. The vegetation density is defined as:

$$\emptyset = N_d d^2 \frac{\pi}{4} \qquad\qquad eq.\,2.23$$

$$a = N_d d \qquad\qquad eq.\,2.24$$

Where N_d is the stem density, defined as the number of vegetation elements per unit area[stems/m^2]; a is the frontal area of vegetation per unit volume [stem/m]; $\emptyset$ is the solid volume fraction of vegetation $[-]$ and d is the stem diameter [m].

Previous studies such as **Järvela (2002)** showed that one of the vegetated parameters that most affects drag resistance is the vegetation density. He ran different experiments using leafless willows with vegetation densities $N_d = 256 - 512$ stems/m^2, obtaining a linear increase in resistance with planting density.

In rivers and vegetated channels, total flow resistance is a combination of both boundary roughness and vegetation drag. However, the contribution of bed resistance has been found to become negligible when vegetation density is high enough (**Temple, 1986**). **Stone and Shen (2002)** ran experiments using dowels to represent stems and different vegetation densities with $N_d = 173 - 696$ stems/m^2. Their results showed that the bed contribution to flow resistance was less than 3 % of the total. **James et al. (2004)** performed experiments considering both natural and artificial vegetation and they concluded that once vegetation density achieved a certain value, resistance contribution from the channel bed could be dismissed. This vegetation density limit was defined as.

$$0.25 N_d \pi d h > 0.1 \qquad\qquad eq.\,2.25$$

2.2.1. Vegetation Configuration

Another factor that affects total vegetated flow resistance is the distribution of vegetation elements. **Li and Shen (1973)** reported that total resistance is higher if vegetation elements are in a staggered distribution rather than in rows. This is because if the elements are configured in a staggered distribution, there are no corridors between stems in which flow can accelerate. Experiments with artificial stems commonly use a staggered distribution to represent the randomness of real vegetation growth (**Nepf, 1999, Stone and Shen, 2002**). **Kim and Stoesser (2011)** performed numerical simulations to study drag coefficient under different test configurations. Their results suggested that there were no differences in flow resistance between staggered and random vegetation distributions. In **Figure 2.4** a diagram is plotted to show row, staggered and random distributions considering a flow from left to right.

Santiago Rojas Arques
Department of Civil and Structural Engineering

Row distribution   Staggered distribution   Random distribution
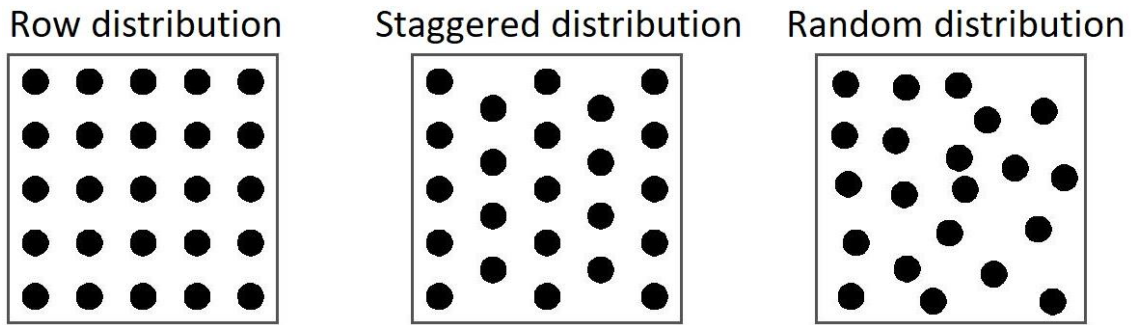
Figure 2.4. Diagram of row, staggered and random stem distributions.

2.2.2. Stem Height

An important characteristic is the ratio between water depth and stem height. This coefficient classifies vegetated flows into emergent vegetated flow conditions (stem height is greater than water depth) and submerged vegetated flow conditions (stem height is smaller than water depth).

Previous researchers have shown the vertical profile of the longitudinal flow velocity within emergent and submerged vegetated flows does not follow the logarithmic law (**eq. 2.10**). Submerged vegetated flows are described in **Section 2.3.1**. In emergent vegetation **Lightbody and Nepf (2006)** showed how the vertical profile of longitudinal velocity changes with the morphology of the vegetation. **Figure 2.5** shows a scheme of **Lightbody and Nepf (2006)** experiments where A_1 and A_2 are the transversal area distribution of the vegetation and u_1 and u_2 are the mean longitudinal velocity in two differently vegetated layers of flow. Thus, longitudinal velocity proportionally decreased in those regions where there was more vegetation mass; and proportionally increased in those regions where the mass decreased. However, in experiments with artificial vegetation, stems are commonly represented as rigid circular cylinders with a uniform mass distribution along their height. Thus, for high enough vegetation densities (**eq. 2.25**), the vertical profile of longitudinal velocity is normally found to be uniform over the depth apart from a small zone close to the bed, which is affected by boundary roughness (**Kouwen et al., 1969; Rowiński et al, 1998**; **Nepf and Vivoni, 2000**). **Stone and Shen (2002)** showed that bed friction only affects the vertical profile in a small region very close to the channel boundary.
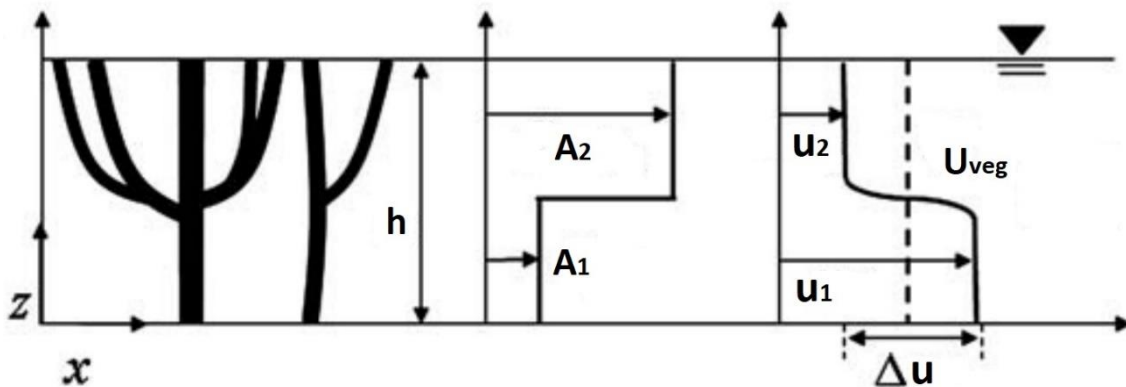
Figure 2.5. Sample of vegetated resistance and longitudinal velocity distribution through a non-uniform canopy height (**Lightbody and Nepf, 2006**).

Santiago Rojas Arques
Department of Civil and Structural Engineering

2.2.3. Flow Resistance within Emergent Vegetated Flows

Petryk and Bosmajian (1975) proposed a model to predict mean velocity within artificial rigid vegetation based on balancing gravitational forces and drag produced by both bed resistance and vegetation. In their model a new Manning coefficient (n_{veg}) was defined, which accounts for both bed resistance and drag produced by vegetation, with vegetated resistance based on the sum of the drag produced by each vegetation element (**eq. 2.22**). Later, **Hoffman (2004)** proposed a similar equation to obtain n_{veg}, but neglecting the effect of bed resistance and assuming that the drag coefficient is a function of the mean flow velocity.

However, the use of the Manning's equation for vegetated channels has been criticised because Manning's coefficient is applied to situations where resistance comes solely from the channel bed and not from drag exerted through the flow depth. In the later situation velocity is essentially uniform over the flow depth (**Lindner, 1982**) rather than being depth-dependent as in the former. The results of **James et al. (2004)** suggested a strong dependence between Manning's n used for vegetated channels and flow depth in contrast with the assumption that the resistance in vegetated flows is produced by stem drag rather than boundaries when density is high enough (**eq. 2.25**). Therefore, the velocity is independent of flow depth, showing the unsuitability of Manning's coefficient.

Several researchers suggested alternate expressions to obtain longitudinal velocity through vegetation (**Stone and Shen, 2002; James et al., 2004**), which are still fundamentally based on the drag equation but without linking it to the Manning's coefficient. **White and Nepf (2008)** proposed an expression for this velocity based on the momentum balance between the drag coefficient and the bed gradient. They assumed a negligible resistance from the channel bed and a uniform distribution of vegetation mass over the depth, i.e. valid for artificial vegetation composed of vertical cylinders.

$$U_{veg} = \sqrt{\frac{2gS_o}{aC_{D_e}}} \qquad eq.\,2.26$$

Where C_{D_e} is the effective drag coefficient of the full vegetation patch. This coefficient depends on both the configuration and characteristics of the vegetated patch and the flow regime as described by the stem scale Reynolds number:

$$Re_{stem} = \frac{Ud}{v} \qquad eq.\,2.27$$

If the stem scale Reynolds number increases, the flow regime changes from a laminar flow to a turbulent flow with a zone behind the obstacle with negative velocity and the formation of eddies. Several previous researchers have studied the drag coefficient for different artificial stems and its dependence on the stem scale Reynolds number (**White, 1991; Pope, 2000**), showing a decrease of the drag coefficient for higher stem scale Reynolds number.

2.3. Velocity Profiles in Vegetated Shear Layers

A shear layer can be defined as a layer of the flow where there is a strong gradient of velocity. In flows with the presence of vegetation, a shear layer is produced when drag induced by stems only affects one area of the flow, but allowing free flow conditions in an adjacent area.

Santiago Rojas Arques
Department of Civil and Structural Engineering

This condition can be achieved with submerged vegetation or with partially vegetated flows (emergent vegetation present over a portion of the width). **Figure 2.6** shows a scheme of the time-averaged longitudinal velocity within the water depth for both emerged (**a**) and submerged vegetated flows (**b**).

2.3.1. Submerged Vegetated Flows

Several researchers have studied the vertical profile of longitudinal flow velocity above submerged vegetation (**Stephan and Gutknecht, 2002; Järvela, 2004**) by considering submerged vegetation height as an extension of the rough bed. Their studies were focused on the adaptation of Prandtl's logarithmic law to describe vertical profiles of primary velocity above vegetation. **Stephan and Gutknecht (2002)** proposed an equivalent roughness height (**eq. 2.10**) using the zero plane displacement (water depth at which the log-law begins) for different discharges and plant types.
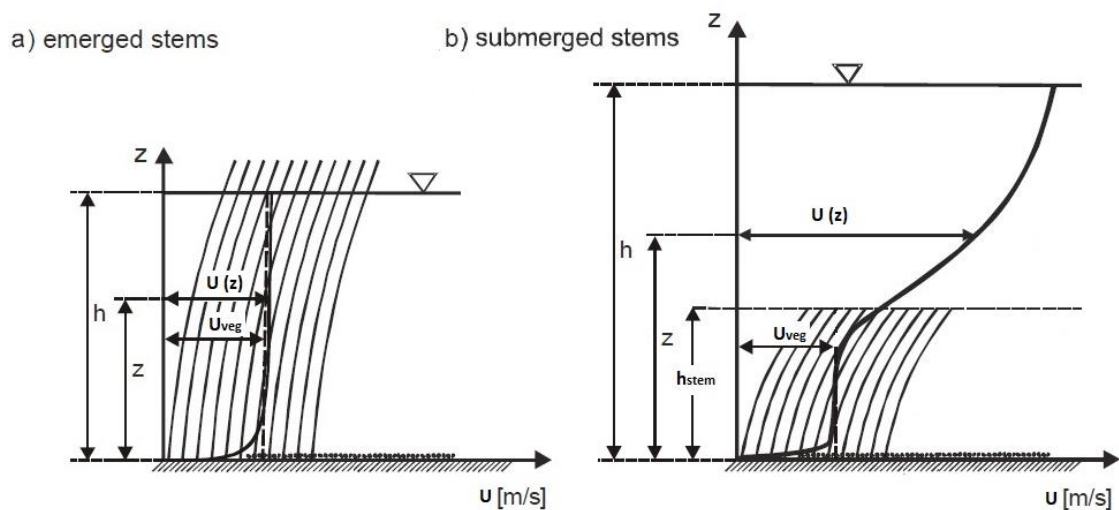
Figure 2.6. Vertical profiles of longitudinal velocity for both emergent vegetated and submerged vegetated flows (**Kubrak et al., 2008**).

The study by **Raupach et al. (1996)** was the first to argue that turbulence structures generated at the top of submerged vegetation is analogous to the flow in a mixing layer. The mixing layer is the region produced between two co-flowing streams with different flow velocities. Because of this velocity difference, a shear velocity is produced between both flows, inducing instability processes in the form of coherent eddies within this layer. This mixing layer is characterised by a strong inflection in the mean longitudinal velocity profile. In submerged artificial vegetated flows, for high enough vegetation densities (**eq. 2.25**), longitudinal velocity within the vegetation under the shear layer can be considered constant over the depth as in emergent vegetated flows. Thus, bed roughness only contributes to flow resistance in a small region close to the channel bed. Above the vegetation, a free open flow region can be considered and as a result, two different flows are generated and a shear layer is produced.

Ikeda and Kanazawa (1996) studied experimental results of longitudinal and vertical velocity components over flexible submerged vegetation. Their results show that the time-averaged longitudinal velocity has an inflection point just above the top of the vegetated elements. They also noticed an increase of both turbulence intensity and Reynolds stress in the mixing layer region, recording their maximum at the top of the vegetation layer.

Santiago Rojas Arques
Department of Civil and Structural Engineering

In addition, **Ghisalberti and Nepf (2002)** observed the creation of coherent large-scale eddies within the shear layer, which dominate the momentum transfer between the vegetated and free flow regions. **Poggi et al. (2004)** argued that the presence of the inflection point in the vertical profile of longitudinal velocity is a necessary condition for the creation of these instabilities. In addition, the magnitude of the Reynolds stress produced at the inflection point is related with the intensity of these instabilities. The increase of vegetation density for a given flow rate will decrease the flow velocity within the vegetation, and thus the velocity over the submerged canopies will increase. As a result, the velocity gradient between two constant velocity flows increases, enhancing the creation of instabilities. For dense vegetation, these vortices can only penetrate a limited distance into the vegetated layer (**Ghisalberti and Nepf, 2009**) as shown in **Figure 2.7**. This phenomenon allows the creation of two different regions within the submerged vegetation. The upper-zone is governed by large-scale eddies generated by the velocity gradient, and the lower-zone is governed by smaller stem-scale eddies. These stem-scale vortices are scaled to either stem diameter or mean stem spacing and produce a lower turbulence and solute transport compared with the upper-zone (**Nepf, 2012**).

Huai et al. (2008) studied both longitudinal velocity and Reynolds stress over the water depth in submerged vegetation. Their experimental results showed that the maximum Reynolds stress is located at the interface between the vegetated layer and the free flow above it. This maximum Reynolds stress was shown to be dependent on the velocity gradient, which increases for denser vegetation. In addition, they showed a strong linear decay of Reynolds stress in both the vegetated and free flow regions.
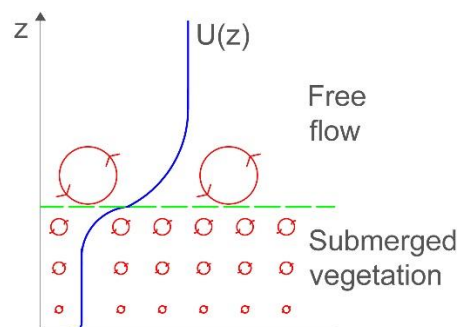
Figure 2.7. Vertical profile schemes of longitudinal velocity for submerged vegetated flows for sufficient density condition. Red circles represent the generated large-scale eddies.

Stoesser at al. (2009) performed a large eddy simulation for a flow through an idealized submerged vegetation. Then, they proposed a scenario similar to the experiments performed by **Liu et al. (2008)** to validate their results, with a ratio between the water depth and the plant height of 1.5, a stem diameter of 6.35 mm and a vegetation density of 496 stems/m^2. Their results showed that presence of the submerged vegetation produces an additional drag that strongly affects the mean longitudinal velocity averaged across the entire cross section, the turbulence and the Reynolds stress. In accordance with **Huai et al. (2008)**, they noticed a retardation of the mean flow within the submerged layer and an acceleration of the mean flow above the canopy. This strong variation in the velocity causes the creation of large coherent eddies that affect the free flow up to the canopies until the free surface. In addition, their results showed that the inflection point of the mean flow is located at the boundary of the vegetated layer and that the maximum Reynolds stress is produced at the same location. This shear stress decays rapidly within the vegetation because of the drag force and in a linear way within the free flow. In addition, **Stoesser at al. (2009)** observed a recirculation of the flow at the top of

- 13 -

Santiago Rojas Arques
Department of Civil and Structural Engineering

the vegetation between consecutive stems due to the difference of pressure between the region upstream and downstream of a cylinder. When the flow approaches a stem, it is forced out of the vegetation layer by the presence of the stems. Then, the flow separates at the free layer and re-joins at the top of the cylinder, producing a small recirculation.

Battiato and Rubol (2014) proposed a two-domain approach to predict the longitudinal velocity profile in submerged vegetated flows. Although this model cannot predict the stem scale turbulence, it allows the quantification of the mean longitudinal flow velocity over the entire depth of a submerged vegetated flow, as well as the momentum transfer over the flow depth. They proposed a modified log – law, similar to those proposed in previous work (**Stephan and Gutknecht, 2002; Järvela, 2004**), but with the novelty of defining all the required parameters based on the permeability of the canopy layer. Then, they validated their model with experimental data recorded by **Ghisalberti and Nepf (2004)** and **Nepf et al, (2007)**. This model only requires the water depth, the height of the stem vegetation, the channel slope and the permeability of the vegetated layer to estimate the rest of parameters, such as the length of the shear layer into the vegetated layer, the bulk velocity or the flow rate. Moreover, **Rubol et al. (2018)** used this approach to predict the mean longitudinal flow velocity in submerged vegetated flows and compared the results with those recorded by previous work using real vegetation (**Shi et al., 1995; Nepf and Vivoni, 2000; Baptist, 2003; Wilson et al., 2003; Velasco et al., 2008; Righetti, 2008; Shucksmith et al., 2010; Siniscalchi et al., 2012 and Cassan et al., 2015**). Their results fitted with the experimental data and suggest that the most important parameters that affects the flow are the vegetation density and the flexibility of stems.

Guo and Zhang (2016) also proposed an approach to estimate the mean longitudinal velocity in submerged vegetated flows using a hyperbolic sine law for the vegetation layer combined with a log function for the free flow region. The results were validated against the experimental results recorded by **Nikora et al. (2013)**. The **Guo and Zhang (2016)** approach divides the vegetated layer into the near bed region and the canopy region. The first is governed by the shear stress produced by the channel bed and the second by the drag force produced by stems. For very sparse vegetation scenarios the near bed region is extended until the vegetation boundary, producing a variable longitudinal velocity within the stem height; and for very dense flows the near bed region becomes negligible and the canopy region is extended until the channel bed, producing a constant longitudinal velocity over most of the stem height.

Yan et al. (2017) presented a large eddy simulation to predict the flow velocity and the scalar transport within submerged vegetated flows. They observed from their results successive events of ejection and sweep along the vegetation boundary. This coherent motion was almost extended until the water surface in the free flow region, but it decayed rapidly into the vegetated region. These results were in accordance with the predicted Reynolds stress distribution, which decayed rapidly toward zero bellow the vegetation boundary. Moreover, their results showed the presence of important secondary currents in the vertical direction. These secondary circulations decreased with the increase of the ratio between the water depth and the stem height. **Yan et al. (2017)** suggested that the secondary currents interfere with the velocity at the top of the vegetated layer and enhance the vertical transport, particularly into the canopy.

Caroppi et al (2018) and **Gualtieri et al. (2018)** studied the influences of the vegetated submergence ratio on the longitudinal velocity distribution in submerged vegetated flows. **Caroppi et al. (2018)** carried out several physical experiments for a fixed solid volume fraction ($\emptyset = 0.020$) and four different aspect ratios (2.4, 2.8, 3.1 and 3.4). For all experimental results,

Santiago Rojas Arques
Department of Civil and Structural Engineering

they observed the sharp decrease of the longitudinal velocity within the vegetation and the presence of a shear layer at the interface between this and the free flow region. Moreover, they recorded that the inflection point was located at the vegetated boundary, matching with the peak Reynolds stress distribution. Based on their results, **Caroppi et al. (2018)** conclude that the aspect ratio does not significantly affect the flow structure over the range tested, but the vegetation density seems to play the major role in the hydrodynamic structure. **Gualtieri et al. (2018)** studied the main flow structure of submerged vegetated flows for high aspect ratios (higher than 5). They used conventional flow resistance equations, such as Chezy and Manning equations, to predict different submerged vegetated flow scenarios recorded by previous research. They conclude that, although these equations are not usually suitable to predict the flow conditions, they can fit experimental data for high submergence ratios as the difference between a rough bed and a vegetated bed can be considered indistinguishable.

2.3.2. Partially Vegetated Flows

In a similar way to submerged vegetated flows, in partially vegetated flows, emergent vegetation only covers some areas of the channel. Vegetated banks are one form of partial vegetation, where vegetation covers the part of the channel close to the banks of the river, allowing free open flow conditions in the centre of the channel. This configuration creates a variation of flow resistance along the transverse direction that affects the distribution of the longitudinal flow velocity. **Nezu and Onitsuka (2002)** measured the longitudinal velocity and the turbulence in an open channel with half of its width covered by artificial vegetation. The transverse profile of longitudinal velocity showed a strong inflected region near the vegetation edge and two regions with different primary velocities on either sides (a lower velocity region within the vegetation and a higher one in the free open region). This inflection profile matched with an increase of the Reynolds stress profile. A well-defined peak was found at the vegetation edge, which increased for higher vegetation densities and for higher Froude numbers. **Nezu and Onitsuka (2002)** showed that, due to the shear instability produced by the flow resistance differences, horizontal vortices are created in the shear layer between the vegetated and non-vegetated layers. These instabilities increase in strength for higher densities. In addition, their results recorded strong secondary currents in the shear layer, which also increased with Froude number.

White and Nepf (2007) performed experiments with artificial vegetation to record velocity and turbulence data for shallow flows with an emergent vegetation patch located at one side of the flume. **Figure 2.8** has been taken from their work and shows the recorded longitudinal velocity and the Reynolds stress within vegetated bank flow. **Figure 2.8** (left) shows the longitudinal velocity profile normalised by the free open flow for different vegetation densities ($\emptyset = 0.02, 0.045$ and 0.10). **Figure 2.8** (right) shows the Reynolds stress recorded for the same flow conditions normalised by the friction velocity. The measurements were taken at mid-depth using a Laser Doppler Velocimetry (LDV) and the transversal position of the vegetation boundary is referred to $y = 0$ cm. The experimental results of **White and Nepf (2007)** plotted in **Figure 2.8** show a low velocity region within the vegetation, a region in the free flow with higher primary velocity and a shear layer between both, similar to the velocity profiles recorded by **Nezu and Onitsuka (2002)**. In addition, the Reynolds stress recorded shows a sharp increase within the shear layer and lower values within the vegetated and the free flow regions. Moreover, **White and Nepf (2007)** recorded an inflection point in the longitudinal velocity profiles close to the vegetation edge ($y \approx 0$ cm).

Santiago Rojas Arques
Department of Civil and Structural Engineering
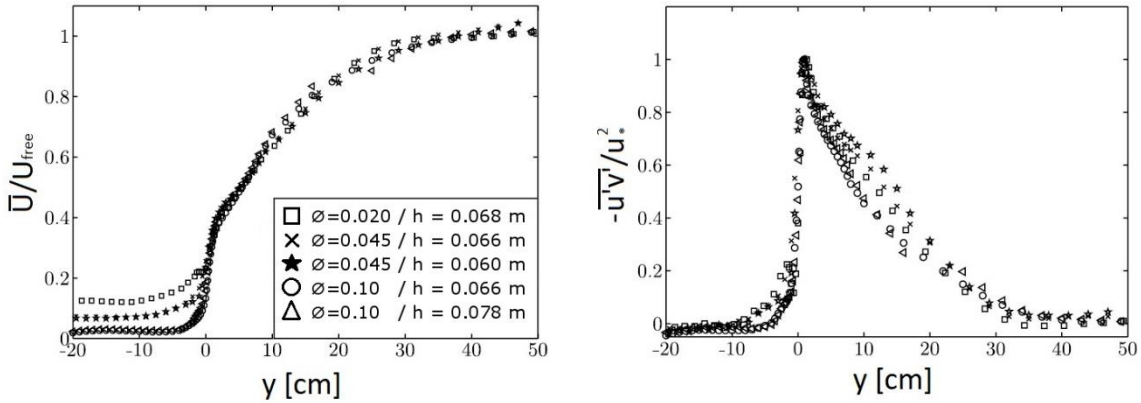
Figure 2.8. Normalised longitudinal velocity and Reynolds stress data along transversal direction for partially vegetated flow (**White and Nepf, 2007**).

Based on their experimental results, **White and Nepf (2007)** defined two different lengths within the shear layer. The inner length is defined from the inflection point to the constant flow region within the vegetation and relates to the penetration of instabilities into the vegetated patch. The outer length goes from the inflection point to the constant free open flow and relates to the size of horizontal vortices generated in the shear layer. **White and Nepf (2007)** pointed out that these two lengths were different, showing an asymmetry of the shear layer. They related the length scale of the inner region to the vegetated resistance.

$$\delta_{Inner} \approx (C_D a)^{-1} \qquad\qquad eq.\,2.28$$

Where δ_{Inner} is the length of the inner layer. However, the outer lengths obtained were found to be independent of vegetation density, suggesting the small influence of vegetation elements in the outer region. In addition, the outer length seemed to be dependent on the water depth and the bed roughness, although a clear relationship was not found. In addition, the position of the velocity inflection point matched with maximum Reynolds stress recorded for all experiments.

White and Nepf (2008) proposed two expressions to define the transversal profile of longitudinal velocity in shear layers generated by partial vegetation. A scheme of this model is plotted in **Figure 2.9**. They ran several experiments using artificial stems to simulate vegetation with different vegetation densities and shallow water depths, recording longitudinal velocity and shear stress. This data was obtained by measuring instantaneous 2-D velocity components with a Laser-Doppler Velocimeter (LDV) at mid-depth.

They considered four different layers along transversal direction with different longitudinal flow velocities. A constant velocity within the vegetation was considered as a momentum balance between gravity and the combination of drag and bed resistance (**eq. 2.26**). In addition, a constant longitudinal velocity was considered in the open flow region far from the vegetation. This velocity was obtained by a balance between bed resistance and gravity force (Manning's and Chezy equations) introduced in **Section 2.1.**

Within the interface between vegetation and the free open flow region, a high shear produces a sharp transition between the vegetated velocity and the faster velocity outside the vegetation. **White and Nepf (2008)** described this velocity profile in the inner region by a hyperbolic tangent shear profile.

$$U_{Inner} = U_{Veg} + U_S * \left(1 + \tanh\left(\frac{y - y_o}{\delta_{Inner}}\right) \right) \qquad eq. 2.29$$

Where y_o is the position of the inflection point and $U_S = U(y_o) - U_{Veg}$ is the slip velocity. They estimated values of δ_{Inner}, y_o and U_S using a non-linear regression (using the Matlab function "NLINFIT.M") based on their experimental values. The results of **White and Nepf (2008)** showed that the inflection point was located at the vegetation limit except for the sparse case ($\emptyset = 0.02$) where it was located at $y_o \approx 2d$. In addition, their results suggested a dependence between δ_{Inner} and the length scale of vegetated drag, with a minimum inner length that penetrated at least into the first row of stems. Thus, they suggested the following empirical expression to obtain the length of the inner layer.

$$\delta_{Inner} = \max(c_1 (C_D a)^{-1}, c_2 d) \qquad eq. 2.30$$

Where parameters $c_1 = 0.5$ and $c_2 = 1.8$ were obtained from experimental results. The outer layer was considered independent of the inner layer. The size of the shear layer outside the vegetation was obtained from the balance between the pressure gradient and the surface slope and considering a constant eddy viscosity (**White and Nepf, 2007**). Thus, the solution follows a quadratic function.

$$U_{Outer} = U_m + \left(U_{free} - U_m\right) * \left[\frac{y - y_m}{\delta_{Outer}} - \frac{1}{4}\left(\frac{y - y_m}{\delta_{Outer}}\right)^2\right] \qquad eq. 2.31$$

Where δ_{Outer} is the length of the outer layer, y_m is the position at which inner and outer slopes match, and $U_m = U_{Outer}(y_m)$. Using experimental data, an initial value for y_m was considered and the value of δ_{Outer} was obtained using a quadratic regression. This process was repeated until the slopes of the inner and outer layers matched at y_m. A scheme with the different parameters introduced by **White and Nepf (2008)** is plotted in **Figure 2.9**.
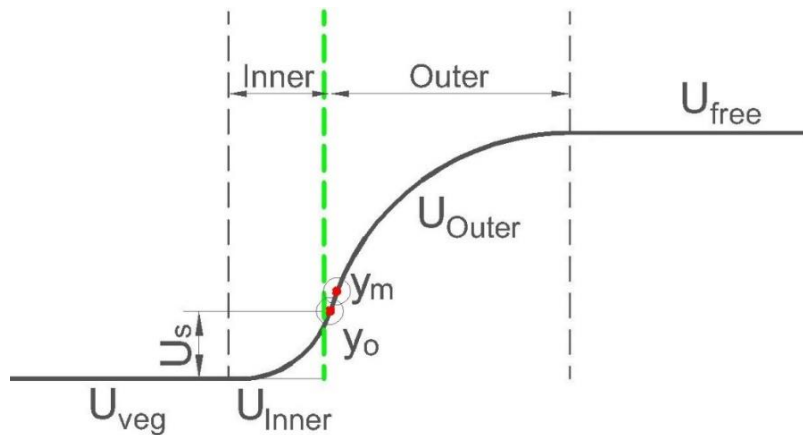
Figure 2.9. Scheme of model proposed by **White and Nepf (2008).**

Later, **Tang et al (2009)** and **Cheng et al (2010)** proposed analytical solutions for partially vegetated compound channels. In both cases, authors considered effects from secondary currents whereby the transverse velocity gradient of secondary currents and the eddy viscosity should be known and introduced into their models. This assumption matched with previous results obtained in shear layers generated in compound channels (**Huai et al., 2008**). However, this assumption was not considered in **White and Nepf (2007)** work, where secondary currents were neglected to obtain the mean longitudinal velocity profile, for an experimental range of $\emptyset = 0.02 - 0.1$, $h = 0.055 - 0.139$ m and $U_{Free} = 0.0382 - 0.2397$ m/s.

Santiago Rojas Arques
Department of Civil and Structural Engineering

More recently, **Meftah and Mossa (2016a** and **2016b)** proposed a different approach to define the longitudinal velocity profile in partially vegetated flows. They ran several experiments in an open channel of 4 m width and installed a uniform patch of artificial cylinders in the centre of the channel with a length of 3 m, allowing a free flow region at each side between the channel wall and the patch. Different vegetated patch widths and water depths were established, and a solid volume fraction of $\emptyset = 0.0028$ was fixed. For each flow condition, the three velocity components were recorded for several transverse profiles using an ADV located at mid-depth.

Their experimental data show that, once the flow enters in the partially vegetated region, the flow within the arrays starts to decelerate due to the increase of drag and the flow velocity within the unobstructed region starts to increase. These effects continue until the flow reaches a point in which both the flow velocity within the obstructed region and within the free flow region no longer change in the lengthwise direction and the shear layer produced between the two constant layers is completely developed. Experimental results with the same flow depth and flow rate, but different contraction ratios (the ratio between the obstructed and the unobstructed widths) show that higher velocities were recorded in the free flow region for higher ratios, and thus narrower unobstructed widths. These results suggest that in real rivers an increase of the contraction ratio could increase the erosion of the riverbanks. Moreover, experimental results show that the peak of the Reynolds stress was shifted away from the vegetation boundary. This displacement of the maximum Reynolds stress is in accordance with that observed by **White and Nepf (2008)** for sparse vegetation densities.

Based on their experimental results, **Meftah and Mossa (2016a** and **2016b)** proposed a modified log–law to describe the longitudinal velocity profiles within the fully shear layer in the outer region (between the free flow region and the inflection point) and a polynomial expression to define the shear layer within the inner region (between the inflection point and the vegetated velocity region). For these proposed expressions, different physical variables were defined using empirical relationships obtained from the experimental data. However, some of the proposed parameters were found to be constant, which may not be applicable to other scenarios, (i.e. with different vegetation densities).

2.4. Mixing Processes

Mixing processes are all mechanisms involved when a solute is introduced into a flow and it starts to spread out from of the source. The key processes that interact in the transporting and spreading of the solute include:

Advection

"*Advection is the bodily movement of a parcel of fluid resulting from an imposed current*" **Rutherford, 1994**. For a given flow, a tracer injected into it will move downstream with a certain velocity, which depends on the velocity of the flow and the buoyancy of the tracer. In a scenario with pure advection without any boundary effect, the cloud of tracer would only move with the flow, without any mixing.

Santiago Rojas Arques
Department of Civil and Structural Engineering

Molecular and Turbulent Diffusion

If a tracer with no buoyancy is introduced into a stagnant water body far enough from any boundary, it will spread out slowly in all directions at the same rate due to random molecular motions. This process is called molecular diffusion and can be described by Fick's first law.

$$J_x = -\eta \frac{\partial c}{\partial x} \qquad eq.\,2.32$$

Where J_x is the mass flux (in this case in the x direction), c is concentration and η is the molecular diffusion coefficient.

However, in most rivers flow is characterised by high Reynolds number and is fully turbulent apart from a small area close to boundaries. When flow is turbulent, the velocity at each spatial point exhibits random fluctuations in time with respect to the time-averaged velocity. These fluctuations increase local concentration gradients by shearing the flow and hence increasing the molecular diffusion. This process is called turbulent diffusion and it can be defined as the accelerated process of molecular diffusion due to the shearing of flow in turbulence regimes.

Shear Dispersion

In a flow with no obstacles, transversal and vertical profiles of longitudinal velocity are not constant due to resistance from channel boundaries (**Section 2.1**). Thus, the tracer near the banks and bed will travel slower than the tracer in the centre of the channel. If an initial transversal line of tracer is considered as it is shown in **Figure 2.10**, this effect mentioned will cause the tracer to take a non-linear shape due to differences in longitudinal velocity. As a result, the transverse concentration gradient increases, promoting transverse mixing. Shear dispersion can be defined as the spreading of tracers due to velocity gradients on the flow velocity profiles (**Rutherford, 1994**). This effect is produced in both transversal and vertical directions, although in most open channel flows the transversal velocity shear is greater than the vertical shear as higher velocity gradients are produced (**Fischer, 1967**).
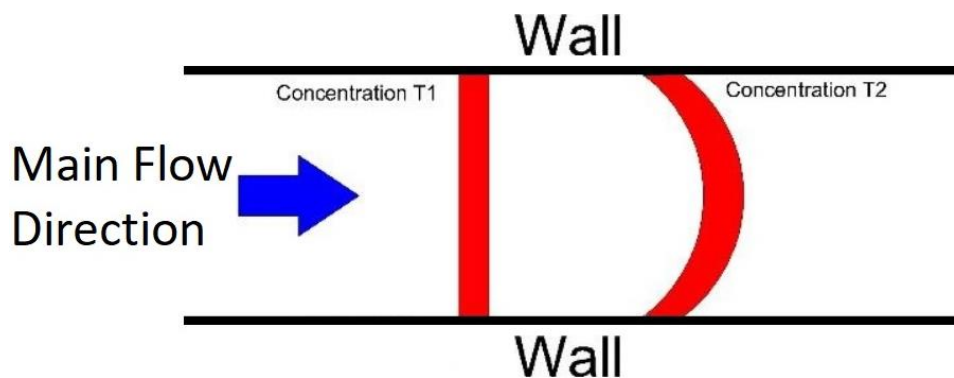
Figure 2.10. Plan view scheme of shear dispersion effect.

In order to define a governing equation for mixing in open channels, a laminar flow condition is first considered. In this flow, there is no diffusion produced by turbulence so only molecular diffusion defined by Fick's first law (**eq. 2.32**) and advection affect mixing. Considering a body of fluid moving with the flow and a solute passing through it, both molecular diffusion and advection processes can be combined by considering conservation of mass as:

Santiago Rojas Arques
Department of Civil and Structural Engineering

$$\frac{\partial c}{\partial t} + \frac{\partial J}{\partial x} = 0 \qquad\qquad eq.\,2.33$$

Combining this equation with Fick's first law (**eq. 2.32**)

$$\frac{\partial c}{\partial t} - \frac{\partial}{\partial x}\left(\eta \frac{\partial c}{\partial x}\right) = 0 \qquad\qquad eq.\,2.34$$

Assuming that mixing is constant along the distance x

$$\frac{\partial c}{\partial t} = \eta \frac{\partial^2 c}{\partial x^2} \qquad\qquad eq.\,2.35$$

Eq. 2.35 is known as the diffusion equation and defines the transport of a solute by a Fickian diffusion process. This expression can be applied to an open channel flow element by considering a steady laminar flow and defining it for all three orthogonal directions. For each direction, the total flux can be defined as:

$$J_x = uc - \eta \frac{\partial c}{\partial x} \qquad\qquad eq.\,2.36$$

$$J_y = vc - \eta \frac{\partial c}{\partial y} \qquad\qquad eq.\,2.37$$

$$J_z = wc - \eta \frac{\partial c}{\partial z} \qquad\qquad eq.\,2.38$$

Where the components uc, vc and wc represent the advection process for each direction. In addition, the mass variation of solute can be defined as:

$$\frac{\partial c}{\partial t}\Delta x \Delta y \Delta z \qquad\qquad eq.\,2.39$$

The total flux (TF) in each coordinate direction can be defined as.

$$TF_x = \left(\frac{\partial J_x}{\partial x}\Delta x\right)\Delta y \Delta z \qquad\qquad eq.\,2.40$$

$$TF_y = \left(\frac{\partial J_y}{\partial y}\Delta y\right)\Delta x \Delta z \qquad\qquad eq.\,2.41$$

$$TF_z = \left(\frac{\partial J_z}{\partial z}\Delta z\right)\Delta x \Delta y \qquad\qquad eq.\,2.42$$

Considering that the total flux produced in all directions must be equal to the mass change of the solute within the fluid element.

$$\frac{\partial c}{\partial t} + \frac{\partial J_x}{\partial x} + \frac{\partial J_y}{\partial y} + \frac{\partial J_z}{\partial z} = 0 \qquad\qquad eq.\,2.43$$

If expressions in **eq. 2.36**, **2.37** and **2.38** are combined and molecular diffusion is considered uniform in all coordinates.

$$\frac{\partial c}{\partial t} + u\frac{\partial c}{\partial x} + v\frac{\partial c}{\partial y} + w\frac{\partial c}{\partial z} = \eta\left(\frac{\partial^2 c}{\partial x^2} + \frac{\partial^2 c}{\partial y^2} + \frac{\partial^2 c}{\partial z^2}\right) \qquad eq.\,2.44$$

Santiago Rojas Arques
Department of Civil and Structural Engineering

Eq. 2.44 is the advection diffusion equation and predicts the concentration of a conservative solute within laminar flow conditions at any position if the molecular diffusion coefficient is known.

However, most of flows in rivers and channels have a turbulence regime and hence turbulent diffusion must also be considered. **Taylor (1921)** analysed theoretically the spreading of a cloud of tracer particles in a stationary homogeneous turbulence field. In this analysis, a coordinate system in which the origin moves with the cloud was considered and the mixing process was studied. This analysis shows that, after a time T_x from the injection of the tracer, the variance of the cloud increases linearly with time and Fick's law can be applied to turbulent flows. Thus, by analogy based on Taylor's analysis the turbulent diffusive flux can be described as.

$$J_x = u'c' = -e_x \frac{\partial \bar{c}}{\partial x} \qquad eq.\,2.45$$

$$J_y = v'c' = -e_y \frac{\partial \bar{c}}{\partial y} \qquad eq.\,2.46$$

$$J_z = w'c' = -e_z \frac{\partial \bar{c}}{\partial z} \qquad eq.\,2.47$$

Where e_x, e_y and e_z are the turbulent diffusion in each direction and $\bar{c}$ denotes the temporally averaged concentration. Using the same steps as followed for the advection diffusion equation for laminar flows, the following equation can be obtained.

$$\frac{\partial \bar{c}}{\partial t} + \bar{u}\frac{\partial \bar{c}}{\partial x} + \bar{v}\frac{\partial \bar{c}}{\partial y} + \bar{w}\frac{\partial \bar{c}}{\partial z} = (\eta_x + e_x)\frac{\partial^2 \bar{c}}{\partial x^2} + (\eta_y + e_y)\frac{\partial^2 \bar{c}}{\partial y^2} + (\eta_z + e_z)\frac{\partial^2 \bar{c}}{\partial z^2} \quad eq.\,2.48$$

In this equation both molecular diffusion and turbulent diffusion are described. However, in turbulent flow molecular diffusion is negligible compared with turbulent diffusion (turbulent diffusion is of the order of 10^{-3} m^2/s, whereas the molecular diffusion is typically 10^{-9} m^2/s). Thus, either if molecular diffusion is neglected or if it is considered into the turbulent diffusion term, **eq. 2.48** becomes:

$$\frac{\partial C}{\partial t} + u\frac{\partial C}{\partial x} + v\frac{\partial C}{\partial y} + w\frac{\partial C}{\partial z} = \frac{\partial}{\partial x}\left(D_x\frac{\partial C}{\partial x}\right) + \frac{\partial}{\partial y}\left(D_y\frac{\partial C}{\partial y}\right) + \frac{\partial}{\partial z}\left(D_z\frac{\partial C}{\partial z}\right) \quad eq.\,2.49$$

Where $C = \bar{c}$ and D_x, D_y and D_z are the longitudinal, transversal and vertical mixing coefficients respectively. This is the general three-dimensional Advection – Diffusion Equation (ADE) conventionally used (**Rutherford, 1994**). However, this equation requires a lot of information about the velocity and mixing coefficients and in most practical cases, **eq. 2.49** can be simplified depending on the scenario studied.

In most real rivers, the channel width is greater than the water depth. With this consideration, three different zones can be defined. If an instantaneous point source is considered, the region just downstream is considered as the near field. In this region the tracer is mixed in all three directions and the full 3-D equation is required (**Rutherford, 1994**). As the water depth is smaller than the channel width, the concentration becomes well mixed first in the vertical direction. The mid field is the region where the concentration gradients in the vertical direction are negligible. Thus, the equation can be averaged over the depth, neglecting vertical components and becoming a 2D equation, where both transverse and longitudinal mixing components are studied.

Santiago Rojas Arques
Department of Civil and Structural Engineering

Finally, in the far field the tracer becomes well mixed also transversally, and **eq. 2.49** can be simplified into a 1D form where only the longitudinal components are studied. In addition, if the problem assumes a steady source rather than an instantaneous one, time dependant elements can be removed and hence longitudinal components can be neglected for each field explained previously. Therefore, after fully cross sectional mixing, concentration at each point in time and space becomes uniform.

2.4.1. Vertical Mixing

In rivers, the main mechanism that promotes vertical mixing is turbulence generated by velocity shear at the channel bed. In a wide open channel flow, where effects from walls are negligible, the vertical mixing coefficient depends on the turbulence generated by the channel bed. Reynolds analogy defines the vertical mixing as a function of the eddy viscosity (ε):

$$D_z = Sc\varepsilon \qquad\qquad eq.\,2.50$$

Where Sc is the Schmidt number. While a universal value for this parameter has not been found, it is commonly assumed that by analogy between momentum and mass transport (Prandtl analogy) $Sc = 1$. However, **Gualtieri et al. (2017)** reviewed different values of Schmidt number obtained from previous work. They noticed that most of the discussed work proposed a Sc value between 0.1 and 1 (**Arnold et al., 1989; Lin and Shiono, 1995** and **Simoes and Wang, 1997**), although results from sediment-laden open channel flows suggest a value of Sc between 1.4 and 2.1. **Djordjevic (1993)** presented a mathematical model for transport processes validated with his own experiments, obtaining a $Sc \approx 1$, same result as that obtained by **Simoes and Wang (1997)** for the vertical mixing. Finally, **Gualtieri et al. (2017)** obtained a value of $Sc = 1.3$ to best predict the transverse mixing in a rectangular open channel flow.

If a value of $Sc = 1$ is taken for neutrally buoyant tracers (**Rutherford, 1994**) Shear stress (**eq. 2.21**) can be considered as

$$\tau_t = \rho u^{*2}\left(1 - \frac{z}{h}\right) = \rho\varepsilon\frac{dU}{dz} \qquad\qquad eq.\,2.51$$

Substituting **eq. 2.50** into **eq. 2.51.**

$$D_z = \frac{\rho u^{*2}\left(1 - \frac{z}{h}\right)}{\rho\frac{dU}{dz}} \qquad\qquad eq.\,2.52$$

Assuming the vertical profile of longitudinal velocity follows a logarithmic law (**eq. 2.10**).

$$D_z = \kappa u^* z\left(1 - \frac{z}{h}\right) \qquad\qquad eq.\,2.53$$

Finally, **Jobson and Sayre (1970)** suggested that vertical concentration profiles are not sensitive to the vertical variation of D_z and hence they defined the overall vertical mixing coefficient over the water depth as.

$$D_z = \frac{\kappa}{6}hu^* = 0.067hu^* \qquad\qquad eq.\,2.54$$

The distance needed for a tracer to become vertically well mixed depends on the water depth, the vertical mixing coefficient and the location of the source (**Rutherford, 1994**).

Santiago Rojas Arques
Department of Civil and Structural Engineering

$$L_{z_{Middle}} = 0.134 \frac{Uh^2}{D_z} \qquad\qquad eq.\,2.55$$

$$L_{z_{Top}} = L_{z_{Surface}} = 0.536 \frac{Uh^2}{D_z} \qquad\qquad eq.\,2.56$$

Where U is the depth-averaged longitudinal velocity, $L_{z_{Middle}}$ is the distance needed for the solute to become vertically well mixed if the point source is located in the middle of the water depth, and $L_{z_{Top}}$ and $L_{z_{Surface}}$ are the distance if the injection point is located at the bottom depth or at the surface respectively (**Rutherford, 1994**).

2.4.2. Transverse Mixing

For a steady-state injection ($\partial C / \partial t = 0$) of a homogeneous vertical line of solute, the vertical concentration gradient becomes negligible and thus the vertical mixing component can be neglected. Therefore, the ADE can be considered as a depth-averaged process.

$$u \frac{\partial hC}{\partial x} + v \frac{\partial hC}{\partial y} = \frac{\partial}{\partial x}\left(hD_x \frac{\partial C}{\partial x}\right) + \frac{\partial}{\partial y}\left(hD_y \frac{\partial C}{\partial y}\right) \qquad\qquad eq.\,2.57$$

If a straight channel is considered, transverse mean velocity is negligible compared with the longitudinal component. In addition, the steady-source injection produces a constant rate of solute injected into the flow and hence the longitudinal mixing component can be neglected (**Rutherford, 1994**).

$$u \frac{\partial hC}{\partial x} = \frac{\partial}{\partial y}\left(hD_y \frac{\partial C}{\partial y}\right) \qquad\qquad eq.\,2.58$$

Under the assumption of all constant longitudinal velocity, water depth and transverse mixing coefficient along the spanwise direction, **eq. 2.58** can be solved as:

$$C(x,y) = \frac{M}{h\sqrt{4\pi D_y Ux}} exp\left[-\frac{U\left(y - y_{Inj}\right)^2}{4D_y x}\right] \qquad\qquad eq.\,2.59$$

Where y_{Inj} is the transversal location of the injection and M is the injection rate. Solute transversal profiles under **eq. 2.59** exhibit a Gaussian shape. Transverse mixing becomes especially important in scenarios where the injection can be considered continuous and longitudinal processes can be neglected. In most wide channels, the velocity gradient is assumed to be zero in the centre of the channel and thus **eq. 2.52** cannot be resolved.

Different methods have been proposed to determinate the transverse mixing coefficients (**Baek and Seo, 2016**). A widely used method for the calculation of transverse mixing coefficient is the moment-based method. This method is based on the growth in the streamwise direction of the second moment (variance) of the concentration data. **Sayre and Chang (1968)** proposed an expression to calculate the transverse mixing coefficient under steady-state conditions by assuming a linear increase of variance with distance.

$$D_y = \frac{U}{2} \frac{d\sigma_y^2}{dx} \qquad\qquad eq.\,2.60$$

Where σ_y^2 is the variance of the transversal solute profile and therefore $d\sigma_y^2/dx$ is the variation of variance along the channel length. This variance was obtained using the standard method of moments (**Rutherford, 1994**) for each transversal concentration profile.

Santiago Rojas Arques
Department of Civil and Structural Engineering

$$M_0 = \int_1^\infty C_i \, dy \qquad\qquad eq.\,2.61$$

$$M_1 = \int_1^\infty (C_i \, dy) y_i \qquad\qquad eq.\,2.62$$

$$M_2 = \int_1^\infty (C_i \, dy) y_i^2 \qquad\qquad eq.\,2.63$$

$$Centroid = \varphi = \frac{M_1}{M_0} \qquad\qquad eq.\,2.64$$

$$Variance = \sigma_y^2 = \frac{M_2}{M_0} - \varphi^2 \qquad\qquad eq.\,2.65$$

Where C_i is the concentration value at each spanwise position y_i. However, when this method is used, errors in the calculation of the transverse mixing coefficient are susceptible to be produced. These errors may be produced as the transverse mixing coefficient is obtained from evaluating the rate of change of the variance of the concentration profiles. This rate is quite sensible to the accurate identification of the end of the concentration profile tails, and thus the "cut off" considered to delimitate the experimental concentration levels from the instrumentation noise critically affects the variance evaluation (**Shucksmith, 2008**; **Baek and Seo, 2016**).

The use of optimization procedures improves the accuracy obtaining of the mixing coefficients by eliminating the errors produced in the variance calculation. These procedures are based on the comparison of experimental concentration data with those predicted using any equation or set of equations that properly describe the behaviour of the pollutant plume under certain conditions (e.g. **eq. 2.59**). **Boxall (2000)** and **Dennis (2000)** suggested that using these optimization procedures the dependence of mixing coefficient results on the cut off level chosen becomes relatively insensitive. Moreover, **Boxall (2000)** argued that a cut off level up to a 10 % of the peak concentration value can still produce accurate mixing coefficients using these optimization procedures. More complex methods rely on fitting models of various complexity to data and calibrating the transverse mixing coefficient directly, such as the Computational Fluid Dynamics (CFD) models, which use numerical methods and algorithms to solve fluid dynamics problems (**Sonnenwald et al., 2019, Ghani et al., 2019**). These solutions require a high computational capacity and they typically require the use of experimental data for their validation.

Webel and Schatzman (1984) ran several experiments in a straight channel to measure transverse mixing coefficients. The solute was injected in the centre of the channel and results showed that for a width-depth ratio large enough ($W_d/h \geq 5$) to avoid any effect of the wall-shear zone in the plume, the transverse mixing coefficient is independent of W_d/h. In addition, for $W_d/h \geq 5$ their results suggested a constant dimensionless transverse mixing value of $D_y/hu^* = 0.13$ in straight, uniform and rectangular channel flows.

Santiago Rojas Arques
Department of Civil and Structural Engineering

Rutherford (1994) collected and compared several previous research data of transverse mixing in natural straight channels and concluded that the value seems to be around.

$$0.15 < \frac{D_y}{hu^*} < 0.3 \qquad\qquad eq.\,2.66$$

However, this range of values is affected by variations in both geometry (meanders) and flow field (secondary currents). In meandering channels, experimental transverse mixing results collected by **Rutherford (1994)** seemed to fall in the range:

$$0.3 < \frac{D_y}{hu^*} < 0.9 \qquad\qquad eq.\,2.67$$

Moreover, for strong curved channels transverse mixing coefficients found are higher.

$$1.0 < \frac{D_y}{hu^*} < 3.0 \qquad\qquad eq.\,2.68$$

Chau (2000) ran several experiments in straight channels using different bed roughness and flow conditions and used a continuous injection of dye located in the centre of the channel width. Average dimensionless transverse mixing coefficient obtained for all conditions was $D_y/hu^* = 0.18$, with an error band of $\pm 15\,\%$.

Lau and Krishnappan (1977) studied transverse mixing in straight laboratory channels and they suggested that coefficients are affected by the ratio between water depth and width. However, **Webel and Schatzmann (1984)** argued that this assumption is only valid for small ratios and they concluded that the most important factor in straight channels is the turbulent diffusion. **Shiono and Feng (2003)** studied both rectangular and compound channels to study the effect of secondary currents. They suggested that for weak secondary currents found in rectangular channels (with secondary current vectors below $1\,\%$ of the main flow), turbulent diffusion is the main factor that affects transverse mixing processes. However, in compound channels, secondary currents become more important (with secondary current vectors around $4-5\,\%$ of the main flow), and they strongly affect the transverse mixing processes. These secondary currents are also produced in channels with a high sinuosity, increasing the overall transverse mixing coefficient (**eq. 2.68**) and producing a displacement of the position of the concentration peaks and a skew in the concentration distribution (**Shiono and Feng, 2003**).

2.5. Transverse Mixing within Emergent Vegetation

As explained in **Section 2.2**, vegetation reduces velocity by increasing drag resistance. In the same way, the dominant turbulent length scale is also reduced from that produced in open channels (no vegetation) to the smaller of the stem diameter (d) or the mean distance between stems (**Tanino and Nepf, 2008b**).

Nepf et al. (1997) measured transversal mixing in vegetated flows using artificial emergent cylinders as vegetation. Their results showed that for $Re_{stem} > 200$ diffusivity in vegetated flows increased compared with non-vegetated scenarios with the same flow velocity. **Nepf (1999)** described diffusion within vegetation as a combination of two processes: turbulent diffusion produced by stem-scale vortices created by vegetation and mechanical diffusion produced by tortuosity paths that the solute follows through between the stems. Her results showed a decrease of diffusivity within emergent vegetated flows compared with non-

Santiago Rojas Arques
Department of Civil and Structural Engineering

vegetated flows with the same water depth. **Nepf (1999)** argued this decrease is related to the decrease of eddy size produced by stems although the turbulence intensity may increase. This is in accordance with experimental results obtained by **De Serio et al. (2018)**, who used artificial rigid emergent cylinders in a row distribution, and measured turbulent intensities and dispersion coefficients at different positions within the vegetation.

      Tanino and Nepf (2008a) studied the relationship between transverse mixing and vegetation density by running several tests using random artificial arrays and different stem densities from $\emptyset = 0.01 - 0.35$ for high stem-scale Reynolds numbers ($Re_{stem} > 250$). Their results are shown in **Figure 2.11**, where the experimental results are plotted in addition to the proposed expression for the net lateral dispersion and the corresponding dispersions produced by each phenomenon (turbulent diffusion and heterogeneous velocity). **Tanino and Nepf (2008a)** suggested a rapid increase of the dimensionless transverse mixing ($D_y/U_{Veg}d$) for densities between $\emptyset = 0 - 0.031$. However, for denser vegetation the dimensionless transverse mixing decreases for values between $\emptyset = 0.031 - 0.2$. Finally, for the densest cases ($\emptyset = 0.2 - 0.35$), the transverse mixing increases again, although this trend is more gradual than for sparse cases.
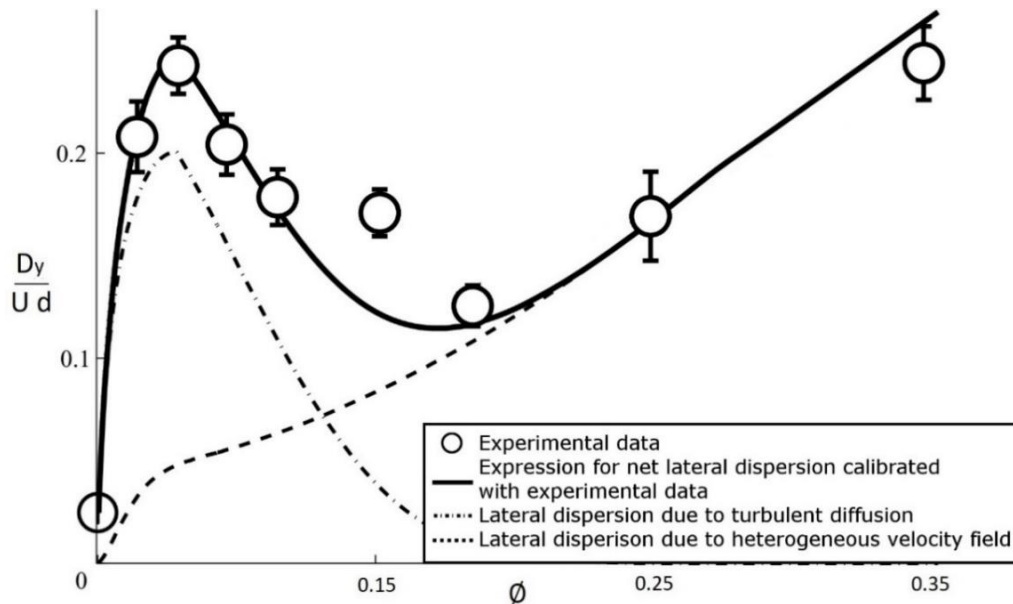
Figure 2.11. Dimensionless transverse mixing coefficients versus vegetation density (**Tanino and Nepf, 2008a**).

      Nepf (2012) argued that for densities smaller than $\emptyset < 0.1$ turbulent diffusion is the dominant effect on transverse mixing, whilst for higher densities $\emptyset > 0.15$ or for vegetated flows without turbulence ($Re_{stem} < 100$) mechanical diffusion is the main contributor. Two different expression were proposed, consistent with previous studies **(Nepf et al., 1997, Nepf, 2004, Tanino and Nepf, 2008a)**, to describe transverse mixing in emergent vegetated flows:

$$D_y = 0.2U_{Veg}d \qquad\qquad if\ \emptyset < 0.1 \qquad\qquad eq.\,2.69$$

$$D_y = U_{Veg}ad^2 \qquad\qquad if\ \emptyset > 0.15\ or\ Re_{stem} < 150 \qquad\qquad eq.\,2.70$$

      However, previous studies suggested a large variability in transverse mixing results within emergent vegetation. One of the factors that results in this variability is produced by the random distribution of vegetation stems, which affects the creation of turbulence structures

Santiago Rojas Arques
Department of Civil and Structural Engineering

within the vegetated flow, and thus the mixing processes. Whilst the periodic distance between stems for staggered configurations generated periodic turbulence structures (**Meftah and Mossa, 2013)**, in random vegetation the variation of space between stems produces a breakdown of these structures and thus affects the local transverse mixing. This effect is also noticed in the experimental results of **Serio et al. (2018).** Their results showed that different turbulent length scales and dispersion coefficients were obtained depending whether the data was measured between two consecutive stems in the flow direction or within the free corridors allowed between rows. Therefore, different transverse mixing may be expected between row, staggered and random vegetation distributions (**Sonnenwald et al., 2017**). This fact was also discussed by **Sonnenwald et al. (2017)**, who compared different results from previous researchers (**Nepf et al., 1997, Nepf, 1999, Serra et al, 2004 and Tanino and Nepf, 2008a**) as well as results obtained from their own experiments. They discussed the variability of the dimensionless transverse mixing coefficient ($D_y/U_{Veg}d$), showing that although the model proposed by **Nepf (2012)** is the most accurate, significant variability is found between results from other experiments and those predicted by this model under the same flow and vegetation conditions.

2.6. Mixing in Vegetated Shear Layers

As explained in **Section 2.3**, shear layers are characterised by two co-flowing layers with different main flow velocities, creating a velocity gradient between both flow layers and thus a shear layer characterised by coherent eddy structures. Therefore, mixing coefficients cannot be considered constant within the shear layer.

Ghisalberti and Nepf (2005) studied the vertical variation of vertical mixing along a shear layer produced by submerged artificial stems. They conducted repeated experiments with the same water depth but with different vegetation densities, producing an increasing shear layer velocity gradient with increasing stem density. They first applied a two-box model to study the exchange coefficient between vegetated and free open flow layers. Their results show that for a given mean flow, the exchange coefficient increases for higher stem densities due to the increase of eddy intensity, obtaining a vertically well-mixed profile more rapidly. They also applied a flux-gradient model to study vertical variability of vertical mixing coefficient along the full water depth. This model assumes that the mass of solute upstream of the control volume (A) must be equal to the mass of solute downstream of the control volume (B) plus the mass flux produced in the vertical direction in the control volume.

$$D_z(z) = \frac{\Delta(\int_0^z UCdz)}{\Delta x \langle \partial C/\partial z \rangle_z} \qquad eq.\,2.71$$

Where $\langle - \rangle$ denotes a longitudinal average between A and B ($\langle \partial C/\partial z \rangle \approx (\partial C/\partial z_A + \partial C/\partial z_B)/2$). Their results are shown in **Figure 2.12**, where data for each vegetation density shows a significant variability of vertical mixing coefficient along the shear layer, achieving a maximum value close to the top of vegetation (dash line) at the location of maximum Reynolds stress. These results were scaled by the velocity increase (ΔU) and the length of the shear layer ($\delta_{V.S.L.}$), suggesting that transport within shear layers can be characterised by properties of the shear layer. In addition, **Ghisalberti and Nepf (2005)** stated two constrain criteria (Cr_1 and Cr_2) to identify the regions of applicability of this model, described in **eq. 2.72** and **2.73** respectively.

Santiago Rojas Arques
Department of Civil and Structural Engineering

$$Cr_1 = \frac{\partial C/\partial z_B}{\partial C/\partial z_A} \leq 3 \qquad\qquad eq.\,2.72$$

$$Cr_2 = \frac{\partial C/\partial z_B}{\max(\partial C/\partial z_A)} = 0.05 \qquad\qquad eq.\,2.73$$
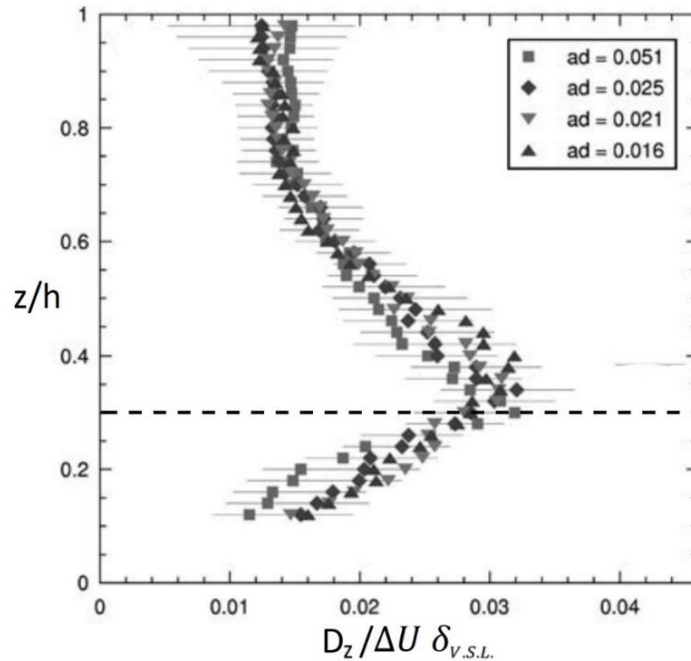
Figure 2.12. Dimensionless variable vertical mixing coefficient within shear layer in submerged vegetated flows **(Ghisalberti and Nepf, 2005).**

Rubol et al. (2016) proposed a semi-empirical model to estimate the variable vertical mixing in submerged vegetated flows. The mean velocity was estimated using the model proposed by **Battiato and Rubol (2014)**, which only requires the value of the permeability of the vegetation and the stem height. Based on their results, **Battiato and Rubol (2014)** suggested that the increase of the vegetation density, and thus the increase of the velocity shear, produces an increase of the asymmetry of the concentration profile. Moreover, they observed that an increase of the vegetation density enhances the vertical mixing, reducing the peak concentration of the plume. **Battiato and Rubol (2014)** concluded that the most important parameter that controls the solute mixing, its asymmetry and the decrease of the peak concentration is the permeability of the vegetated layer. In addition, **Rubol et al. (2016)** used the experimental results obtained by **Ghisalberti and Nepf (2005)** to validate their model. The vertical mixing coefficients were obtained by fitting the experimental concentration data to their proposed model. Their results suggest that a constant value of the vertical mixing coefficient may be accurate enough to reproduce the concentration profiles through and over submerged vegetated flows for dense vegetation. They obtained a constant vertical mixing coefficient of $D_z = 1.9\ \text{cm}^2/\text{s}$ for the first concentration profile that increased for downstream profiles until reaching a constant value of $D_z = 4.5\ \text{cm}^2/\text{s}$. These values agree with the overall vertical mixing obtained by **Ghisalberti and Nepf (2005)** and with those results obtained by **Termini (2019)**, who obtained an overall vertical mixing of $D_z = 5\ \text{cm}^2/\text{s}$ for submerged vegetated flows with a vegetation density $\emptyset = 0.135$.

Santiago Rojas Arques
Department of Civil and Structural Engineering

Variable mixing coefficients were also studied in shear layers generated in compound channels. **Zeng et al. (2008)** studied eddy viscosity in a compound channel. They measured instantaneous longitudinal and transversal velocity component using a 2D Laser Doppler Anemometry (LDA) along the spanwise direction. From this data, turbulent velocity was obtained and eddy viscosity was calculated using the analogy between the Reynolds stress and the viscosity shear stress.

$$\varepsilon_{xy} = \frac{\overline{u'v'}}{\partial U / \partial y} \qquad\qquad eq.\,2.74$$

The eddy viscosity results were averaged for each sub section (the main channel, the floodplain and the side slope between them). In addition, they injected Rhodamine WT constantly and ten transversal tracer profiles were measured by sample tubes connected to a fluorometer. Three different injection locations were considered along the spanwise direction to record tracer concentrations along each subsection, and a constant transverse mixing coefficient was obtained for each sub-section using **eq. 2.59**. Results suggested an increase of transverse mixing processes within the side slope between the two channel sub-sections.

From the same study, **Guymer and Spence (2009)** studied the longitudinal velocity and the variable transverse mixing coefficient in compound channels. Profiles of longitudinal velocity along the channel width presented a similar shape to those obtained in previous studies for partially vegetated flows (**Knight and Shiono, 1996**). The longitudinal velocity results showed a velocity shear layer between two constant velocity regions and an inflection point located at the edge between the floodplain and the side slope. The transverse mixing coefficients were obtained using the generalized change of moment method proposed by **Holley et al. (1972),** which relates the variation of the transverse mixing coefficient with the longitudinal rate of change of mass flux variance**.** The variation of the variance between consecutive transverse concentration profiles was studied by assuming three sections with different transverse mixing coefficient (the main channel, a region on the floodplain far from the slope and sloping the region between them). Results suggested an increase of the transverse mixing coefficient for the region located at the side slope, matching with the increase of the Reynolds stress. However, the generalised change of moment method accounts for the variance of narrow portions of the concentration profiles. This parameter is quite sensitive to the values of concentration at each position, and thus small errors or variations in the measurement of the concentration profile may produce high variations in the variance. Moreover, as it was discussed in **Section 2.4.2**, the variance obtained from the concentration profiles is quite sensible to the cut-off level applied to the profiles, and thus errors in the calculation are susceptible to be produced.

Besio et al. (2012) ran several experiments to measure variable transverse mixing coefficients in compound channels by injecting the solute in the main channel or in the floodplain. From these experiments, they calculated different constant transverse mixing coefficients for the main channel and the floodplains respectively. Their results suggest a dependence between constant transverse mixing coefficients and depth ratio between the main channel and the floodplain. Results showed high transverse mixing coefficients for higher depth ratios and a decrease of the coefficients when the depth ratio became close to 1. This trend suggests a dependence between the increase of the overall transverse mixing processes and the increase of the longitudinal flow velocity gradient between the main channel and the floodplain.

Santiago Rojas Arques
Department of Civil and Structural Engineering

Tabatabei et al. (2013) measured constant values of transverse mixing coefficients in channels with dunes introduced into the bed. They ran different experiments with and without vegetation at the channel walls to study the variation of the overall transverse mixing with the presence of riparian vegetation. This riparian vegetation was located at each channel wall with a water depth range of $28 - 36$ cm and a mean longitudinal velocity flow range of $24 - 24.87$ cm/s. Instantaneous longitudinal, transversal and vertical velocity components were recorded for each test. Their results showed an increase of the overall transverse mixing coefficient if the riparian vegetation was installed at both sides of the channel.

West (2016) studied variable transverse mixing coefficients in channels with vegetation at one bank using both artificial and real vegetation. The vegetated bank of artificial vegetation was designed using two different vegetation densities ($\emptyset = 0.02$ and $\emptyset = 0.005$). In the same way, two different scenarios were studied using real vegetation. For these cases, Cattail reeds (*typha*) were cultivated in winter and summer seasons to study real vegetation at two different stages. Real vegetation presented a non-homogenous distribution over the vegetated bank with an average vegetation density of $\emptyset = 0.012$ and $\emptyset = 0.037$ for the winter and summer stages respectively.

The applicability of the flux gradient model proposed by **Ghisalberti and Nepf (2005)** (**eq. 2.71**) was studied considering the constraint criteria defined in **eq. 2.72** and **2.73**, and using new experimental data. Experimental data recorded for the lowest, artificial vegetation density ($\emptyset = 0.005$) was fitted for both upstream and downstream concentration profiles with a 3rd order Gaussian distribution. The constraint criteria were applied to the fitted concentration profiles within the shear layer and the regions where the flux gradient model cannot be applied were studied. First, two small violating regions close to the maximum concentration were observed. These two regions were attributed to differences in the sign of the concentration gradients. These regions produced a discontinuity between the regions where the criteria were not violated, resulting in a transverse mixing profile with a reduced physical meaning. In addition, two violating regions were observed at the tails of the concentration profiles, these regions being wider than those obtained at the peak of concentration profiles.

Moreover, **West (2016)** noticed that the violating regions influenced the estimation of the transverse mixing coefficients within the non-violating regions, distorting the $D_y(y)$ profile. Furthermore, the flux gradient model cannot be used in those regions where there is a change in the concentration gradient sign from upstream to downstream concentration profiles, and thus the model produced unreliable values of $D_y(y)$ in the vicinity of the shear layer. As a result, the flux gradient model cannot be certified as an accurate method to quantify a variable transverse mixing coefficient profile in partially vegetated flows. Therefore, **West (2016)** proposed a Finite Difference Model (F.D.M.) to simplify the ADE for a steady-source and considering a vertically well-mixed concentration profile.

$$U(y)h(y)\frac{\partial C(x,y)}{\partial x} = \frac{\partial}{\partial y}\left[h(y)D_y(y)\frac{\partial C(x,y)}{\partial y}\right] \qquad eq.\,2.75$$

Steps considered for the F.D.M. are further described in **Section 2.6.1**. An optimization routine was performed in order to obtain the variable transverse mixing profiles $D_y(y)$ that maximised the fit between the predicted concentration profiles and the experimental concentration profiles. However, in order to reduce computational demand and to give a physical meaning to the variable $D_y(y)$, **West (2016)** proposed some initial shapes of $D_y(y)$ based on results obtained by **Ghisalberti and Nepf (2005)**, and **Guymer and Spence (2009)**.

Santiago Rojas Arques
Department of Civil and Structural Engineering

Three different shapes were proposed by **West (2016)** as shown in **Figure 2.13**, including two constant transverse mixing layers within the vegetation and in the free open flow respectively, a triangular transverse mixing profile and a Gaussian transverse mixing profile. For the last two types of profile, results obtained based on the optimization showed a peak of D_y within the shear layer. The length of variable transverse mixing region was fixed using the shear layer length ($\delta_{Inner} + \delta_{Outer}$).
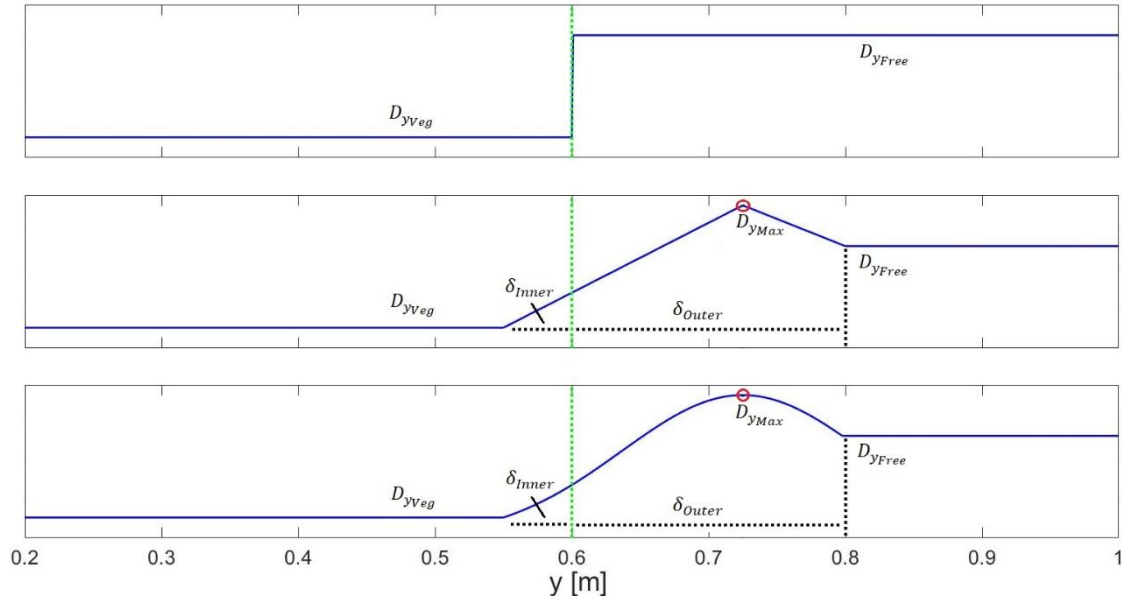
Figure 2.13. Schemes of $D_y(y)$ proposed by **West (2016).**

Results obtained by **West (2016)** by assuming two constant D_y regions (**Figure 2.13 a**) showed a trend between the increase of the overall $D_{y_{Free}}$ and the increase of the velocity difference ($\Delta U = U_{Free} - U_{Veg}$). These results agree with previous results obtained by **Ghisalberti and Nepf (2005)** for submerged vegetation and those obtained by **Zeng et al. (2008), Guymer and Spence (2009)** and **Besio et al. (2012)** in compound channels as explained previously in this section.

For the results obtained by assuming the triangular and the Gaussian shapes, the optimization routine was designed to find the maximum transverse mixing value ($D_{y_{Max}}$) and its position. The results for the variable $D_y(y)$ profile agreed with previous results, with better fits between predicted and experimental concentration profiles. For all different flow conditions, an increase of the transverse mixing coefficient was obtained within the shear layer, with a $D_{y_{Max}} > D_{y_{Free}}$. This maximum value seems to increase for higher vegetation density and velocity differences for artificial vegetation cases, although a clear relationship was not found for all conditions tested. However, the maximum transverse mixing obtained for real vegetation tests laid within the range of those obtained for artificial vegetation, even when higher densities were considered for real vegetation experiments. In addition, although slightly higher maximum transverse mixing coefficients were obtained for the summer season compared with the winter season for triangle shapes, higher $D_{y_{Max}}$ values were obtained for winter seasons using the Gaussian shape. In addition, the position of $D_{y_{Max}}$ was expected to be found close to the vegetation edge, matching with the location of peak turbulence as found by **Ghisalberti and Nepf (2005)**. This match was observed for results obtained by assuming the triangular shape, where position of $D_{y_{Max}}$ matched with the limit of the vegetated region for both artificial and

Santiago Rojas Arques
Department of Civil and Structural Engineering

real vegetation tests. However, for results obtained by assuming the Gaussian shape, the position of $D_{y_{Max}}$ for sparse artificial vegetation density ($\emptyset = 0.005$) seemed to be moved 0.121 m to 0.144 m further from the vegetation boundary, although no trend was found in this displacement. No displacement of the $D_{y_{Max}}$ value was observed for the dense artificial vegetation case. However, a different behaviour was observed for real vegetation cases, where a displacement of the $D_{y_{Max}}$ value was observed for both densities, being higher for denser scenarios (0.072 m for the winter season and 0.095 m for the summer season respectively).

Finally, the best fit between predicted and experimental concentration profiles were obtained by assuming the Gaussian shape. A higher correlation was obtained for artificial vegetation ($R^2 = 0.9118$ and $R^2 = 0.9702$ for high and low density respectively) than for those obtained for real vegetation, where a high correlation was obtained for the winter season ($R^2 = 0.9603$) but a low correlation was obtained for the summer season ($R^2 = 0.1012$). This poor correlation for summer real vegetation was attributed to the split of the peak concentration into two local peaks, which was translated across the length of the channel. **West (2016)** argued that the presence of local peaks in the concentration profiles were produced as a result of the heterogeneous stem distribution of the real vegetation. This heterogeneous distribution produces a poorly defined vegetation limit with the free flow region. Therefore a more complex longitudinal velocity profile within the shear layer is produced, which induces the presence of local concentration peaks.

Later, **West et al. (2020)** studied the sensitivity of the results obtained by this model to possible numerical errors caused by the spatial discretization. In addition, they compared the results with those obtained by two analytical solutions proposed by **Rutherford (1994)** and **Kay (1987)** to test the model. Results show an independence of the grid scale and a successfully reproduction of 2D concentration distributions compared with those obtained by the analytical solutions. Moreover, **West et al. (2020)** proposed a skewed-Gaussian shape to describe the variable transverse mixing profile within the shear layer. They assumed that the maximum transverse mixing coefficient value ($D_{y_{Max}}$) is achieved at the vegetation boundary and that two constant transverse mixing values are achieved within the vegetation and in the free flow region at large distances from the vegetation boundary. They used the same optimization routine and experimental results as **West (2016)**. However, no trend was found in the variation of the $D_{y_{Max}}$ with the vegetation density.

2.6.1. Finite Difference Model Analysis

A Finite Difference Model (F.D.M.) was proposed by **West (2016)** for those scenarios in which the longitudinal velocity and the transverse mixing coefficient should be considered variable in the spanwise direction $\left(D_y(y), U(y) \right)$. The governing equation used for the F.D.M. was obtained from the ADE equation by considering a steady source injection $\left(\partial C / \partial t = 0, D_x = 0 \right)$ and vertically well-mixed concentration profiles ($D_z = 0$) along the length:

$$h(y)\, U(y)\, \frac{\partial C(x,y)}{\partial x} = \frac{\partial}{\partial y}\left[h(y)\, D_y(y)\, \frac{\partial C(x,y)}{\partial y} \right] \qquad eq.\,2.76$$

Santiago Rojas Arques
Department of Civil and Structural Engineering

For **eq. 2.76,** a finite difference solution was used considering the channel as a uniform rectangular grid with $i \times j$ nodes where $h(y), U(y)$ and $D_y(y)$ were available at each node. Then, the equation was discretised for each node. The transversal mixing part of the equation (right part) was discretised using a central approximation, and the longitudinal advection part (left part) was discretised using an upwind approximation.

The central approximation is a tool used to solve a function $f(x)$ which can be computed but from which there is no information about how to solve $f'(x)$. Thus, $f'(x)$ is solved using small interval values x_s at each side of a specific point x.

$$f'(x) \approx \frac{f(x + x_s) - f(x - x_s)}{2x_s} \qquad eq.\,2.77$$

Meanwhile, the upwind approximation considers node values in the direction of propagation to solve it. Applying both discretization methods to **eq. 2.76** for each node in which i and j represent the node location in the x and y direction respectively, both left and right parts of the equation become:

$$\frac{h_j\,U_j\,\left(C_{i,j} - C_{i-1,j}\right)}{\Delta x} \qquad eq.\,2.78$$

$$\frac{1}{\Delta y}\left[\left(\frac{h_{j+1}D_{y_{j+1}} + h_jD_{y_j}}{2}\,\frac{C_{i,j+1} - C_{i,j}}{\Delta y}\right) - \left(\frac{h_jD_{y_j} + h_{j-1}D_{y_{j-1}}}{2}\,\frac{C_{i,j} - C_{i,j-1}}{\Delta y}\right)\right] \qquad eq.\,2.79$$

Then, terms from **eq. 2.78** and **eq. 2.79** were grouped:

$$\alpha_{j-1}C_{i,j-1} + \beta_j C_{i,j} + \gamma_{j+1}C_{i,j+1} = \delta_j \qquad eq.\,2.80$$

Where:

$$\alpha_{j-1} = \frac{-\left(h_{j-1}D_{y_{j-1}} + h_jD_{y_j}\right)}{2\,\Delta y^2} \qquad eq.\,2.81$$

$$\beta_j = \frac{h_j\,U_J}{\Delta x} + \frac{h_{j+1}D_{y_{j+1}} + 2h_jD_{y_j} + h_{j-1}D_{y_{j-1}}}{2\,\Delta y^2} \qquad eq.\,2.82$$

$$\gamma_{j+1} = \frac{-\left(h_{j+1}D_{y_{j+1}} + h_jD_{y_j}\right)}{2\,\Delta y^2} \qquad eq.\,2.83$$

$$\delta_j = \frac{h_jU_j}{\Delta x}C_{i-1,j} \qquad eq.\,2.84$$

Considering a grid with N nodes in the transversal direction and boundary conditions for $j = 1$ and $j = N$, a system with $N - 2$ equations was generated. This system was solved using the Thomas algorithm approach (**Lee, 2011**) to solve the tri-diagonal matrix generated. Then **eq. 2.80** for $j = 2$ became:

$$\alpha_1 C_1 + \beta_2 C_2 + \gamma_3 C_3 = \delta_2 \qquad eq.\,2.85$$

Santiago Rojas Arques
Department of Civil and Structural Engineering

As C_1 was given by the transverse boundary condition, it was moved to the right part of equation:

$$\beta_2 C_2 + \gamma_3 C_3 = \delta_2 - \alpha_1 C_1 \qquad eq. 2.86$$

And this equation was re-written as:

$$p_2 C_2 + q_3 C_3 = r_1 \qquad eq. 2.87$$

Then, **eq. 2.80** for $j = 3$ was:

$$\alpha_2 C_2 + \beta_3 C_3 + \gamma_4 C_4 = \delta_3 \qquad eq. 2.88$$

Then, substituting C_2 using **eq. 2.87**:

$$\alpha_2 \frac{r_1 - q_3 C_3}{p_2} + \beta_3 C_3 + \gamma_4 C_4 = \delta_3 \qquad eq. 2.89$$

And, as r_1 was known, it was moved to the right part of the equation and the rest of terms were substituted in the same way as **eq. 2.87**:

$$p_3 C_3 + q_4 C_4 = r_2 \qquad eq. 2.90$$

Then, following the same process for $j = 4$ and follows:

$$p_4 C_4 + q_5 C_5 = r_3 \qquad eq. 2.91$$

In the same way, **eq. 2.80** for $j = N$ was re-written as:

$$p_{N-1} C_{N-1} + q_N C_N = r_{N-2} \qquad eq. 2.92$$

And, as C_N was also given by transverse boundary conditions; C_{N-1} was solved as:

$$C_{N-1} = \frac{r_{n-2} - q_N C_N}{p_{N-1}} \qquad eq. 2.93$$

This process was applied for all different longitudinal profile locations i.

2.6.1.1. Model Modification

West (2016) proposed this modification to consider the lateral boundary condition $dC/dy = 0$. So, instead of considering the value C_1, the value dC/dy_1 was specified. So, using **eq. 2.80** for node $j = 1$:

$$\alpha_0 C_0 + \beta_1 C_1 + \gamma_2 C_2 = \delta_1 \qquad eq. 2.94$$

Thus, the new boundary condition established $C_0 = C_2$:

$$\beta_1 C_1 + (\alpha_0 + \gamma_2) C_2 = \delta_1 \qquad eq. 2.95$$

Then for the node $j = 2$, the **eq. 2.80** became:

$$\alpha_1 C_1 + \beta_2 C_2 + \gamma_3 C_3 = \delta_2 \qquad eq. 2.96$$

Replacing the value C_1 from **eq. 2.95**:

$$\alpha_1 \frac{\delta_1 - (\alpha_0 + \gamma_2) C_2}{\beta_1} + \beta_2 C_2 + \gamma_3 C_3 = \delta_2 \qquad eq. 2.97$$

Santiago Rojas Arques
Department of Civil and Structural Engineering

Then:

$$\frac{-\alpha_1(\alpha_0 + \gamma_2)C_2}{\beta_1} + \beta_2 C_2 + \gamma_3 C_3 = \delta_2 - \frac{\alpha_1 \delta_1}{\beta_1} \qquad eq.\,2.98$$

Grouping terms, the following equation was obtained:

$$p_2 C_2 + q_3 C_3 = r_1 \qquad eq.\,2.99$$

Where:

$$p_{2=} \frac{-\alpha_1(\alpha_0 + \gamma_2)}{\beta_1} + \beta_2 \qquad eq.\,2.100$$

$$q_3 = \gamma_3 \qquad eq.\,2.101$$

$$r_1 = \delta_2 - \frac{\alpha_1 \delta_1}{\beta_1} \qquad eq.\,2.102$$

The same modification was applied to the other boundary condition at C_N, where the new condition ${dC}/{dy_N} = 0$ was considered, resulting in $C_{N+1} = C_{N-1}$

$$p_{N-1}C_{N-1} + q_N C_N = r_{N-2} \qquad eq.\,2.103$$

$$p_N C_N + q_{N+1}C_{N+1} = r_{N-1} \qquad eq.\,2.104$$

Since $C_{N+1} = C_{N-1}$ for the new boundary condition, C_N was solved:

$$\frac{p_{N-1}\,(r_{N-1} - p_N C_N)}{q_{N+1}} + q_N C_N = r_{N-2} \qquad eq.\,2.105$$

$$-\frac{p_{N-1}p_N}{q_{N+1}}C_N + q_N C_N = r_{N-2} - \frac{p_{N-1}r_{N-1}}{q_{N+1}} \qquad eq.\,2.106$$

$$C_N \left(-\frac{p_{N-1}p_N}{q_{N+1}} + q_N \right) = r_{N-2} - \frac{p_{N-1}r_{N-1}}{q_{N+1}} \qquad eq.\,2.107$$

Solving for C_N:

$$C_N = \frac{q_{N+1}r_{N-2} - p_{N-1}r_{N-1}}{-p_{N-1}p_N + q_{N+1}q_N} \qquad eq.\,2.108$$

For C_{N-1}:

$$C_{N-1} = \frac{r_{N-2} - q_N C_N}{p_{N-1}} \qquad eq.\,2.109$$

Iteratively all different concentration values were solved from node $j = N - 2$ to $j = 2$. Finally, concentration value C_1 was obtained from **eq. 2.95**:

$$C_1 = \frac{\delta_1 - (\alpha_0 + \gamma_2)C_2}{\beta_1} \qquad eq.\,2.110$$

In addition, as $C_0 = C_2$, then $\alpha_0 = \alpha_2, \gamma_0 = \gamma_2, h_0 = h_2$ and $D_{y_0} = D_{y_2}$

Santiago Rojas Arques
Department of Civil and Structural Engineering

2.7. Previous Measurement Techniques

As explained in **Section 2.4**, experimental studies are commonly used to study solute transport and quantify mixing processes in open channel flows under different complex hydraulic situations such as compound or sinuous channels, or vegetated flows (**Seo et al., 1994; Boxall et al., 2003; Zeng et al., 2008**). Turbulent diffusion is one of the most important processes that drives mixing, as well dispersion effects due to shear layers and secondary currents. Therefore, it is desirable to obtain simultaneous information of both mixing processes and velocity fields and coherent structures in complex flows.

The most common method to quantify mixing processes is to inject a fluorescing dye or saline tracer into the flow and measure the concentration downstream, where the dye concentrations are measured by the florescence emitted under a constant light of a given wavelength and the saline concentration is measured by conductivity. These measurements are typically taken as point measurements by devices such as fluorometers (**Pilechi et al., 2016; Seo et al., 2016**) or conductance meters (**Colombani et al., 2015**). However, these techniques can be time-consuming and require of lots of individual measurement points, which also increases the experimental complexity and cost. Moreover, for those situations in which the tracer injected is both temporally and spatially variable, the use of these techniques can become particularly difficult as numerous measurements may be required to understand the spread of solute in time and space. Finally, these techniques generally preclude the measurement of velocity at the same time due to obstructions produced by tracer measurement devices.

Other techniques are used to measured velocity and mixing processes at the same time without the use of intrusive devices, such as thermographic cameras (**Cardenas et al., 2009; Andrews et al., 2011**). However, this method is limited by the differential of temperature needed between the tracer and the main flow, which is usually around 50 degrees Celsius. Moreover, the temperature difference may produce convection effects, which can increase the flow complexities.

In previous research, Laser Induced Fluorescence (LIF) technique has also been applied to study mixing processes in laboratory channels under different conditions such as partially vegetated channels (**West, 2016**), sinuous channels (**Hilderman and Wilson, 2006**) and vegetated flows (**Nepf et al., 1997**). This technique consists of the use of a laser directed at a section of the flow (usually a spanwise laser transversal to the main flow direction). When dye flows through the light sheet, a proportion of the light power is absorbed and re-emitted by the tracer, hence allowing the distribution of concentration over the width/depth to be quantified. A camera located below a glass panel under the bed records the resulting light intensity within the dye's excitation wavelengths, relating the measured light intensity with the dye concentration via a calibration. These laser techniques can record very low concentration values (in the order of 10^{-3}mg/L) and a positive linear relationship between light intensity and concentration values can be obtained. However, this technique requires the use of expensive lasers and associated equipment and only narrow regions of the flow can be studied.

An additional method to study mixing processes in shallow water is by using conventional video cameras to observe the spreading of tracer over a large area. In contrast with laser-induced fluorescence techniques, where the recorded fluorescence intensity is produced by a laser, the direct measurement of dye concentration using cameras is based on the light absorption by the dye and hence an inverse relationship between light intensity and concentration is obtained. Using this technique higher dye concentrations are required and the

Santiago Rojas Arques
Department of Civil and Structural Engineering

relationship between measured intensity and concentration is not linear, with the resulting measurement sensitive to both flow depth and lighting conditions, hence requiring more complex calibration steps. The first description of such techniques can be found in **Ward (1973)** who was the first to measure concentration of a dye in a laboratory channel using cameras. Then, **Balachandar et al. (1999)** and **Balu et al. (2001)** obtained instantaneous dye concentration measurements by using a video imaging technique in shallow water. **Rummel et al. (2002)** ran an experiment to analyse a depth-averaged mass concentration in shallow turbulent flow by a single camera recording an area of $1.4 \times 1 \text{ m}^2$. This experiment provided a new time/cost effective measuring technique called Planar Concentration Analysis (PCA) to measure depth-averaged concentrations of a conservative tracer in shallow water conditions.

Zhang and Chu (2003) and **Chu and Zhang (2004)** measured the spreading of mass of a shallow jet injected into a stagnant water body by a video imaging technique. They performed a spatially averaged calibration over the recorded area to quantify concentration levels of dye injected. Both **Balachandar et al (1999)** and **Zhang et al (2003)** applied a fitting to relate spatially averaged brightness values to know concentration values, while **Balu et al (2001)** applied a neural network approach to obtain dye concentration from red/green/blue (RGB) image values.

Carmer et al. (2009) designed a PCA experiment to study both mixing processes and the shape of the large-scale eddy structures around a large cylinder obstacle in a shallow water flow by injecting a conservative tracer. However, they measured separately the surface velocity using a PIV technique. Their experiment used a similar technique as **Rummel et al. (2002)** by using a single camera video at three different positions to record an area of $1.6 \times 1.2 \text{ m}^2$ for each position.

To obtain measurement of velocity-fields, Particle Image Velocimetry (PIV) is a technique performed quite often, using lasers to illuminate a plane of neutrally buoyant particles in the flow to obtain velocity fields. With this technique, one or more cameras record the movement of tracer particles. Then, the technique tracks windows of particle patterns between two temporary consecutive frames and displacement is calculated from the spatial variation of the particle patterns. If particles over the water surface are recorded, a Surface Particle Image Velocimetry (SPIV) can be used (**Weitbrecht et al., 2002, Muste et al., 2014, Novak et al., 2017**). This surface technique is easier to implement than the conventional PIV technique as buoyant particles are used instead of neutrally buoyancy tracers. Moreover, the recorded area and scales can be greater and no complex laser or camera arrangements are required. This technique has been used previously to study processes associated with large stream areas (**Juez et al., 2019**). The main disadvantage of the SPIV technique is that only surface velocities can be recorded, and thus only 2D measurements can be obtained and hence is generally used in shallow water flows. However, this technique allows the recording of larger experimental area compared with 3D PIV techniques. In addition, the SPIV technique is more efficient in terms of time, increasing the number of experiments and thus the amount of recorded data.

Santiago Rojas Arques
Department of Civil and Structural Engineering

2.8. Literature Review Summary

Previous literature discussed in this section shows that the presence of vegetation in an open channel flow produces a reduction in flow velocity due to an increased drag. The resistance added by vegetation depends on several parameters such as the vegetation density, the stem diameter, the canopy configuration and the stem height. All of these parameters vary from one plant species to another and thus artificial vegetation offers a repeatable approach to simulate vegetated flows.

Further researchers have demonstrated the creation of shear layers in flows where vegetation partially covers the flow area, such as submerged vegetated flows or flows with a vegetated bank. These configurations produce two co-flows with different primary velocities and a shear layer that originates between these two regions. This shear layer is associated with the creation of large-scale coherent eddies, which increase the turbulence intensity along the shear layer.

Some researchers have studied the influence of this shear layer in the mixing processes. The results of **Ghisalberti and Nepf (2005)** in submerged vegetated flows show that the creation of coherent turbulence structures enhance the mass transport, increasing the vertical mixing compared with non-vegetated flows. In addition, some researchers have studied the transverse mixing processes in shear layers produced by compound channels (**Guymer and Spence, 2009; Besio et al., 2012**), where a differential of primary velocity is produced between the main channel and the floodplain, generating a shear layer. Results suggest an overall increase of the transverse mixing coefficient is produced within the sloping region between the main channel and the floodplain, compared with those observed within the main channel and the floodplain. In addition, the increase of the transverse mixing coefficient seems to depend on the increase of the velocity gradient between the main channel and the floodplain.

West (2016) studied the variable $D_y(y)$ profile within the shear layer produced by a vegetated bank flow and proposed different shapes to represent the variable $D_y(y)$ profile. His results showed that a Gaussian shape is a good approximation to represent the variation of $D_y(y)$. Moreover, his results showed an increase of $D_{y_{Max}}$ for higher velocity gradients and a displacement of the position of $D_{y_{Max}}$ far from the vegetation boundary for sparser densities. However, a direct relationship between the transverse mixing coefficient and the variation of the vegetation density and resulting velocity gradient was not found for vegetated bank flows. Therefore, the shear layer produced in these flows requires experimental data to further study its effects on the transverse mixing processes.

This thesis aims to use experimental data gathered from vegetated bank flows with different vegetation densities to study both transverse mixing processes and 2D velocity fields in shallow water flows. To obtain this experimental data, a PCA technique is applied to measure the concentration distribution of dye downstream of the injection, and a SPIV technique is applied to record the 2D velocity fields. These techniques are considered as:

- They allow the characterization of spreading over the length and width of the flume, obtaining data over a large studied area.
- They allow more experiments to be carried out, which allows sufficient data to perform predictive analytical relationships.

Santiago Rojas Arques
Department of Civil and Structural Engineering

- Previous work suggest that in flows with vegetated banks the dominant processes occur over the width, and charactering the vertical processes is not that critical for understanding the mixing processes.

The variation of the transverse mixing coefficient within the shear layer is obtained in a similar way as previous researchers. Then, the relationship between this variation and the velocity fields produced in this type of flow is studied to propose an easy-to-apply model to predict the effects of a vegetated bank on the transverse mixing processes. In addition, previous researchers have studied these effects only for one vegetated bank, but there is a current lack of knowledge regarding the influence of two vegetated banks and the potential overlapping of their associated shear layers on the longitudinal velocity and the mixing processes. Therefore, a set of experiments with two vegetated banks is analysed to provide a new understanding of the shear layer interaction and its effects on transverse mixing. In addition, analytical relationships provided from previous experiments are validated in this new configuration.

Finally, most previous experimental studies obtained the tracer concentration profiles using laser techniques such as the Laser Induced Fluorescence (LIF) or direct sampling and measurement by fluorometers. However, these techniques limit the number of concentration profiles that can be recorded along the streamwise direction, increasing the demand of time and precluding the simultaneous measurement of velocity. Therefore, a new measurement technique is required to record the tracer concentration distribution along a large studied area. This technique would allow to increase the number of concentration profiles available for further analysis and to improve the understanding of processes happening under different flow conditions.

Santiago Rojas Arques
Department of Civil and Structural Engineering

3. Objectives of Thesis Study

The aim of this thesis introduced previously in **Section 1.1** is to quantify the influence of vegetated banks on transverse mixing processes in open channel flows. To achieve this, and based on the knowledge gaps in previous research identified in **Section 2**, the objectives proposed during this study are the follows:

1. Development of a new measurement technique to obtain rapid synchronous measurement of velocity and concentration at high resolution across the full 2D surface area of the flow.
2. Using the output of objective 1, collect a rigorous and novel data set of time-averaged longitudinal velocity and depth-averaged concentration distributions of a neutral tracer in flows with a vegetated bank.
3. Using the data set demanded by objective 2, develop a model to predict both time-averaged longitudinal velocity and transversal mixing coefficients based on the experimental results obtained in the previous step.
4. Using the output of objective 1, collect a novel first data set of time-averaged longitudinal velocity and depth-averaged concentration distribution of a neutral tracer in flows with two vegetated banks.
5. Using the data obtained from objective 4, validate the proposed model obtained in objective 3.
6. Using the proposed model from objective 3 in a hypothetical scenario, study whether the increase of mixing caused by a vegetated bank is of sufficient scale to have a notable and considerable impact on the mixing of a soluble material over and above that of a non-vegetated channel.

Santiago Rojas Arques
Department of Civil and Structural Engineering

4. Experimental Design and Methodology

In this section, the new measurement technique is explained in detail, including the set-up used and calibrations required. Then, a detailed description and the purpose of the experimental set ups are described. Finally, measurements from a first set of experiments are compared against data obtained by conventional measurement techniques to validate results, as well as some improvements discussed in the last section. Several sections of this chapter have been published in **Rojas-Arques et al. (2018)**.

4.1. Measurement Strategy

Based on previous work introduced in **Section 2** and in order to achieve the objectives explained in **Section 3**, surface velocity fields and depth-averaged concentration distributions were obtained for different shallow flow conditions. The velocity study was focused on the measurement of 2-D velocity fields to study vertically-oriented coherent structures produced within the shear layer (**White and Nepf, 2008; West, 2016**). Depth-averaged concentration distributions were studied by injecting a tracer (Rhodamine WT), later explained in **Section 4.2.3,** into the flow. The variation of the distribution of tracer concentration downstream of the injection point provided information about transport and mixing processes for different flow conditions.

The system explained below was designed to measure this velocity and mixing processes along the open channel. The velocity fields were obtained using a Large-Scale PIV technique and the concentration distribution using a PCA technique.

The successful use of Large-Scale PIV measurements depends on the particles used and their distribution along the recorded area. These particles must produce a clear contrast against the channel bed and their size should be sufficient to allow their identification. Moreover, particles density should be lower than of water to avoid settlement, but not too low to avoid buoyancy effects. Based on **Weitbrecht et al. (2002)** work, 2 mm black polypropylene particles with a density of 0.9 g/cm^3 are considered, which produce a sufficient contrast using the cameras setup described below (**Section 4.2.2**). In addition, particles should be uniformly distributed in the streamwise and spanwise directions, with a distribution dense enough to identify the particle patterns for each instantaneous frame. **Weitbrecht et al. (2002)** considered a minimum of 6 particles for each tracked window. In previous work, a homogenous particle distribution in uniform flows was achieved using a particle dispenser to release uniformly the particles upstream of the recorded area (**Rojas-Arques et al., 2018**). However, for tests with high velocity flow gradients along the spanwise direction, a homogeneous particle density was found to be difficult to control. Therefore, the particles were released manually upstream of the recorded area, avoiding any turbulence derived from this process, and raw recorded frames were further analysed to remove spurious high velocities and zero velocities obtaining from tracked windows with not a dense enough particle distribution.

Santiago Rojas Arques
Department of Civil and Structural Engineering

These PIV and PCA techniques mostly require the use of cameras to record the movement of surface particles and the distribution of an injected tracer respectively along a continuous area. Therefore, experimental data along a continuous studied area can be recorded, providing more information for further analysis. In addition, these techniques provide an easy and quick way to record the information, reducing the time demand and increasing the number of tests that can be performed.

4.2. Set-up Description

4.2.1. Channel Set-up

Experiments were conducted within the University of Sheffield hydraulics laboratory. All tests described used an open channel constructed of reinforced glass fibre panels. The channel had a constant width of 1.22 m, a maximum depth of 0.5 m and an experimental length of 14.5 m. The channel slope was 0.00123, which was verified by measuring the water depth of a stationary body of water along the channel length.

To allow the installation of vegetation of different densities, a 1.5 mm thick stainless steel panel was installed over the channel bed, with a 100 mm layer of stryofoam beneath the steel panel to ensure the securely installation of stems. This steel panel was perforated by 6 mm holes in a hexagonal arrangement with a 9 mm pitch. This arrangement allows the installation of artificial stems in a staggered distribution, which is commonly used to represent the randomness of real vegetation growth (**Nepf, 1999; Stone and Shen, 2002**). In addition, this arrangement allows a maximum stem density of $\emptyset \approx 0.15$, which is higher than those used in previous work (**White and Nepf, 2008** and **West, 2016**) and is in the range of real vegetation studied in rivers (**Huang et al., 2008** and **Sun et al., 2010**). Finally, this homogeneous distribution of perforations provides a homogeneous bed roughness over the channel width and length. In addition, the smooth surface of installed walls decreases the effects of wall roughness in the overall channel.

A constant-head tank controlled by a valve supplied a constant discharge into the flume. The constant-head tank was fed from the main laboratory sump by a pump. A scheme of the laboratory flume is plotted in **Figure 4.1**. A flow baffle was fitted at the upstream end of the channel to dissipate turbulent structures produced by flow injection and a tailgate weir was fitted downstream to control downstream boundary conditions. The flow rate was measured by an additional cistern downstream of the channel to which the full flow could be deflected by a manual gate. The measurement cistern could be blocked at outlet using a manual gate, and the rise in water level, and hence steady flow rate, could be monitored by a float level. For each test, 10 different flow rate measurements were recorded and the mean flow rate value was calculated from these.

Santiago Rojas Arques
Department of Civil and Structural Engineering
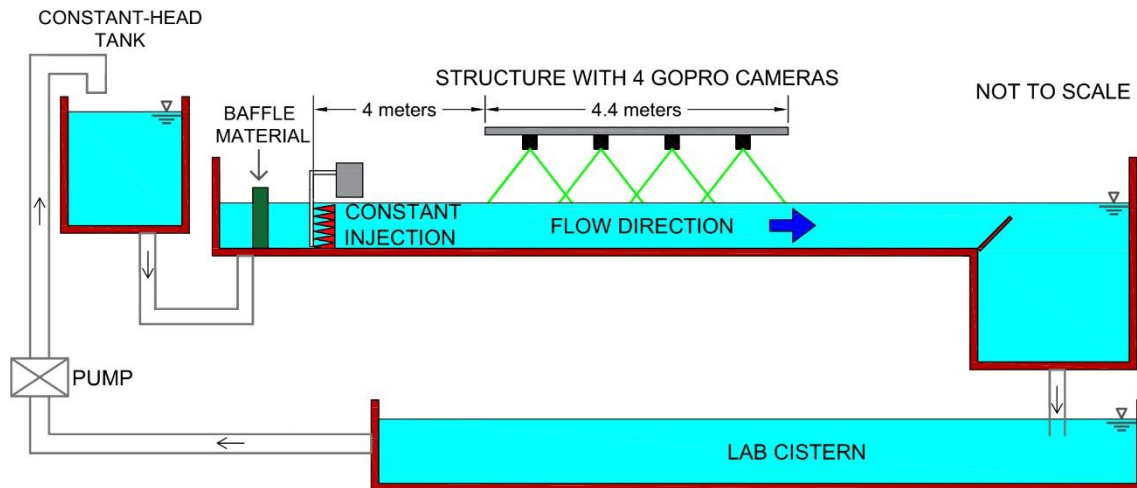
Figure 4.1. Longitudinal scheme profile of the experimental model.

4.2.2. Cameras

As shown **Figure 4.1**, four GoPro Hero 4 Black Edition cameras were installed above the channel to record video images during experiments for Particle Image Velocimetry (PIV) and Planar Concentration Analysis (PCA) techniques. Cameras were installed using a structure fixed to the channel with aluminium beams with a double T section called *Rexroth Aluminium* struts.

Cameras were set to record video frames with a frequency of 80 Hz and an image size of 1440×1920 pixels. Cameras were positioned above the centreline of the channel width at a height of 1.2 m above the stainless steel perforated sheet, obtaining an image resolution of approximately 1×1 mm. Each camera was located at 1.2 m intervals along the streamwise direction. However, the edges of each frame were strongly distorted due to lens distortion and hence the edges were overlapped and cropped. The cameras recorded the videos in RGB format, therefore from each frame three matrices were generated with the red, green and blue components of each pixel respectively. The intensity value of each matrix was in the range of $0 - 255$ (8 bit image), where a value of 0 means no representation of the colour and 255 means the highest possible concentration of the colour. A RGB value of $(0,0,0)$ would hence be black, and a value of $(255,255,255)$ would be white. For PIV videos, all three colour components were considered. However, for PCA videos only the green matrix was used, hence measuring the absorbance of the injected dye as explained in the following section.

4.2.3. Dye Injection

The dye used for all tests was Rhodamine WT. This fluorescent component had an absorption/fluorescence spectrum as shown in **Figure 4.2** obtained from **Melton and Lipp (2003)**. Its absorption has a maximum at a wavelength of 555 nm and its maximum fluorescence is at 583 nm. Based on this, commercial green LEDs were used to illuminate the full recorded area. The green spectrum was around 520 nm to 560 nm, a range that was strongly absorbed by Rhodamine WT and it was away from the maximum Rhodamine WT fluorescence region. Therefore, the dye used in experiments absorbed green light along the recorded area, producing a lower green intensity where the dye is present. This intensity decrease was related with the local amount of Rhodamine WT present for each water depth (explained in more details in **Section 4.4**).

Santiago Rojas Arques
Department of Civil and Structural Engineering
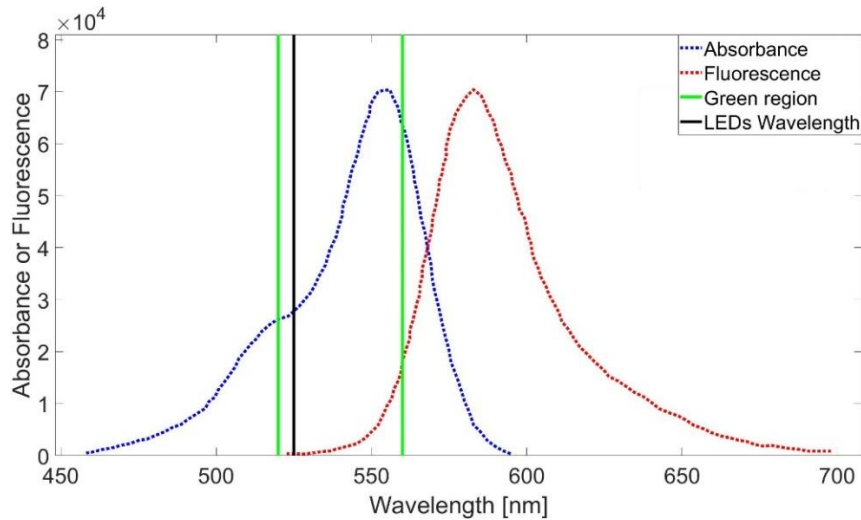
Figure 4.2. Absorbance and fluorescence spectra for Rhodamine WT from **Melton and Lipp (2003)** and green spectra (the wavelength emitted by LED lights).

This fluorescent dye was found to have low background fluorescence, which allowed a higher sensitivity and lower concentrations to be recorded (**Smart and Laidlaw, 1977; Trudgill, 1987**). However, it was found to be affected by water temperature and water pH, and also presented a decay due to sunlight. Due to these reasons, tap water was used for calibration to avoid any reaction with chemicals that could have been added into the water system, such as bleach; which could distort the calibration. Moreover, regular temperature recordings were taken to ensure a constant water temperature and Rhodamine WT was stored into an opaque bottle far from sunlight. Nevertheless, the decay of Rhodamine WT is not significant over the time-scale of a measurement.

A constant head tank was installed at 4 m upstream the recorded area to supply the Rhodamine WT dye to a vertical pipe with an internal diameter of 4 mm. This pipe was perforated with 1 mm diameters holes separated a distance of 10 mm along the pipe height. For each test, holes along the water depth released several continuous injections into the stream along the water depth, promoting a uniform vertically well-mixed condition in the measurement area. In addition, holes above the water surface were covered to avoid a higher concentration at the top of the water depth. The injector was located at a distance of 4 m upstream of the recorded area to ensure vertically well-mixed conditions. This distance was obtained by considering the expression to obtain the distance for complete vertical mixing (**Rutherford, 1994**). If a point source at mid-depth was considered, the expression to obtain the vertically well-mixed distance could be obtained as:

$$L_{z_{Middle}} = 0.134 \frac{Uh^2}{D_z} \qquad\qquad eq.\,4.1$$

Where $L_{z_{Middle}}$ is the distance needed for a vertically well-mixed condition, h is the water depth, U the depth-averaged longitudinal velocity and $D_z = 0.067hu^*$ is the vertical mixing coefficient, where u^* the shear velocity. This shear velocity could be considered as $u^* = \sqrt{hS_o g}$, where S_o is the channel slope and g is the acceleration due to gravity. If the deepest water depth $h = 0.09$ m was considered (see **Section 4.5.1**) and its corresponding time-averaged longitudinal velocity for non-vegetated flow conditions $U = 0.41$ m/s (see **Section 6.1.1**, **Table 6.1**), a minimum distance for a vertically well-mixed condition for a point source

Santiago Rojas Arques
Department of Civil and Structural Engineering

located at mid-depth is $L_{z_{Middle}} = 2.24$ m. This result suggests that the distance used in these tests (4 m) was enough to ensure a vertically well-mixed condition.

4.2.4. PCA Illumination

Commercial green LED lights were used to illuminate the flume. Light strips were installed along the channel at different positions to ensure an approximately homogeneous distribution of green intensity over the recorded area. An initial configuration schematised in **Figure 4.3.** was designed with two LED strips along the top of each channel wall and one strip located on the beam used to fix the cameras, facing the channel bed.
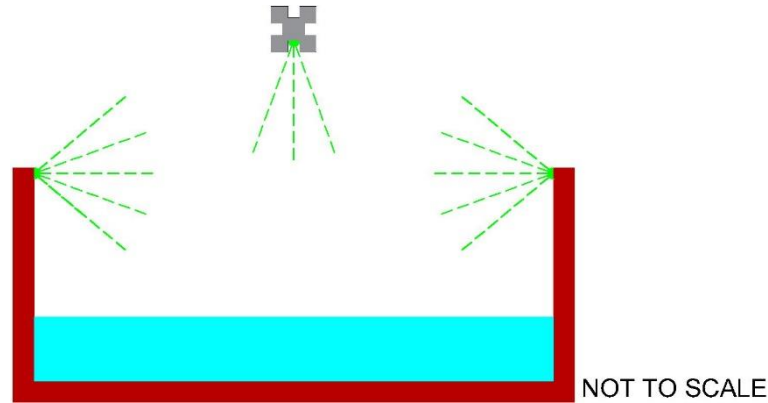
Figure 4.3. First light configuration.

4.3. Image Calibration

Camera set-up is described in **Section 4.2.2**. A procedure for spatial calibration, synchronization and stitching between cameras was conducted to obtain a full frame video of the entire measurement area. These procedures are described below.

4.3.1. Spatial Calibration

Each frame produced by the cameras was distorted due to the fisheye effect of the camera. This effect was corrected by using a chequerboard pattern placed on the channel bed under each camera. These chequerboards consisted of an 18 mm thick marine wood sheet and an area of 180×110 cm, with black and white rectangles of 10×10 cm applied via a precision vinyl decal sticker. The centre of the sheet was located in the centre of the recorded frame for each camera, so that the flume area recorded by each camera was covered by the chequerboard. In addition, the black and white pattern was placed a distance from the channel bed equal to each water depth planned for the tests. This was achieved using wood strips with a thickness of 18 mm as packing pieces. Once the chequerboard was placed correctly under the camera, a video of 2 s was recorded, obtaining the mean frame of the video. For each mean frame, the Matlab algorithm "detecCheckerboardPoints" detected the chequerboard pattern giving the x and y coordinates of each vertex as it was shown in **Figure 4.4**.

Santiago Rojas Arques
Department of Civil and Structural Engineering
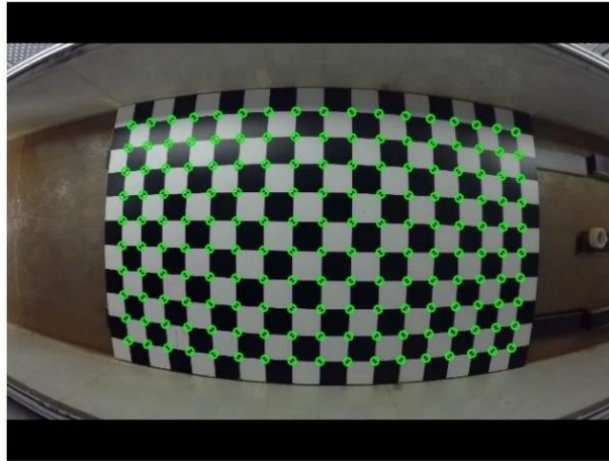
Figure 4.4. Mean frame recorded by the first upstream camera of the chequerboard pattern with corners identified by "detecCheckerboardPoints" algorithm for a water depth of 54 mm.

Once the coordinates of each vertex were identified, the real world positions of them without fisheye distortion were introduced with the same resolution as frame pixels (1×1 mm), into Matlab program to relate the positions of vertex recorded with their real positions along the channel. Then, the Matlab function "fitgeotrans" inferred a geometric transformation to convert the vertices located by the "detecCheckerboardPoints" algorithm (known as "Moving Points") onto the real ones (known as "Fixed Points"). In this case, a 2D Piecewise Linear Transformation was applied, obtaining a spatial transformation as observed in **Figure 4.5**.
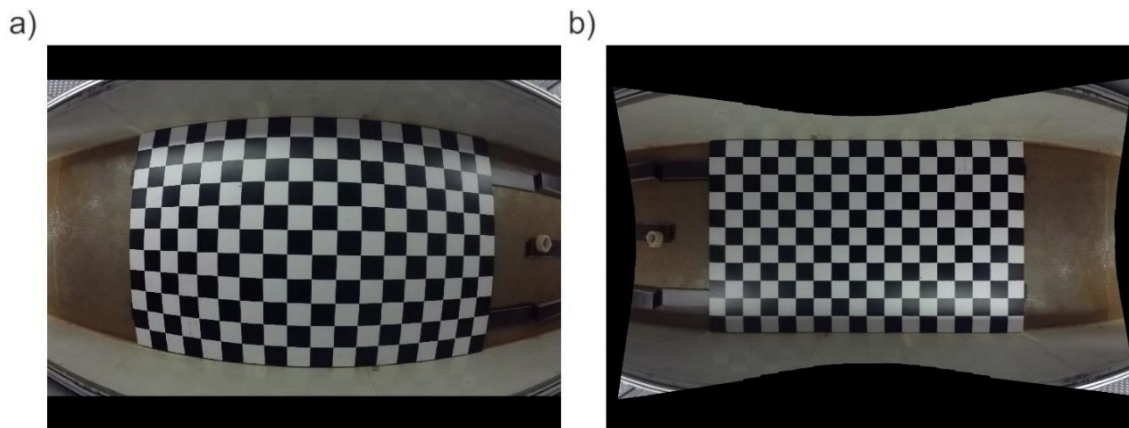
Figure 4.5. Mean frame of chequerboard before (a) and after (b) spatial calibration.

Note that in **Figure 4.5** the frame produced after spatial calibration was flipped horizontally. This change was considered later for PIV and PCA techniques. Once the mean frame was obtained without fisheye distortion, the image was cropped so that only the calibrated region where the chequerboard appeared was used finally. The final calibrated example frame is shown in **Figure 4.6**.

Santiago Rojas Arques
Department of Civil and Structural Engineering
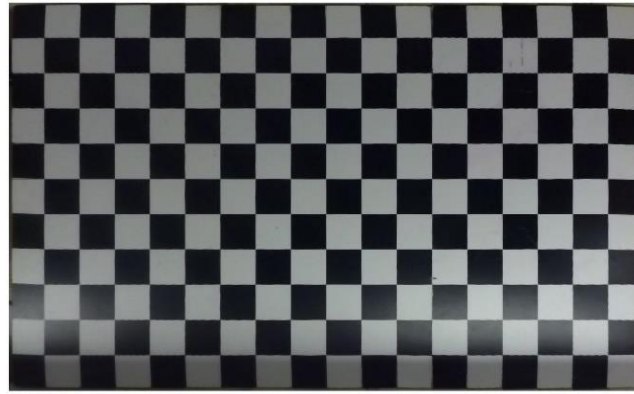
Figure 4.6. Mean frame of chequerboard after spatial calibration and edges cropped.

Figure 4.6 shows how the outer perimeter of squares includes some distortion as they are outside the area of detected vertices, therefore the spatial transformation is extrapolated in this region. This extrapolation can induce some spatial errors in analysed data. However, dye plume is not studied close to the channel walls (upper and lower outer perimeter regions) and left and right outer perimeter regions are neglected later during stiching process (see **Section 4.3.3**).

Next, the quality of the transformation was assessed. Once the spatial calibration was performed for each camera and water depth, coordinates of new corners were again obtained using the Matlab algorithm "detectCheckerboardPoints" and differences between these new points and the real corner positions were obtained. Results are shown in **Table 4.1,** where $\Delta D = \sqrt{\Delta x^2 + \Delta y^2}$. Results suggest a good calibration with mean displacement errors smaller than 0.2 mm and maximum displacement errors smaller than 0.75 mm.

Table 4.1. Differences between calibrated and real chequerboard corners.

Depth	Camera	Mean Δx [mm]	Mean Δy [mm]	Mean ΔD [mm]	Max Δx [mm]	Max Δy [mm]	Max ΔD [mm]
36	1	0.007	0.024	0.102	0.307	0.301	0.434
	2	0.033	0.024	0.085	0.208	0.216	0.295
	3	0.003	0.009	0.079	0.190	0.220	0.269
	4	0.003	0.026	0.088	0.169	0.240	0.343
54	1	0.008	0.075	0.088	0.196	0.126	0.623
	2	0.029	0.002	0.088	0.178	0.228	0.280
	3	0.020	0.013	0.105	0.232	0.141	0.469
	4	0.035	0.033	0.087	0.169	0.184	0.284
72	1	0.017	0.025	0.108	0.222	0.383	0.359
	2	0.027	0.014	0.119	0.266	0.246	0.745
	3	0.027	0.001	0.088	0.227	0.332	0.356
	4	0.013	0.045	0.081	0.212	0.264	0.300
90	1	0.007	0.008	0.089	0.211	0.202	0.298
	2	0.030	0.009	0.088	0.231	0.160	0.327
	3	0.026	0.013	0.085	0.133	0.383	0.320
	4	0.010	0.086	0.098	0.281	0.341	0.397

Santiago Rojas Arques
Department of Civil and Structural Engineering

4.3.2. Synchronization

Once instantaneous frames recorded by each camera were calibrated spatially, a synchronization between cameras was needed in order to combine the frames from all cameras such that they aligned in time. For each test, cameras were controlled by a GoPro Wi-Fi Remote control. However, this trigger only could synchronize cameras to within $0.1\,s$, which in this case meant within 8 frames. In order to reduce this recorded time difference between cameras, a LED timer was used to provide an external absolute time for each camera. This timer consists on 6 columns of 10 LEDs, so each column represents a different rate of time. From right to left, each column is set to switch at a rate ten times slower than the previous column. In this manner, each LED for first column represents 1 ms and each one of the last column measures 100 s.

For each test and once 4 cameras started to record, the LED timer was switched on and placed in the field of view of each camera in turn, leaving it enough time under each camera to record the LEDs (approx. $2\,s$). Then, for each camera, one frame with the LED timer was analysed, obtaining the absolute time reference for that frame. The delayed between cameras was calculated considering the absolute time showed by the LED timer for each camera and the frame in which the timer was recorded (**eq. 4.2**).

$$\Delta t = \frac{t_{cam\,B_{LEDs}} - t_{cam\,A_{LEDs}}}{(Frame_{cam\,B} - Frame_{cam\,A})/80} \qquad eq.\,4.2$$

Where Δt was the desynchronization between two cameras, $t_{cam\,B_{LEDs}}$ was the time recorded by LEDs timer for camera B and $Frame_{cam\,B}$ the frame number. Frame differences were divided by the frequency (80 Hz) to obtain time units. An example is visualised in **Figure 4.7**.
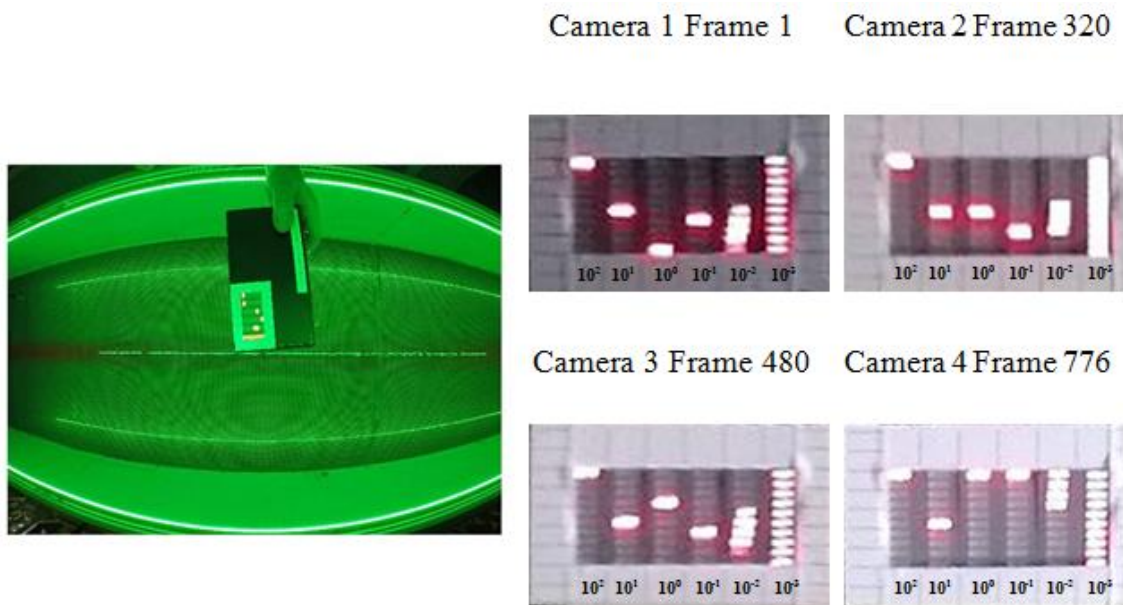
Figure 4.7. Example of frames recorded for camera synchronization.

Santiago Rojas Arques
Department of Civil and Structural Engineering

4.3.3. Stitching

Once the recorded frames were calibrated and synchronised, a junction between consecutive frames was needed to convert four 1440×1920 pixels frames into a full frame that covered the recorded area. For this, it was necessary to obtain the number of pixels overlapping between each adjacent pair of cameras (pixels for a single position which were recorded by two cameras). A 18 mm thick marine wood plank with a black and white rectangle pattern of 95×65 mm was placed on the channel bed between two consecutive cameras and it was recorded for 5 s as shown **Figure 4.8**. The plank was placed at the same level as the calibration chequerboards for each water depth using the 18 mm spacers. Then, the overlapped area was obtained from each mean frame recorded by each camera, using the pattern as help.

As a result, four synchronised frames generated individually by each camera were merged to generate a final frame for the full recorded area with a dimension of 1.22×4.48 m (1220×4480 pixels). In addition, **Figure 4.8** shows the resulting stitching of two consecutive cameras. Coins were used to identify better the overlapped area and to demonstrate that the stitching method worked appropriately.
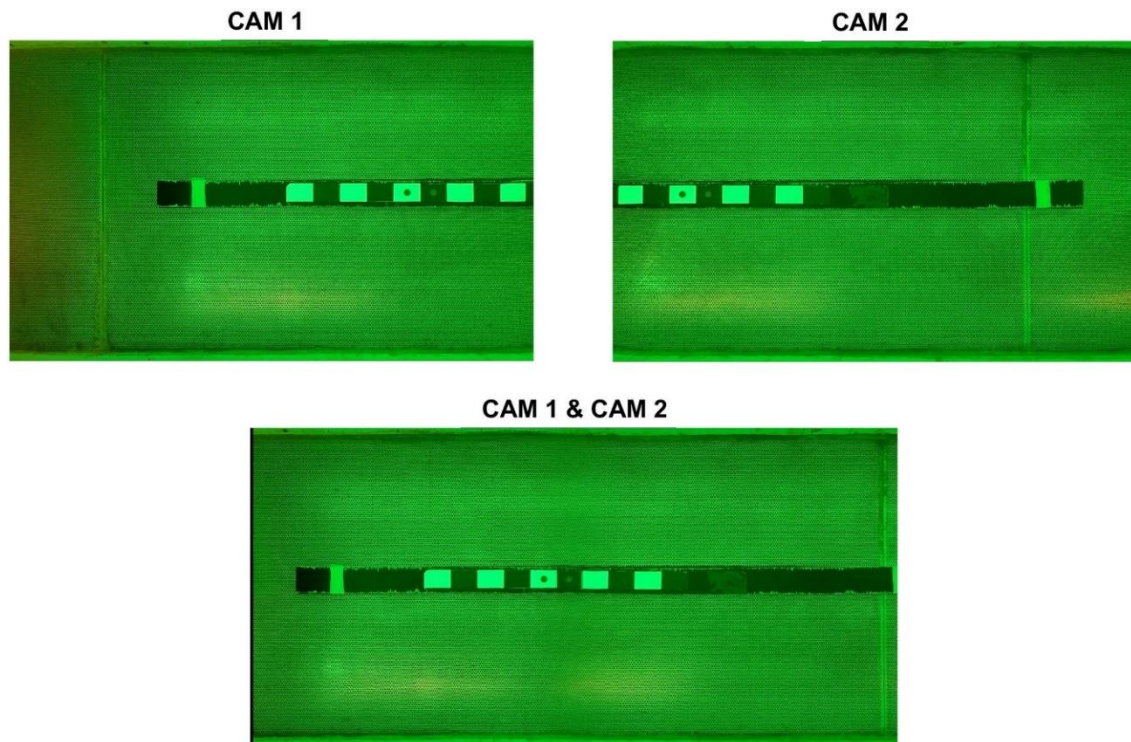
Figure 4.8. Example of two frames recorded by consecutive cameras and the final frame as the combination of them.

For each pair of frames recorded by two consecutive cameras, it was observed that approximately 70 cm were recorded by both cameras. In order to avoid the spatial distortions along the outer perimeter described in **Section 4.3.1,** the first and last 18 cm of each frame were neglected, as these sections were recorded reliably by the adjacent camera. As a result, an overlapped area of 34 cm length was finally considered. Pixel values inside this region were generated using a function that combined RGB values for the same spatial pixel recorded by both cameras. This function created values based on a weighted average of the RGB values of the two frames so there was a gradual transition from one camera to the next. The weighting

value of one camera increased sinusoidally from 0 to 1, while the weighting value of the other camera decreased in the same way. A graphical example of this weighted function and a real case are illustrated in **Figure 4.9**. To more clearly illustrate the method, the example (**Figure 4.9 a**) considers a hypothetical image pair where all intensity pixels for Camera 1 are equal to 1 and all intensity values for Camera 2 are equal to 2. As a result, a transition function is created between the values of the two cameras. **Figure 4.9 b** shows a real stitching between two arrays of two consecutive cameras. The same weighted function was applied and the result obtained was a transitional set of data between both cameras based on the recorded pixel values from each one. The black line (result) matches the blue line (Camera 1) on the left, and gradually transitions to matching the red line (Camera 2) on the right.
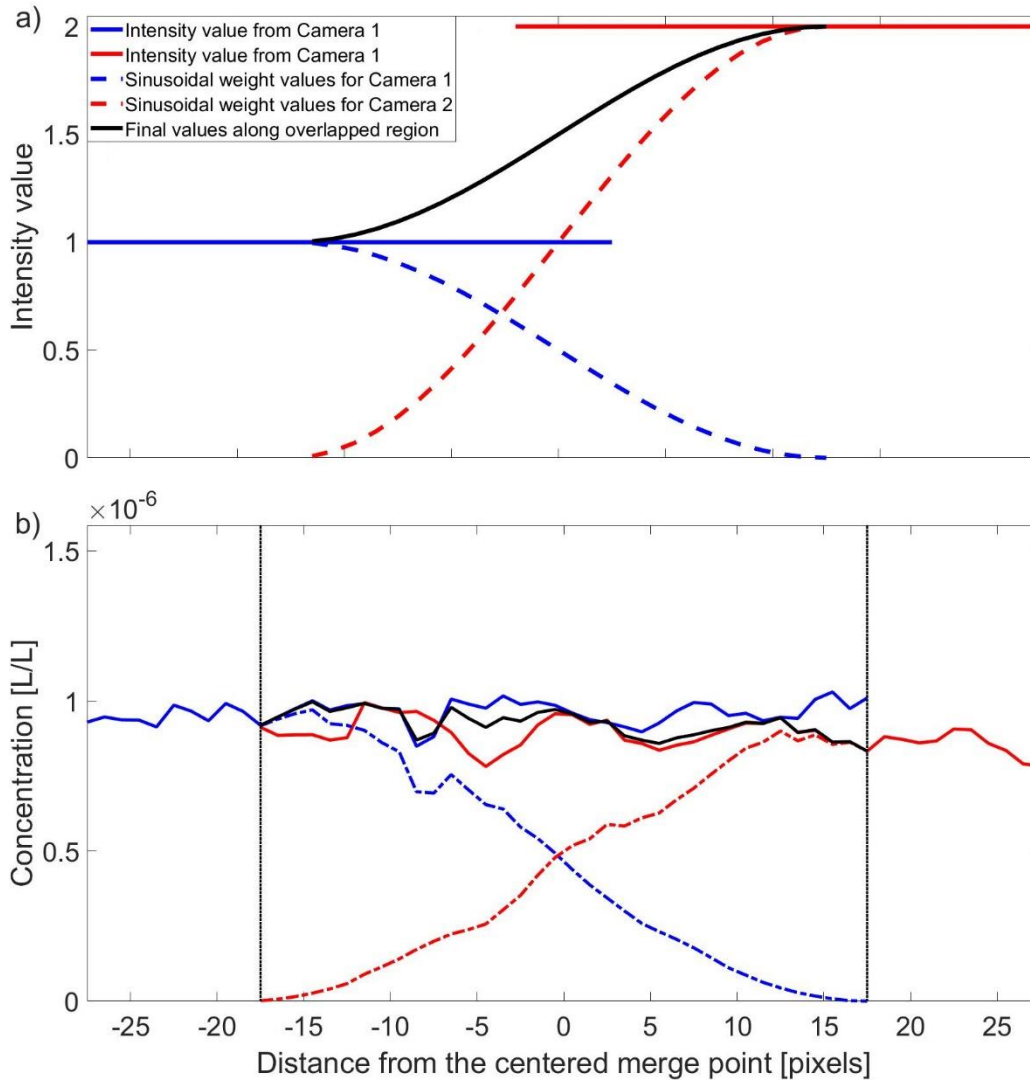
Figure 4.9. Sinusoidal weight function examples. (a) considering a hypothetical image pair and (b) two recorded arrays of two consecutive cameras with a concentration pixel resolution of 10×10 mm.

In order to reduce the high computation demand induced by full concentration maps obtained after the stitching process (1220×4480 pixels), and to reduce errors produced by small light reflections, concentration map dimensions were reduced by calculating the average of 10×10 cells. Therefore, concentration frames recorded by each camera had a dimension of 122×180 cells with a resolution of 10×10 mm.

Santiago Rojas Arques
Department of Civil and Structural Engineering

4.4. Dye Calibration

Rhodamine WT concentration for each single spatial position was related with light intensity recorded by each camera via a dye calibration. A length of the channel of 7.59 m, which contained the recorded channel area, was isolated using two vertical plywood panels sealed with silicone. Then the isolated flume section was filled with tap water from an external cistern by a submerged pump to reach each water depth selected for the tests described in **Section 4.5.1**. For each water depth calibrated, cameras recorded eleven different Rhodamine WT concentrations (including the zero concentration case) with the illumination system described in **Section 4.2.4** switched on and with camera settings as explained in **Section 4.2.2.** This number of calibration points is similar to that used in previous work using similar techniques (**Rummel et al., 2002** and **Carmer et al., 2009**). Moreover, a similar number of calibrated points were used in previous works that used the LIF technique (**West, 2016**). For each concentration, a 10 s video was recorded once the water was still and well mixed with the dye. Then, a time-averaged frame was obtained, spatial calibration as described in **Section 4.3** was applied and average intensity of each 10×10 cells was calculated as explained in **Section 4.3.3.** Thus, an intensity map of 122×180 cells was obtained for each camera and concentration with a cell size of 10×10 mm.

Table 4.2. Concentration used for dye calibration.

Concentration [10^{-6} L/L]	0.00	1.07	2.13	3.19	4.25
Test number	1	2	3	4	5

Concentration [10^{-6} L/L]	5.31	6.36	7.42	8.47	9.51	10.56
Test number	6	7	8	9	10	11

For each cell, an expression was used to relate green intensity with concentration values. The same form of expression was used for all different cells but with different coefficients. Different functions were considered to fit the relationship between concentration values and green intensity. **Rummel et al. (2002)** and **Carmer et al. (2009)** applied an exponential relationship to relate intensity decay with concentration increase. This relationship was used to describe the behaviour recorded for very high concentrations, where the recorded intensity exhibits a vertical asymptote for higher concentration values. For the current dye calibration, the asymptote region was avoided in contrast to the work of **Rummel et al. (2002)** and **Carmer et al. (2009)**, and only the region where a more linear relationship between the green intensity and the dye concentration was calibrated. As a result, and in order to avoid errors in the calibration produced by the sensitivity of an exponential fitting due to extreme values, a third order polynomial function was proposed to fit the relationship between the green intensity decay and the concentration increase. This function agreed with an exponential shape far from the asymptote region and produced good relationships for the specific range of concentrations used during calibration as shown in **Figure 4.10**. The time-averaged intensities for a representative cell located at $x = 1.5$ m downstream of the first measurement profile location and in the centre of the width ($y = 0.61$ m), for the range of water depths are plotted in **Figure 4.10** against their corresponding concentration values, along with the fitted functions. In addition, the fitted expressions and the Pearson correlation between the fitting and the experimental data are shown in the figure. The errorbars show the temporal standard deviation of the recorded green intensity for the total recorded range (10 s).

Santiago Rojas Arques
Department of Civil and Structural Engineering
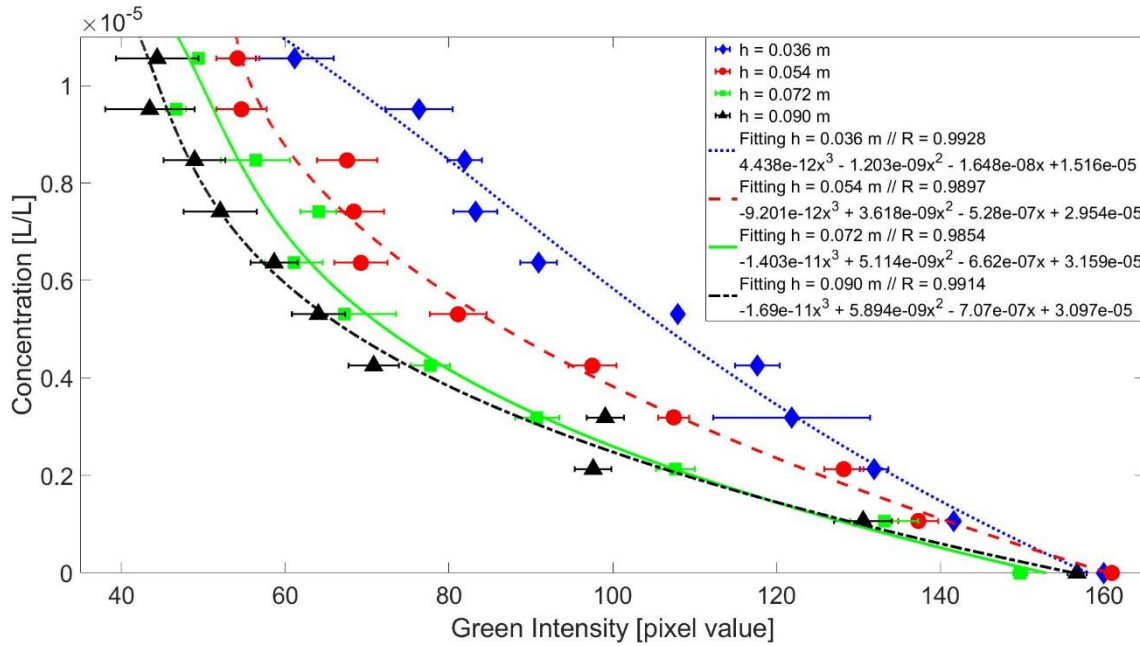
Figure 4.10. Example of concentration calibration for $10 \text{ mm} \times 10 \text{ mm}$ cell at $x = 1.5 \text{ m}$ and $y = 0.61 \text{ m}$.

Figure 4.10 shows relationships between the green intensity and recorded dye concentrations avoiding the constant green intensity asymptote for very high dye concentrations. The variation of the pixel values are produced by the residual movement of the water and the dye within it, producing some concentration variations for a fixed cell over time. This example highlights the importance of leaving enough time after the mixing of the dye so that the water is completely quiet and well-mixed before the calibration videos are captured, reducing the variability of pixel values. In addition, **Figure 4.10** shows a strong gradient of the green intensity values for high concentration levels and deeper water depths (and hence lower measurement sensitivity). These gradients could induce errors that could later affect the recorded concentration maps. To avoid that, maximum concentration values recorded within the experimental campaign were kept below $5 \ 10^{-6}$ L/L. It should be noted that after initial testing and refinement of the technique, the calibration was repeated and updated (see **Section 5.5.1**).

4.5. Experiments

Several sets of tests were performed to achieve the objectives proposed in **Section 3.**

4.5.1. No Vegetation Tests

A first set of experiments with no vegetation was performed using laboratory set up explained in **Section 4.2**. The aim of this set of experiments was firstly to validate method developed for this study (**Section 4.1** to **Section 4.4**), and then to obtain a first set of results that were used and compared later with results obtained in more complex vegetated experiments. Experiments were undertaken using 4 different uniform flow conditions (**Table 4.3**).

Santiago Rojas Arques
Department of Civil and Structural Engineering

Table 4.3. Water depth test conditions.

I. D.	h [m]	W_d/h [$-$]	S_0 [$-$]
$D36$	0.036	33.89	0.00123
$D54$	0.054	22.59	0.00123
$D72$	0.072	16.94	0.00123
$D90$	0.090	13.56	0.00123

These water depths were selected in order to achieve a range of shallow flow conditions ($W_d/h \geq 10{\sim}20$), usually found in low gradient, meandering alluvial channels with floodplain regions (**Rosgen, 1994**). For all the tests described in this thesis uniform flow conditions were achieved by controlling both the tailgate weir downstream and the valve for flow rate explained in **Section 4.2.1** until a constant water depth was achieved for the full channel length. The water depth was measured by Vernier gauges located at a distance of 0.25 m upstream and downstream of the recorded area and with an accuracy of 0.1 mm. Before each test, the pointers were calibrated to zero by touching the channel bed and then they were fixed at the desired water depth. Then, the system was turned on and the valve and the tailgate weir were controlled until the flow was adjusted so that the point gauge made contact with the flow surface for approximately 50 % of the time.

From this set of experiments, an injection located at the centre of the channel was released for each tested water depth/flow rate to ensure no effects on the plume from the channel walls. Then, time-averaged transversal profile of longitudinal flow velocity and transverse mixing were quantified. The description of analysis process and results are shown in **Section 5** and **Section 6.1.**

4.5.2. Single Vegetated Bank Tests

Experiments were performed to study the influence of a partially vegetated channel on the hydrodynamic and mixing processes. These tests were configured in a similar way to those designed by **White and Nepf (2008)** and **West (2016)**. This set of experiments allowed the recording of data along the full recorded area to obtain a general understanding of processes and the results that could be compared with those obtained in previous experiments.

Vegetation was simulated using plastic artificial emergent arrays similar to those used in previous experiments (**James et al, 2004; Tanino and Nepf, 2008b**) with a stem diameter $d = 0.005$ m disposed in a staggered distribution, similar to those found in previous work (**Hirschowitz and James, 2008**). **White and Nepf (2008)** conducted similar experiments to study longitudinal flow velocity profiles along partially vegetated channels, using a vegetation density of $\emptyset = 0.02, 0.045$ and 0.1, where $\emptyset$ is the solid volume fraction introduced in **Section 2.2**. **West (2016)** also studied an emergent partially vegetated layer in ponds, using a density of $\emptyset = 0.005$ and 0.02. **Huang et al (2008)** and **Sun et al. (2010)** observed different densities for different real vegetation species. Based on these previous studies, three different vegetation densities were considered for these experiments:

Santiago Rojas Arques
Department of Civil and Structural Engineering

Table 4.4. Vegetation density test conditions.

I. D.	$\emptyset \; [-]$
Veg_1	0.0015
Veg_2	0.006
Veg_3	0.025

Vegetation densities shown in **Table 4.4** were chosen to be similar to those used in previous works by **White and Nepf (2008)** and **West (2016)**, so results could be compared. In addition, these densities were in the range of those observed by **Hung et al. (2008)** and **Sun et al. (2010)** in real vegetated rivers. In addition, **Figure 4.11** shows a scheme of the stem distribution for each vegetation density.
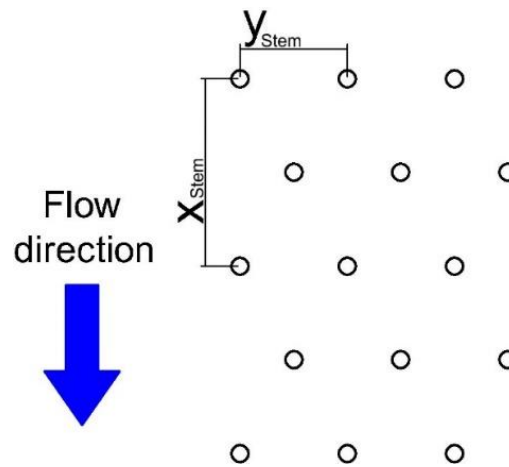
Figure 4.11. Scheme of stem configuration.

Where x_{Stem} and y_{Stem} are the distances between stem centres in the streamwise and spanwise direction respectively. The corresponding values for each vegetation density are $x_{Stem} = 0.21$ m, 0.1050 m and 0.0525 m and $y_{Stem} = 0.12$ m, 0.06 m and 0.03 m for $\emptyset = 0.0015$, 0.006 and 0.025 respectively.

A constant vegetated bank width (W_{veg}) was installed along the flume for each density. This vegetated width was designed in order to ensure the creation of a fully developed shear layer for all different water depth and density conditions.

In order to achieve this, data from previous experiments performed by **White and Nepf (2008)** and **West (2016)** were considered. The minimum vegetated bank width should allow the full development of the inner layer. **White and Nepf (2007)** proposed that this length depends on the stem drag properties ($\delta_{Inner} \approx (C_D a)^{-1}$) and **White and Nepf (2008)** obtained a maximum inner length of 0.062 m corresponding to $\emptyset = 0.02$, $h = 0.068$ m and $U_{free} = 0.1768$ m/s. They used artificial cylinders to simulate vegetation with a stem diameter $d = 0.0065$ m and a vegetated bank of width $W_{veg} = 0.4$ m. Later **West (2016)** also used artificial vegetation with a stem diameter of $d = 0.004$ m, obtaining a maximum inner length $\delta_{Inner} = 0.28$ m for $\emptyset = 0.005$, $h = 0.15$ m and $U_{free} = 0.1$ m/s.

Santiago Rojas Arques
Department of Civil and Structural Engineering

In the same way, the maximum vegetated bank width should allow full development of the outer layer, allowing a region with a constant free open flow velocity with no wall effects. **White and Nepf (2008)** obtained a maximum outer length $\delta_{Outer} = 0.22$ m and **West (2016)** of $\delta_{Outer} = 0.31$ m.

Based on these results, a vegetated bank width $W_{Veg} = 0.42$ m was designed. This width represented $^1/_3$ of the total channel width. This width was designed to allow full development of both the inner and outer layer, and would leave enough space in the free open region to achieve a constant longitudinal free open flow with no wall effects. In addition, 10 different injection positions were used to each water depth and vegetation density, shown in **Figure 4.12** as red dots. The first injection was located at y $= 0.48$ m from the right wall and at 0.06 m from the limit of the vegetated bank. Then the injector was moved 0.04 m each time to record the depth-averaged concentration distribution for different injections along the shear layer, and therefore, to obtain a better understanding of the mixing processes within this layer. The scheme of test configurations is shown in **Figure 4.12** and the results from these test conditions are presented in **Section 6.2.**
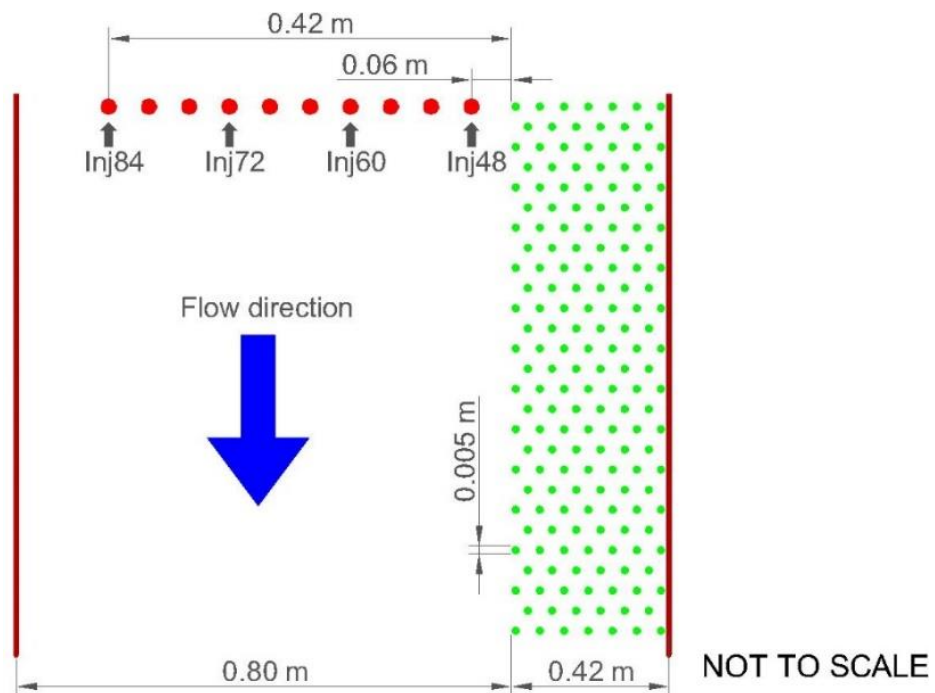
Figure 4.12. Scheme of one side vegetation configuration.

Santiago Rojas Arques
Department of Civil and Structural Engineering

4.5.3. Two Vegetated Banks Tests

A set of experiments was designed with vegetation at both sides of the channel width. The purpose of these tests was to study the behaviour and interaction of two velocity shear layers produced by vegetated banks. The width of free flow region (W_{Free}) was considered based on results from previous experiments shown in **Section 6.2**. The initial free width region was first designed to allow the full development of both shear layers generated by each vegetated bank with no overlap. Then, in subsequent experiments the free flow region was narrowed gradually to force an interaction between both shear layers. The width of vegetated patches was fixed for all experiments as $W_{Veg} = 0.21$ m. This width of each patch was half of those used in previous experiments such that the total amount of vegetation remained constant compared with previous experiments. Therefore, the same amount of stems were used to cover both vegetated banks to keep a constant relationship between water depth and flow resistance and thus remain a quasi-constant flow rate for tests at each flow depth irrespective of vegetation arrangement (i.e. single or double bank).

Rhodamine WT was injected in the centre of the channel for all different water depths shown in **Table 4.4** (represented in **Figure 4.13** as a red dot), vegetation densities and values of W_{Free}. When W_{Free} became narrower, the injected dye entered further into the vegetated patches. This phenomenon affects to the recorded concentration videos as stems created visual barriers and concentration could not be recorded properly within the vegetated region. This effect also became more prominent for higher densities. Therefore, four "windows" were designed to solve this problem. These windows were transversal gaps in the vegetated patch that allowed cameras to record the full transverse profile of dye injections. These gaps were located just below each camera to optimise the quality of recorded concentration profiles, with a longitudinal distance between gaps of 1.2 m as shown **Figure 4.13**. Results from these test conditions are presented in **Section 6.3.**
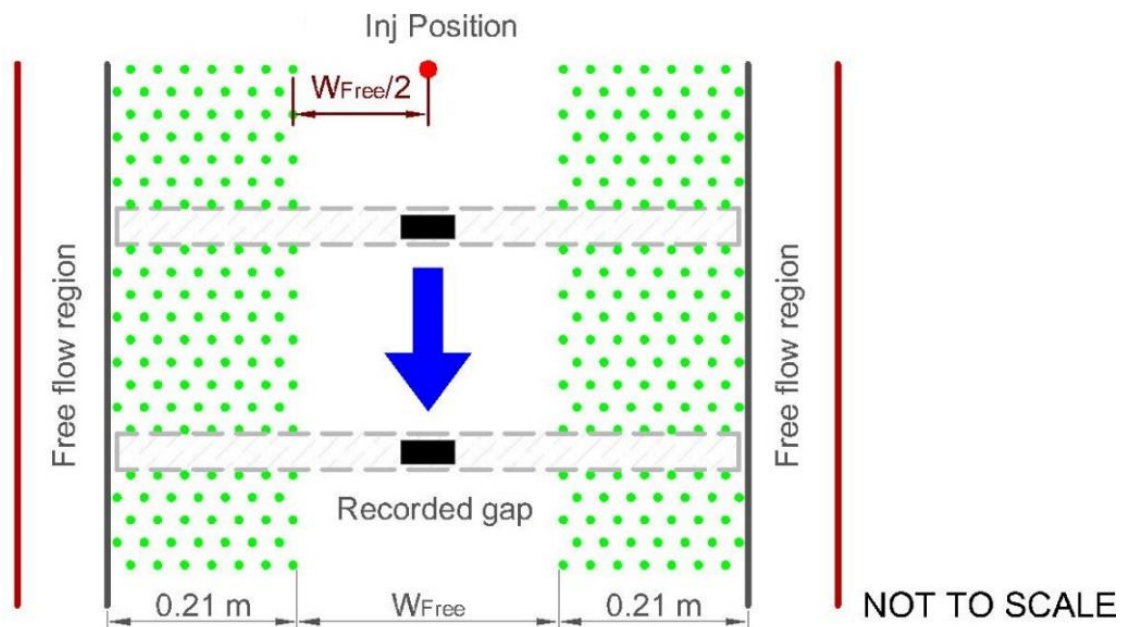
Figure 4.13. Scheme of both sides vegetation configuration. Black rectangles represent camera positions.

Santiago Rojas Arques
Department of Civil and Structural Engineering

In order to achieve W_{Free} values (and given a constant W_{Veg}), a free flow region was created at both channel edges between vegetated patches and channel walls as shown in **Figure 4.13**. In order to isolate the central studied region of the channel and to avoid any interactions with free flow regions created at each side; thin plastic walls were installed just outside the vegetated patches. These wall sections had an "L" shape, with a height of 0.1 m to avoid overflow, and a length of 0.92 m, so several of these wall sections were installed to cover the entire length of the channel. The base was perforated with holes following the same pattern as stem arrays and attached with four stems along their lengths as shown in **Figure 4.14**.
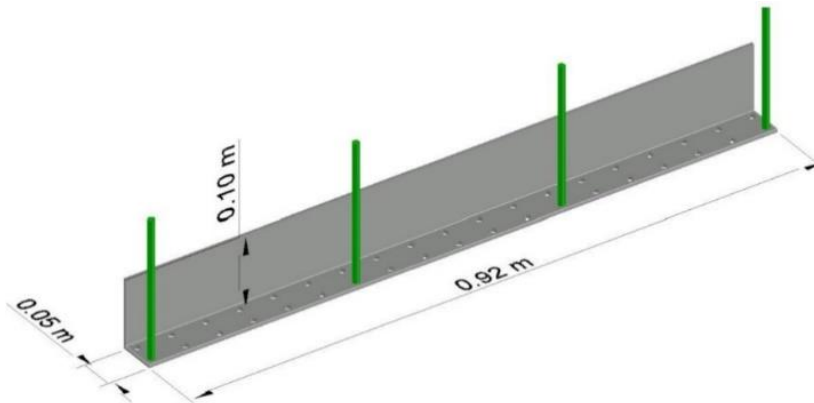
Figure 4.14. Scheme of walls used to isolate central region.

Santiago Rojas Arques
Department of Civil and Structural Engineering

5. Data Analysis and Validation of Methodology

In this section, the processes taken to analyse the experimental data obtained by the methodology explained in **Section 4** are described. In the first part of this section the processes used with PIV velocity data are explained and in the second part a brief description of those used to analyse PCA data are discussed. In addition, measurements of longitudinal flow velocity, concentration profiles and transverse mixing behaviour were obtained using different methods to validate the new methodology explained in **Section 4**. Finally, some improvements are discussed and further details of the techniques applied to analyse PCA data are explained.

5.1. Velocity Data Analysis

For each video recorded using the Large-Scale PIV technique, individual frames were dewarped to correct lens distortions and rotation produced by each camera using the spatial calibration described in **Section 4.3.1**. Then, videos were converted into black and white using Matlab function *rgb2gray*, and a mean frame for each camera was obtained by averaging over the 10 seconds recorded, obtaining a "background" frame over the analysed time. This frame was subtracted for each individual frame to delate the pattern of the metal grid used in the channel to fix cylinders, which otherwise could produce erroneous data during the PIV analysis. After this process, the main background of the channel was black and tracers were white, enhancing the particle identification. Finally, a single wide frame was generated for each instantaneous time by combining the frames for each camera considering synchronization explained in **Section 4.3.2** and **Section 4.3.3.** An example of this process is shown in **Figure 5.1**, where in **Figure 5.1 (a)** an instantaneous black and white image from PIV videos is shown with a physical size of 1.22×1.80 m and a pixel resolution of 1×1 mm. Then, in **Figure 5.1 (b),** the time-averaged frame over 10 s is shown and in **Figure 5.1 (c)** the resulting image from removing the background image (**Figure 5.1 (b)**) from the instantaneous frame (**Figure 5.1 (a)**), obtaining a particle density of around 9 particles/cm^2.

Figure 5.1. Example of background removal for PIV. a) Instantaneous black and white frame; b) mean black and white background over 10 seconds and c) same instantaneous frame without background.

5.1.1. Length of Videos

For each test configuration, enough frames must be analysed to ensure all cameras recorded enough tracers travelling along the recorded area, and thus the time-averaged primary velocities obtained are representative of the flow conditions. Therefore, for each test configuration, a PIV video with a length of 90 s was recorded and a longitudinal velocity map was obtained for each couple of instantaneous frames. Then, the accumulative longitudinal mean velocity over time was calculated for different spatial points:

Santiago Rojas Arques
Department of Civil and Structural Engineering

$$Acc\ \overline{U_x}_j = \frac{\sum_{i=1}^{j} U_{x_i}}{j} \qquad\qquad eq.5.1$$

Where U_x was the longitudinal flow velocity for a specific spatial position and time and j was the number of time samples used. For this temporal analysis, experimental configurations with the deepest water depth ($h = 0.090$ m) and the densest vegetation density ($\emptyset = 0.025$) were considered for each test configuration. These experiments were selected because highest eddies should be produced in these conditions (**White and Nepf, 2007**) due to the highest velocity gradient and hence, more time would be recorded to achieve a real time-averaged longitudinal velocity.

Results for accumulative time-averaged velocities for different test configurations are plotted in **Figure 5.2**. Values are normalised by the time-averaged longitudinal velocity considering the full video length. For no vegetation tests, the spatial point considered in **Figure 5.2** was located at $x = 1.5$ m and $y = 0.61$ m for $h = 0.090$ m experiment. The point for one vegetated bank test was located at $x = 1.5$ m and $y = 0.70$ m for $h = 0.090$ m $- \emptyset = 0.025$ experiment and the point for both vegetated banks experiments was located at $x = 1.5$ m and $y = 0.90$ m for $h = 0.090$ m $- \emptyset = 0.025 - W_{free} = 0.7$ m. These transverse locations were chosen because this is where large eddy structures were expected to be created (e.g. for one and two vegetated bank flows) and therefore where more variation of the instantaneous primary velocity was expected.
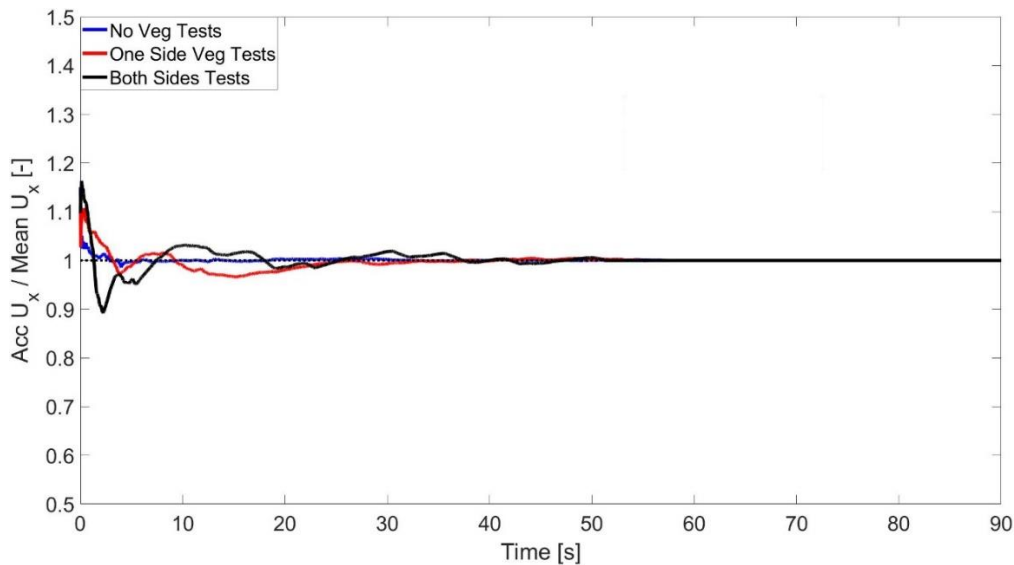
Figure 5.2. Accumulative time-averaged longitudinal velocities normalised by total time-averaged longitudinal velocity for different test configurations and spatial points.

Figure 5.2 shows how when the recorded time used to obtain the time-averaged longitudinal velocity increases, the mean value obtained converges to a constant time-averaged value, which is representative of the real time-averaged velocity of the flow. The figure shows an increase of time required to achieve a quasi-constant accumulative mean velocity for one vegetated and two vegetated banks flow respectively, suggesting an increase of the large eddy structures generated for each flow condition. Based on this, for each test configuration, time length was selected for analysis of the PIV videos are shown **Table 5.1**.

Santiago Rojas Arques
Department of Civil and Structural Engineering

Table 5.1. Video lengths analysed for each test configuration.

Test Configuration	Video Length Analysed
No Vegetation Tests	10 s
One Side Vegetation Tests	40 s
Both Sides Vegetation Tests	60 s

PIV videos were supplied to the commercial PIV software Dynamic Studio, by DantecDynamics Ltd. In this program, all selected frames for a single test were loaded and dimensions of pixel frames and video frequency were introduced. The steps taken to process image files and obtain final velocity maps are described below.

5.1.2. Adaptive Correlation

Once instantaneous frames were loaded to the program, a first step was taken to obtain instantaneous velocity vectors based on the identification of the PIV tracer positions and their spatial movement between consecutive frames. A final interrogation area $M \times N$ was selected from different available options. In addition, a factor $F_{AdapCorr}$ was introduced to define the first interrogation area $\left(M \, F_{AdapCorr}\right) \times \left(N \, F_{AdapCorr}\right)$. The program divided each frame using this grid size, identifying particles movement between each consecutive pair of frames and obtaining a single velocity vector for each grid cell. After this first iteration, velocity vectors obtained for each cell were used as the starting point to calculate velocity vector in the next iteration with a new interrogation area with dimensions: $\left(M \, (F_{AdapCorr} - 1)\right) \times \left(N \, (F_{AdapCorr} - 1)\right)$. This process was performed until final interrogation area defined was reached.

Different final interrogation areas with the same $F_{AdapCorr} = 3$ were studied and time-averaged longitudinal flow velocity for three fixed point were calculated as shown **Figure 5.3**. These points were located in the centre on the channel length ($x = 2.2$ m) and at three different positions along the channel width ($Point \ A$ was located at $y = 0.61$ m, $Point \ B$ at $y = 0.3$ m and $Point \ C$ at $y = 0.05$ m). In addition, same interrogation area size (16×8) was studied considering two different factors ($F_{AdapCorr} = 3$ and 5) for the same fixed points.
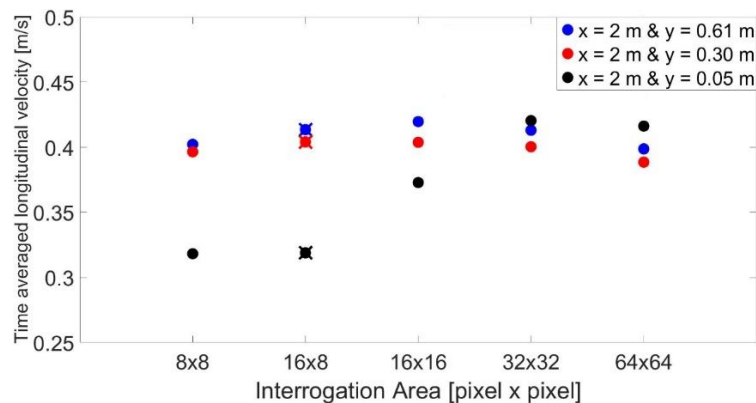
Figure 5.3. Time-averaged longitudinal velocity for fixed points located in the middle of the channel length (x = 2 m) and at different transversal positions. Crosses represent same Interrogation Area but with a Factor = 5. Data were obtained for test h = 0.090 m without vegetation.

Figure 5.3 shows for both $Point \ A$ ($y = 0.61$ m) and $Point \ B$ ($y = 0.30$ m) that there was not a significant change in longitudinal flow velocity as the interrogation area size was varied, but nevertheless an increase of longitudinal velocity close to the wall ($y = 0.05$ m) was

Santiago Rojas Arques
Department of Civil and Structural Engineering

produced when the interrogation area was increased. This increase was produced because of a loss of precision in regions where a rapid velocity variation was expected. The same results were found for the same interrogation area size but with different $F_{AdapCorr}$ values, represented in **Figure 5.3** as crosses. In order to not to lose information in areas with high velocity gradients, an interrogation area of 16×8 was introduced for all tests. The M dimension, corresponding to the channel length, was longer to ensure that particles do not move out of the interrogation window between the two frames. In addition, the default factor $F_{AdapCorr} = 3$ was selected as not significant differences were found when $F_{AdapCorr}$ was changed.

In addition, the minimum size of the interrogation area is defined by the particle density inside the interrogation area. Particle density should be sufficient such that enough particles are present in each interrogation area for two consecutive frames to ensure a good particle detection. A minimum specified density of 6 particles for each interrogation area was considered in previous works (**Weitbrecht et al., 2002**). However, a homogeneous particle density was found to be difficult to control for tests with high velocity flow gradients. Thus, further analysis explained below was applied to ensure the velocity vectors recorded over the analysed area were representative of the flow.

5.1.3. Range Validation

After the Adaptive Correlation process, a single velocity vector map with a dimension of 274×559 pixels and a pixel resolution of 4.45×8.01 mm was generated for each pair of frames. Then, a Range Validation process was performed to validate the generated vectors and remove spurious high velocities and zero velocities obtaining from interrogation areas with no PIV tracers recorded. Each single vector was validated against a defined expected range of velocity values, deleting all vectors outside this range.

As different test configurations were ran, the variation of Range Validation was studied for no vegetated flows and for one vegetated bank flows by testing different validation ranges in order to find the appropriate values. The four parameters introduced in the Range Validation were maximum and minimum longitudinal and transversal velocity components ($U_{x_{max}}$ $U_{x_{min}}$ and $\pm U_{y_{max}}$). For all different options studied, same positive and negative values were considered for transversal velocity components.

Three different scenarios were studied in which two of the primary velocity components were fixed and the other was changed. For all iterations, time-averaged and standard deviation of longitudinal velocity were obtained and data from same spatial points as in **Figure 5.3** were plotted in **Figure 5.4** (left axis). In addition, for all iterations, the percentage of vectors rejected was obtained as shown **Figure 5.4** (right axis) to ensure that fewer than 5 % of vectors were rejected (**Adrian, 1991; Martins et al. 2018**).

Figure 5.4 (a) shows the variation of primary velocity when $U_{x_{max}}$ changes. The results show how for smaller $U_{x_{max}}$ values the primary velocity is smaller and, when $U_{x_{max}}$ increases, the longitudinal velocity flow obtained for each position increases. This behaviour is explained as for lower values of $U_{x_{max}}$ values, range validation deletes both spurious and valid velocity vectors, obtaining smaller time-averaged velocity values. In addition, once $U_{x_{max}}$ is increased, small variations in time-averaged longitudinal velocity are observed, showing a quasi-constant velocity value for higher $U_{x_{max}}$. This quasi-constant behaviour for higher values suggests that most of high velocity vector values are included in the range, and therefore the value of $U_{x_{max}}$ defined for the range validation is broad enough to include most of valid velocity vectors.

Figure 5.4 (b) shows time-averaged primary velocity values for same spatial positions for different $U_{x_{min}}$. The results show that values remain quasi-constant for lower $U_{x_{min}}$ values.

Santiago Rojas Arques
Department of Civil and Structural Engineering

However, if $U_{x_{min}}$ is too high, velocity results start to increase, with a stronger variation for the point closest to the wall ($y = 0.05$ m). This trend agrees with the behaviour described previously for $U_{x_{max}}$ and suggests that for values of high $U_{x_{min}}$, some valid velocity vectors are deleted, increasing the overall time-averaged velocity. **Figure 5.4 (c)** shows time-averaged longitudinal velocity obtained for different $\pm U_{y_{max}}$. The results show a quasi-constant trend for all different $\pm U_{y_{max}}$ values, suggesting that there is not a strong transverse velocity component.
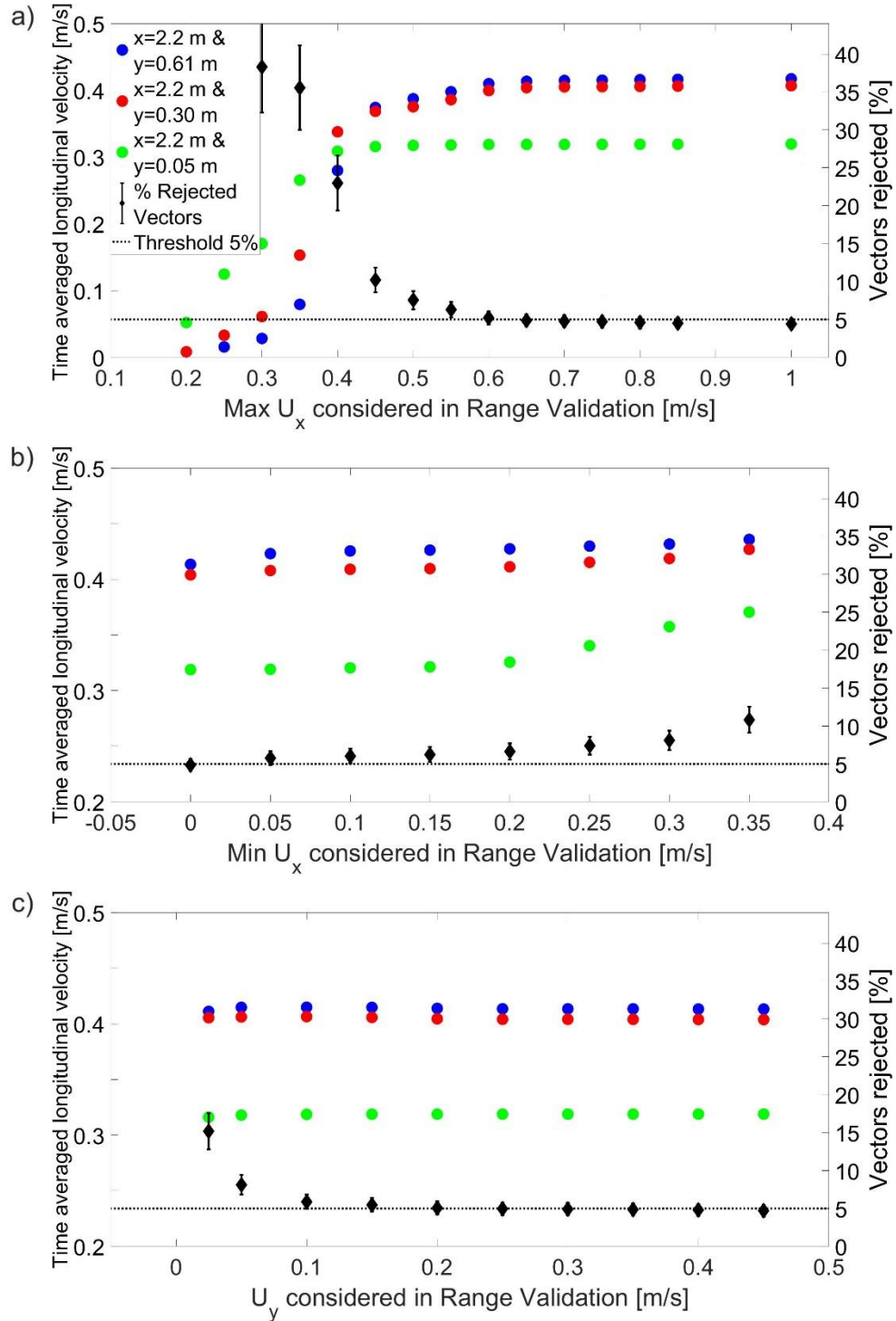
Figure 5.4. Left axis) Time-averaged primary velocity results using different range validation values for three different spatial positions for test h = 0.090 m without vegetation. Right axis) Percentage of vectors rejected for different velocity component combinations for same flow conditions.

Santiago Rojas Arques
Department of Civil and Structural Engineering

Figure 5.4 (right axis) shows the percentage of vectors rejected for same range validation component combinations as in **Figure 5.4** (left axis). Each graph represents the variation of one of the components whilst fixing the other two. The results plotted in **Figure 5.4** show the highest variability in time-averaged primary velocity was obtained by changing the $U_{x_{max}}$, suggesting that this component is the most sensitive in order to obtain suitable results. In addition, percentages of rejected vectors in $U_{x_{min}}$ and $\pm U_{y_{max}}$ components only were higher than 5 % when they started to reach values of 0.15 m/s for the case of $U_{x_{min}}$ and close to 0.1 m/s for the $\pm U_{y_{max}}$ component respectively.

The range values were also studied for longitudinal velocity for one side vegetated bank flows. For this case, different $U_{x_{min}}$ were used and $U_{x_{max}}$ and $\pm U_{y_{max}}$ values were fixed. Then, longitudinal velocity values within the vegetated banks were compared to study how variation of $U_{x_{min}}$ could affect velocity results. As in the range comparison for no vegetated flows, three different spatial point were selected for each vegetation density and water depth. These three points were located at the same streamwise position as those considered previously ($x = 2.2$ m) and at three different spanwise positions ($Point\ A$ was located at $y = 0.2$ m, $Point\ B$ at $y = 0.42$ m and $Point\ C$ at $y = 0.52$ m). Therefore, $Point\ A$ was located within the vegetated bank, $Point\ B$ was located in vegetated limit and $Point\ C$ was located within the shear layer. For each point, $U_{x_{min}}$ was changed from 0 m/s to 0.25 m/s in increments of 0.05 m/s. Time-average longitudinal velocity results for $h = 0.090$ m for each vegetation density were plotted in **Figure 5.5**.

- 63 -
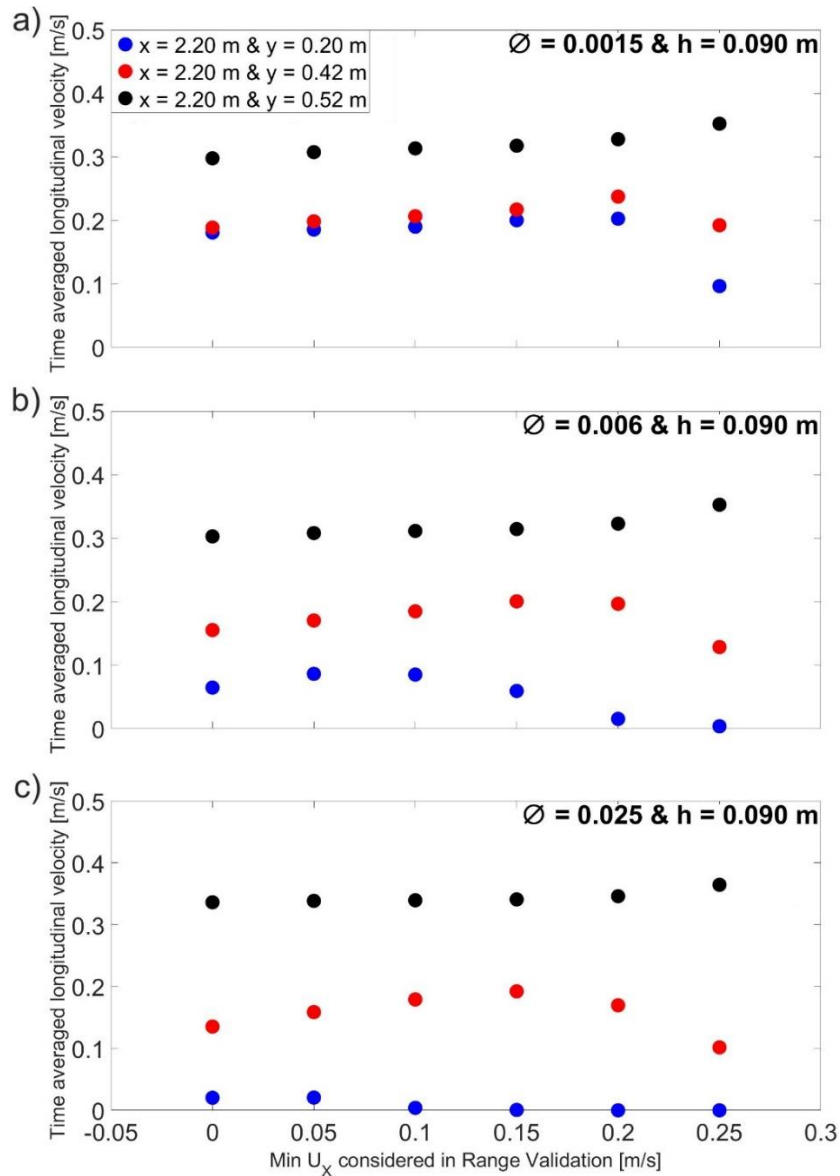
Figure 5.5. Time-averaged primary velocity results using different range validation values for three different spatial positions for test h = 0.090 m with one vegetated bank.

In **Figure 5.5**, the $U_{x_{min}}$ values within the vegetated patch ($y = 0.2$ m) show an increased for tests $\emptyset = 0.0015$ and $\emptyset = 0.006$, shown in **Figure 5.5 (a)** and **Figure 5.5 (b)** respectively; when the limit values increase until they reach a limit value from which $U_{x_{min}}$ values start to decrease. Similar behaviour was observed for the point located at the vegetated boundary ($y = 0.42$ m) for the same vegetation densities. This behaviour is produced because of the elimination of small velocities within the vegetation as the validation limit is raised. The decrease observed for the higher $U_{x_{min}}$ values is produced as most of valid velocity vectors are out of the defined range, and therefore they are neglected.

Results from $\emptyset = 0.025$ (**Figure 5.5 (c)**) only shows same behaviour for the *Point B* ($y = 0.42$ m), but *Point A* ($y = 0.2$ m) only presents a decrease of velocity values when $U_{x_{min}}$ increases. This behaviour is produced as very low velocities are recorded within the vegetation for this density, and therefore even small increases of $U_{x_{min}}$ produce that most of recorded velocity vectors are out of the valid range. In addition, the $U_{x_{min}}$ values for the point

- 64 -

located within the shear layer ($y = 0.52$ m) do not decrease for the higher values for any vegetation density, as some higher velocity vectors are still included in the range. Results plotted in **Figure 5.5** show a strong dependence on the $U_{x_{min}}$ limit of the time-averaged velocity results. In addition, they suggest that a $U_{x_{min}}$ value of 0 m/s in the range validation was required to not to lose valid velocity information within the vegetated patch.

Based on previous discussed results, a different $U_{x_{max}}$ was defined for each water depth. This value was chosen as the lower in the quasi-constant region discussed in **Figure 5.4 (a)**, which percentage of rejected values was smaller than 5 % as shown in **Figure 5.5 (a)**. In addition, same $U_{x_{max}}$ was defined for those test configurations with the same water depth but with different vegetation configurations (non-vegetated flow, one vegetated bank flow and two vegetated banks flow), as similar time-averaged free longitudinal flow velocity were expected to obtain. The setting for different $U_{x_{max}}$ for each water depth shown in **Table 5.2** was based on the different maximum longitudinal flow velocities expected for each flow condition. Hence, the selected $U_{x_{max}}$ should be large enough to allow all real instantaneous velocities recorded by cameras, but not so large that any erroneous high velocity values will be included.

The same U_{min} was set as 0 m/s for all test configurations. This value was chosen so as to not eliminate information within the low velocity areas, such as the vegetated banks or close the channel wall as shown **Figure 5.5**.

Finally, the transversal velocity component was defined as $U_{y_{max}} = \pm 0.35$ m/s for all test configurations. The variation of this value did not affect to the time-averaged longitudinal velocity as shown **Figure 5.4 (c)** and allowed the correct identification of all valid vectors within the shear layer for the vegetated flows. Parameters are shown in **Table 5.2**.

Table 5.2. Range validation parameters used during velocity analysis for all different vegetated and non-vegetated tests.

Depth [m]	$U_{x_{max}} - U_{x_{min}}$ [m/s]	$\pm U_{y_{max}}$ [m/s]
0.036	0.50 – 0	$\pm$ 0.35
0.054	0.55 – 0	$\pm$ 0.35
0.072	0.60 – 0	$\pm$ 0.35
0.090	0.65 – 0	$\pm$ 0.35

5.1.4. Moving Average Validation

Finally, velocity vector maps produced were validated using the Moving Average Validation. This step was taken to detect any vector that its value was into the previous defined range but it was deviated from their neighbourhood values. These vectors can be or low velocity vectors recorded along the free flow region or rapid velocity vectors recorded along the vegetated bank. These vectors are produced during the Adaptive Correlation and they are not discarded during the Range Validation, but do not represent the real behaviour of the flow.

Each velocity vector was compared with values in the neighbourhood of a defined size area of $M \times N$. If vector was deviated more than the Acceptance Factor (F_{MovAv}), it was substituted by a new value generated by a local interpolation of n_{iter} iterations. Program allows to choose between three different size areas ($M = N = 3, 5$ or 7). These three different options were studied considering the default values of Acceptance Factor $F_{MovAv} = 0.1$ and $n_{iter} = 3$ as shown **Figure 5.6**. Different size areas were considered and time-averaged longitudinal flow velocity was obtained for three fixed cells located at different transversal positions ($Point\ A$ at

Santiago Rojas Arques
Department of Civil and Structural Engineering

$y = 0.61$ m, $Point\ B$ at $y = 0.3$ m and $Point\ C$ at $y = 0.05$ m) and fixed in the centre of the channel length ($x = 2.2$ m).
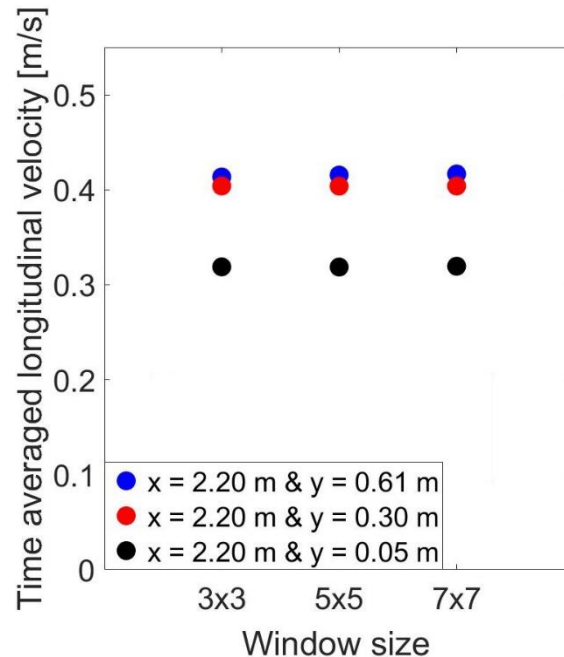
Figure 5.6. Time-averaged longitudinal velocity for fixed points located in the middle of the channel length (x $=$ 2.2 m) for test h $=$ 0.090 m without vegetation for different Moving Average size area.

Figure 5.6 shows longitudinal velocity results from same points represented in **Figure 5.3** and **Figure 5.4**. In the graph, different window sizes were selected using the rest of parameters as the default values. Results suggested that changes in size did not affect final results. Thus, a size area of $M = N = 3$ was selected, and rest of values were defined as $F_{MovAv} = 0.1$ and $n_{iter} = 3$.

5.1.5. Temporal Analysis

Instantaneous velocity vector maps generated after these steps (**Sections 5.1.2**, **5.1.3** and **5.1.4**) were exported to Matlab, producing a matrix of longitudinal velocity data and another matrix of transversal velocity data. Then, a time series analysis was applied to obtain the temporal mean velocity field and temporal standard deviation values for longitudinal velocity to identify and remove any extreme outlying velocity value.

For any single spatial position, the distribution of velocity data over time can be represented as a histogram as shown **Figure 5.7**. **Figure 5.7 (a)** shows the histogram related to a spatial point located at a streamwise position $x = 1.75$ m and in the centre of the spanwise ($y = 0.61$ m) for the water depth $h = 0.090$ m with no vegetation. In addition, **Figure 5.7 (c)** and **Figure 5.7 (e)** show the histograms for two different spatial points located at the same streamwise position for the water depth $h = 0.090$ m with the densest vegetated bank ($\emptyset = 0.025$). **Figure 5.7 (c)** is located within the vegetated bank ($y = 0.2$ m) and **Figure 5.7 (e)** is located within the shear layer ($y = 0.5$ m). In addition, **Figure 5.7 (b), Figure 5.7 (d)** and **Figure 5.7 (f)** show the longitudinal velocity signal over time for each spatial point respectively.

The histogram plotted in **Figure 5.7 (a)** shows that the resulting distribution for those points located in the free open flow region was unimodal and roughly symmetrical. This distribution presents most of the velocity values (80 %) within a narrow velocity range (0.35 – 0.45 m/s). Some low velocity values were recorded, represented in **Figure 5.7 (b)** as spurious velocity values in blue. These velocities may be produced as not enough PIV tracers

Santiago Rojas Arques
Department of Civil and Structural Engineering

were recorded for this specific time and position, and they were not properly removed by previous analysis steps (**Sections 5.1.3** and **5.1.4**). However, these values represent a very low portion (< 5 %) of all instantaneous values recorded, suggesting the suitability of the technique and the analysis applied.

Moreover, the histogram distribution of longitudinal velocity within the vegetation in **Figure 5.7 (c)** presented half of a unimodal distribution, with its maximum close to zero. This behaviour is produced as within the vegetation very low velocity values were observed. Moreover, the plot shows the velocity for the densest scenario, so very low velocity values are expected to be recorded. Similar to previous case, **Figure 5.7 (d)** shows in blue that the discarded values represent high spurious velocities recorded in some instantaneous frames. These instantaneous velocities could be recorded as a results of a very low concentration of PIV tracers. In addition, these values could also been produced for an accumulation of PIV tracers within the stems, producing some velocity errors. However, both **Figure 5.7 (c)** and **Figure 5.7 (d)** show that these spurious values represent a very low portion (< 5 %) of the full time series data.

Finally, for the point located within the shear layer a bimodal distribution is shown in **Figure 5.7 (e)**. This bimodal distribution agrees with the histogram obtained from the ADV mid-depth longitudinal velocity signal recorded by **Dupuis et al. (2017)**, where the shear layer generated within a compound channel with vegetation along the floodplain was studied and the longitudinal velocity signal at the edge of the floodplain was recorded. The histogram in **Figure 5.7 (e)** shows a wide range of velocity values. This is also plotted in **Figure 5.7 (f)** and suggests an increase of the turbulence within the shear layer compared with that recorded in the free flow region. Similar to previous cases, some very low or very high spurious velocity values seem to be recorded, representing a very low portion of the full time series data and suggesting the suitability of the technique and the analysis applied.

For each pixel, mean velocity value and standard deviation in time were obtained and values outside the region $\overline{U}_{x,y} \pm 3 * std(U_{x,y})$ were discarded. The allowed region represents 99.7 % of the total values inside a normal distribution.

Santiago Rojas Arques
Department of Civil and Structural Engineering
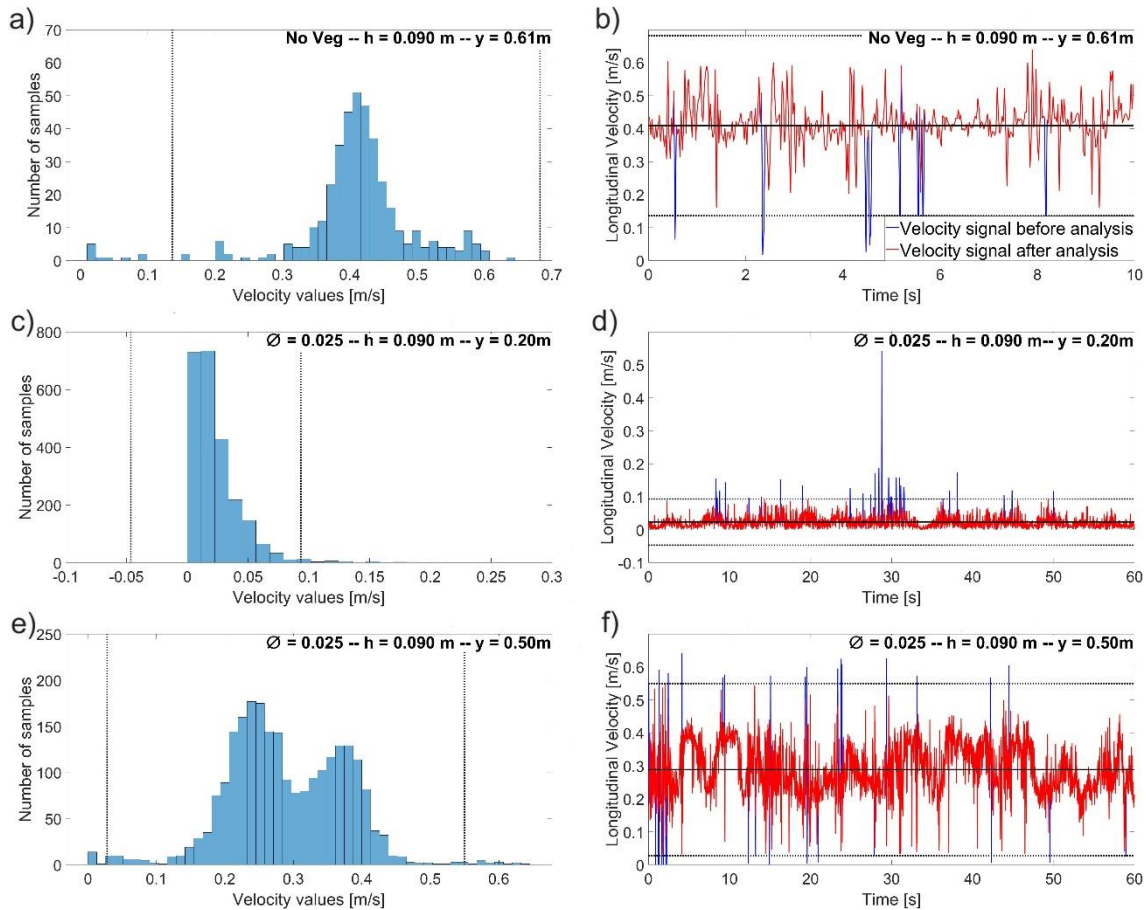
Figure 5.7. (Left) Histogram of velocity values along time for a single pixel. Dots represent $\overline{U}_{x,y} \pm 3 * std(U_{x,y})$ region and (right) time series data for the same pixel.

The mean velocity value is represented in **Figure 5.7 (b), Figure 5.7 (d)** and **Figure 5.7 (f)** as the black line, and boundaries of the defined region $\overline{U}_{x,y} \pm 3 * std(U_{x,y})$ are represented in all figures as black dots. In addition, blue longitudinal velocity signals plotted in **Figure 5.7 (b), Figure 5.7 (d)** and **Figure 5.7 (f)** show the velocity signal for each spatial point before time series analysis was applied; and red signals show those values of the signals which are inside the defined region. As **Figure 5.7** shows, this temporal analysis properly discards all extreme values over time for each spatial point. Once values outside the acceptable region were discarded, a time-averaged velocity value for each pixel was obtained.

5.1.6. Overlapping Regions

Time-averaged results presented a decrease of velocity values around the area where frames were overlapped. This decrease was produced during frame analysis due to missing and appearance of PIV particles between consecutive interrogation areas in the region between two cameras. The Matlab code *ndnanfilter.m* (**Vargas, 2016**) was used to smooth these junctions.

Figure 5.8 (a) and **Figure 5.8 (b)** show the time-averaged longitudinal velocity values along a streamwise profile located in the centre of the spanwise ($y = 0.61$ m) for each water depth of no-vegetated flow experiments before and after the code *ndnanfilter.m* was applied respectively. In addition**, Figure 5.8 (c)** and **Figure 5.8 (d)** show the time-averaged longitudinal velocity map for water depth $h = 0.054$ m before and after the code was applied respectively.

Santiago Rojas Arques
Department of Civil and Structural Engineering
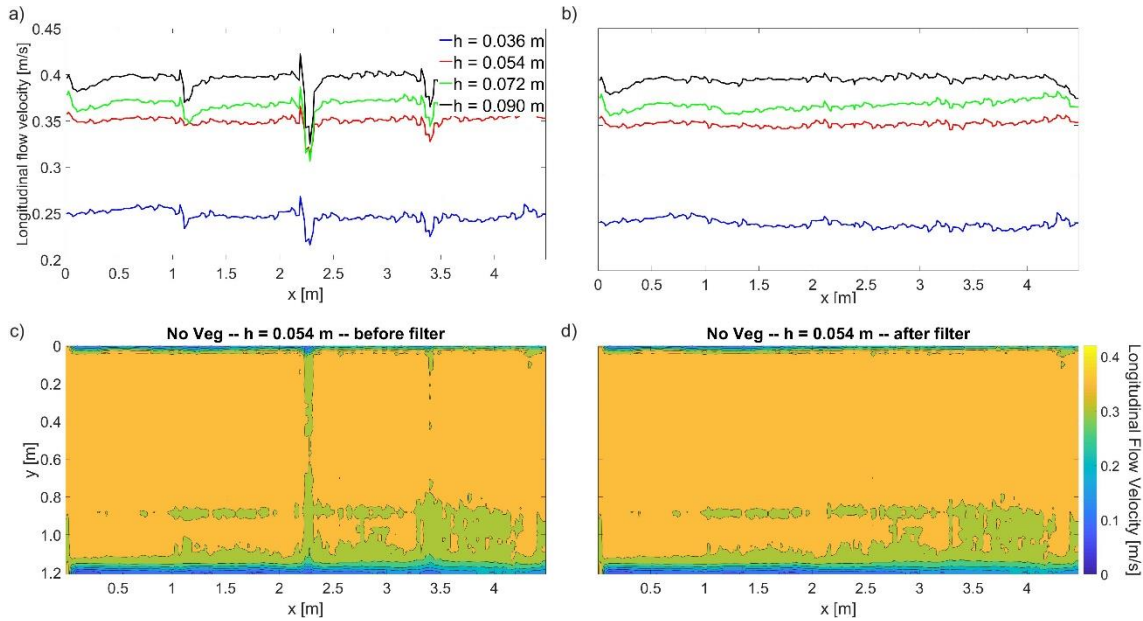
Figure 5.8 a) Time-averaged longitudinal velocity in the centre of the channel along the channel length. b) shows the same velocity after ndnanfilter.m filter.

Figure 5.8 (a) shows three regions with a width of approximately 0.2 m (20 values) with an attenuation of velocity values for different tests, in agreement with the overlapping regions between two consecutive cameras. These areas were converted into NaN values and *ndnanfilter.m* was applied with the option $WNAN = 2$ and a window size of $20 + n_{values}$, with $n_{values} = 4$. This option configured the program to work as a NaN-interpolant/GAP-filling, so NaN values were substituted by new ones generated running a weighted mean using information from n_{values} considered, giving more weight to those values closer to the substituted NaN values.

5.1.7. Two-dimensional Median Filter

Finally, a 3rd-order two-dimensional median filter was applied to time-averaged velocity maps to delete any spikes produced during the process explained previously. For this filter, an area was considered using the neighbourhood given around each single pixel (3×3 pixels) and producing an ouput pixel with the median value of the selected area. **Figure 5.9 (a)** shows the time-average longitudinal velocity map for water depth $h = 0.054$ m and no-vegetated flow condition before the filter was applied; and **Figure 5.9 (b)** shows the same map after the median filter was applied. In addition, **Figure 5.9 (c)** shows the resulting averaged transverse profile for both velocity maps. In addition, in **Figure 5.9 (c)** maximum and minimum longitudinal values over the streamwise direction were plotted for each transverse position.

Santiago Rojas Arques
Department of Civil and Structural Engineering
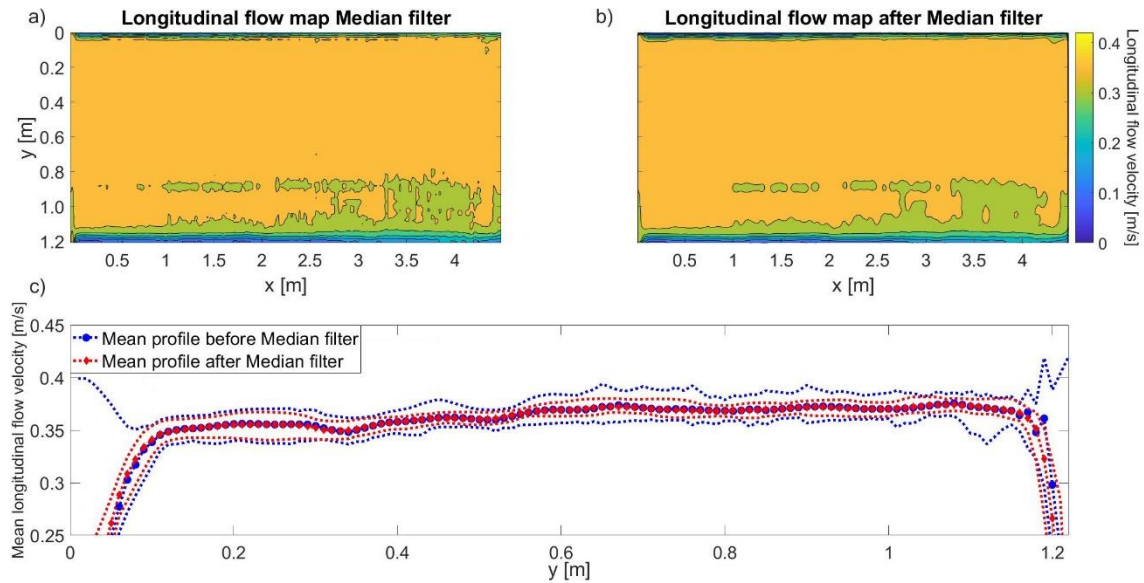
Figure 5.9. Longitudinal flow maps and mean transversal flow with maximum and minimum (dots) velocity with and without filters for $h = 0.054$ m.

Both time-averaged longitudinal velocity maps (**Figure 5.9 (a)** and **(b)**) show a sharp decrease of velocity close the channel walls. In addition, some areas with a lower longitudinal velocity than that recorded in the rest of the main channel were recorded on the lower right zone. This decrease of velocity may be produced as not enough PIV tracers were recorded at certain instantaneous frames, generating lower instantaneous velocity values that later would affect the time-averaged ones. However, these lower areas do not affect the averaged transverse profiles plotted in **Figure 5.9 (c)**.

Moreover, transverse profiles shown in **Figure 5.9 (c)** indicate how median filter applied to the velocity did not change the mean value but decreased the variation of data along the channel length smoothing some spurious values. In addition, **Figure 5.9 (c)** shows that the highest spurious values before the filter was applied were obtained at the channel boundaries. These spurious velocities were present there as this is the region where it is more difficult to record a sufficient amount of PIV tracers. In addition, due the presence of the channel walls, there could be some accumulations of PIV tracers that would affect the recorded velocities. These spurious instantaneous velocities, although do not represent real velocities, may have values within the Range Validation defined in **Section 5.1.3**. However, as **Figure 5.9 (c)** shows, the amount of these false velocities that have been considered as valid values is negligible and they have no effect on the mean longitudinal velocity profile.

Three different points ($Point\ A, Point\ B$ and $Point\ C$) were selected along the time-averaged mean longitudinal velocity profiles for tests with no vegetation to show differences. As in previous comparisons, these points were located at $y_A = 0.61$ m, $y_B = 0.3$ m and $y_C = 0.05$ m. For each spatial position, time-averaged mean longitudinal velocity values and their corresponding coefficient of variation ($C.V.$) were obtained from transversal profiles before and after median filter was applied. The $C.V.$ was calculated to quantify the variability of velocity data around the mean value along the streamwise direction. Results are shown in **Table 5.3**.

- 70 -

Table 5.3. Time-averaged mean longitudinal velocity results with and without filter and their coefficient of variation for non-vegetated tests.

Point A	U_x before Median	U_x after Median	$C.V.$ before Median	$C.V.$ after Median
$h = 0.036\,m$	0.242	0.243	2.24 %	1.66 %
$h = 0.054\,m$	0.369	0.369	1.50 %	1.02 %
$h = 0.072\,m$	0.399	0.401	1.84 %	0.90 %
$h = 0.090\,m$	0.416	0.418	2.26 %	1.11 %

Point B	U_x before Median	U_x after Median	$C.V.$ before Median	$C.V.$ after Median
$h = 0.036\,m$	0.250	0.251	2.37 %	1.57%
$h = 0.054\,m$	0.353	0.355	1.86 %	1.74%
$h = 0.072\,m$	0.360	0.362	2.70 %	2.09%
$h = 0.090\,m$	0.396	0.399	3.15 %	1.75%

Point C	U_x before Median	U_x after Median	$C.V.$ before Median	$C.V.$ after Median
$h = 0.036\,m$	0.218	0.223	7.88 %	6.49 %
$h = 0.054\,m$	0.246	0.261	7.59 %	3.56 %
$h = 0.072\,m$	0.261	0.274	9.16 %	5.30 %
$h = 0.090\,m$	0.290	0.307	8.40 %	3.82 %

Results in **Table 5.3** show mean longitudinal velocity was not affected by median filter applied to time-averaged longitudinal velocity maps. Only $Point\ C$ presented some increases, with relative differences around 5 %. These differences suggested that main erroneous data could be produced close to the wall. In addition, coefficient of variation results show low variations for most of transversal points, suggesting a quasi-constant longitudinal velocity obtained along the channel length. In addition, the variation decreases when median filter was applied, suggesting a decreased of highest and lowest erroneous velocity data. Highest variations were observed for point closer to wall, where it seems most of erroneous velocity data were produced.

5.2. PIV Validation

Time-averaged longitudinal flow velocity was obtained for tests with no vegetation described in **Section 4.5.1** for each water depth. Cameras recorded instantaneous PIV tracers and frames were analysed as described in **Section 5.1.**

Another two methods were used to validate the PIV velocity results. Firstly, longitudinal flow velocity for each water depth was measured manually by recording the travel time of small patches of floating tracers over 6 m of the channel length. Measurements were made at three spanwise positions situated at 150 mm, 250 mm and 610 mm from the channel wall. Each measurement was repeated three times by two different researchers to quantify errors in results, as shown in **Table 5.4**.

Santiago Rojas Arques
Department of Civil and Structural Engineering

Table 5.4. Manual longitudinal velocity measurements.

$h = 0.036$ m	$y = 0.61$ m	$y = 0.25$ m	$y = 0.15$ m
$U_{x\,1}$ [m/s]	0.321	0.316	0.300
$U_{x\,2}$ [m/s]	0.328	0.326	0.308
$U_{x\,3}$ [m/s]	0.330	0.326	0.316
$U_{x\,4}$ [m/s]	0.331	0.328	0.314
$U_{x\,5}$ [m/s]	0.330	0.317	0.314
$U_{x\,6}$ [m/s]	0.324	0.323	0.311

$h = 0.054$ m	$y = 0.61$ m	$y = 0.25$ m	$y = 0.15$ m
$U_{x\,1}$ [m/s]	0.438	0.420	0.405
$U_{x\,2}$ [m/s]	0.444	0.411	0.392
$U_{x\,3}$ [m/s]	0.444	0.435	0.400
$U_{x\,4}$ [m/s]	0.441	0.422	0.403
$U_{x\,5}$ [m/s]	0.441	0.417	0.373
$U_{x\,6}$ [m/s]	0.448	0.414	0.380

$h = 0.072$ m	$y = 0.61$ m	$y = 0.25$ m	$y = 0.15$ m
$U_{x\,1}$ [m/s]	0.526	0.504	0.484
$U_{x\,2}$ [m/s]	0.545	0.496	0.472
$U_{x\,3}$ [m/s]	0.504	0.488	0.476
$U_{x\,4}$ [m/s]	0.540	0.496	0.480
$U_{x\,5}$ [m/s]	0.540	0.500	0.476
$U_{x\,6}$ [m/s]	0.522	0.492	0.488

$h = 0.090$ m	$y = 0.61$ m	$y = 0.25$ m	$y = 0.15$ m
$U_{x\,1}$ [m/s]	0.561	0.522	0.492
$U_{x\,2}$ [m/s]	0.536	0.522	0.513
$U_{x\,3}$ [m/s]	0.571	0.504	0.522
$U_{x\,4}$ [m/s]	0.522	0.509	0.484
$U_{x\,5}$ [m/s]	0.545	0.504	0.504
$U_{x\,6}$ [m/s]	0.556	0.513	0.496

For further validation, time-averaged longitudinal flow velocity was obtained using an Acoustic Doppler Velocimetry (ADV) probe situated in the centre of the recorded area at $x = 2$ m from the first recorded spanwise profile. Velocity data was recorded at three different spanwise positions situated at 150 mm, 300 mm and 610 mm from the channel wall. For each spanwise position, between 6 to 13 different vertical positions were recorded (depending on the water level) from close to the channel bed to near the water surface. For each location, instantaneous flow velocity was measured in the three main directions (x, y and z) during a recorded time of 60 s with a sampling rate of 160 Hz. Signals collected from longitudinal flow velocity were filtered using a despiking ADV process (**Botev et al. 2010; Islam and Zhu, 2013**).

Santiago Rojas Arques
Department of Civil and Structural Engineering

Table 5.5. Location of recorded ADV points from channel bed.

$h = 0.036$ m	$h = 0.054$ m	$h = 0.072$ m	$h = 0.090$ m
0.003 m	0.003 m	0.003 m	0.003 m
0.005 m	0.005 m	0.005 m	0.005 m
0.010 m	0.010 m	0.010 m	0.010 m
0.015 m	0.015 m	0.015 m	0.015 m
0.020 m	0.020 m	0.020 m	0.020 m
0.025 m	0.025 m	0.025 m	0.030 m
−	0.030 m	0.030 m	0.040 m
−	0.035 m	0.035 m	0.050 m
−	0.040 m	0.040 m	0.055 m
−	0.045 m	0.045 m	0.060 m
−	−	0.050 m	0.065 m
−	−	0.055 m	0.070 m
−	−	0.060 m	0.075 m

For each ADV test position, the accumulative longitudinal mean velocity was studied to ensure recorded time was long enough to represent mean real primary velocities. Two examples regarding to test $h = 0.090$ m $- z = 0.003$ m and 0.075 m are plotted in **Figure 5.10.** It was found that for recorded time larger than 60 s, variations in mean primary velocities are smaller than 0.2 %.
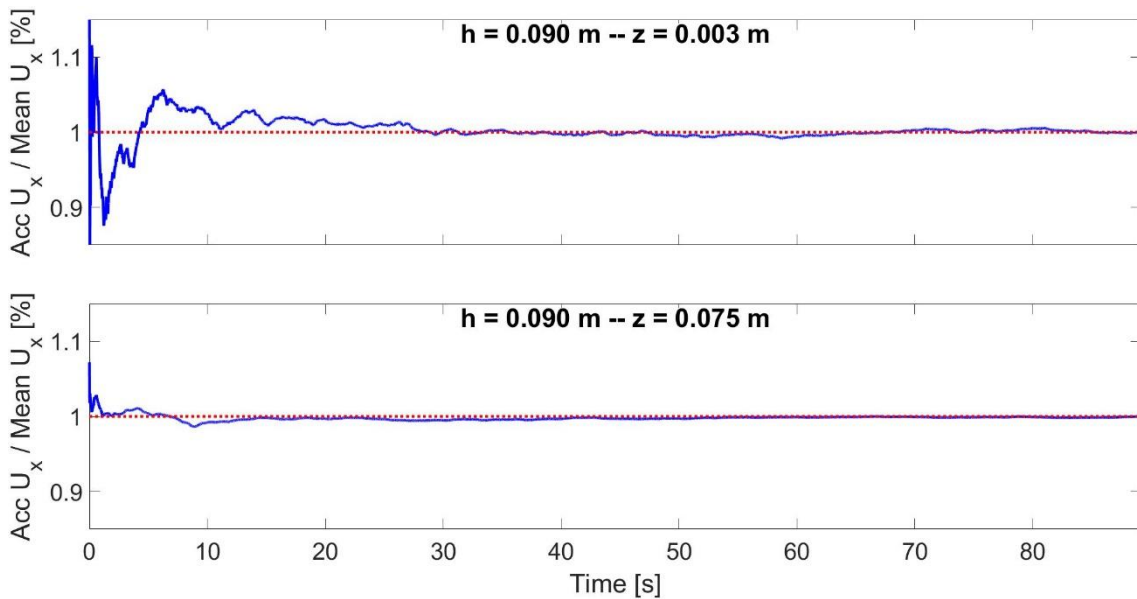
Figure 5.10. Accumulative time-averaged longitudinal velocities normalised by total time-averaged longitudinal velocity for different water depth positions.

In addition, the power spectral density (PSD) was obtained for each signal and plotted in **Figure 5.11**. This plot identifies the dominant frequency range in the recorded signals, and thus it helps to identify the minimum frequency required to record properly the instantaneous velocity deviations produced by the turbulence in the flow. **Figure 5.11** shows the PSD results for the same tests as in **Figure 5.10** using a log scale for each axis.

Santiago Rojas Arques
Department of Civil and Structural Engineering
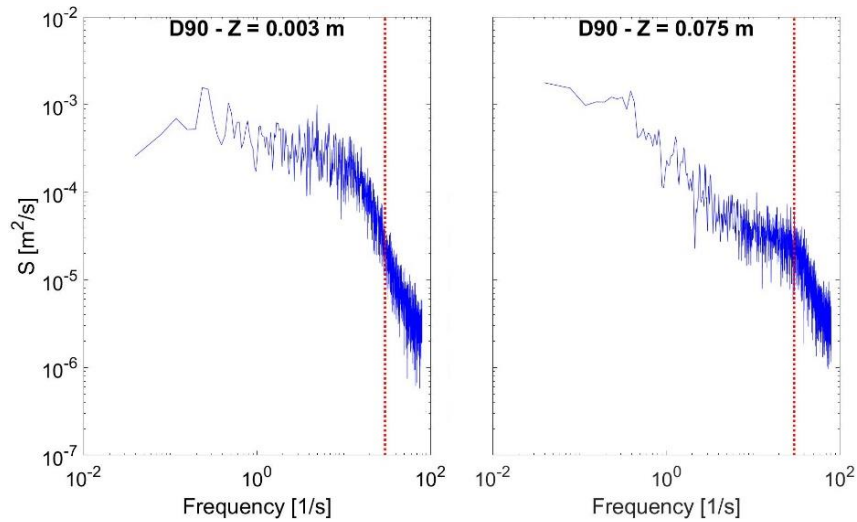
Figure 5.11. Discrete Fourier transformation for ADV signals for different water depth positions.

Results plotted in **Fig 5.11** show that the bulk of the dynamic content is below a frequency of 30 Hz (represented as the red lines), showing that the recorded values for higher frequencies are two to three orders of magnitude smaller and confirming that a frequency of 160 Hz is more than enough to record all fluctuations produced in test flows. For each signal sample recorded at each water depth position, the time-averaged longitudinal velocity value was obtained and velocity data over each water depth was fitted using the expression introduced in **Section 2.1**:

$$\frac{U(z)}{u^*} = \frac{1}{\kappa} ln \frac{z}{k_s} \qquad\qquad eq.\,5.2$$

Where $u^* = \sqrt{g\,h\,S_o}$. Each vertical profile of longitudinal velocity data was fitted by **eq. 5.2**, obtaining a value of κ and k_s for each test. Each vertical profile showed a good fitting with logarithmic profile with a mean correlation $R = 0.975$ and a fixed equivalent roughness height of 0.3 mm. Two examples of recorded ADV longitudinal velocity data and their fittings are plotted in **Figure 5.12**. Tests shown correspond to $y = 0.61$ m for $h = 0.072$ m and $h = 0.090$ m water depths.
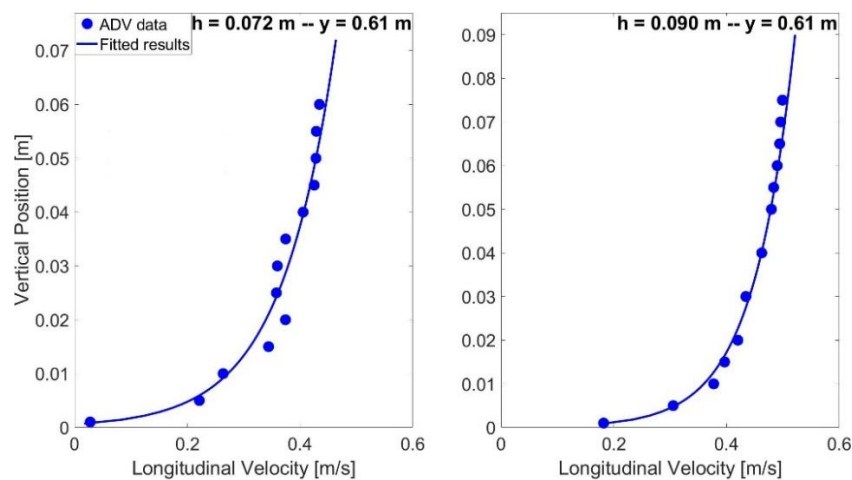
Figure 5.12. Examples of longitudinal ADV velocity data and their logarithmic fitting for y = 0.61 m and water depths h = 0.072 m and h = 0.090 m.

Santiago Rojas Arques
Department of Civil and Structural Engineering

From each logarithmic fitting result, the longitudinal surface velocity was obtained. In addition, for each measured vertical position, the longitudinal velocity predicted by the logarithmic law was calculated and the absolute differences between these values and those recorded by the ADV were obtained. Finally, the mean errors were obtained by averaging the calculated differences over the vertical profile.

Finally, results obtained by both methods (manual tracer and ADV profile) were compared with time-averaged longitudinal surface velocity obtained by the PIV technique. PIV outputs were averaged in time, and the variability in space was plotted as a range from minimum to maximum in **Figure 5.13**. Surface velocity estimated from ADV data is also plotted. The error bars show the average variation between ADV data and logarithmic fit across the vertical range.
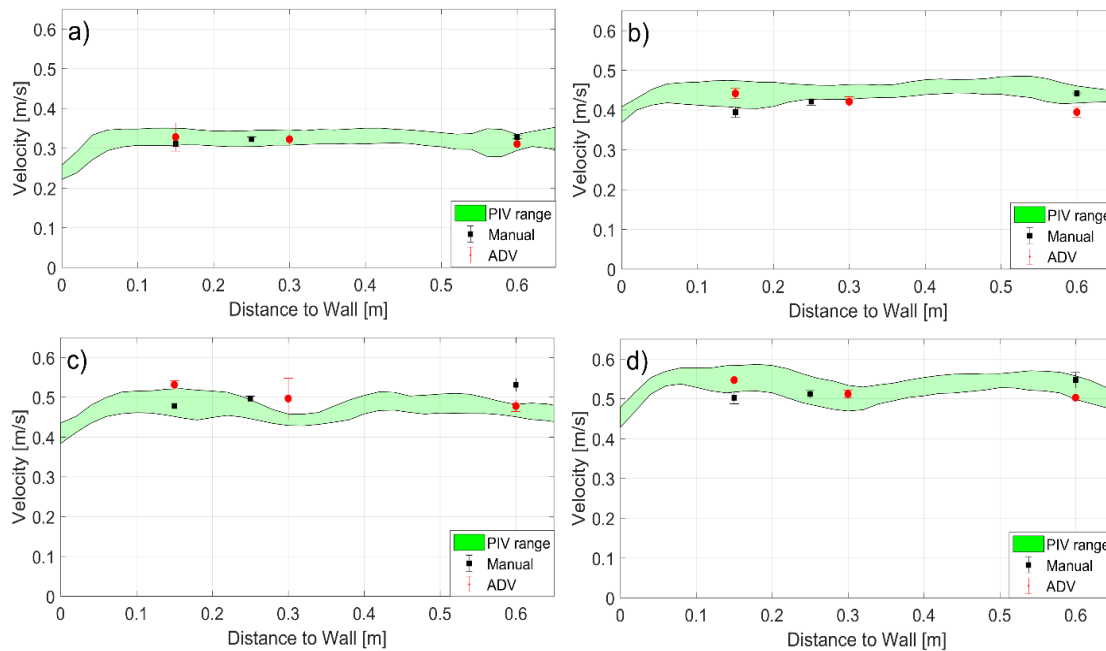
Figure 5.13. Comparison of time-averaged longitudinal velocity profiles between PIV results, manual and ADV measurement a) $h = 0.036 \text{ m}$, b) $h = 0.054 \text{ m}$, c) $h = 0.072 \text{ m}$ and d) $h = 0.090 \text{ m}$.

Figure 5.13 shows that the overall velocities obtained by manual and ADV technique are within the PIV range. Some variances are observed between each measurement technique ($\pm 5.17 \%$ between PIV and manual technique and $\pm 4.26 \%$ between PIV and ADV results) that could be produced by effect of some light reflections not effectively removed from raw frames, which could affect PIV analysis. However, **Figure 5.13** confirms that results obtained by PIV technique are suitable to estimate time-averaged surface flow velocity.

In addition, the flow rate measured for each flow condition as described in **Section 4.2.1.** was compared against the flow rate obtained by integrating the recorded PIV velocities plotted in **Figure 5.13** over the channel width. The different flow rates and the relative differences for each water depth are shown in **Table 5.6**.

Santiago Rojas Arques
Department of Civil and Structural Engineering

Table 5.6. Differences between the measured flow rate and that obtained by integrating the PIV velocity data.

$Depth$ [m]	Q [L/s]	Q_{PIV} [L/s]	$R\,D_Q$ [%]
0.036	12.1749	13.7961	11.75
0.054	21.6586	24.3154	10.93
0.072	35.0996	38.6930	9.29
0.090	52.2124	56.4218	7.46

Where Q is the flow rate measured for each flow condition, Q_{PIV} is the flow rate obtained by integrating the PIV velocity over the width and $R\,D_Q$ is the relative difference between both data, obtained as:

$$R\,D_Q = \frac{Q_{PIV} - Q}{Q_{PIV}} \qquad eq.\,5.3$$

Table 5.6 shows that different flow rates are obtained by integrating the PIV velocity as those recorded for each flow condition, with relative differences between 7.5 and 11.6 %. Higher flow rates are estimated when using the PIV data for each flow depth, which is expected as PIV technique measured surface velocity, rather than mid depth or depth averaged velocity.

It should be noted that previous work considering flow structures in vegetated flows has obtained experimental longitudinal flow velocity using different techniques, recording velocity data at different vertical positions along the flow depth. **Nezu and Onitsuke (2002)** used a argon-ion laser system to measure the velocity at 65 mm above the bed in a flow with a water depth of 70 mm, whilst **White and Nepf (2007)** recorded velocity using a laser-Doppler velocimetry system at the mid-depth in flows with a water depth range of 53 – 139 mm and **Besio et al. (2012)** recorded surface velocity using a PIV technique. Therefore, the differences between the recorded surface longitudinal velocity data and those expected at the mid-depth of an open channel flow without vegetation were estimated. The logarithmic fitting of vertical profiles of longitudinal velocity obtained previously (**Section 5.2**) were used to calculated the expected longitudinal velocity at the mid-depth and the differences between this velocity and that recorded at the surface by the PIV system were calculated for each water depth condition.

$$R\,D_U = \frac{U_{Surface} - U_{Mid-depth}}{U_{Surface}} \qquad eq.\,5.4$$

Where $U_{Surface}$ is the longitudinal surface velocity and $U_{Mid-depth}$ is the longitudinal velocity at the mid-depth. Results are shown in **Table 5.7**.

Table 5.7. Estimated differences between surface and mid-depth longitudinal velocity within experimental facility for each depth.

Depth [m]	$U_{Surface} - U_{Mid-depth}$ [m/s]	$R\,D_U$ [%]
0.036 m	0.042 m/s	12.78 %
0.054 m	0.041 m/s	10.71 %
0.072 m	0.039 m/s	8.71 %
0.090 m	0.029 m/s	5.70 %

Results in **Table 5.7** show a decrease of the difference between the surface and the mid-depth longitudinal velocity for deeper flows. This decrease may be produce as the bed effect becomes more important for shallower flow conditions. Moreover, if the calculated mid-depth longitudinal velocities are considered to obtain the flow rate for each water depth, the differences observed in **Table 5.6** are almost eliminated, with relative differences of $RD_Q =$ 6.02 %, 5.79 %, 3.23 % and 2.03 % for $h = 0.036\,\text{m}$, $0.054\,\text{m}$, $0.072\,\text{m}$ and $0.090\,\text{m}$ respectively. The differences between surface longitudinal velocity and mid-depth longitudinal velocity within the vegetated regions may be expected to be insignificant as velocity is approximately uniform over the depth when using stems of a constant diameter (**Kouwen et al., 1969, Rowiński et al, 1998**, **Nepf and Vivoni, 2000**). However, these differences between surface longitudinal velocity and mid-depth longitudinal velocity should be considered when considering measurements in the free flow region.

5.3. Concentration Data Analysis

In this section, a brief description of the different steps taken to convert raw light intensity data from cameras into spatial concentration data is introduced. In addition, steps applied to analyse and validate the measurement technique using the first light configuration (as described in **Section 4.2.4**) are explained in the Section below. However, a more detailed description of steps used to analyse raw data is explained later in **Section 5.6** with the revised light configuration explained in **Section 5.5,** and the corresponding concentration results.

For each test explained in **Section 4.5**, a video for each dye injection was recorded during $180\,\text{s}$ and a time-averaged frame was produced taken central $60\,\text{s}$. In addition, a video with no injection was recorded for each flow condition with a length of $30\,\text{s}$ to obtain the concentration level with no injections, or background concentration. Then, a mean value taken 10×10 pixels were obtained, creating new images of 122×180 pixels and a resolution of $10 \times 10\,\text{mm}$. Both spatial and dye calibration explained in **Section 4.3.1** and **Section 4.4** were applied, obtaining a time-averaged concentration map with a resolution of $10 \times 10\,\text{mm}$ over a recorded area of $1.22 \times 1.80\,\text{m}$ for each camera. Then, measured background levels from concentration frames were removed for each pixel.

Once background concentration levels were removed from the time-averaged concentration map recorded by each camera, a concentration map over the full analysis length was obtain. Therefore, concentration maps of each camera required to be merged as explained in **Section 4.3.3.** Thus, first and last 18 pixels for each concentration map recorded by each camera were neglected, then the last and the first 35 pixels ($0.35\,\text{m}$) for each pair of consecutive cameras were taken respectively and a sinusoidal weight function was applied to create a transition function between both cameras.

Then, remaining noise from concentration map was eliminated. This noise is mostly produced by reflections of green light on the water surface, which produces some erroneous values when compared with those values recorded in their local neighbourhood. For this first light configuration, a 6th-order one-dimensional median filter was applied and a threshold value of 3 % was fixed, defined as a percentage of the maximum concentration value recorded for each concentration profile. For a generic median filter, neighbourhood values around each single pixel are considered. In the case of an "nth-one-dimensional median filter", only the "n" neighbourhood values at each side in the spanwise direction are considered; and in the case of

- 77 -

an "n^{th}-two-dimensional median filter", neighbourhood values in an area of "n × n" around the single pixels are considered. Once the neighbourhood values are defined, an output pixel value is produce with the median value of the selected area for the single pixel. For the filtering techniques introduced here, a 6th-order one-dimensional median filter considers the values of 6 pixels at each side of the filtered pixel in the spanwise direction. In addition, the threshold filtering technique was applied to delimitate the boundaries of the transverse concentration profiles from the residual background level. This cut off technique identifies the maximum concentration value for each profile and delete all values lower than the "n %" of this maximum value. As it was discussed in **Section 2.4.2**, **Boxall (2000)** and **Dennis (2000)** argued that when an optimization process is applied to obtain mixing coefficients, accurate mixing coefficients can be obtained even when the cut off applied to delimitate the concentration profiles is up to the 10 % of the peak concentration value. Thus, a 3 % of the maximum concentration value were applied to the different proposed filtering techniques.

Post filtering, to ensure mass conservation a mass balance was applied along all profiles. The mass over each transversal profile was obtained and the corresponding mean profile of mass for each injection was calculated as the mean of all lateral mass profiles. Then, a correction factor between the mass of each profile and the mean mass was obtained for each concentration profile. Finally, each single pixel value for a specific profile was divided by the factor obtained for this profile, obtaining the same mass for each lateral concentration profile

5.4. PCA Validation

The PCA technique was validated by comparing concentration fields recorded by cameras with concentration levels recorded by Cyclops-7F^{TM} submersible sensors for a continuous injection of Rhodamine WT. Due to obstruction effects produced by sensors and differences between the sensitivity of each instrument, PCA and Cyclops measurements could not be taken at the same time. Instead, separate tests were run with injections with different dye injection concentrations. Then, results were compared using variance and ADE transverse mixing coefficients obtained from each test, such that the mixing rates of the solute quantified using each measurement technique were compared. For each test, the same flow conditions were established with a constant water depth of $h = 0.09$ m and with no vegetation.

The Cyclops probe was calibrated using 11 concentrations, including zero concentration; in a container of 5 L as shown in **Figure 5.14** to produce a linear function relating concentration to probe output.
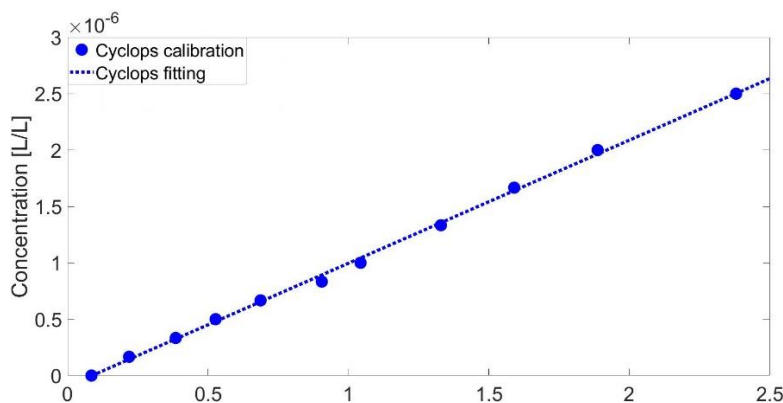
Figure 5.14. Cyclops calibration.

Santiago Rojas Arques
Department of Civil and Structural Engineering

Four concentration profiles were recorded with the Cyclops sensor, situated at $5, 6, 7$ and 8 m downstream of the injection point and within the PCA recorded area. For each recorded profile, 20 different points along the spanwise direction were recorded, where 16 points were taken in increments of 20 mm to record the dye plume and the other 4 measurements were taken far from the dye plume to establish background levels. From these 4 measurements, the lowest value recorded considering the four concentration profiles was considered as the background level and it was subtracted from the rest of measurements as explained below.

To ensure reliable recorded data, each point was recorded for the same time as the video recordings (60 s, see **Section 5.3**) and a time-averaged value was obtained. Then, a process similar to that applied to PCA data was used: the background level was removed from concentration profiles and values lower than 3 % of maximum peak concentrations were also eliminated to remove instrument noise effects. After this filtering process, a mass balance factor was applied to profiles located at $6, 7$ and 8 m downstream of the injection point. Mass balance factors obtained showed a variation of ± 2.2 % over the recorded concentration profiles, indicating a good level of mass conservation.

PCA raw concentration maps were obtained as explained in **Section 4.3** and **Section 4.4**. Then, concentration maps were analysed using the processed explained in **Section 5.3**, with the filtering technique explained in **Section 5.3**: background levels were removed from the concentration map, a 6th-order one-dimensional median filter was applied to eliminate noise and all values smaller than 3 % of the peak concentration were removed. Post-filtering, a mass balance was applied to ensure mass concentration obtaining a variation of 5 %, indicating good mass conservation. **Figure 5.15** shows a comparison between non-dimensional concentration profiles obtained using both Cyclops sensors and the PCA technique. Profiles were located at $5, 6, 7$ and 8 m from the injection point. All values were normalised by the maximum concentration value of the first profile.

Error bars for Cyclops data were calculated as the standard deviation of the signal recorded for each measured point. In addition, during the calibration process (**Section 4.4**), absolute differences between concentration predicted by the 3rd polynomial order function and calibrated concentrations were calculated for each concentration value. Then, the average error value for all 11 calibrated points was calculated for each map position. This estimated mean error was then used to show PCA variation plots in **Figure 5.15**.

Santiago Rojas Arques
Department of Civil and Structural Engineering
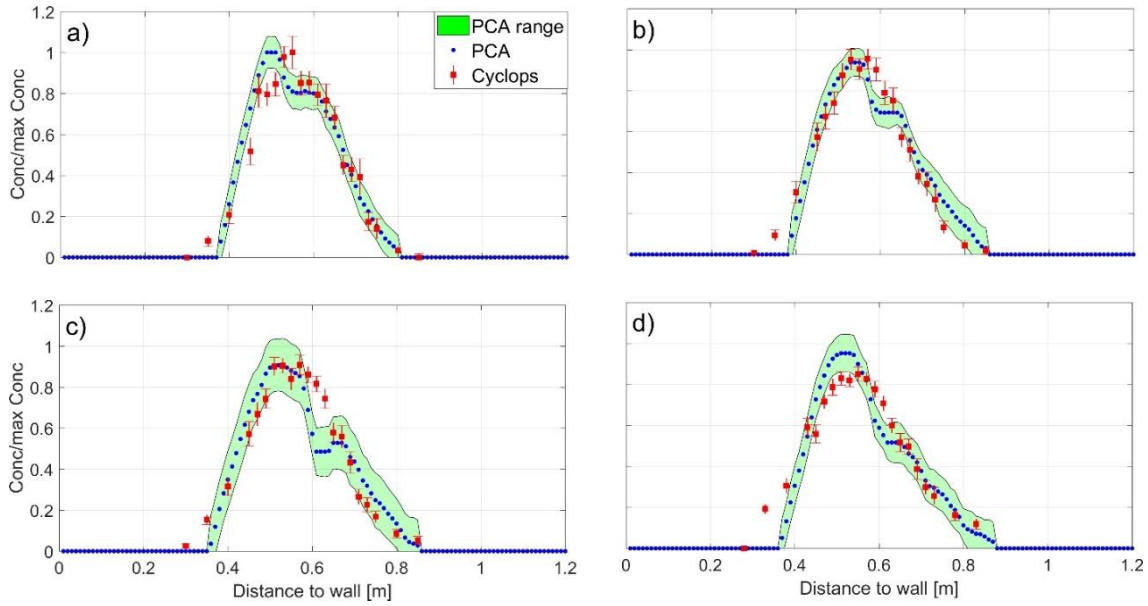
Figure 5.15. Comparison between PCA and Cyclops non-dimensional concentration profiles (case $a = 5$ m, case $b = 6$ m, case $c = 7$ m and case $d = 8$ m).

Concentration profiles shown in **Figure 5.15** suggest an overall good match between both measurement techniques. A small but consistent variation was observed in the centre of each profile where the PCA concentration data were lower than the Cyclops values. These differences were likely produced by direct light reflections produced over the water surface and recorded by the cameras. These reflections may also affect the left part of the plume ($y = 0.3$ m), where the concentrations recorded by the PCA technique were smaller than those obtained with the Cyclops. This miss-recording produces that the concentration profiles recorded using the PCA do not spread in a similar manner on the left and right side of the flume, producing a significant difference between the PCA and the Cyclops measurements. These differences observed between both techniques suggest that some further refinements of light configurations could be applied to improve the technique. In addition, the Pearson correlation between PCA concentration profiles and data recorded by Cyclops was calculated.

$$R = \frac{n_{values} \sum C_e C_c - (\sum C_e \ \sum C_c)}{\sqrt{[n_{values} \sum C_e^2 - (\sum C_e)^2][n_{values} \sum C_c^2 - (\sum C_c)^2]}} \qquad eq.\,5.5$$

Where n_{values} is the number of values and C_e and C_c are the concentration values recorded by the PCA technique and by Cyclops respectively. Only PCA concentration values were considered for those spanwise positions where Cyclops concentration data were available. The Pearson correlation results show, a good correlation between each pair of concentration profiles: $R_{5m} = 0.97$, $R_{6m} = 0.98$, $R_{7m} = 0.95$ and $R_{8m} = 0.93$.

In addition, the spatial variance of the transverse concentration profiles was obtained and a linear fitting was applied to calculate the variance slope along the streamwise direction using the expression proposed by **Sayre and Chang (1968)** introduced in **Section 2.4.2**.

$$D_y = \frac{U}{2} \frac{d\sigma_y^2}{dx} \qquad eq.\,5.6$$

Santiago Rojas Arques
Department of Civil and Structural Engineering

The variance of each transversal concentration profile was calculated using the discretised solutions of **eq. 2.61**, **2.62** and **2.63**.

$$M_0 = \sum_{y=1}^{y=1.22} C(y) \qquad\qquad eq.\,5.7$$

$$M_1 = \sum_{y=1}^{y=1.22} C(y)y \qquad\qquad eq.\,5.8$$

$$M_2 = \sum_{y=1}^{y=1.22} C(y)y^2 \qquad\qquad eq.\,5.9$$

$$Centroid = \varphi = \frac{M_1}{M_0} \qquad\qquad eq.\,5.10$$

$$Variance = \sigma_y^2 = \frac{M_2}{M_0} - \varphi^2 \qquad\qquad eq.\,5.11$$

Where $C(y)$ is the concentration value recorded at each cell located at the transversal position y. **Figure 5.16** shows the variation (increase) in spatial variance of each profile over the experimental length obtained using both measurement techniques and linear fitting applied to each case using the expression $a_{\sigma^2}x + b$, where a_{σ^2} is the variance slope and b is the independent term. As results from the two measurement techniques are taken from separate experiments, results are plotted in terms of variation in variance from a reference point taken at $x = 5$ m (position of the first cyclops profile from the injection point). The variance slope obtained for each case was $a_{PCA} = 14.5$ and $a_{Cyclops} = 13.9$, with a Pearson correlation of $R = 0.94$ for the PCA measurements and $R = 0.97$ for the Cyclops measurements respectively. These results indicate a similar mixing process recorded by each technique, as similar variance slopes were obtained (**eq. 5.6**).
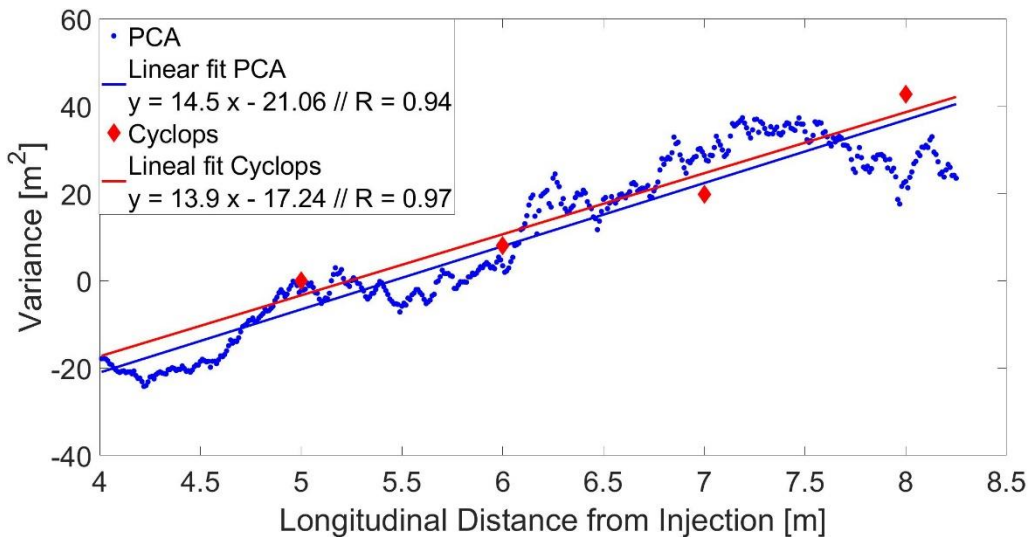
Figure 5.16. Comparison between PCA and Cyclops variance.

Results plotted in **Figure 5.16** suggest that the increase of variance for both measurement techniques follow the same trend. However, a diminution of variance is observed for the PCA concentration profiles after 7.5 m. This decay may be produced because of the lower

- 81 -

concentration values recorded at the edges of the PCA concentration profiles as shown in **Figure 5.15** (around $0.3 - 0.4$ m from the wall). This decay was likely produced when the concentration profiles fell into the areas significantly affected by the light reflections produced along the channel (as seen in **Fig 5.15 (d)**).

5.4.1. Analytical Solution

In addition, the ADE transverse mixing coefficient (D_y) was obtained from concentration measurements obtained with both PCA and Cyclops measurement techniques.

In this set of experiments with a straight open channel with no vegetation, the transverse mixing coefficient $D_y(y)$ was considered constant along the channel width. Thus, the analytical solution introduced in **Section 2.4.2** was considered for the unbounded flow condition and considering no flux of concentration at the channel walls:

$$C(x,y) = \frac{M}{h\sqrt{4\pi D_y U x}}\, exp\left[-\frac{U(y - y_{Inj})^2}{4 D_y x}\right] \qquad eq.\,5.12$$

Where M is the total mass inflow rate and y_{Inj} is the transversal position of tracer injection. This simplification considers both the longitudinal flow velocity and the water depth to be constant along both the transversal and longitudinal direction. The mean velocity value used in the equation was obtained from the time-averaged longitudinal PIV velocity obtained in **Section 5.2**. Values at the three different spanwise positions considered to validate PIV results were considered ($y = 0.61,\ 0.25$ and 0.15 m), and the mean value between them was calculated.

A simple optimization routine was developed to find the optimised D_y value that provided predicted concentrations that fitted best with experimental concentration data. The routine was developed using the Matlab optimization function *fmincon,* which finds the minimum solution for a given function. The value being minimised was $-R$, where R was the Pearson correlation between the experimental concentration data and the concentration data generated by the **eq. 5.12** considering all profiles recorded over the analysis area (**eq. 5.5**).

The first concentration profile was introduced as an input along with the water depth value and the longitudinal flow velocity. Thus, the routine started with a given initial transverse mixing coefficient D_{y_0} and concentration profiles downstream were predicted using input data into **eq. 5.12**. The correlation R between the ADE concentration map and the experimental data was calculated and the objective value $-R$ was obtained. The function repeated this process changing the variable D_y until the solution $-R$ was minimised. In addition, for each iteration, the allowed D_y values were constrained within the range $0 - 1$. The optimised results obtained from each technique were shown in **Table 5.8**. In addition, non-dimensional transverse mixing coefficients (D_y/hu^*) and Pearson correlations were shown.

Table 5.8 Transverse mixing coefficients from PCA and Cyclops measurement techniques and correlations between data and ADE optimization.

Test	D_y [m^2/s]	D_y/hu^* [$-$]	R
$h = 0.090$ m (PCA)	0.000365	0.142	0.983
$h = 0.090$ m (Cyclops)	0.000381	0.143	0.994

Santiago Rojas Arques
Department of Civil and Structural Engineering

The results in **Table 5.8** show a very similar optimised transverse mixing coefficient for data from both PCA and Cyclops techniques. These results are in agreement with slopes of transverse profiles variances obtained previously and suggested a similar mixing process recorded by each measurement technique. In addition, these transverse mixing coefficients are in the line with expected values for straight channels $0.15 < D_y/hu^* < 0.3$ (**Rutherford, 1994**).

5.5. Light Configuration Improvement

As discussed in **Section 5.2** and **Section 5.4**, reflections from the water surface created by the LEDs were found to produce some errors in measurements at specific locations due to direct reflections. Therefore, different light configurations were tested to obtain the most uniform green intensity distribution over the recorded area and minimise the occurrence of direct reflections. Reflective and dispersive materials were used in order to avoid direct light reflections over the water surface and to distribute better the LED light. The material chosen was *Reflex Diamond Reflective Sheeting*.

For the first new light configuration tested, LEDs at both sides of channel walls were left but the strip on the top was substituted by four strips with two on either side of the beam. This new distribution avoided direct light reflection over the recorded area. Finally, a rigid structure covered by the reflective/dispersive sheeting was installed on the top of the channel to reflect light downwards. It was situated 8 cm above the beams on the top of the channel and covered them with two sheets with a length of 27cm and with an angle of 45°. This configuration is schematised in **Figure 5.17**.
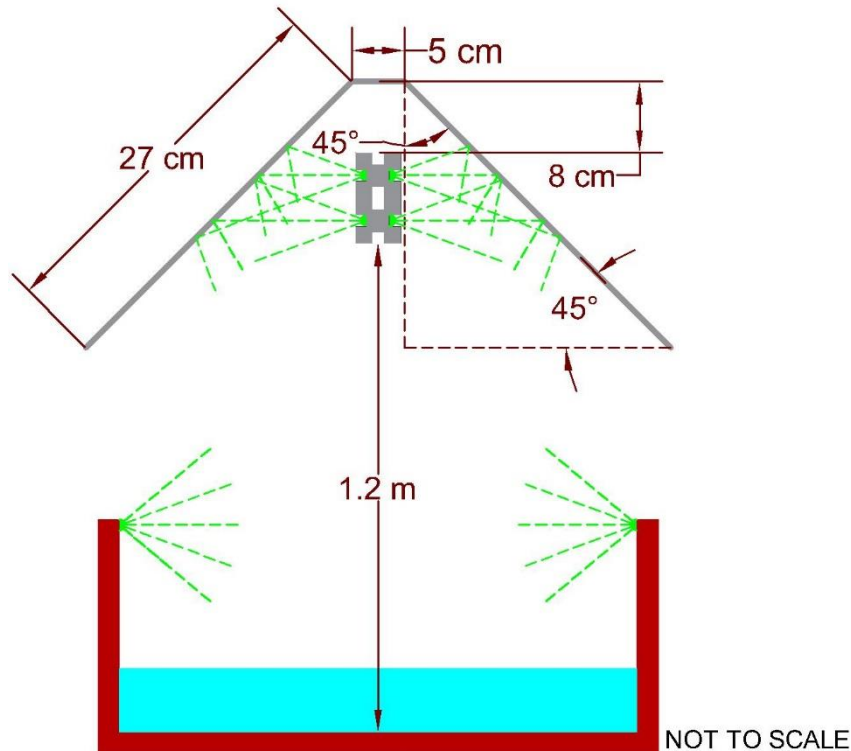
Figure 5.17. Scheme of first light improvement configuration.

Santiago Rojas Arques
Department of Civil and Structural Engineering

For the second light configuration, lights at both sides of the wall channel were moved to a height just over the beams where cameras were installed. In addition, reflective material was used to cover completely the recorded area as illustrated in **Figure 5.18**.
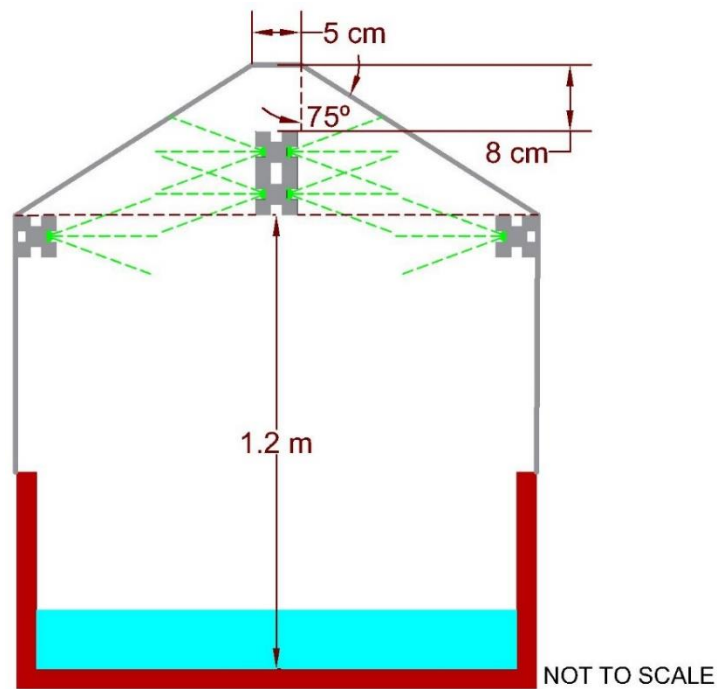
Figure 5.18. Scheme of second light improvement configuration.

This configuration increased the reflective area and smoothed the light reflection of the top LEDs over the material, distributing more homogeneously the light over the full-recorded area. In order to study the green intensity distribution of each configuration, the recorded area was isolated and filled with tap water as described in **Section 4.4**. A video of 10 s was recorded for each case for the same water depths used previously and a time-averaged map of the green component was obtained from each camera. Finally, frames from different cameras were merged as explained in **Section 4.3.3**. Green intensity maps obtained from different water depths and light configurations are plotted in **Figure 5.19, Figure 5.20** and **Figure 5.21** for the first light configuration and both new configurations explained in this section respectively.

Santiago Rojas Arques
Department of Civil and Structural Engineering
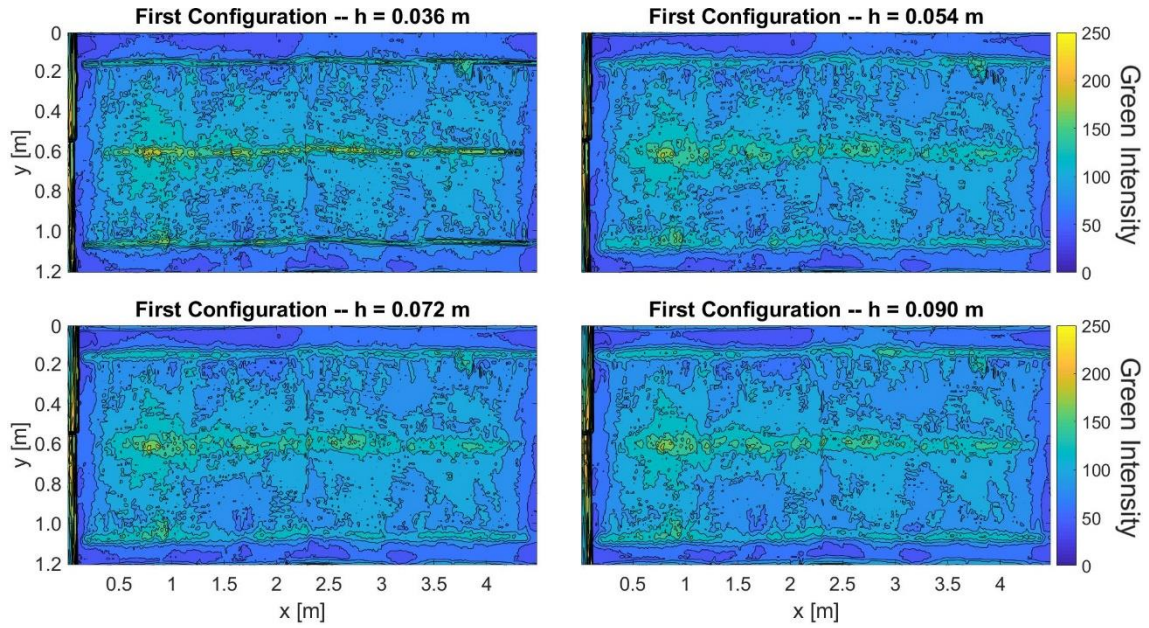
Figure 5.19. Time-averaged green intensity maps for previous light configuration.
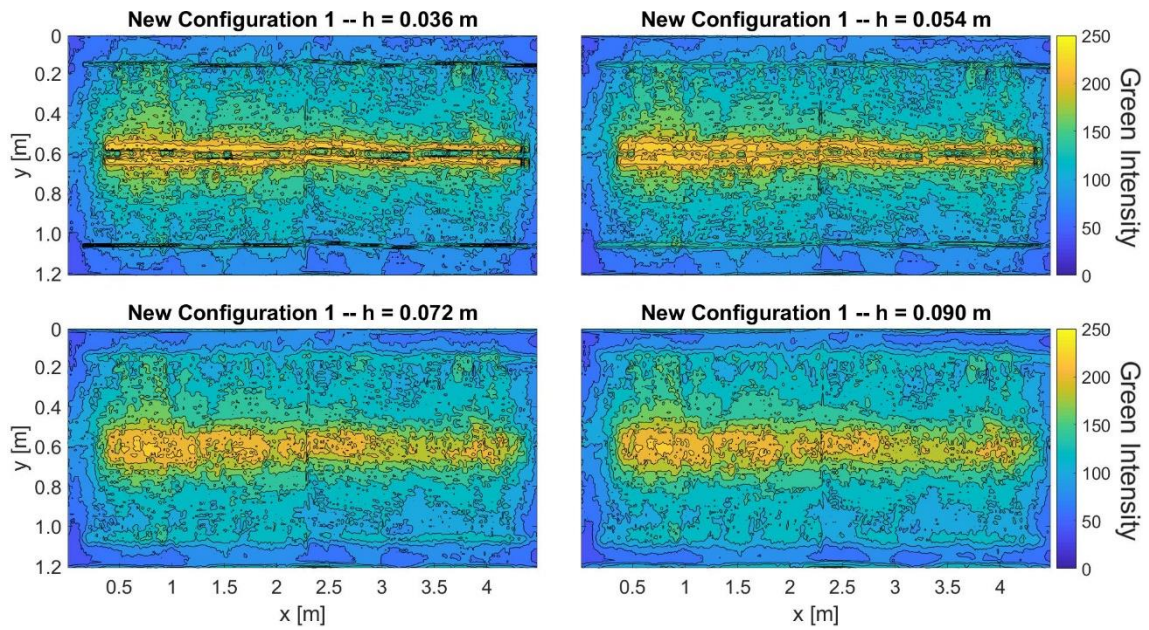
Figure 5.20. Time-averaged green intensity maps for first new light configuration.

Santiago Rojas Arques
Department of Civil and Structural Engineering
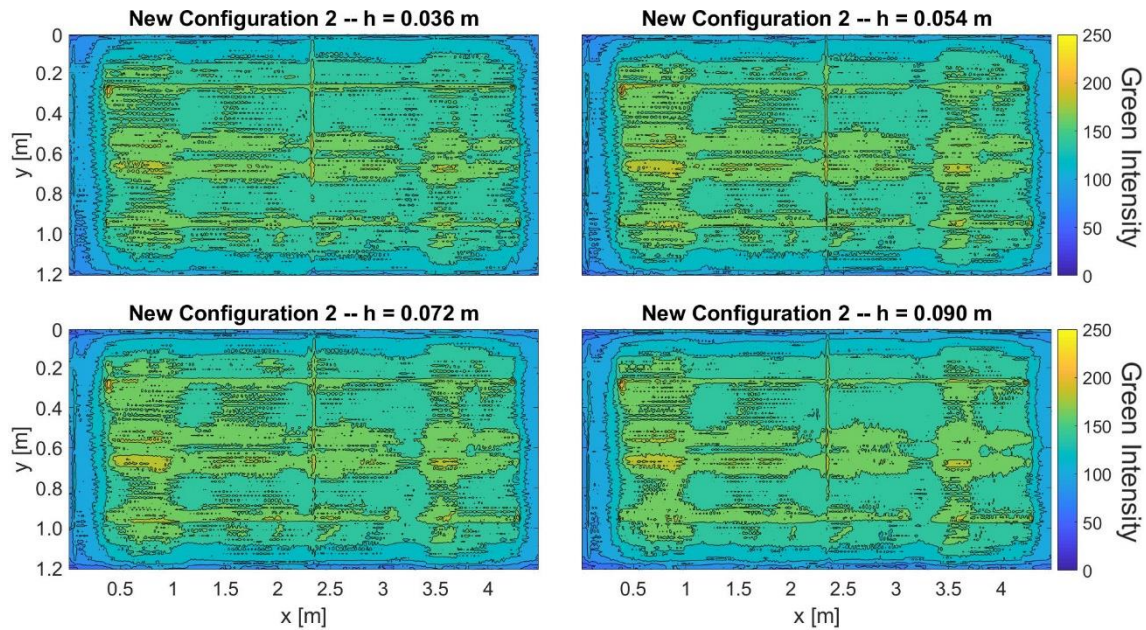
Figure 5.21. Time-averaged green intensity maps for second new light configuration.

Figure 5.19, Figure 5.20 and **Figure 5.21** shows time-averaged green intensity maps for the previous light configuration and the new ones proposed in this section respectively. In addition, **Figure 5.22** represents green intensity over a transversal section of the recorded area situated at 1.5 m from the first recorded spanwise profile for different water depths and light configurations.

The figures show three strips with higher intensity for the first light configuration. These lines corresponded to light reflections over the water surface, and they could potentially produce some errors in PCA and PIV data as was discussed in **Section 5.2** and **5.4**. The first new configuration increased the overall green intensity but produced a wide reflection strip along the centre of the channel. This increase was mostly produced by reflection of lights installed over the channel. The second new configuration produced a more homogeneous increase of green intensity over the full-recorded area without lines with significant peaks of intensity produced by reflections. **Figure 5.22** also agrees with this.

Figure 5.19, Figure 5.20, **Figure 5.21** and **Figure 5.22** indicate that the second new light configuration produced an improvement of light conditions over the recorded area increasing the green intensity homogeneously and without generating regions with high light reflections. Based on that, the second new light configuration was chosen to run all experiments described in **Section 4.5**.

Santiago Rojas Arques
Department of Civil and Structural Engineering
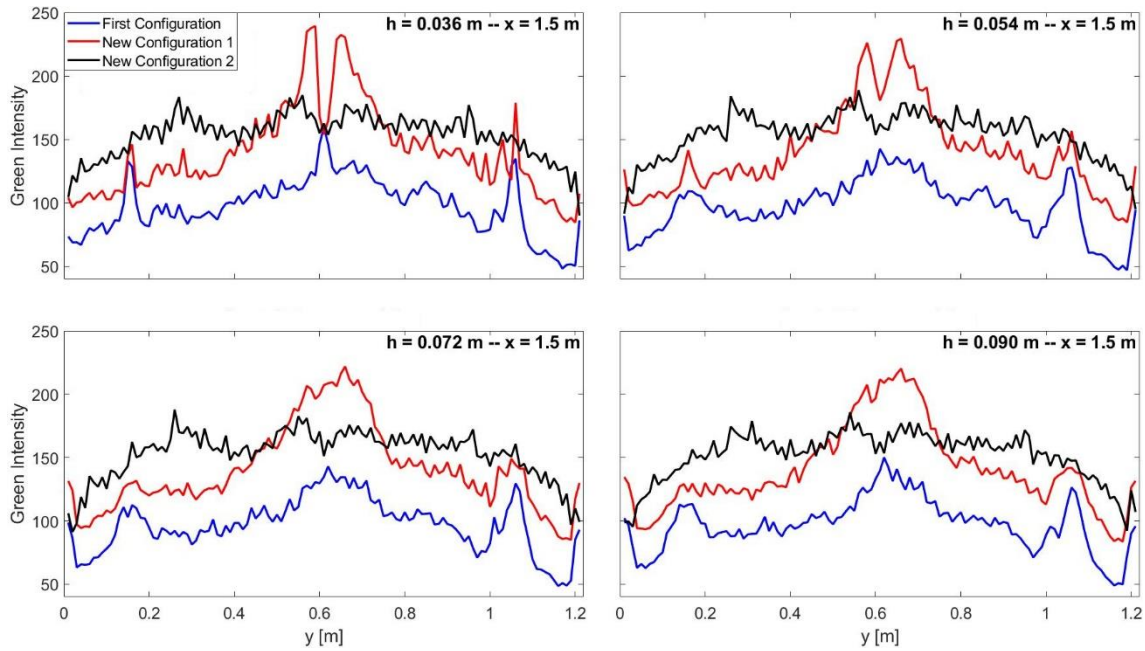
Figure 5.22. Time-averaged green intensity profiles for different water depths and light configurations.

5.5.1. Final Dye Calibration

As the lighting configuration was changed, a new camera calibration was required. It was performed in the same way as explained in **Section 4.4,** applying the same spatial and dye calibration processes**.** For dye calibration, thirteen different concentration values were recorded (including zero concentration) as shown **Table 5.9**.

Table 5.9. Concentration used for dye calibration for new light configuration.

Concentration [10^{-6}L/L]	0.00	0.30	0.74	1.24	1.74	2.49
Test number	1	2	3	4	5	6

Concentration [10^{-6}L/L]	2.99	3.99	4.99	6.99	7.99	9.49	12.03
Test number	7	8	9	10	11	12	13

Frames recorded by cameras had a pixel dimension of 1×1 mm. The same spatial average was performed for dye calibration, using the average value of each 10×10 pixels and obtaining a frame dimension of 10×10 mm. The same third order polynomial function was used to relate concentration values with corresponding green intensity for each cells. **Figure 5.23** shows the time-averaged intensities for the same representative cell showed in **Figure 4.10**, located at $x = 1.5$ m downstream of the first recorded profile and in the centre of the width ($y = 0.61$ m), for the range of water depths against their corresponding concentration values, along with the fitted functions. The errorbars show the temporal standard deviation of the recorded green intensity durng the total recorded range (10 s).

Santiago Rojas Arques
Department of Civil and Structural Engineering
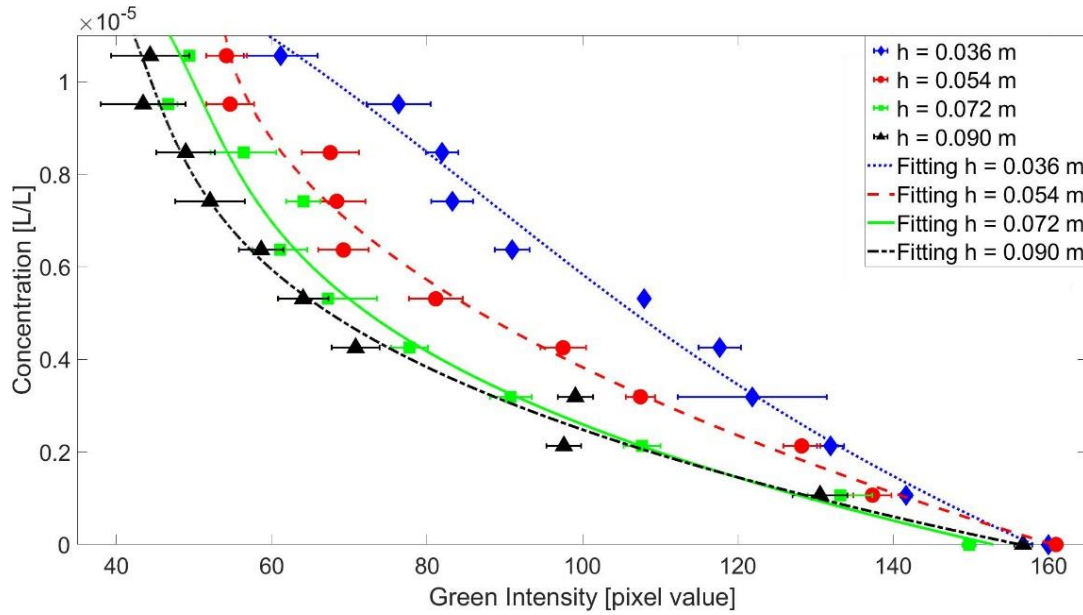
Figure 5.23. Example of dye calibration for new light configuration for a cell at $x = 1.5$ m and $y = 0.61$ m.

A comparison between the previous and new dye calibrations is shown in **Figure 5.24**. In this figure, the example pixel was located at the mid length of the recorded area ($x = 1.5$ m) and at $y = 0.25$ m from the left wall. Visual comparison shows the new light configuration produced a dye calibration with the same trend as the previous one, but with higher values of green intensity for the same concentration amount. These differences seem to be higher for deeper water depths. In addition, the slope of the dye calibration for the higher concentration values seem to be smoother, producing a trend closer to a linear variation and therefore reducing the minor errors produced for the higher concentration values.
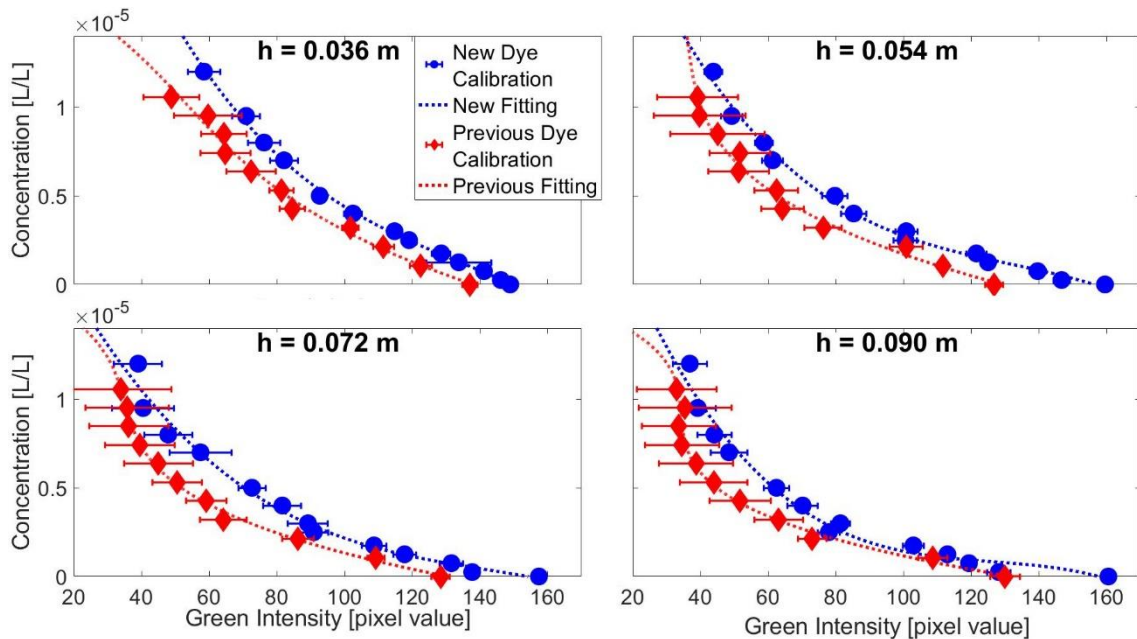
Figure 5.24. Comparison between new and previous dye calibration for a cell at $x = 1.5$ m and $y = 0.25$ m.

Santiago Rojas Arques
Department of Civil and Structural Engineering

5.6. Concentration Data Analysis with New Light Configuration

Steps taken to analyze raw light intensity data obtained with the new light configuration explained in **Section 5.5** are explained below. In addition, a comparison between new experimental data and that obtained using the first light configuration is conducted.

5.6.1. Background Concentration Removal

As it was introduced in **Section 5.3**, a time-averaged frame over the central 60 s was produced for each dye injection video. Then, a mean value taken 10×10 pixels were obtained, creating new images of 122×180 pixels and a resolution of 10×10 mm. In a similar way, a time-averaged frame over 30 s was taken for each no injection video and the same spatial averaged was applied. Both spatial and dye calibration explained in **Section 4.3.1** and **Section 5.5.1** were applied, obtaining a time-averaged concentration map with a resolution of 10×10 mm over a recorded area of 1.22×1.80 m for each camera. **Figure 5.25 (a)** shows the time-averaged concentration map for the no-vegetated flow condition and water depth $h = 0.036$ m and **Figure 5.25 (b)** shows the corresponding background concentration map. Then, measured background levels from concentration frames were removed for each pixel as shown **Figure 5.25 (c)**.
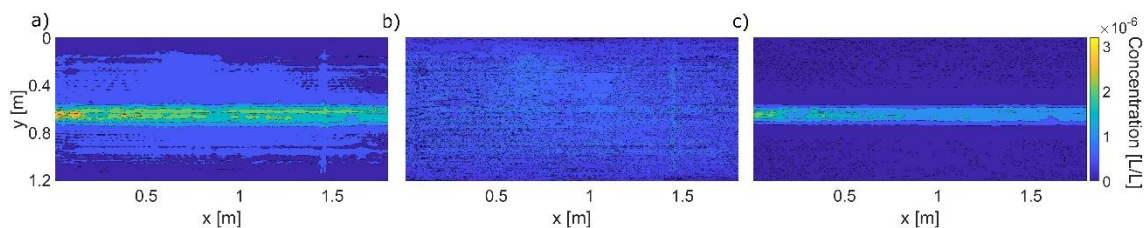
Figure 5.25. Time-averaged concentration profiles from camera 2 for: a) before background removal; b) background map; c) map with background removed.

In addition, in **Figure 5.26** a concentration profile over the spanwise direction is shown for the same flow condition, located at $x = 2$ m. **Figure 5.26** shows both transversal dye concentration profile and the concentration level recorded for no injection conditions. In addition, the black profile shows the same concentration profile with the background concentration level removed.
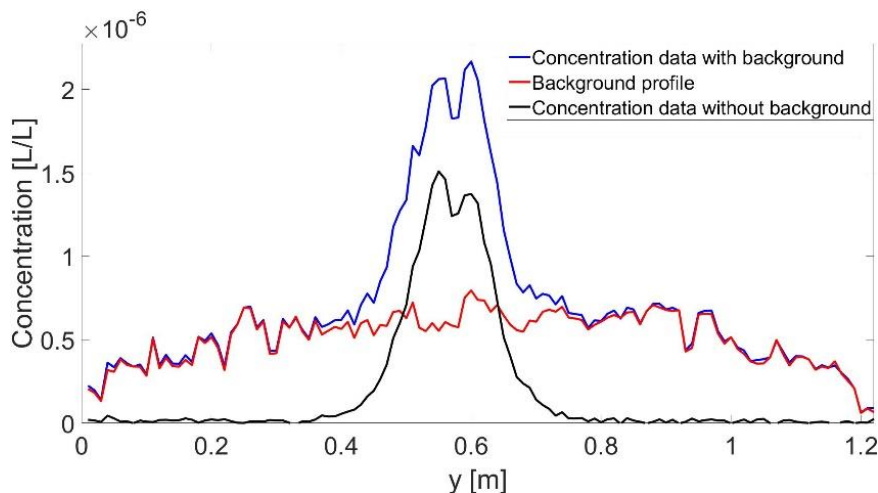
Figure 5.26. Concentration profiles located in the middle of camera 2 with and without background.

Santiago Rojas Arques
Department of Civil and Structural Engineering

5.6.2. Concentration Maps Stitching

The same process as explained in **Section 5.3** was applied to stich the time-averaged concentration maps with the background removed, obtaining a concentration map over the full analysis length. **Figure 5.27** shows the time-averaged concentration map used from each camera and the full concentration map resulting after the stitching step for the no-vegetated flow condition and the water flow depth $h = 0.036$ m.
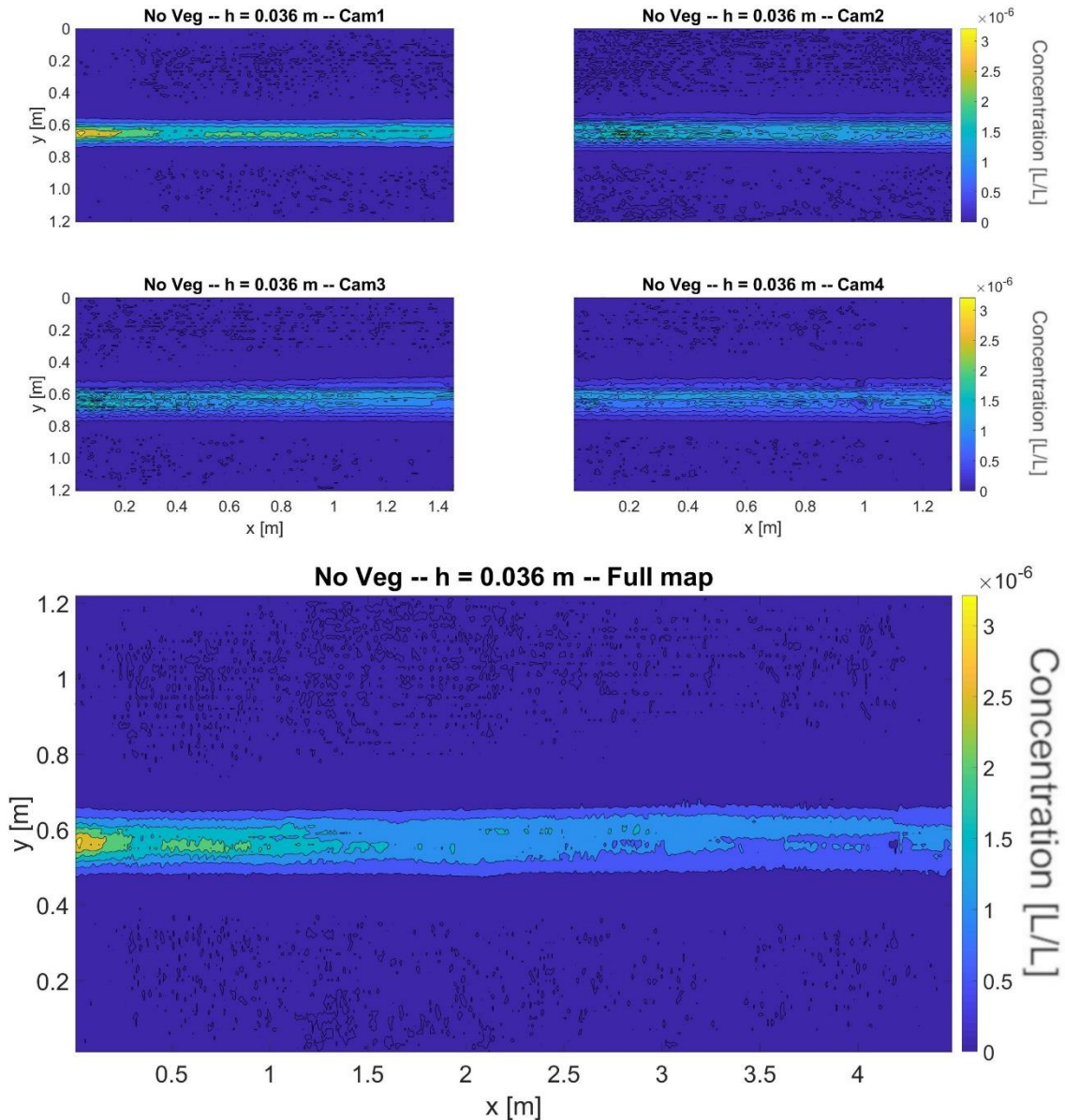
Figure 5.27. Concentration map for each camera and full concentration map.

In addition, **Figure 5.28** shows three different longitudinal profiles from the concentration maps plotted in **Figure 5.27** to improve the visualization of the merger of the different time-averaged concentration maps from the different cameras, merged using the weighted sinusoidal function explained in **Section 4.3.3**. The first longitudinal concentration profiles correspond to the centre of the channel width ($y = 0.61$ m). Then, the second profile is located between the maximum concentration and the end of the concentration tail ($y = 0.50$ m); and the last profile is located close to one tail of the plume ($y = 0.45$ m).

Santiago Rojas Arques
Department of Civil and Structural Engineering
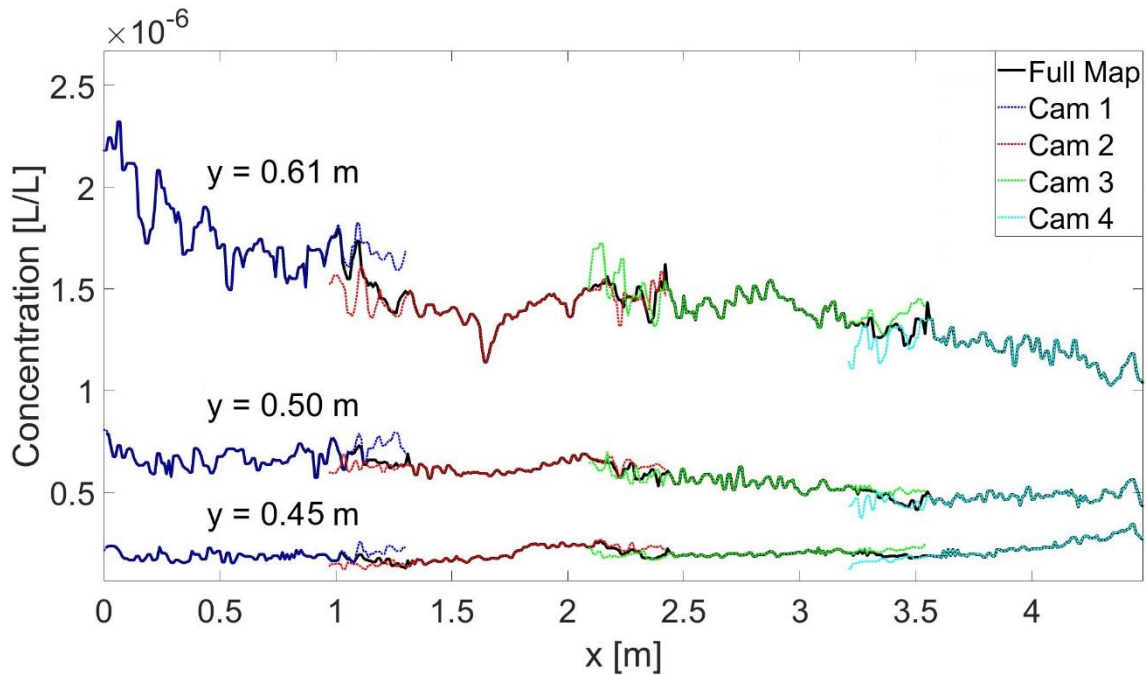
Figure 5.28. Longitudinal profiles for each camera and full concentration map.

5.6.3. Filtering Techniques

Same filtering technique as that described in **Section 5.3** was applied to full time-averaged concentration maps. In addition, other four different filtering techniques were applied to eliminate to study the possible variations in final concentration maps resulting from each different process and the effects that these variations can produce in the results discussed in **Section 6.1.** For each filtering technique, a different median or mean filter was applied to the full concentration map. In addition, a threshold value was fixed to delimitate the plume from the remaining background noise. The different filtering techniques considered are the follows:

- Filter 1: 6th-order one-dimensional median filter and a threshold of 3 %.
- Filter 2: 6th-order one-dimensional median filter and a threshold of 5 %.
- Filter 3: 3rd-order two-dimensional median filter and a threshold of 3 %.
- Filter 4: 6th-order two-dimensional median filter and a threshold of 3 %.
- Filter 5: 6th-order two-dimensional mean filter and a threshold of 3 %.

The generic operation of the median filter was explained in Section 5.3. Moreover, the mean filter works in the same way, but using the mean value instead of the median one. In addition, two different thresholds were considered to delimitate the boundaries of the transverse concentration profiles. As it was explained in **Section 5.3**, both percentages were defined lower than 10 % of the maximum concentration value (**Boxall, 2000** and **Dennis, 2000**).

An example is shown in **Figure 5.29**. In **Figure 5.29 (a),** the same concentration profile as shown in **Figure 5.18 (b)** is plotted. Then, in **Figure 5.29 (b)** the same profile is plotted after a 6th-order one-dimensional median filter was applied and in **Figure 5.29 (c)** a threshold of 3 % of the maximum concentration is applied, removing all values bellow this threshold.

Santiago Rojas Arques
Department of Civil and Structural Engineering
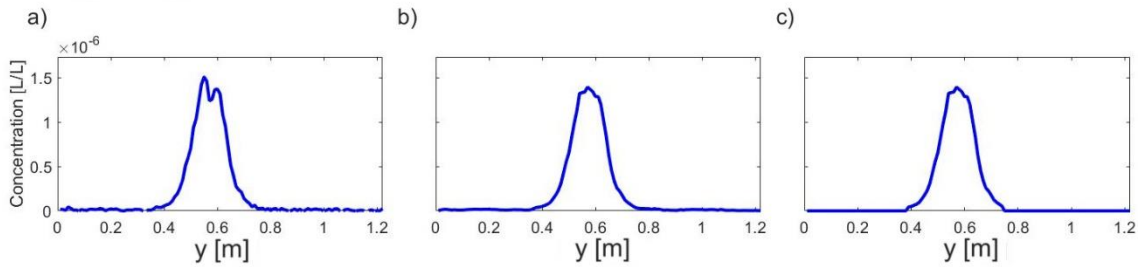
Figure 5.29. Concentration profiles located in the middle of camera 2: a) before applied filter 1; b) after applied 6th-order one-dimensional median filter; c) after applied 3 % threshold.

As **Figure 5.29** shows, the filtering technique attenuated the low concentration value recorded in the centre of the concentration profile, but the shape of the full profile was not modified. In addition, all low concentration values far from the tracer plume remained were effectively removed.

5.6.4. Mass Balance Factor

Finally, a mass balance was applied to concentration maps obtained by each filtering technique to ensure mass conservation. The mass over each transversal profile was obtained and the corresponding mean profile of mass was calculated for each injection. Then, the correction factor was obtained for each transverse profile and each single pixel for a specific profile was divided by its corresponding factor. The mean mass balance factors applied for the no vegetation tests for each filtering technique are shown in **Figure 5.30**.
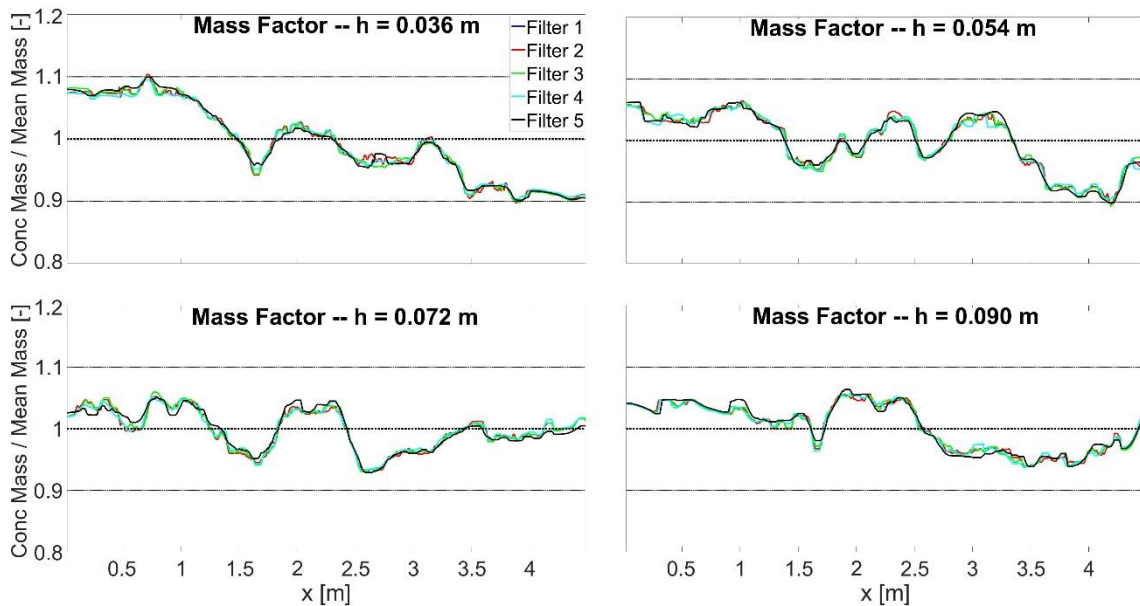
Figure 5.30. Mass balance factor applied for each filtering technique and water depth. Black lines indicate the mean mass and a deviation of $\pm\,10$ %.

Results in **Figure 5.30** show the relative variation in mass of the concentration profiles within the lengthwise for the different water depths and filters. Results show that the variation for the same water depth is quite similar for the different filters, suggesting that the different filtering techniques did not affect the overall concentration profiles but only removed extreme values along them. In addition, results show a decrease of the maximum mass variation for deeper flow conditions, with a maximum mass variation of 20 %, 15 %, 12 % and 10 % for the water depths

Santiago Rojas Arques
Department of Civil and Structural Engineering

$h = 0.036\,\text{m}$, $h = 0.054\,\text{m}$, $h = 0.072\,\text{m}$ and $h = 0.090\,\text{m}$ respectively. The mass variation recorded for $h = 0.036\,\text{m}$ may be produced as a consequence of some reflections produced within the recorded area, which could produce a miss-recording of some parts of the plume downstream, decreasing the total mass amount recording within the transverse concentration profiles.

5.6.5. Filtering Techniques Comparison

The experimental data from first set of experiments described in **Section 4.5.1** were analysed by using each filter process and the post filtering mass balance described in this section. Final concentration distribution maps and spanwise concentration profiles at two different longitudinal positions regarding to $h = 0.090\,\text{m}$ are shown in **Figure 5.31** and **Figure 5.32** respectively, as well as the time-averaged concentration map and the concentration profiles without any filtering process (i.e. with only the background levels subtracted).
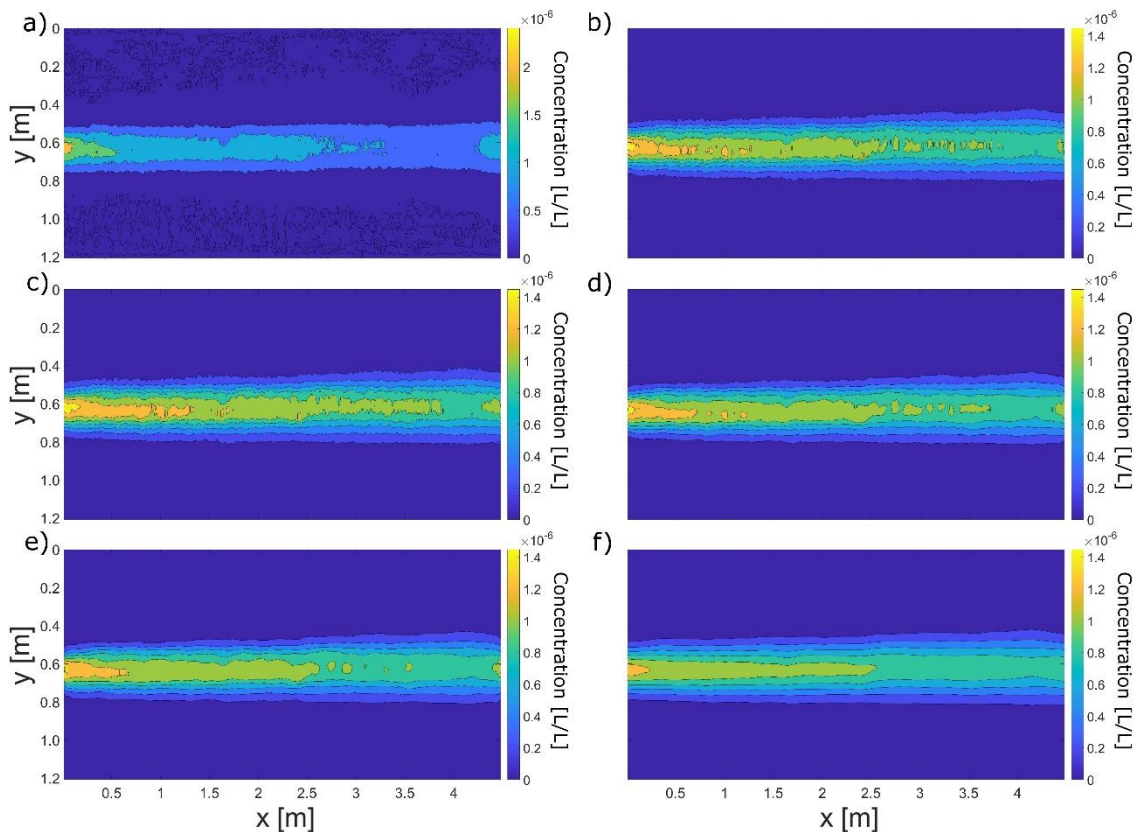
Figure 5.31. Final concentration maps without vegetation and h = 0.090 m test: a) without filter; b) using Filter 1; c) using Filter 2; d) using Filter 3; e) using Filter 4; f) using Filter 5.
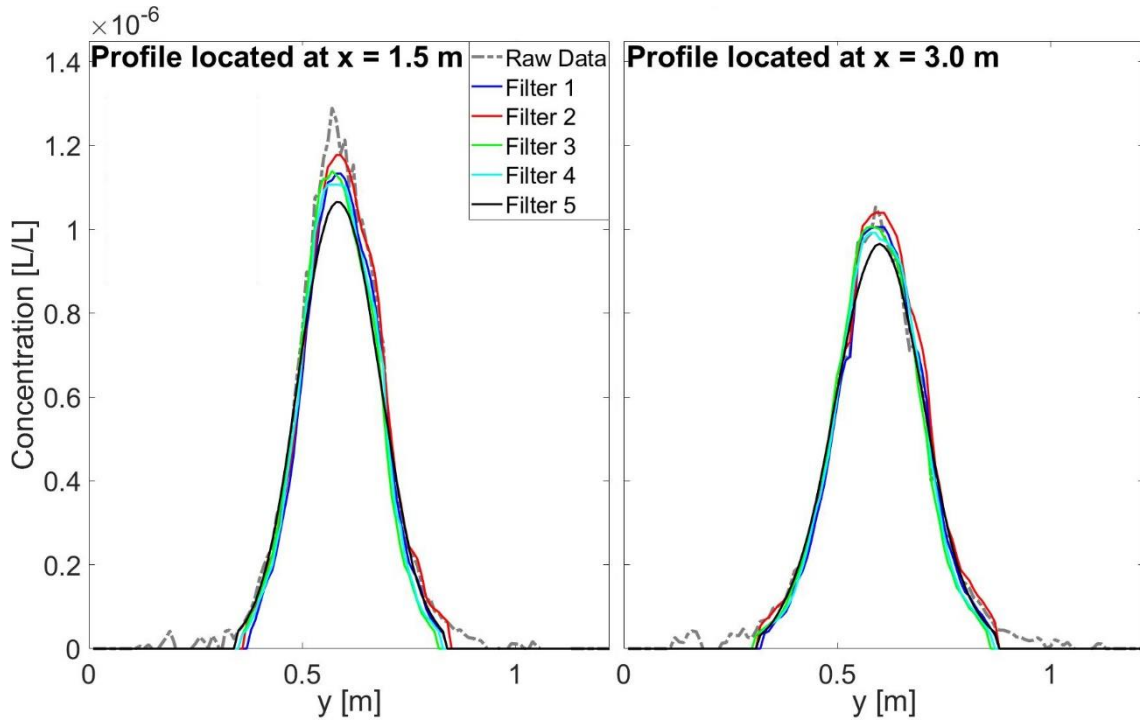
Figure 5.32. Comparison between experimental concentration profiles obtained using different filter for test h = 0.090 m.

Figure 5.31 shows time-averaged concentration maps using the different filters for the test $h = 0.090$ m. Also **Figure 5.32** represents two different concentration profiles at different positions ($x = 1.5$ m and $x = 3.0$ m downstream of the first recorded area) obtained using different filters. In addition, in both figures the concentration data without any filtering technique applied was plotted. Correlations between raw data and profiles with different filtering techniques were calculated to quantify the differences between different processes as shown **Table 5.10**.

Table 5.10. Correlation values between different filtering techniques results with raw data.

Corr R	Filter 1	Filter 2	Filter 3	Filter 4	Filter 5
$h = 0.036$ m	0.982	0.981	0.981	0.982	0.967
$h = 0.054$ m	0.991	0.990	0.991	0.990	0.983
$h = 0.072$ m	0.993	0.993	0.993	0.993	0.989
$h = 0.090$ m	0.987	0.987	0.987	0.988	0.985

For all cases shown in **Table 5.10**, results from no filtering technique were used as reference and all values were obtained comparing results from rest of filters with the raw data. The results plotted in **Figure 5.31** and **Figure 5.32** show all different filters produced the same overall concentration tracer distribution. Moreover, results show that concentration profiles obtained from different filters are similar to those recorded directly from videos. These results agree with those obtained in **Table 5.10** and confirm that the different filtering techniques proposed do not change the main shape of the concentration maps, but eliminate any spurious value that could be recorded. In addition, results show the differences between filter processes were found around the location of maximum concentration values. Concentration distributions plot in **Figure 5.31** show that for some of filter processes local increases of maximum

Santiago Rojas Arques
Department of Civil and Structural Engineering

concentration values are produced along the streamwise direction, instead of a constant decay as shown (for example) in results from Filter 5. This behaviour could be produced due to some spurious concentration values recorded due to light reflections that are not properly removed during filter process. In the following section, the experimental concentration distributions for no vegetated flows obtained from each different filtering techniques were analysed in order to discuss the accuracy of each filtering technique.

5.6.6. PCA Results Comparison

The results obtained with this new light configuration and using the filtering technique discussed in **Section 5.6** were compared against those results obtained with both the previous light configuration and the Cyclops results shown in **Section 5.4** for the same water depth and flow conditions and by applying the same filtering technique (Filter 1).

Mass balance factors along the streamwise direction obtained in **Section 5.6.4** were compared against the mass balance factors obtained from previous light configuration experiments as shown **Figure 5.33**.
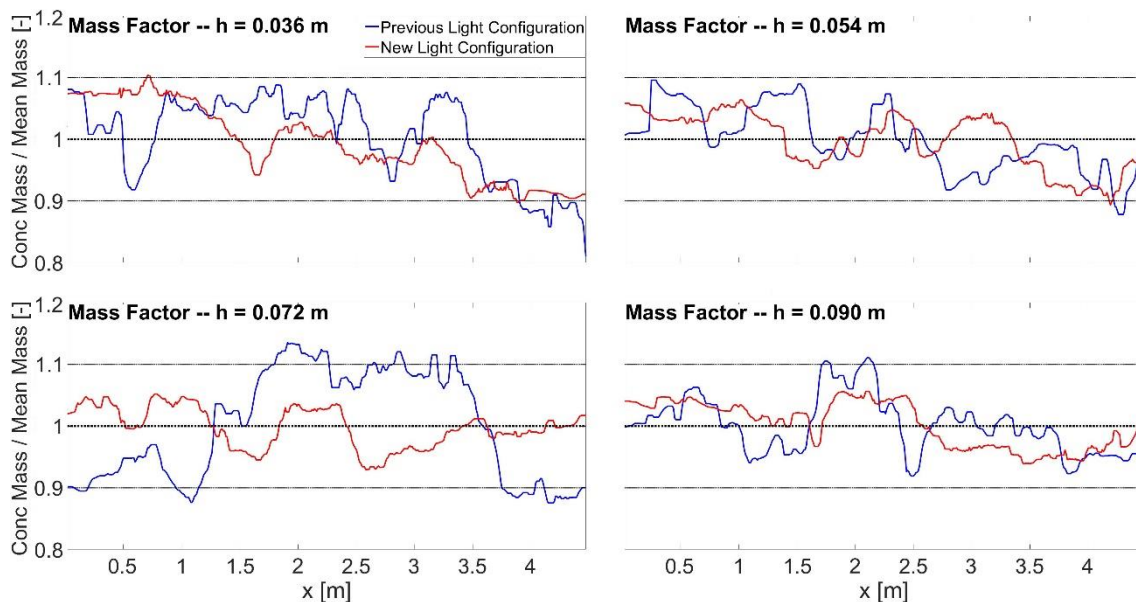
Figure 5.33. Mass Balance factors applied for each light configuration and water depth. Black lines indicate the mean mass and a deviation of ± 10 %.

Figure 5.33 shows that the concentration maps recorded with the new light configuration present a lower variation in mass along the streamwise direction compared with those recorded with the previous light configuration. These differences suggest that the errors produced by light reflections discussed in **Section 5.4** are improved with the new light configuration, resulting in a better conservation of mass along the streamwise direction.

In addition, a comparison of the filtered concentration results was performed to analyse the improvement of this new light configuration in the data. As the light reflections reported previously only affected to the edge of the dye plume, a visual comparison between individual profiles does not reflect the overall change between both light configurations. In contrast, the study of the spatial variances along the streamwise direction shows a general view of the concentration distribution. In addition, as the variance is quite sensitive to small changes in the edges of the concentration profile, the comparison of the variances obtained by using both light

Santiago Rojas Arques
Department of Civil and Structural Engineering

configurations is a good approach to study any possible improvement in the obtaining of the concentration maps.

The spatial variance was obtained for each profile obtained with the new light configuration along the streamwise direction in the same way as variances from previous light configuration and Cyclops results were calculated in **Section 5.4** (i.e. increases in variance relative to the measurements at $x = 5$ m). In addition, the same linear fitting was applied to each case using the same expression as previously ($a_{\sigma^2}x + b$). **Figure 5.34** shows the spatial variance obtained from each measurement technique and their corresponding linear fit.
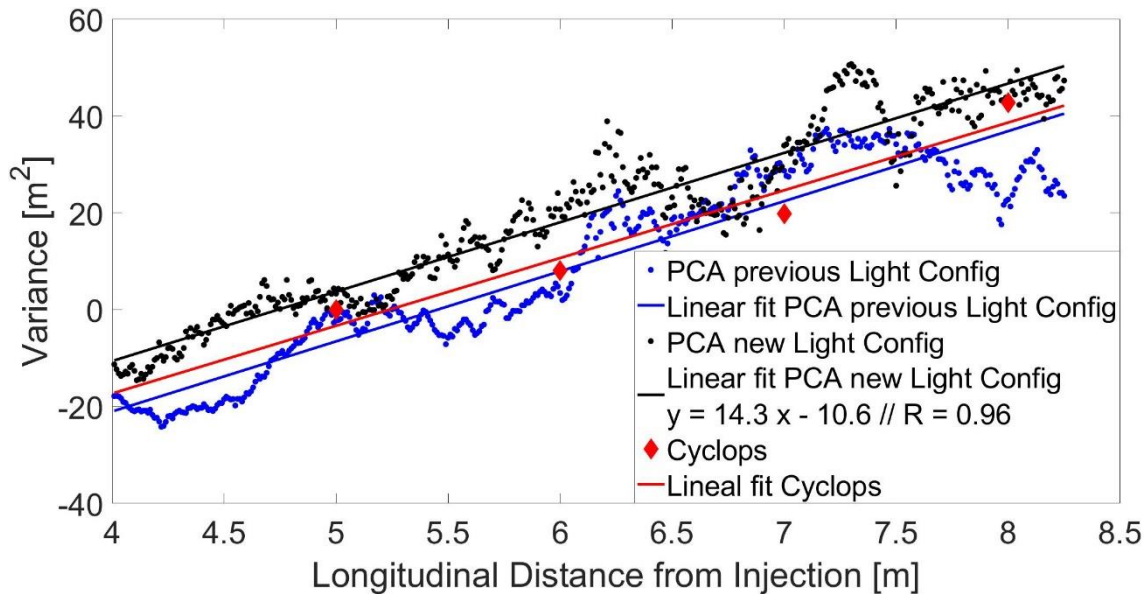
Figure 5.34. Comparison between PCA with each light configuration and Cyclops variance.

In **Figure 5.34**, spatial variance of all recorded concentration profiles obtained by each measurement technique are plotted. The important point to note is the expected increase in variance for the PCA concentration profiles after 7.5 m when using the new light configuration. The variances obtained with the new light configuration for these last profiles show a trend more consistent with the overall increase of variance. In addition, a linear fitting was applied to each case as in **Section 5.4**. The variance slope obtained for the PCA profiles with the previous light configuration and for the Cyclops data were $a_{PCA\ Previous} = 14.5$ and $a_{Cyclops} = 13.9$ respectively, with a Pearson correlation of $R = 0.94$ for the PCA technique and $R = 0.97$ for the Cyclops respectively. For the new light configuration, the variance slope obtained was $a_{PCA\ New} = 14.3$ and the Pearson correlation was $R = 0.96$.

The higher similarity between the Cyclops and the new light configuration slopes and the increase of the Pearson correlation compared with those results obtained with the previous configuration (**Figure 5.16**) show that the new light system improves the results compared with the previous configuration. In addition, a similar mixing process was recorded by each measurement technique, concluding the suitability of this technique for quantifying mixing processes along the experimental length.

Santiago Rojas Arques
Department of Civil and Structural Engineering

6. Results

In this section, the analysis processes described previously are applied to the experimental data for each set of experiments to obtain time-averaged longitudinal velocity profiles and concentration distributions of Rhodamine WT downstream of injections. In addition, experimental relationships are proposed to relate the longitudinal velocity flow distributions and the transverse mixing processes in one vegetated bank flows. Finally, the proposed new models are applied to predict the longitudinal velocity and the tracer concentration profiles in flow with two vegetated banks. The results are compared with experimental data to show the accuracy of the proposed models.

6.1. No Vegetation Tests Results

The initial set of experiments were carried out in a channel without any vegetation as explained in **Section 4.5.1**. The results obtained from these tests were used to provide baseline results. For each water depth, videos were recorded to obtain PIV data, concentration background levels and concentration maps of the injections released in the centre of the channel; and were analysed following the steps described in **Section 5.1** and **Section 5.6** respectively. From 2-D surface velocity experimental data, only longitudinal velocity were used in further analysis as is the main component which affects the transverse mixing processes for a continuous release (**eq. 2.58**) and it was the component analysed in previous work about transverse mixing in vegetated bank flows (**West, 2016**).

Figure 6.1 shows time-averaged longitudinal velocity maps for non-vegetation tests after steps described in **Section 5.1** were applied. In **Figure 6.1**, each water depth used for experiments are shown as $D36 = 0.036\,\text{m}$, $D54 = 0.054\,\text{m}$, $D72 = 0.072\,\text{m}$ and $D90 = 0.090\,\text{m}$ respectively.
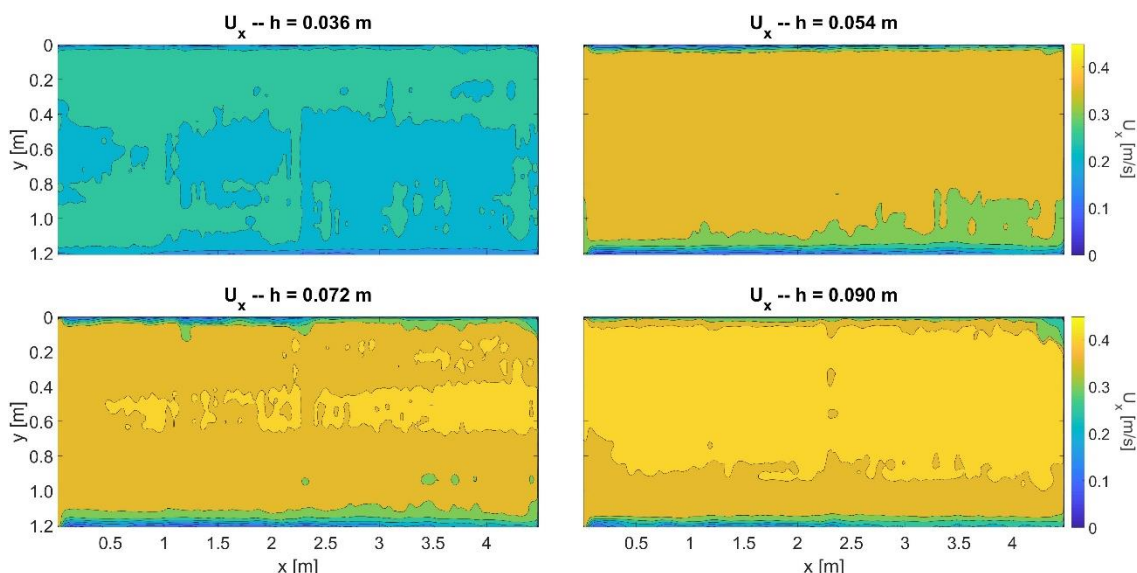
Figure 6.1 Time-averaged longitudinal velocity maps for non-vegetation tests.

In addition, **Figure 6.2** shows the time-average longitudinal velocity profile along the stremwise direction at $y = 0.61\,\text{m}$. Results show an approximate constant longitudinal velocity profiles over the length of the analysis area, confirming the presence of uniform flow.

Santiago Rojas Arques
Department of Civil and Structural Engineering
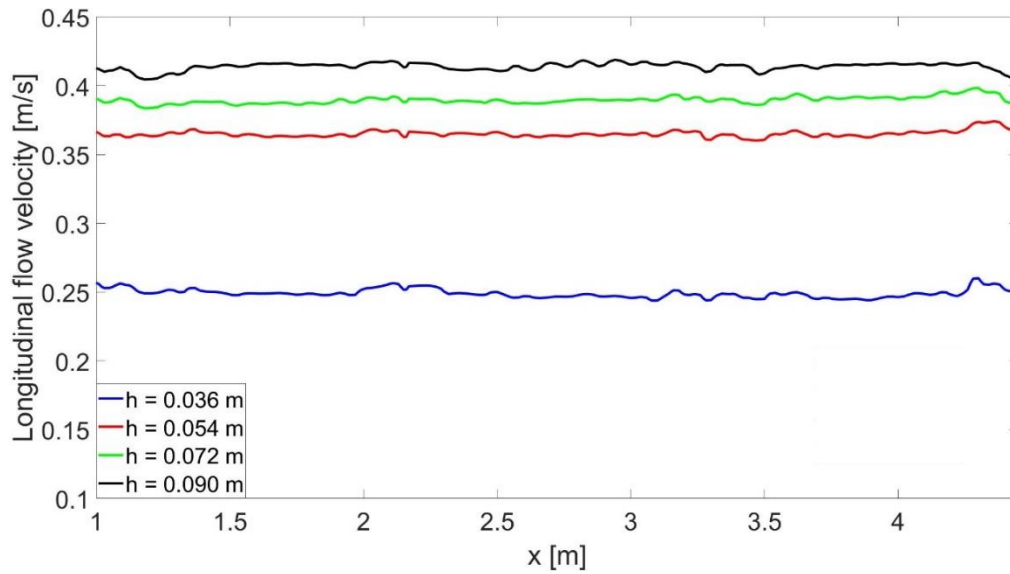
Figure 6.2. Time-averaged longitudinal velocity along the streamwise direction at $y = 0.61$ m.

For each time-averaged longitudinal velocity map obtained, **Figure 6.3** shows resulting averaged transverse profiles of primary longitudinal velocity for the four no vegetation tests. The mean values were obtained from the time-averaged velocity maps (e.g. see **Figure 6.1**). For each transverse position, the mean and standard deviation of primary velocity values over the streamwise direction were calculated.
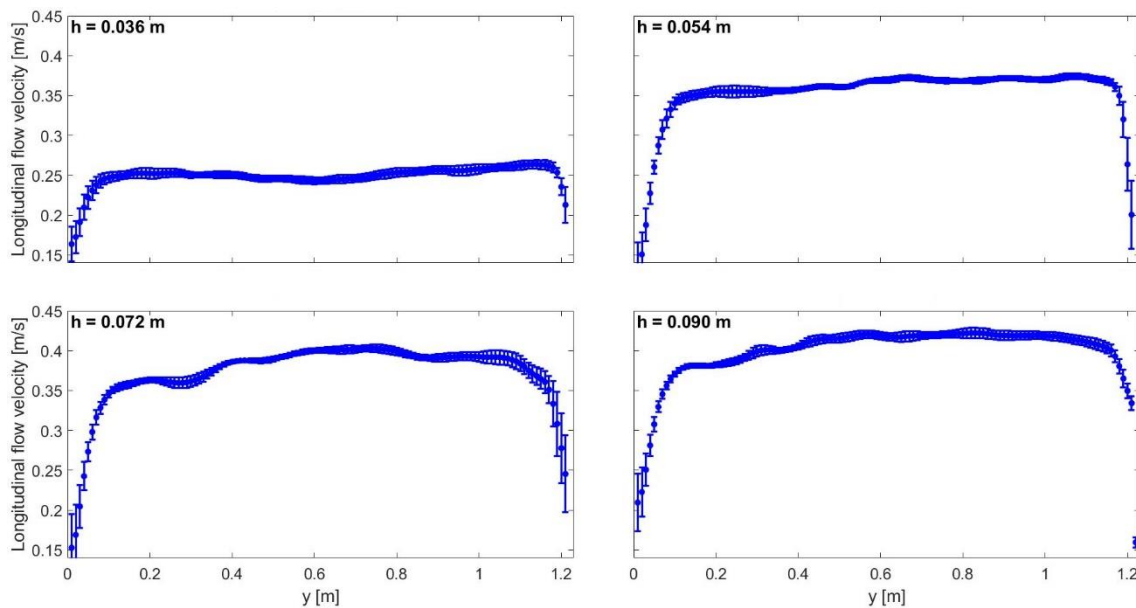
Figure 6.3. Mean transverse velocity profiles for non-vegetation tests.

The results plotted in **Figure 6.3** show a quasi-uniform longitudinal velocity distribution over the centre portion of the channel for the two shallower water depths. However, the longitudinal velocity distributions regarding to $h = 0.072$ m and $h = 0.090$ m show some variations along the spanwise direction with higher standard deviations. These variations could be produced as these flows were those with highest Reynolds number and thus they are the most turbulent flows. This turbulent behaviour could produce the increase of reflections over

- 98 -

the water surface by the LED lights, affecting the instantaneous frames and thus producing some variations in the results or because of minor irregularities in the flume. In addition, the highest standard deviations were found close the walls. This increase could be produced due to the lack of particles close the walls as these sections were on the boundaries of the recorded frames.

The concentration data was obtained from videos recorded and using five different filter processes (by using different mean and median filters with different windows) as it was explained in **Section 5.6.3**. The transverse mixing coefficients from each concentration map and filtering technique were obtained and the results compared to examine the effects of using different filters.

The transverse mixing coefficients D_y were obtained for each different filter result using the Advection-Diffusion Equation (ADE). The ADE introduced in **Section 2.4.2** was simplified as dye was released using a vertically well-mixed and continuous injection as explained in **Section 4.2.3**. Therefore, the simplified governing equation for the Advection-Diffusion Equation for tests with a steady vertical line source is:

$$h(y)\, U(y)\, \frac{\partial C(x,y)}{\partial x} = \frac{\partial}{\partial y}\left[h(y)\, D_y(y)\, \frac{\partial C(x,y)}{\partial y}\right] \qquad eq.\,6.1$$

Where $C(x,y)$ was the concentration for a specific spatial position x, y; being x and y longitudinal and transversal spatial coordinates respectively. $h(y)$ was the water depth, $U(y)$ the longitudinal flow velocity and $D_y(y)$ the transverse mixing coefficient.

6.1.1. Analytical Solution

In this set of experiments with a straight open channel with no vegetation, the transverse mixing coefficient $D_y(y)$ was considered constant along the channel width. In addition, for all experiments carried out in this thesis, the water depth was fixed for a given flow rate $(h(y) = cte)$. Therefore, the same procedure as explained in **Section 5.4.1** was implemented, where the analytical solution for **eq.6.1** was considered for the unbounded flow condition and considering no flux of concentration at the channel walls:

$$C(x,y) = \frac{M}{h\sqrt{4\pi D_y U x}}\, exp\left[-\frac{U(y - y_{Inj})^2}{4D_y x}\right] \qquad eq.\,6.2$$

Where both the longitudinal flow velocity and the water depth were considered constant along both the transversal and longitudinal direction. Then, the same simple optimization routine as that explained in **Section 5.4.1** was developed to find the optimised D_y value that provided predicted concentrations that fitted best with experimental concentration data. The routine was developed using the Matlab optimization function *fmincon,* which finds the minimum solution for a given function. The value being minimised was $-R$, where R was the Pearson correlation between the 2D experimental concentration data and the concentration data generated by the **eq. 6.2** considering all profiles recorded over the analysis area.

$$R = \frac{n_{values} \sum C_e C_p - (\sum C_e\, \sum C_p)}{\sqrt{\left[n_{values} \sum C_e{}^2 - (\sum C_e)^2\right]\left[n_{values} \sum C_p{}^2 - \left(\sum C_p\right)^2\right]}} \qquad eq.\,6.3$$

Where n_{values} is the number of values and C_e and C_p are the experimental and the generated concentration dataset respectively. The first concentration profile for each water depth was introduced as an input along with the water depth value and the longitudinal flow

Santiago Rojas Arques
Department of Civil and Structural Engineering

velocity. Thus, the routine started with a given initial transverse mixing coefficient D_{y_0} and the concentration profiles downstream were predicted using input data into **eq. 6.2**. The correlation R between the ADE concentration map and the experimental data was calculated and the objective value $-R$ was obtained. The function repeated this process changing the variable D_y until the solution $-R$ was minimised. In addition, for each iteration, the allowed D_y values were constrained within the range $0 - 1$ to avoid unreliable results.

The mean velocity value used in the equation was obtained from the transversal flow velocity profiles by not considering the velocity close to the walls, avoiding wall effects. The regions affected by the wall were identified by studying the longitudinal velocity gradient of transversal profiles. The regions affected by walls were considered as those where the velocity gradient was greater than the 5 % of the maximum value. Longitudinal velocity gradients for each water depth were plotted in **Figure 6.4** with the threshold used for each water depth. This threshold was selected as it was the mean value obtained in the centre of the channel between $y = 0.31$ m and $y = 0.91$ m, were the longitudinal flow was considered constant. The results obtained were 0.11 m, 0.13 m, 0.13 m and 0.14 m for tests $h = 0.036$ m, $h = 0.054$ m, $h = 0.072$ m and $h = 0.090$ m respectively.
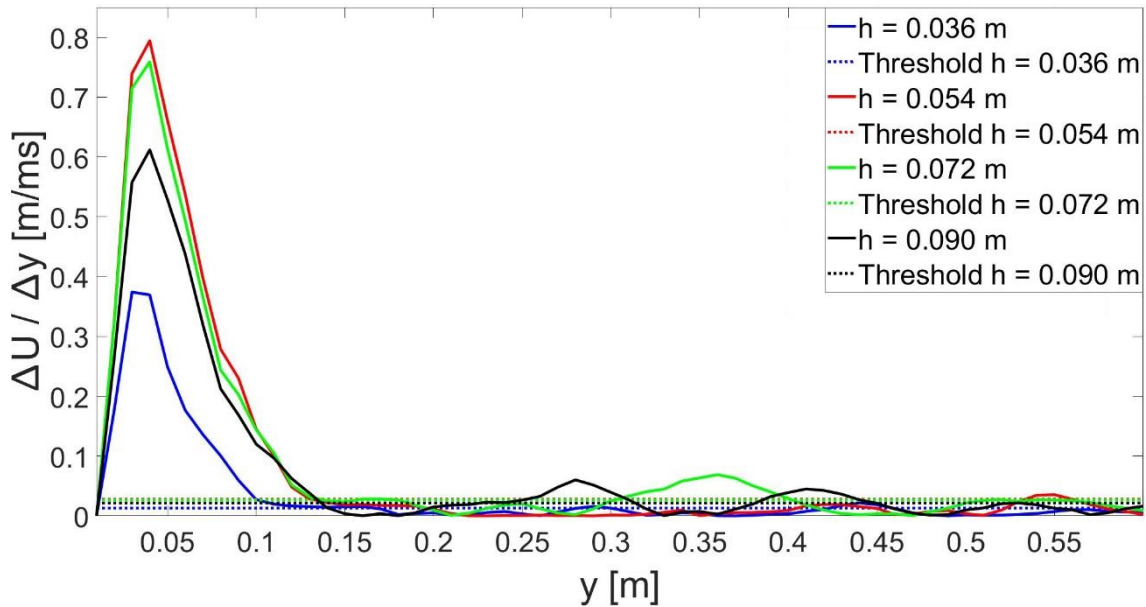
Figure 6.4. Longitudinal velocity gradients across the flume width obtained from the mean longitudinal velocity profiles.

Therefore, the mean longitudinal value used in the **eq. 6.2** for each water depth are shown in **Table 6.1**.

Table 6.1. Mean longitudinal free flow velocity without considering near-wall velocities.

$I.D.$	Water Depth [m]	Mean U [m/s]
$D36$	0.036	0.251
$D54$	0.054	0.364
$D72$	0.072	0.385
$D90$	0.090	0.410

Santiago Rojas Arques
Department of Civil and Structural Engineering

6.1.2. Finite Difference Model Grid Scale Dependence

Before the Finite Difference Model was applied to optimize the transverse mixing coefficient for the different tests, a simple example was proposed to check the grid scale dependence of the model. Numerical models are usually affected by some numerical diffusion produced as a result of the discretization of the continuous differential equations and it must be considered before their application (**Piasecki and Katopodes, 1999**). For the study, two Gaussian distributions upstream and downstream were defined to represent the two concentration profiles located at $x = 0$ m and $x = 0.25$ m in a channel with a width of 1 m. The point of this is to represent a simple scenario of a continuous injection with no wall effects, similar to that studied in this section. In addition, the same flow conditions as those used in the experimental tests within this thesis were considered, with a uniform water depth of $h = 0.054$ m, a mean longitudinal velocity profile of $U = 0.364$ m/s and a channel slope of $S_o = 0.00123$. Then, different transverse cell dimensions were considered for the same scenario (40 mm, 20 mm, 13.33 mm, 10 mm, 4 mm, 2 mm, 1.33 mm and 1 mm) as shown **Figure 6.5** (blue). As a first step, the analytical model was applied to optimize the transverse mixing coefficient for the different transversal resolutions, obtaining the optimised transverse profiles plotted in **Figure 6.5** (red) and the non-dimensional transverse mixing coefficients (D_y/hu^*) plotted in **Figure 6.6.** In addition, the same process was carried out but using the Finite Difference Model instead of the analytical method. In the same way, the optimised profiles plotted in **Figure 6.5** (black) and the non-dimensional transverse mixing coefficients plotted in **Figure 6.6** were obtained for each pixel resolution.
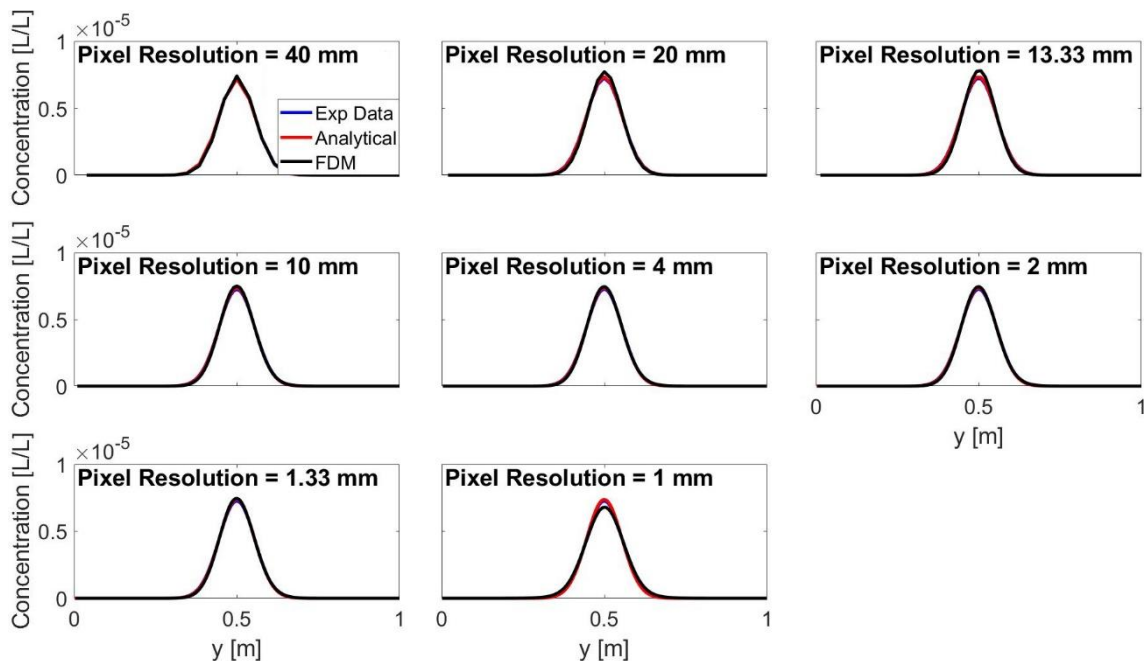
Figure 6.5. Optimised profiles for different pixel resolutions using both the analytical model and the F.D.M.

Santiago Rojas Arques
Department of Civil and Structural Engineering
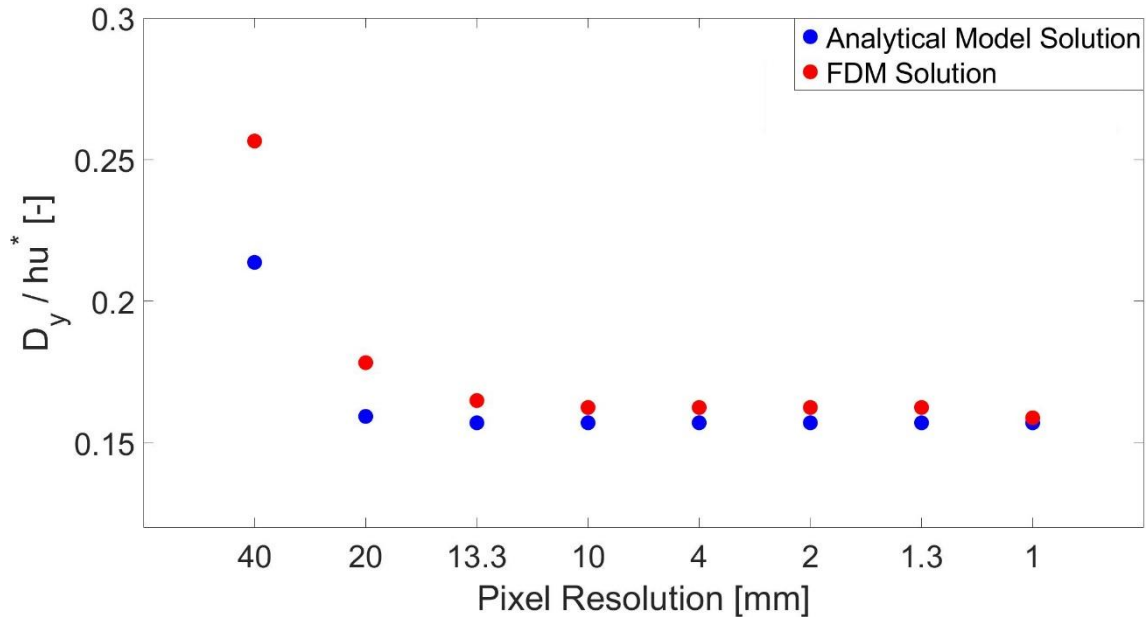
Figure 6.6. Optimised non-dimensional transverse mixing coefficients for different pixel resolution using both the analytical model and the F.D.M.

The results plotted in **Figure 6.6** show a variation in the non-dimensional results for the lowest pixel resolution obtained with the analytical model, with values of $D_y/hu^* = 0.2137$ and $D_y/hu^* = 0.1593$ respectively. Moreover, higher values were also obtained for the two lowest resolution using the F.D.M., with values of $D_y/hu^* = 0.2565$ and $D_y/hu^* = 0.1783$ respectively. For higher resolutions, both models converge to a constant value of $D_y/hu^* = 0.1570$ for the analytical model and $D_y/hu^* = 0.1625$ for the F.D.M. respectively. This convergence seems to start for a pixel resolution of 20 mm for the analytical model and 13.3 mm for the F.D.M., higher than the 10×10 mm pixel resolution of the experimental data. Therefore, results suggest that once the grid scale is small enough (13.3×13.3 mm) there is no variation in results for different resolution sizes and thus no grid dependence is appreciated for these scales. Moreover, the results also suggest that the pixel resolution considered in this thesis (10×10 mm) is appropriate to describe the transverse concentration profiles and thus to obtain suitable transverse mixing results.

6.1.3. Finite Difference Model Analysis

The use of **eq.6.2** is limited to those tests in which longitudinal flow velocity water, depth and transversal mixing coefficient can be considered constant along the width. The Finite Difference Model (F.D.M.) proposed by **West (2016)** and explained in **Section 2.6.1** was therefore required to identify D_y values in those cases where this assumption was not valid. An initial test was conducted in which results obtained using the F.D.M. and analytical solutions were compared in the non-vegetated case.

6.1.3.1. F.D.M. Solution for Different Filtering Techniques

The routine developed was the same as described in **Section 6.1.1**, considering $1 - R$ as the objective function, R being the correlation between experimental data and data generated by the F.D.M. solution. In the same way as in **Section 6.1.1**, the allowed D_y values during the iterations were constrained between 0 and 1. For the no vegetation tests, the F.D.M. was

- 102 -

simplified by considering a constant flow velocity and transverse mixing coefficient along the channel width $U(y) = cte, D_y(y) = cte$. This method was used to obtain transverse mixing coefficients for different filters and their corresponding correlations as shown **Table 6.2** and **Table 6.3** respectively. The transverse mixing results were normalised by hu^*, where $u^* = \sqrt{hgS_0}$ is the shear velocity:

Table 6.2. Normalised transverse mixing coefficient results from different filtering techniques and using F.D.M. model.

D_y/hu^*	Filter 1	Filter 2	Filter 3	Filter 4	Filter 5
$h = 0.036\,\mathrm{m} - \mathrm{F.D.M.\,Solution}$	0.146	0.145	0.163	0.218	0.141
$h = 0.054\,\mathrm{m} - \mathrm{F.D.M.\,Solution}$	0.128	0.144	0.194	0.251	0.128
$h = 0.072\,\mathrm{m} - \mathrm{F.D.M.\,Solution}$	0.153	0.169	0.195	0.249	0.158
$h = 0.090\,\mathrm{m} - \mathrm{F.D.M.\,Solution}$	0.136	0.139	0.174	0.233	0.137

Table 6.3. 2D correlation between experimental data and results from different filtering techniques and using F.D.M. model.

$Correlation\ R$	Filter 1	Filter 2	Filter 3	Filter 4	Filter 5
$h = 0.036\,\mathrm{m} - \mathrm{F.D.M.\,Solution}$	0.994	0.994	0.993	0.988	0.999
$h = 0.054\,\mathrm{m} - \mathrm{F.D.M.\,Solution}$	0.995	0.995	0.994	0.991	0.999
$h = 0.072\,\mathrm{m} - \mathrm{F.D.M.\,Solution}$	0.996	0.996	0.995	0.990	0.999
$h = 0.090\,\mathrm{m} - \mathrm{F.D.M.\,Solution}$	0.997	0.997	0.994	0.987	0.999

The results from **Table 6.2** show a variation in the optimised transverse mixing coefficient depending on the filtering technique applied. Transverse mixing results for Filter 1, Filter 2 and Filter 5 are those that produce closer results while Filter 3 and Filter 4 produce higher transverse mixing results for all water depths. In addition, correlation results between experimental data and results in **Table 6.3** show that lower correlations are obtained for Filter 3 and Filter 4 than for the rest of results. Moreover, the best correlations are obtained for Filter 5 for all water depths. Based on this results, Filter 5 was considered as the most accurate filtering technique and hence was used later to analyse the rest of experiments.

6.1.3.2. Comparison between F.D.M. and Analytical Model Solutions

Finally, constant transverse mixing results obtained from the F.D.M. optimization routine were compared with those produced by the analytical method described in **Section 6.1.1.** For both methods, experimental data using filtering technique Filter 5 were used as discussed in **Section 6.1.2.1** and same mean velocity value was considered for each water depth. Results for both normalised transverse mixing coefficients and their corresponding correlations are shown **Table 6.4** and **Table 6.5** respectively.

Table 6.4. Normalised transverse mixing coefficient results using filtering technique Filter 5 and using both F.D.M. and analytical model.

D_y/hu^*	$h = 0.036\,\mathrm{m}$	$h = 0.054\,\mathrm{m}$	$h = 0.072\,\mathrm{m}$	$h = 0.090\,\mathrm{m}$
$\mathrm{F.D.M.\,solution}$	0.141	0.128	0.158	0.137
Analytical solution	0.133	0.130	0.131	0.108

Santiago Rojas Arques
Department of Civil and Structural Engineering

Table 6.5. 2D correlation between experimental data and results using filtering technique Filter 5 and using both F.D.M. and analytical model.

$Correlation\ R$	$h = 0.036\ \mathrm{m}$	$h = 0.054\ \mathrm{m}$	$h = 0.072\ \mathrm{m}$	$h = 0.090\ \mathrm{m}$
F. D. M. solution	0.999	0.999	0.999	0.999
Analytical solution	0.992	0.994	0.997	0.997

Results show in **Table 6.4** suggest that both optimization models produced accurate results to reproduce mixing processes for each water depth. Mean transverse mixing results present a similar value to this proposed by **Webel and Schatzman (1984)** for straight laboratory flumes ($D_y/hu^* = 0.13$).

In addition, differences between different solutions for the same water depth are appreciated, being higher for the deeper water depths. These differences obtained between each model may be produced as the F.D.M. used a mathematical approximation to solve **eq. 6.1** and therefore, it does not produce identical value as the analytical solution. In **Figure 6.7** the optimised concentration profiles located at x $=$ 1.5 m and $x =$ 3.0 m downstream of the first recorded profile obtained by each model are plotted as well as the experimental concentration profiles to visualise the differences in results.

Santiago Rojas Arques
Department of Civil and Structural Engineering
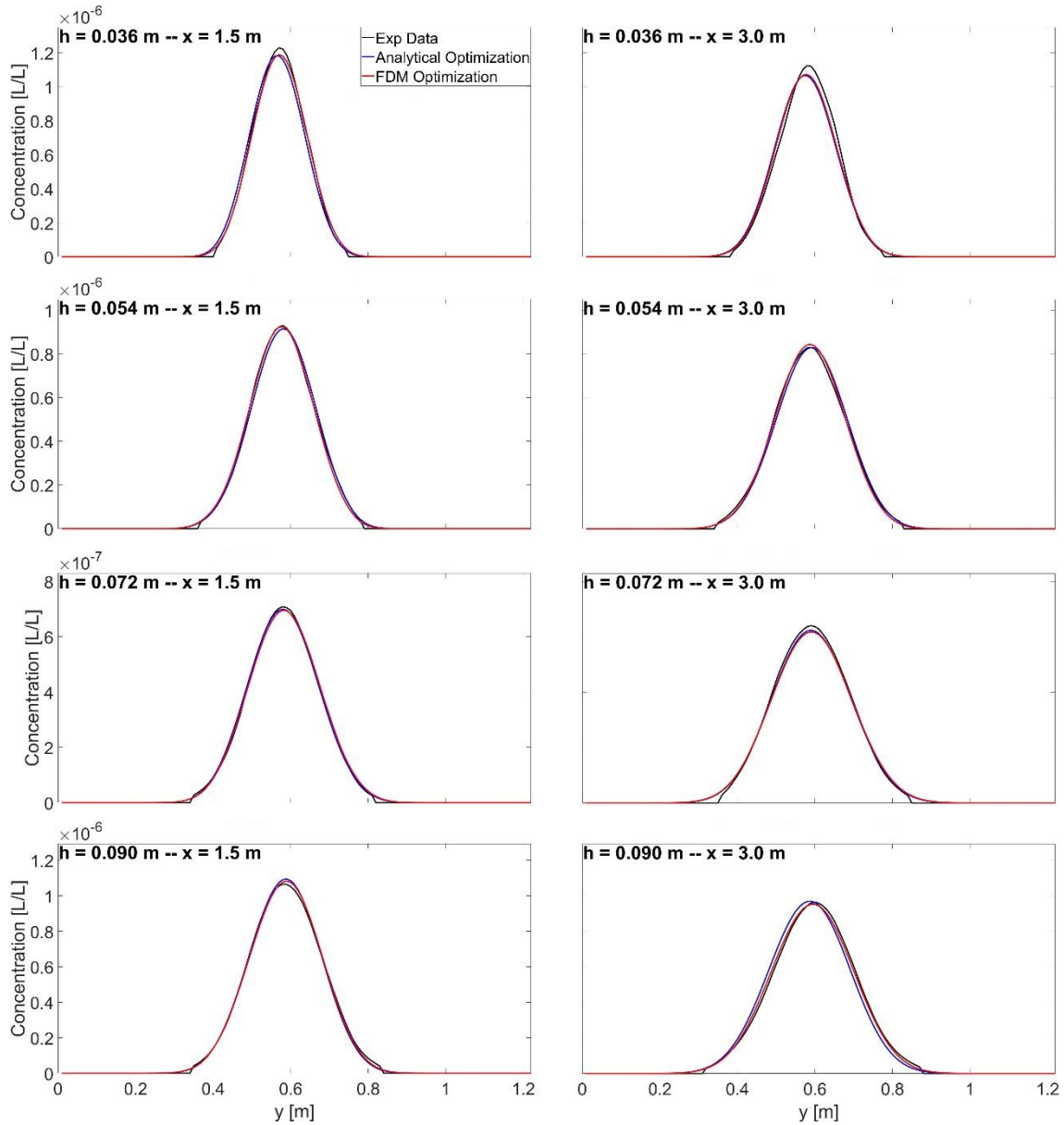
Figure 6.7. Comparison between experimental profiles and optimised concentration profiles obtained by each model.

Figure 6.7 shows the significant similarity of the optimised concentration profiles generated by each model. In addition, both models produced similar concentration profiles to those obtained experimentally. Therefore, this visual comparison and the high Pearson correlation values provided in **Table 6.5** suggest that the F.D.M. method is a suitable approach to analyse the more complex flow conditions described later in this section.

Santiago Rojas Arques
Department of Civil and Structural Engineering

6.2. Single Vegetated Bank Tests Results

For the second set of tests, artificial vegetation was installed along one bank of the channel as explained in **Section 4.5.2**. Three different vegetation densities were considered ($Veg_1 - \emptyset = 0.0015$; $Veg_2 - \emptyset = 0.006$; $Veg_3 - \emptyset = 0.025$) with a patch width of 0.42 m and a stem diameter of 0.005 m. The same four water depths as used in previous tests ($h = 0.036, 0.054, 0.072, 0.090$ m) were considered. Both longitudinal velocity and concentration distribution were recorded using the same techniques described previously and data was analysed as described in **Sections 5.1** and **Section 5.6**.

6.2.1. Velocity Results

Flow velocity videos were analysed in the same way as data in **Section 5.1**, using the same parameters during both the *DantecDynamics Ltd* and Matlab processes. Then, time-averaged longitudinal velocity maps were obtained for each water depth and vegetation density as shown **Figure 6.8**. In this figure, the vegetation edge is represented as white dots. In addition, for each spanwise cell position, time-averaged mean longitudinal velocity and standard deviation values were obtained by considering all the time-averaged values along the streamwise direction as shown **Figure 6.9.**

Santiago Rojas Arques
Department of Civil and Structural Engineering
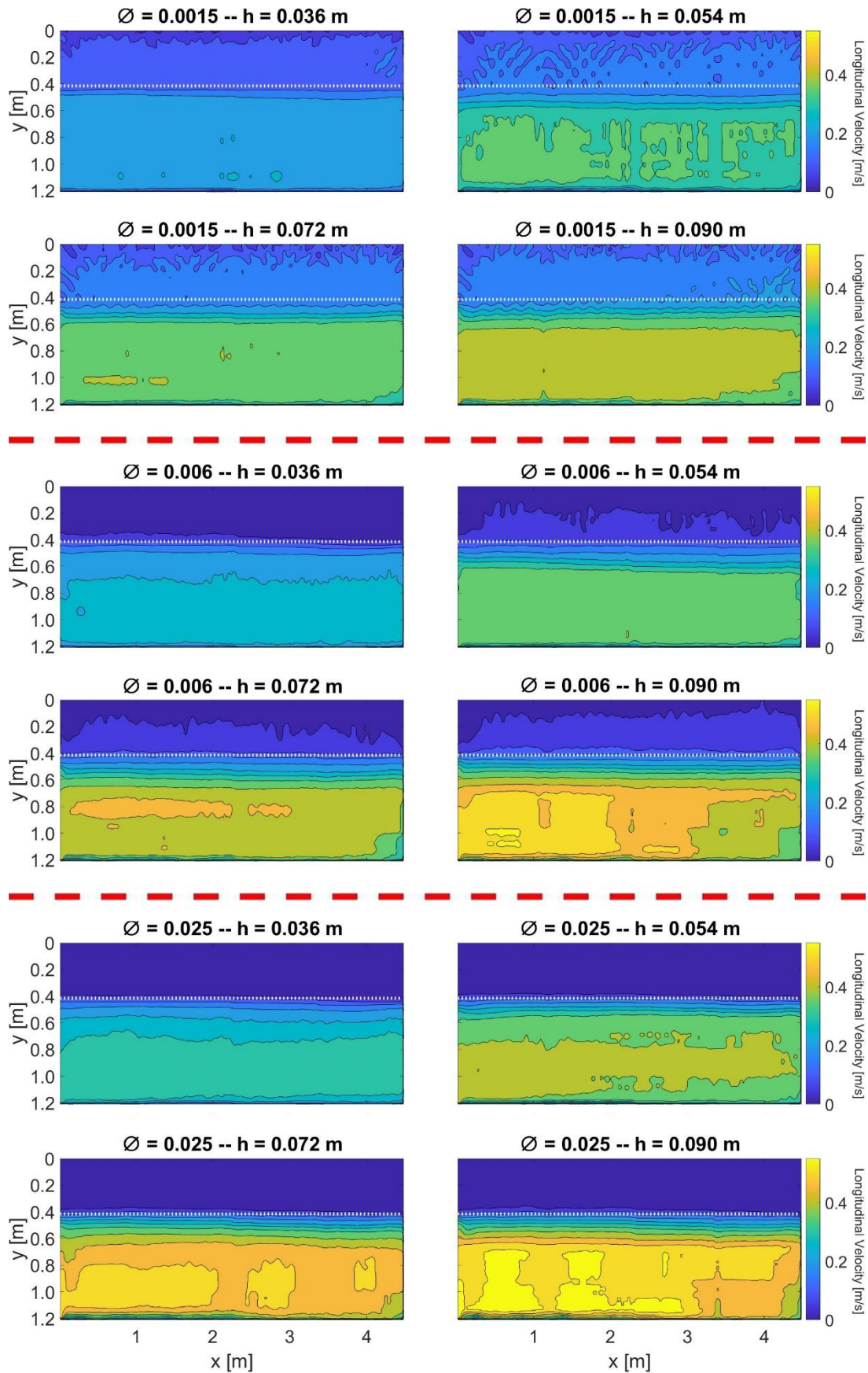
Figure 6.8. Time-averaged longitudinal flow velocity maps for different one vegetated bank conditions.
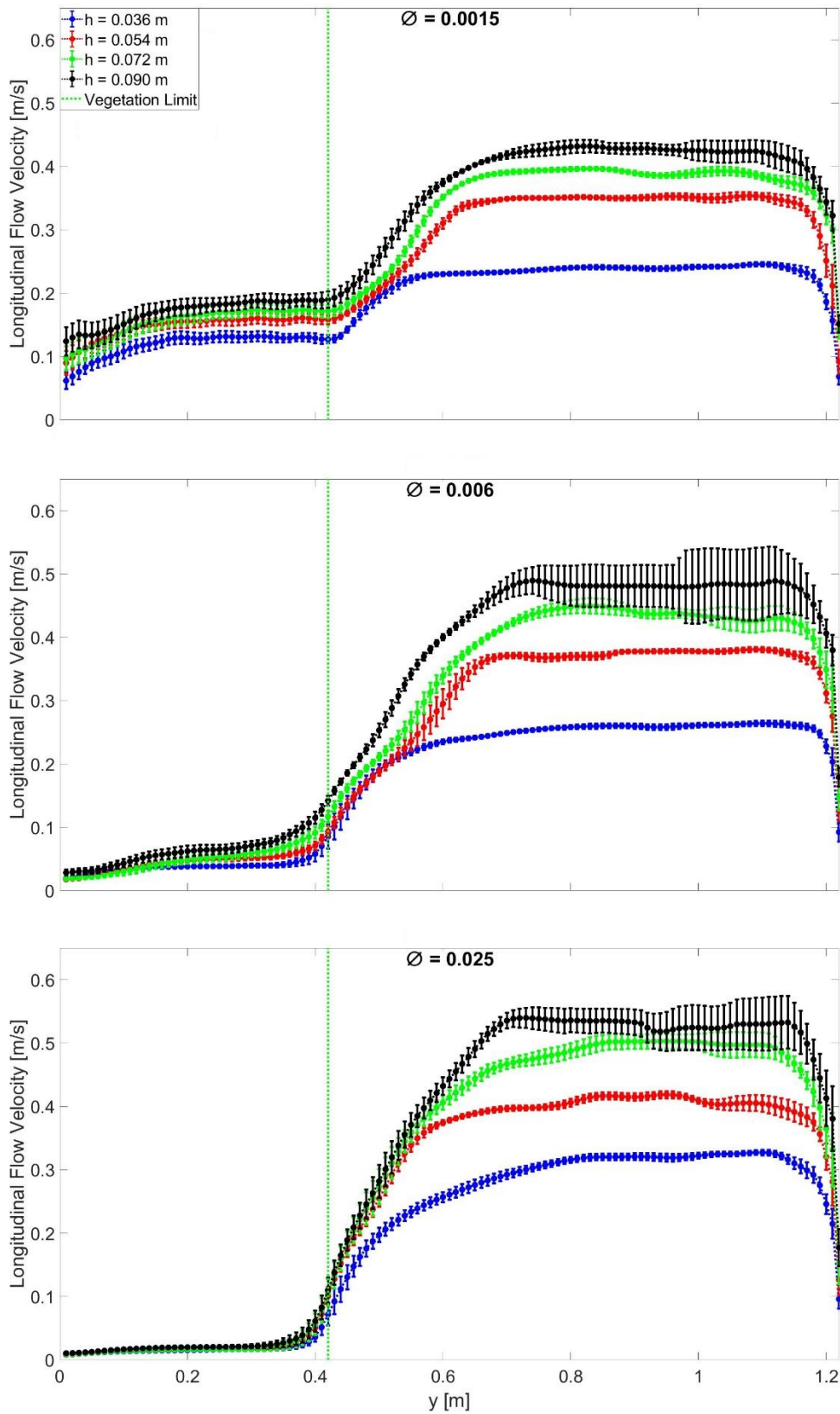
Figure 6.9. Lengthwise average longitudinal velocity distributions along channel width for each vegetation configuration and water depth. Error bars show their temporal standard deviation.

Santiago Rojas Arques
Department of Civil and Structural Engineering

Figure 6.9 shows a strong diminution of flow velocity produced within the vegetated patch and a shear layer developed between the vegetated and the non-vegetated regions. For all configurations, the highest variabilities over the analysed length were found for the deepest test ($h = 0.090$ m). These variabilities could be produced due to higher turbulences produced for the deepest configurations. In addition, high variabilities of the mean longitudinal velocity values were also recorded close to the right wall. As note before, these variabilities were produced as it may be harder to get enough particles in these region to obtain proper instantaneous velocity values for each frame. Moreover, **Figure 6.9** shows a decrease of the longitudinal velocity within the vegetation close to the wall. This decrease may be produced as not enough PIV tracers were recorded during experiments in that region, resulting in both high spurious instantaneous velocities and instantaneous velocities closer to 0, which did not correspond to the real velocity. High spurious velocities could be removed using the steps described in **Section 5.1**, but the lower velocities were considered as valid values, producing a decrease of the time-averaged longitudinal velocity in that region. Moreover, mean longitudinal velocity plotted in **Figure 6.9** for $\emptyset = 0.006$ and $h = 0.090$ m shows a high standard deviation close the right boundary. This high variation can be also appreciated in **Figure 6.8**, where a variation of the longitudinal velocity in the free flow region along the length is observed for the deepest flow conditions. This variation may be produced as a homogeneous distribution of PIV tracers may not have been fully achieved for these tests. Therefore, more spurious instantaneous velocities were produced, some of which entered the range defined in **Section 5.1.3** and were hence considered as valid vectors; producing a variation in the time-averaged longitudinal velocity map. Moreover, these variations are more visible for deeper flow conditions because higher longitudinal velocities and turbulence intensities were produced, producing that PIV tracers flow faster within the recorded area, and thus increasing the sensitivity of results to a homogeneous PIV tracer distribution. These figures highlight the importance of a homogeneous PIV tracer distribution and a proper definition of the range validation to avoid erroneous values that could affect time-averaged velocity results.

From all tests, mean longitudinal velocity within the vegetated bank and free flow region were obtained as the mean value inside the area from where velocity gradients were considered negligible (this threshold was considered when the velocity gradient was smaller than 5% of the maximum velocity gradient as discussed in **Section 6.1.1**) as shown in **Table 6.6**. In addition, **Figure 6.10 (a)** shows the mean longitudinal velocity within the vegetated bank for each water depth, as well as the velocity differences ($\Delta U = U_{free} - U_{veg}$) between the mean longitudinal velocity within the vegetation and in the free flow region are shown in **Figure 6.10 (b)**.

Table 6.6. Mean longitudinal flows recorded along the vegetated patch and the free flow regions.

a [stems/m]	h [m]	Q [l/s]	U_{free} [m/s]	U_{veg} [m/s]
0.397	0.036	8.302	0.241	0.129
0.397	0.054	16.018	0.351	0.156
0.397	0.072	24.529	0.391	0.166
0.397	0.090	34.816	0.427	0.180
1.587	0.036	7.070	0.261	0.038
1.587	0.054	13.910	0.377	0.048
1.587	0.072	21.658	0.438	0.051
1.587	0.090	30.621	0.482	0.064
6.349	0.036	7.140	0.322	0.016
6.349	0.054	13.756	0.412	0.017
6.349	0.072	20.683	0.500	0.017
6.349	0.090	29.218	0.529	0.020

Santiago Rojas Arques
Department of Civil and Structural Engineering
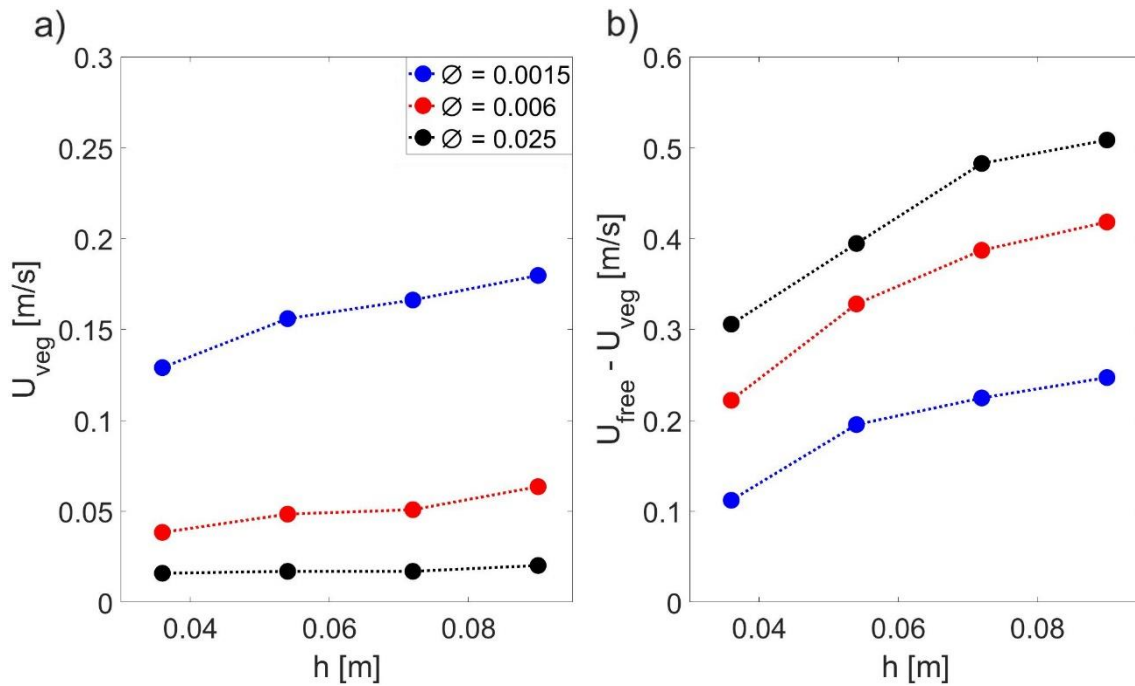
Figure 6.10. a) Mean longitudinal velocities recorded along vegetated patch for each water depth. b) Velocity differences between vegetated and non-vegetated velocities for each water depth.

Figure 6.10 (a) shows the mean longitudinal velocity flows recorded within the vegetated patch for each test. Results show a decrease of U_{veg} when the vegetation density increased as expected due to increased resistance. As a result, a higher velocity difference of mean longitudinal velocity between the vegetated and non-vegetated regions was produced for higher density patches as shown **Figure 6.10 (b)**. These results agree with past work (e.g. **White and Nepf, 2007 and West, 2016**).

However, as discussed in **Section 5.2**, the velocity data recorded in this thesis represents the surface flow velocity whilst the experimental data recorded by **White and Nepf (2007)** to develop the model explained below were recorded at the mid-depth. Therefore, the differences expected by assuming the surface velocity equivalent to that at mid-depth must be discussed. Regarding the longitudinal velocity within the vegetation, insignificant differences between surface and mid-depth velocity may be expected, as the vertical profile of longitudinal velocity remains constant along most of the water depth for emergent vegetated flows (**Kouwen et al., 1969, Rowiński et al, 1998**, **Nepf and Vivoni, 2000**).

However, the vertical profile of the longitudinal velocity follows a logarithmic law in free open flows, and therefore some differences may be expected between the surface and the mid-depth velocity. In **Section 5.2**, the fitted logarithmic law for each free condition was obtained based on experimental longitudinal velocities recorded along the water depth, and the differences between the surface longitudinal velocity and the mid-depth longitudinal velocity were calculated as shown **Table 5.6.** These differences were used below in this section to analyse how sensitive the proposed relationships introduced later are to the value of U_{free} varying in the range identified.

Santiago Rojas Arques
Department of Civil and Structural Engineering

All time-averaged mean longitudinal velocity profiles were fitted with the expression proposed by **White and Nepf (2008)** and both experimental data and fitted results are plotted in **Figure 6.11**. Their experimental results showed there are two main structures across a shear layer: a strong velocity variation inside the vegetation and a more gradual one in the outer region. In the inner region, **White and Nepf (2008)** proposed a hyperbolic expression to describe the strong velocity transition:

$$U_{Inner} = U_{veg} + U_s \left(1 + \tanh \left(\frac{y - y_0}{\delta_{Inner}} \right) \right) \qquad eq. 6.4$$

Where $U_s = U(y_0) - U_{veg}$, y_0 is the inflection point, δ_{Inner} is the length of the shear layer inside the vegetation patch and U_{veg} and U_{Inner} are the longitudinal flow velocities inside the vegetation and within the inner length respectively.

For the outer region of the shear layer, **White and Nepf (2008)** proposed a parabolic flow distribution:

$$U_{Outer} = U_m + (U_{free} - U_m) \left[\frac{y - y_m}{\delta_{Outer}} - \frac{1}{4} \left(\frac{y - y_m}{\delta_{Outer}} \right)^2 \right] \qquad eq. 6.5$$

Where $U_m = U(y_m)$ is the velocity of the point where the slopes of both inner and outer layers match (y_m); δ_{Outer} is the length of the outer layer and U_{free} and U_{Outer} are the longitudinal flow velocity in the free open channel region and along the outer layer respectively.

The inner layer was fitted using a nonlinear least-squares regression in Matlab (*nlinfit*) using **eq. 6.4** and obtaining δ_{Inner}, y_0 and U_s for each velocity profile. To fit the outer layer, an initial y_m was estimated as ($y_{m_{guess}} = y_0$) and δ_{Outer} was obtained using the same regression function but using **eq. 6.5**. Then values of each function were compared at y_m. The procedure was repeated until minimum differences between U_{Inner} and U_{Outer} were obtained at y_m. Results obtained from the experimental data are shown in **Table 6.7** and a visual comparison is plotted in **Figure 6.11**.

Table 6.7. Flow velocity parameters obtained from **White and Nepf (2008)** approximation.

Q[l/s]	a [stem/m]	h [m]	U_{free} [m/s]	U_{veg} [m/s]	ΔU [m/s]	δ_{Inner} [m]	δ_{Outer} [m]	y_0 [m]
8.30	0.397	0.036	0.241	0.129	0.112	0.010	0.281	0.046
16.02	0.397	0.054	0.351	0.156	0.195	0.042	0.280	0.108
24.53	0.397	0.072	0.391	0.166	0.225	0.045	0.264	0.126
34.82	0.397	0.090	0.427	0.180	0.247	0.061	0.316	0.098
7.07	1.587	0.036	0.260	0.038	0.222	0.076	0.295	0.016
13.91	1.587	0.054	0.377	0.048	0.328	0.098	0.365	0.027
21.66	1.587	0.072	0.438	0.051	0.387	0.141	0.400	0.053
30.62	1.587	0.090	0.482	0.063	0.418	0.136	0.346	0.023
7.14	6.349	0.036	0.322	0.016	0.306	0.066	0.389	0.008
13.76	6.349	0.054	0.411	0.017	0.394	0.074	0.272	−0.007
20.68	6.349	0.072	0.500	0.017	0.483	0.081	0.354	−0.002
29.22	6.349	0.090	0.528	0.020	0.508	0.083	0.334	−0.003

Santiago Rojas Arques
Department of Civil and Structural Engineering
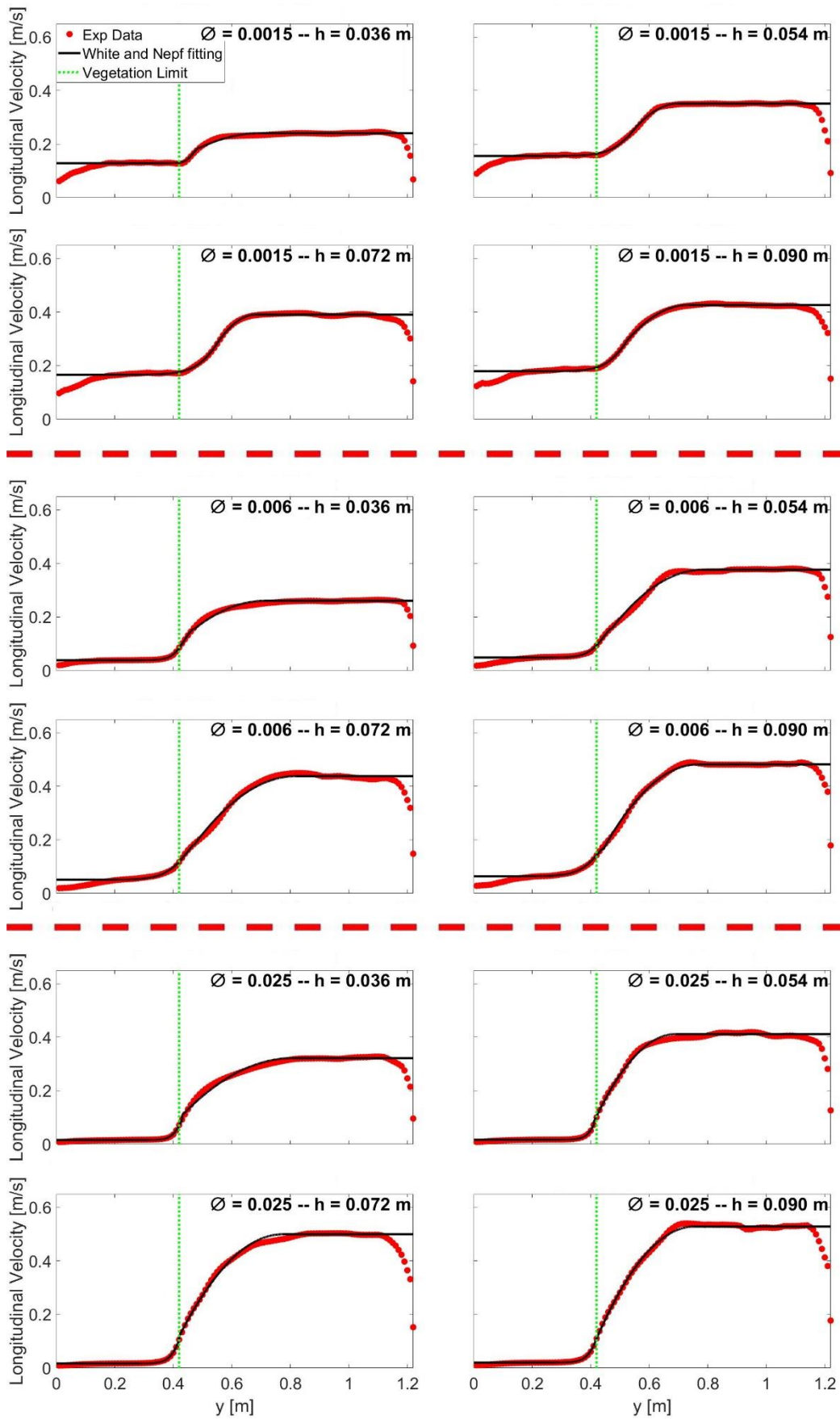
Figure 6.11. Fitted experimental data using **White and Nepf (2008)** approximation.

Figure 6.11 shows both experimental time-averaged mean longitudinal velocity profiles and the velocity profiles obtained by using **White and Nepf (2008)** proposed fitting. The goodness of **White and Nepf (2008)** fitting was obtained for each test condition by calculating the Pearson correlation and the mean absolute relative differences between fitted and experimental results as shown **Figure 6.12.**
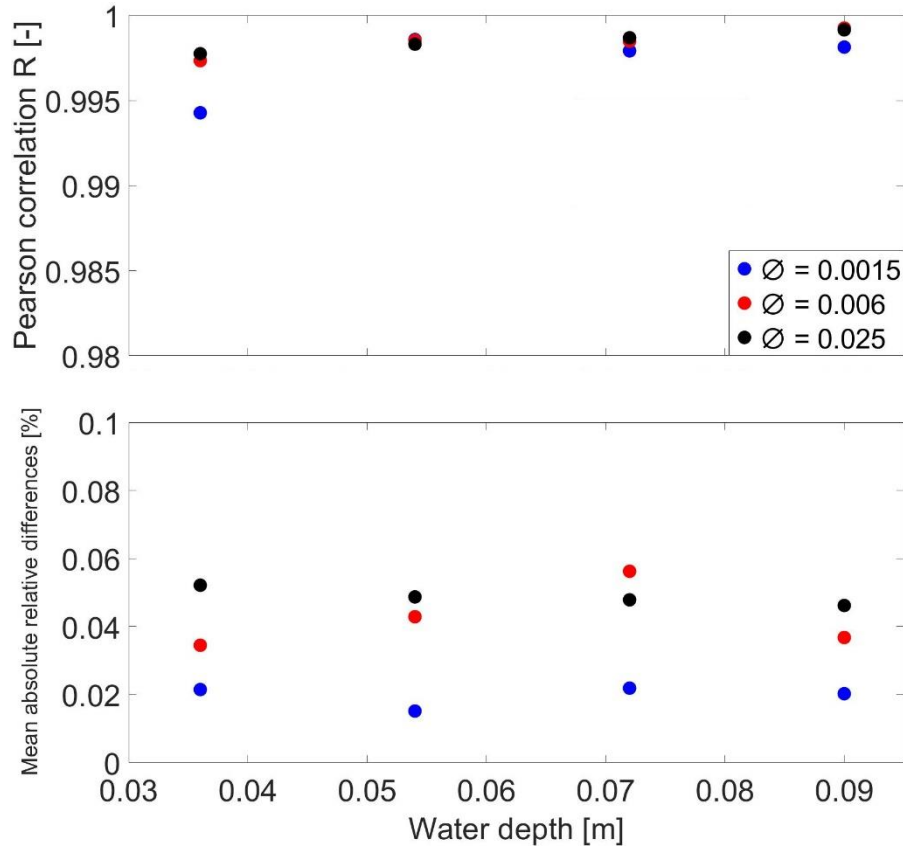
Figure 6.12. Pearson correlation and mean absolute relative differences between longitudinal velocity profiles obtained by **White and Nepf (2008)** approximation and experimental data.

Figure 6.11 and **Figure 6.12** show a high level of agreement obtained between experimental data and those obtained by the **White and Nepf (2008)** methodology. Therefore, this indicates that the length of the outer and the inner layer (δ_{Outer} and δ_{Inner} respectively) and the position of inflection point (y_0) for each test condition can be determined from the fitted equation.

Figure 6.13 shows the inflection point positions from the vegetation edge (y_0) obtained from fitting **eq. 6.4** to the experimentally obtained velocity profiles (red points) and those obtained previously by **White and Nepf (2008)** by fitting their experimental data to the same equation (black points). The results suggest a horizontal asymptote to 0 when vegetation density becomes high ($a \approx 6$ stems/m), which means the inflection point is located at the vegetation edge in these conditions. When vegetation density decreases ($a < 6$ stems/m), the inflection point moves further from the vegetation boundary. This behaviour was previously described by **White and Nepf (2008),** who noticed that for a vegetation density of $\emptyset > 0.02$ (or $a > 3.91$) the inflection point could be considered on the vegetation edge, but for sparse tests ($\emptyset = 0.02$) the inflection point was moved a distance of $2d$ away from the vegetation edge. This trend agrees with the results obtained here.

Santiago Rojas Arques
Department of Civil and Structural Engineering

Based on the results shown in **Figure 6.13**, a new relationship was proposed to obtain the displacement of the inflection point from the vegetation boundary:

$$y_0 = \frac{1}{26.35\,a} \qquad\qquad eq.\,6.6$$

Where y_0 was the position of the inflection point from the vegetation edge and 26.35 was a coefficient obtained empirically from the results shown in **Figure 6.13**. The Pearson correlation obtained between the proposed relationship and the data was $R = 0.913$. The new proposed relationship is also plotted in **Figure 6.13** (blue dots), showing a high level of agreement with experimental data.
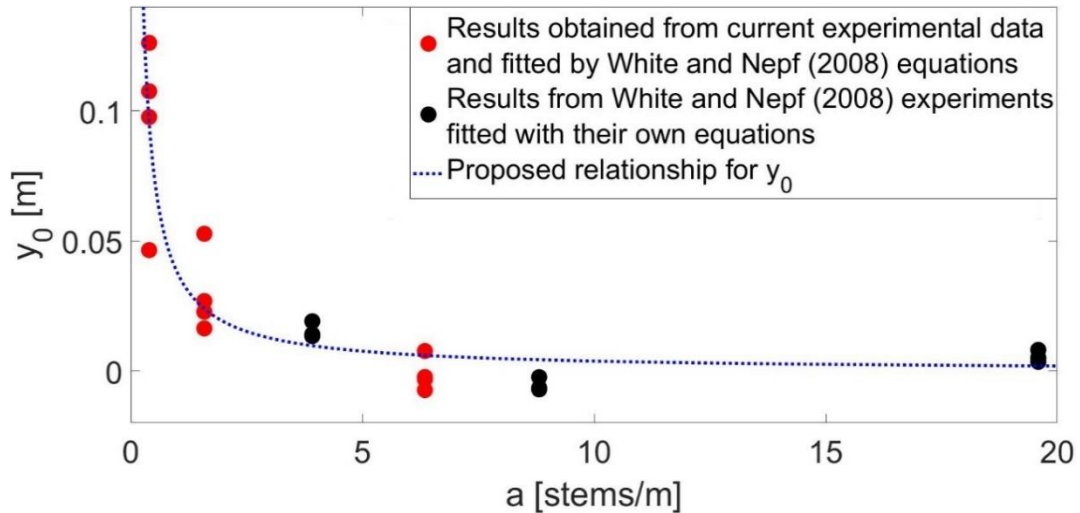
Figure 6.13. Relationship between vegetation density (a) and the position of inflection point from vegetation edge (y_0).

Following the same procedure, shear layer lengths (δ_{Outer} and δ_{Inner}) obtained from the fitted equation (**eq. 6.4** and **eq. 6.5**) and experimental longitudinal velocity differences ($\Delta U = U_{free} - U_{veg}$) were studied together with those obtained by **White and Nepf (2008)** and **West (2016)**. The ratio between velocity differences normalised by the velocity within the vegetation ($^{\Delta U}/_{U_{veg}}$) and the lengths of different shear layer regions were obtained from each case and related to the vegetation density (a). **Figure 6.14** shows a scheme with each variable labelled.
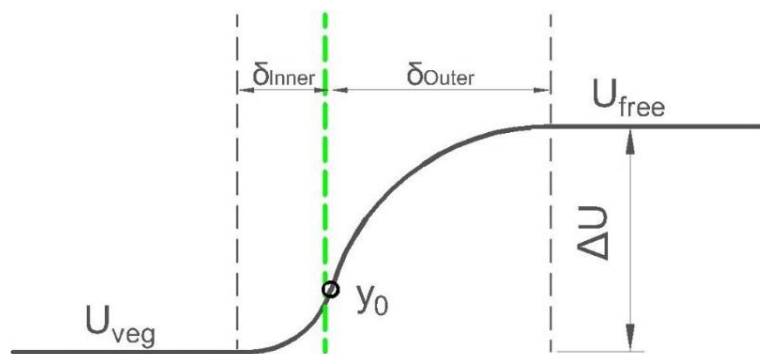
Figure 6.14. Scheme with all different dimensions used for proposed model.

Figure 6.15 shows the relationship between velocity ratios and the vegetation density considering the length of the outer region (**a**); and the total length of the shear layer (**b**) for all sets of experimental data. Results suggests a linear relationship with vegetation density:

$$\frac{\Delta U / U_{Veg}}{\delta_{Outer}} = 11.19 \, a \qquad\qquad eq. 6.7$$

$$\frac{\Delta U / U_{Veg}}{\delta_{Outer} + \delta_{Inner}} = 10.08 \, a \qquad\qquad eq. 6.8$$

Where 11.19 and 10.08 were obtained empirically. The Pearson correlation between the data and the proposed relationships were obtained, being $R = 0.981$ and $R = 0.977$ for **eq. 6.7** and **eq. 6.8** respectively.
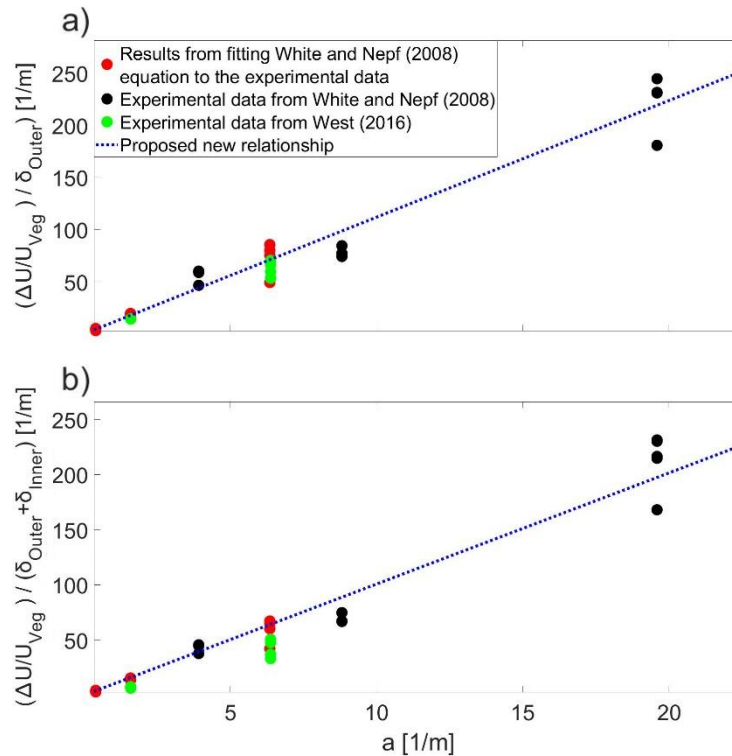
Figure 6.15. Relationship between ratio of velocity increment normalised by vegetated velocity and shear layer length and vegetation density a) outer region length; b) total shear layer length.

With the relationships obtained in **eq. 6.6**, **eq. 6.7** and **eq. 6.8**; an empirical model can be proposed to predict longitudinal flow velocity profile within partially vegetated flows given only the vegetation density and both velocities within the vegetation and free open flow layer. For a given condition, both U_{veg} and U_{free} are divided by U_{veg}. The length of the outer region (δ_{Outer}) and total shear layer ($\delta_{Outer} + \delta_{Inner}$) can be calculated using both **eq. 6.7** and **eq. 6.8**. and a linear increase can be defined between U_{veg}/U_{veg} and U_{free}/U_{veg}, obtaining the dimensionless parameter $U_{Linear\,Step}$ connecting these two constant ratios. Then, from **eq. 6.6** the position of the inflection point can be obtained and an assumption of $U(y_0)/U_{veg} = U_{Linear\,Step}(y_0)$ can be made.

Santiago Rojas Arques
Department of Civil and Structural Engineering

The longitudinal flow velocity within the inner layer can then be obtained by fitting the structure generated using a hyperbolic tangent function and velocity along the outer layer is obtained by solving a parabolic function.

$$\frac{U(y)}{U_{veg}} = 1 \qquad\qquad 0 \leq y \leq y_{Inner} \quad eq.\,6.9$$

$$\frac{U(y)}{U_{veg}} = U(y_0) + \frac{U_{max} - 1}{2}\tanh\left[\left(\frac{\alpha}{2\delta_{Inner}}y\right) - \left(\frac{\alpha}{2\delta_{Inner}}y_0\right)\right] \quad y_{Inner} \leq y \leq y_0 \quad eq.\,6.10$$

$$\frac{U(y)}{U_{veg}} = C_1 y^2 + C_2 y + C_3 \qquad\qquad y_0 \leq y \leq y_{Outer} \quad eq.\,6.11$$

$$\frac{U(y)}{U_{veg}} = \frac{U_{free}}{U_{veg}} \qquad\qquad y \geq y_{Outer} \qquad eq.\,6.12$$

Where y_{inner} is the position inside the vegetation where the inner layer started and y_{Outer} is the point where the outer layer ends and velocity becomes equal to U_{free}. **Eq. 6.10** is solved using the same nonlinear least-squares regression used previously to fit the inner velocity profile. In this case, U_{max} and α were obtained from this regression. Then, coefficients from **eq. 6.11** are solved given the known values y_0 and y_{outer}:

$$\frac{U(y_0)}{U_{veg}} = U_{Linear\,Step}(y_0) \qquad\qquad eq.\,6.13$$

$$\frac{U(y_{Outer})}{U_{veg}} = \frac{U_{free}}{U_{veg}} \qquad\qquad eq.\,6.14$$

$$\left(\frac{U(y_{Outer})}{U_{veg}}\right)' = 0 \qquad\qquad eq.\,6.15$$

And coefficients from **eq. 6.11** are solved as:

$$C_1 = \frac{\left(U_{free}/U_{veg} - U_{Linear\,Step}(y_0)\right)}{y_{Outer}^2 + y_0^2 - 2y_0 y_{Outer}} \qquad\qquad eq.\,6.16$$

$$C_2 = -2y_{Outer}C_1 \qquad\qquad eq.\,6.17$$

$$C_3 = \frac{U_{free}}{U_{veg}} - C_1 y_{Outer}^2 - C_2 y_{Outer} \qquad\qquad eq.\,6.18$$

For all tests conducted, transverse profiles of longitudinal velocity were obtained using the procedure described above and compared with experimental values and velocity fitted by the **White and Nepf (2008)** expressions as shown **Figure 6.17**. For this procedure, the normalised longitudinal velocity at the inflection point was assumed to be $U(y_0)/U_{veg} = U_{Linear\,Step}(y_0)$ as it was discussed previously. In order to study the accuracy of this assumption, the differences of velocity between predicted and experimental data at y_0 were obtained and results are presented in **Figure 6.16**. The maximum difference of $0.08\ m/s$ was obtained, suggesting the assumption $U(y_0)/U_{veg} = U_{Linear\,Step}(y_0)$ is appropriate.

Santiago Rojas Arques
Department of Civil and Structural Engineering
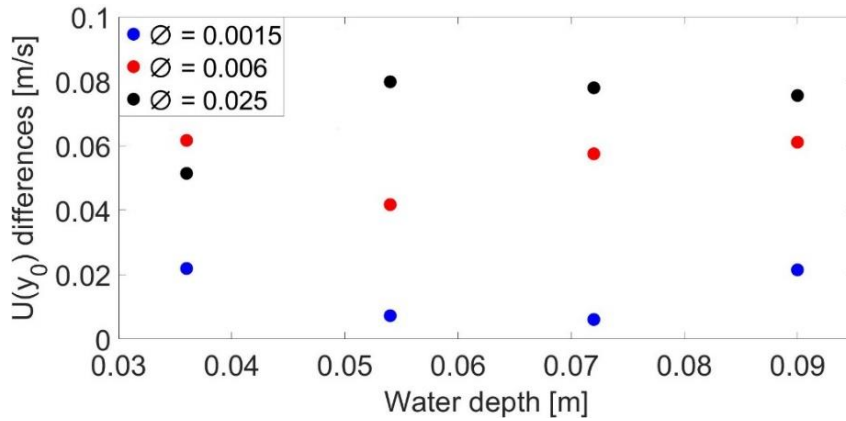
Figure 6.16. Absolute differences of longitudinal velocity at the predicted inflection point between experimental data and empirical model (**eq. 6.9 – 6.10**).

As it was discussed previously at the beginning of this section, the sensitivity of the relationships proposed in **eq. 6.7** and **eq. 6.8** were studied. In the same way as in **Figure 6.15**, the relationships between the vegetation density and the velocity ratios ($\left(\Delta U/U_{Veg}\right)/\delta_{Outer}$ and $\left(\Delta U/U_{Veg}\right)/\left(\delta_{Outer} + \delta_{Inner}\right)$) were studied, but in this case the velocity increment was calculated by considering the expected longitudinal velocity at the mid-depth ($\Delta U = U_{Mid-depth} - U_{veg}$). The mid-depth longitudinal velocity was calculated using the surface velocity for each water depth and vegetation density, and the absolute differences obtained in **Table 5.6** for each water depth. The new empirical coefficients obtained were 11.12 to relate the vegetation density and the velocity ratio considering the length of the outer region ($\left(\Delta U/U_{Veg}\right)/\delta_{Outer}$) and 10.02 to relate the vegetation density and the velocity ratio considering the total length of the shear layer ($\left(\Delta U/U_{Veg}\right)/\left(\delta_{Outer} + \delta_{Inner}\right)$). These coefficients are very similar to those obtained in **eq. 6.7** and **eq. 6.8** as shown **Table 6.8**, where $Coeff$ are the empirical coefficients obtained by considering the surface longitudinal velocity data (called as Original Coefficients) and those obtained by considering the expected mid-depth longitudinal velocity (called as Adjusted Coefficients).

Table 6.8. Empirical coefficients obtained by considering both surface and mid-depth longitudinal velocity.

Empirical Coefficients	Original Coefficients	Adjusted Coefficients
$\dfrac{\Delta U/U_{Veg}}{\delta_{Outer}} = a\,Coeff$	11.19	11.12
$\dfrac{\Delta U/U_{Veg}}{\delta_{Outer} + \delta_{Inner}} = a\,Coeff$	10.08	10.02

Santiago Rojas Arques
Department of Civil and Structural Engineering

In addition, absolute differences between predicted shear layer lengths were calculated by assuming each empirical coefficient (11.19 or 11.12 to obtain the length of the outer region and 10.08 or 10.02 to obtain the total length of the shear layer). The absolute differences obtained are no longer than 0.05 m for the obtaining of the length of the outer region, and no longer than 0.06 m for the obtaining of the total shear layer length. In **Figure 6.17** the predicted profiles obtained by using the proposed model with the original coefficients and the surface velocity data are compared with those profiles obtained by using the same proposed model but with the adjusted coefficients and the expected mid-depth longitudinal velocity data.
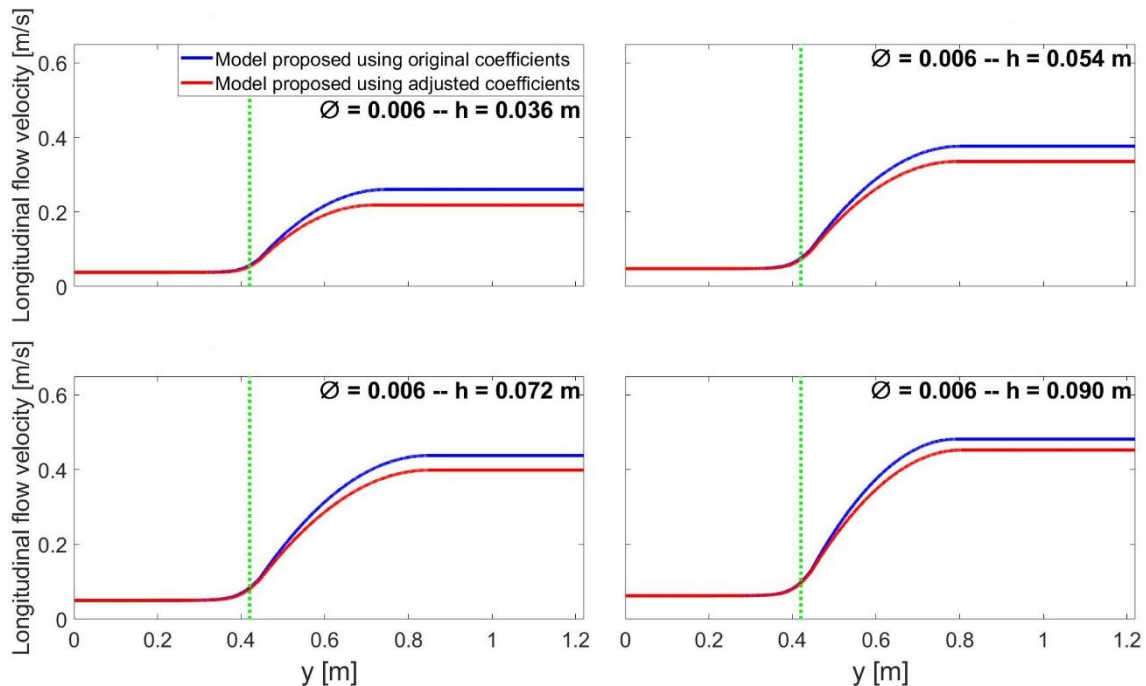
Figure 6.15. Comparison between predicted profiles by using the original coefficients and the surface velocity data and those predicted with the adjusted coefficients and the expected mid-depth velocity.

Figure 6.17 shows a low variability in the length of the predicted shear layers and only a difference between the surface and the mid-depth velocity is observed in the free flow region, in agreement with those differences obtained in **Section 5.2**. The similarities in results suggest the suitability of the proposed relationships.

6.2.1.1. Comparison of Proposed Model against Experimental Data

Figure 6.18 shows relationships proposed using the **White and Nepf (2008)** model and the velocity profiles from the model proposed by using the original coefficients obtained in **eq. 6.7** and **eq. 6.8** in this section along with experimental results. Plots suggest a good fit of the proposed expressions to experimental data. Pearson correlations between experimental data and both results were obtained along the shear layer (constant velocity regions were not considered).

Santiago Rojas Arques
Department of Civil and Structural Engineering
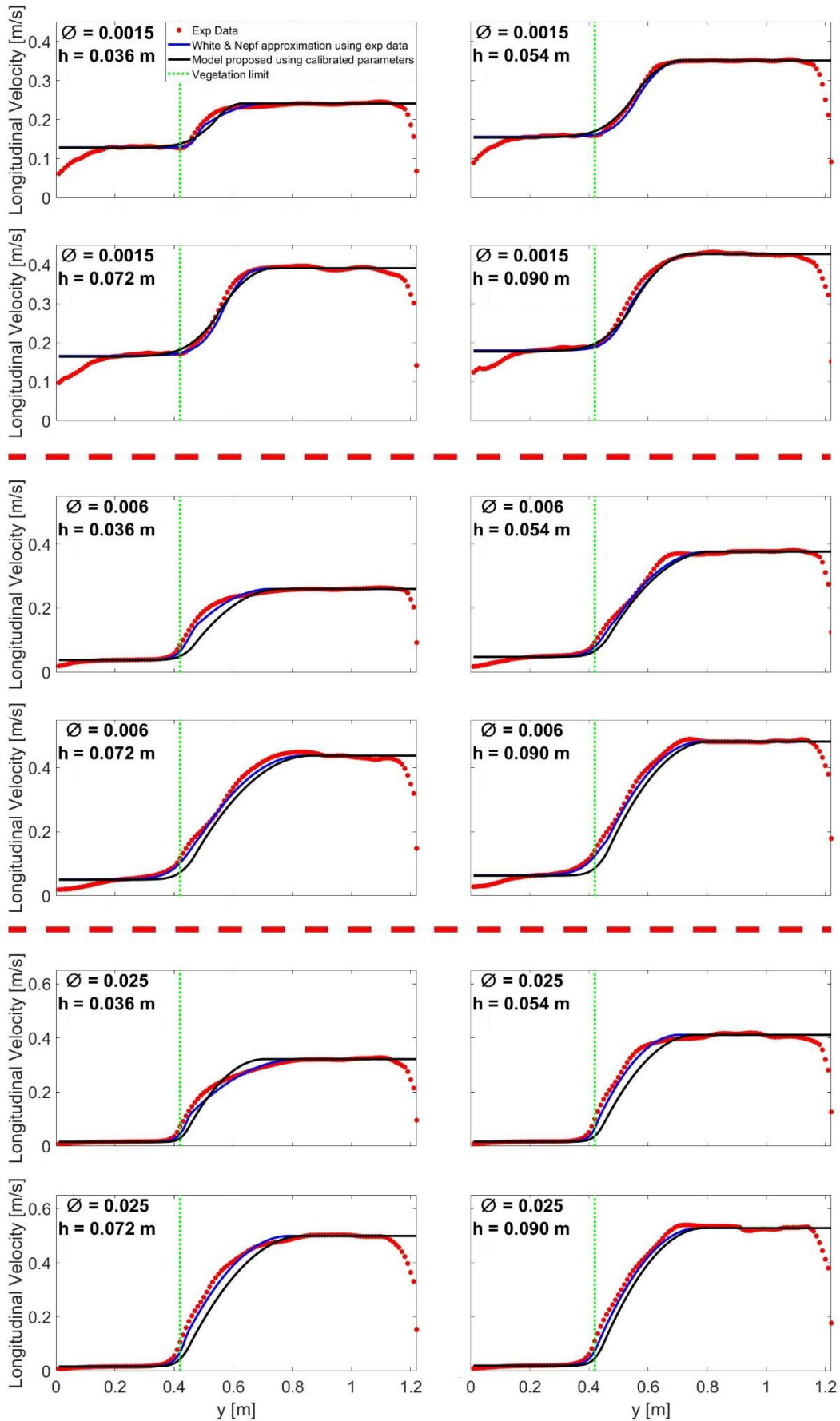
Figure 6.18. Fitted experimental data using **White and Nepf (2008)** approximation and model proposed.

Santiago Rojas Arques
Department of Civil and Structural Engineering

Table 6.9 shows Pearson correlation values between the experimental data and both models. Values for the model proposed here are similar to values using the **White and Nepf (2008)** relationship, which suggests that this new approach is a suitable model to predict transverse profiles of longitudinal flow velocity in partially vegetated layers. This proposed model only requires the vegetation density and both longitudinal velocity within vegetation and free flow velocity, in contrast with expression proposed by **White and Nepf (2008)** where experimental data from inner and outer shear layer and both the velocity slip and the velocity at the inflection point (U_m and U_s) are required. In addition, free flow velocity can be approximated by Manning's equation and longitudinal velocity within vegetation can be calcualted from a force balance type equation introduced in **Section 2.2.3** if data is not available.

Table 6.9. Correlation values between experimental data and both **White and Nepf (2008)** approximation and new model proposed along the shear layer region.

Correlation R	$\emptyset = 0.0015$ White & Nepf	$\emptyset = 0.0015$ Model	$\emptyset = 0.006$ White & Nepf	$\emptyset = 0.006$ Model	$\emptyset = 0.025$ White & Nepf	$\emptyset = 0.025$ Model
$h = 0.036$ m	0.974	0.938	0.989	0.944	0.993	0.981
$h = 0.054$ m	0.995	0.999	0.996	0.993	0.994	0.971
$h = 0.072$ m	0.996	0.996	0.999	0.996	0.996	0.981
$h = 0.090$ m	0.996	0.992	0.999	0.994	0.999	0.993

For experiments presented in this thesis, surface 2-D velocity data was recorded and the current model was proposed based on this data. Therefore, based on findings discussed in this section, the proposed model is presented to predict longitudinal surface velocity in shallow water flows, where flow structures is previously considered as a 2-D flow field and minimal differences are expected. Note that these relationships were obtained from flows with artificial, idealized cylinders to represent vegetation. Although the use of these type of stems has been widely used in previous researchers (**Nepf, 1999, Stone and Shen, 2002, De Serio et al., 2018**) to simplify the complexities of real vegetation, it is important to highlight that some differences may be expected for results obtained from real vegetation. This model represents a simple approach to a complex problem, and thus future researches may compare the results estimated by this model with velocity distributions recorded in real partly vegetated flows.

6.2.2. Solute Transport Results

In these tests, vegetation installed along one bank produced a velocity gradient in the longitudinal velocity component over the transverse direction (illustrated in **Section 6.2.1**). This velocity variation has shown in previous researches to induce a variability of mixing processes along the transverse direction (**Besio et al., 2012; West, 2016; West et al., 2020**); and therefore transverse mixing coefficient could not be considered constant as it was assumed non-vegetated conditions described in **Section 6.1**. (**Zeng, Y. et al, 2008; Sonnenwald, F. et al., 2019**).

To examine mixing processes under these conditions, ten continuous injections were recorded with the injector fixed at different positions (y_{Inj}) along the channel width to record mixing behaviour in different areas (see **Section 4.5.2**). Concentration maps were obtained in the same way as tests with no vegetation explained in **Section 5.6** and final concentration maps were obtained using Filter 5 as it was concluded in **Section 6.1.2.3**. **Figure 6.19** and **Figure 6.20** present data from three different injection positions for water depths $h = 0.036$ m and $h = 0.072$ m; and for the three different vegetation densities. In addition, the edge of the vegetated region is represented using white dots.

Santiago Rojas Arques
Department of Civil and Structural Engineering
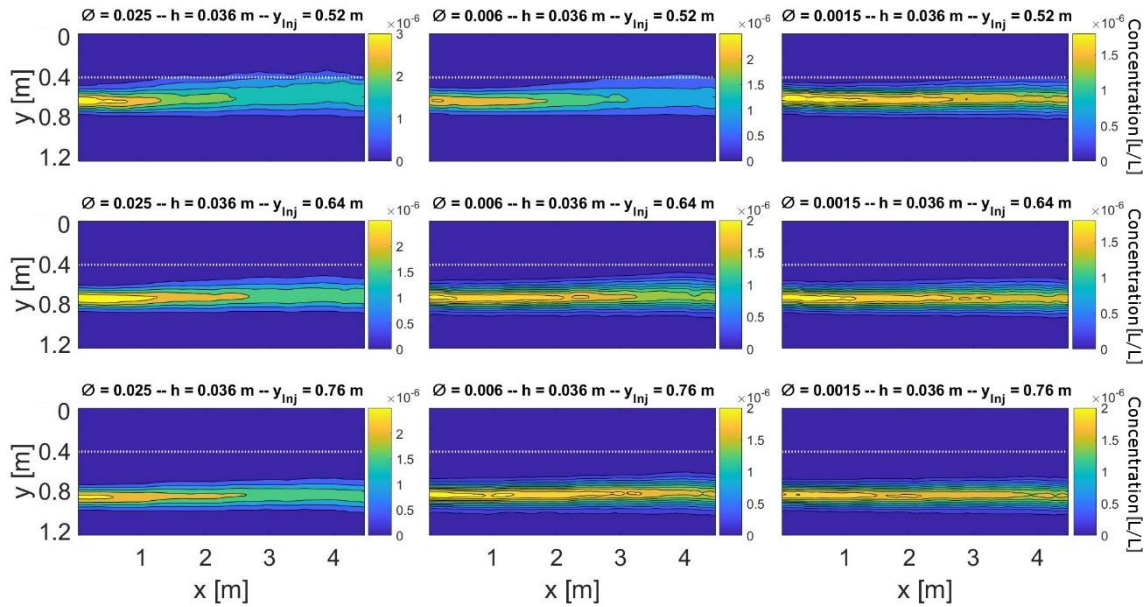
Figure 6.19. Concentration maps with vegetation at one side for water depth h=0.036 m.
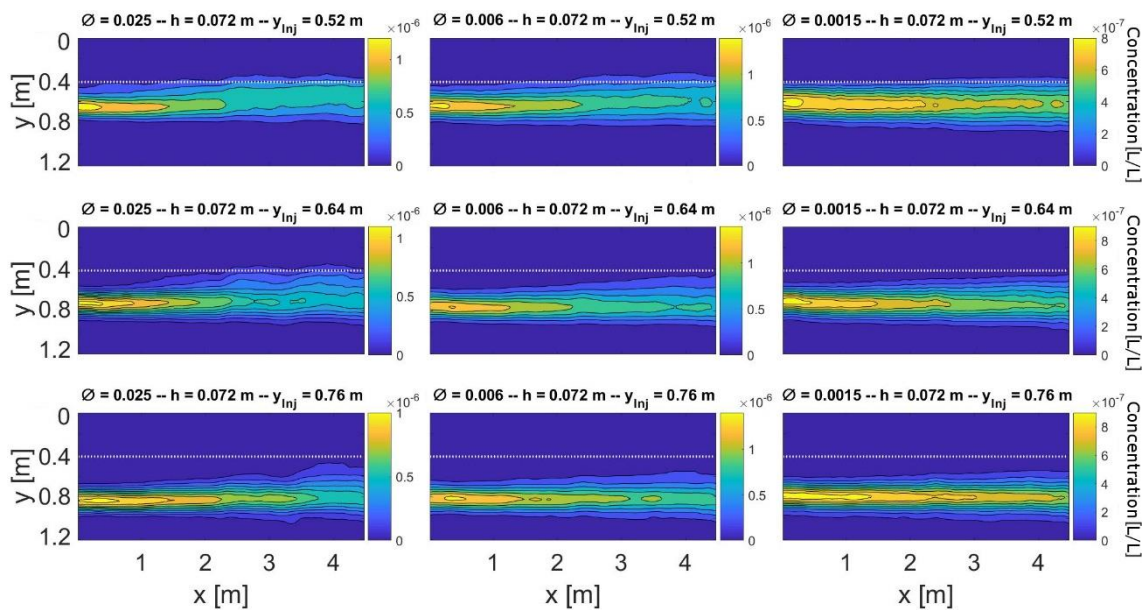
Figure 6.20. Concentration maps with vegetation at one side for water depth h=0.072 m.

Concentration maps recorded for $\emptyset = 0.025$ tests show an increase of mixing processes in the region close to vegetation. This effect looks more significant for higher flow depths. When vegetation density decreases, mixing close to vegetation also visibly decreases. All these considerations suggest a region close to the vegetation where an increase of transverse mixing is produced.

For these tests, the Finite Difference Model presented in **Section 6.1.2** was used to obtain variable transverse mixing coefficients over the width for each test. Previously the model was used considering a constant velocity and transverse mixing coefficient along the width. Now, variable longitudinal velocity and transverse mixing coefficient profiles were considered to represent processes in these tests. The longitudinal velocity profile predicted by the model introduced in **Section 6.2.1** were introduced into the Finite Difference Model as the velocity

Santiago Rojas Arques
Department of Civil and Structural Engineering

input. Potentially, by considering the resolution of the experimental data, different mixing coefficients over the width could be determined by the model (corresponding to each single velocity cell). However, solving the F.D.M. equation at this resolution would mean a significant and unfeasible processing time.

Based on previous research discussed in **Section 2.6**, a fixed shape for the variable transverse mixing coefficient profile was considered. Therefore, only parameters that defined the transverse mixing coefficient shapes were optimised, reducing the number of optimised variables needed. A similar skewed Gaussian shaped as obtained in **Sonnenwald et al. (2019)** and in **West et al. (2020)** was proposed to optimised transverse mixing coefficients (**eq. 6.19** and **eq. 6.20**). This Gaussian connected two constant mixing values produced within the vegetation ($D_{y_{veg}}$) and in the free open channel flow region ($D_{y_{free}}$). As shown in **Figure 6.21**, only 6 variables, including constant transverse mixing values within vegetation ($D_{y_{veg}}$) and in the open free flow ($D_{y_{free}}$), were needed to define the proposed variable mixing profile, where $D_{y_{max}}$ is the maximum transverse mixing coefficient value and y_{max} its position; and σ_1^2 and σ_2^2 are the variance of both parts of the function.

$$D_y(y) = D_{y_{max}} \exp\left(\frac{-(y - Y_{max})^2}{2\sigma_1^2}\right) \quad for \quad y \leq y_{max} \qquad eq.\,6.19$$

$$D_y(y) = D_{y_{max}} \exp\left(\frac{-(y - Y_{max})^2}{2\sigma_2^2}\right) \quad for \quad y \geq y_{max} \qquad eq.\,6.20$$
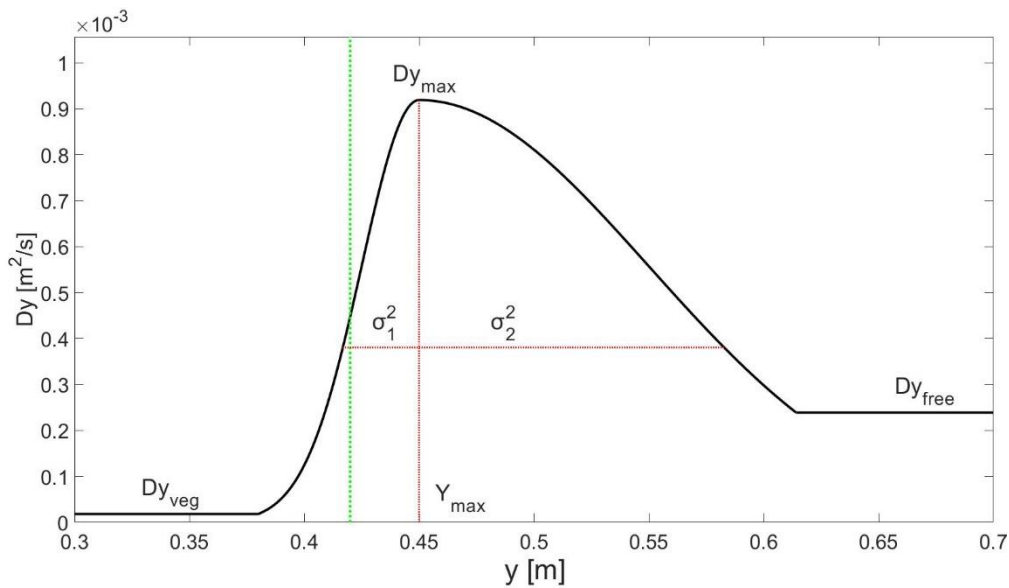
Figure 6.21. Scheme of skewed Gaussian function of transverse mixing coefficient.

Experimental data obtained by **White and Nepf (2008)** were analysed to study how the longitudinal velocity gradient and the Reynold stress distribution are related. Velocity gradients were obtained from experimental longitudinal velocity profiles obtained by **White and Nepf (2008)** and are represented in **Figure 6.22** as blue dots. In addition, Reynolds stress distributions recorded by them under the same flow conditions were plotted as red dots. Both profiles were normalised by their corresponding maximum value to match both scales.

Santiago Rojas Arques
Department of Civil and Structural Engineering
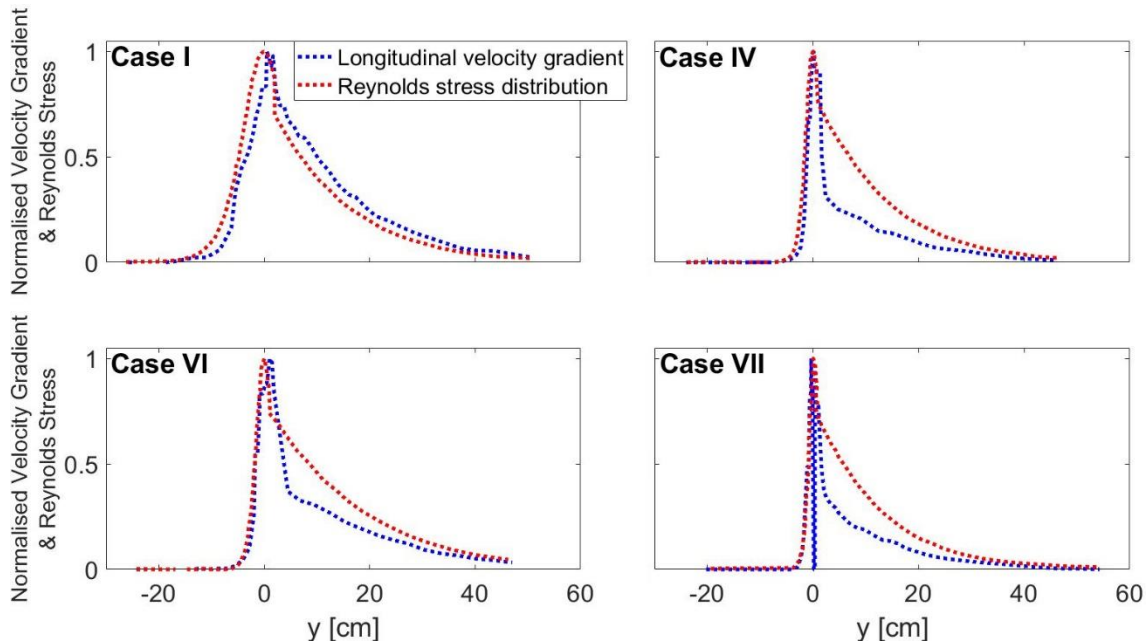
Figure 6.22. Gradients in longitudinal velocity over the channel width (ΔU/Δy) and Reynolds stress distribution from **White and Nepf (2008)**.

Results from **White and Nepf (2008)** plotted in **Figure 6.22** show that the position of the peak in Reynolds stress closely matches with the inflection point of longitudinal velocity profiles. In addition, both Reynolds stress distribution and longitudinal velocity gradient are elevated within the same region of the channel. Therefore, if the position where the maximum transverse mixing coefficient is produced (Y_{max}) matches with the position of maximum Reynolds stress (**Ghisalberti and Nepf, 2005**), hence it can be assumed that this position also matches with the position of the inflection point (y_0) of the longitudinal velocity profile. In addition, if the increase of transverse mixing is related with the increase of the Reynolds stress (**Guymer and Spence, 2009**), it can be assumed that the region with a variable transverse mixing coefficient matches with the shear layer region. This assumption was also previously proposed by **West (2016)** for partially vegetated flows.

Based on these previous results, some assumptions were made to reduce the number of unknown variables:

I. Constant mixing coefficients obtained in **Section 6.1** using F.D.M. were considered in these tests as $D_{y_{free}}$ to describe mixing coefficients in the free flow region.

II. Constant mixing coefficient within vegetation layer was obtained using **Nepf (2012)** proposed expression $D_{y_{veg}}(Ud)^{-1} = 0.2$ when $\emptyset < 0.1$. Whilst previous research showed variability of transverse mixing coefficient predictions within vegetated flows (**Sonnenwald, F et al., 2017; Tanino and Nepf, 2008a; Serra et al, 2004; Nepf et al, 1997**). The model prediction proposed in this section is focused on the shear layer region outside vegetation and it is therefore expected that concentration profiles will be reasonably insensitive to this value for the test reported here.

III. The region with a variable transverse mixing coefficient was considered to match with the shear layer region. This shear layer was defined based on the relationships and assumptions discussed in **eq. 6.7** and **eq. 6.8**.

- 123 -

IV.   The position of maximum transverse mixing coefficient was assumed to correspond with the inflection point of longitudinal flow velocity profile, where maximum Reynolds stress is produced. This inflection point was estimated using the proposed relationship in **eq. 6.6.**

With assumptions III and IV both variances can be obtained for a given $D_{y_{max}}$:

$$\sigma_1 = \sqrt{\frac{-(y_{Inner} - y_0)^2}{2 \ln\left(D_{y_{veg}}\Big/D_{y_{max}}\right)}} \qquad\qquad eq.\,6.21$$

$$\sigma_2 = \sqrt{\frac{-(y_{Outer} - y_0)^2}{2 \ln\left(D_{y_{free}}\Big/D_{y_{max}}\right)}} \qquad\qquad eq.\,6.22$$

Where y_{Inner} and y_{Outer} are the position where longitudinal velocity become constant within vegetation patch and in the free open flow region respectively. These points were calculated based on the position of the inflection point (**eq. 6.6**), and the length of each part of the shear layer (**eq. 6.7** and **eq. 6.8**). With these assumptions, the problem can be simplified into a one variable optimization ($D_{y_{max}}$).

The same optimization routine as described in **Section 6.1.2** was applied to obtain the variable transverse mixing coefficient profiles that best reproduced experimental concentration data. As a first step, an optimization was performed for each vegetation density, water depth and injection position. For each case, a $D_{y_{max}}$ was optimised: the transverse mixing coefficient profile was obtained by applying **eq. 6.19** to **eq. 6.20** for a given $D_{y_{max}}$ and longitudinal velocity profile, the concentration map was generated using F.D.M. solution. Then, the objective function $1 - R$ resulting from the F.D.M. solution and the observed concentration map was obtained by considering the data recorded over the analysis area (i.e. 2D correlation). This process was performed until the objective function $1 - R$ was minimised. Similar to **Section 6.1.1.** and **6.1.2.**, the allowed $D_{y_{max}}$ values during the iterations were constrained between $D_{y_{free}} - 1$ for each flow condition to avoid any problem with the proposed expressions. As a result, an optimised $D_{y_{max}}$, and its corresponding transversal mixing coefficient profiles was obtained for each vegetation density, water depth and injector position (so ten different results were obtained for the same flow condition).

Figure 6.23 shows a scheme of this optimization routine, where for a given $D_{y_{max}}$ value (called as "$D_{y_{max}}\ Guess$" in the scheme) generates a concentration map (called as "$Predicted\ Conc\ Map$"). This predicted concentration map is compared against the observed one ("$Exp\ Conc\ Map$") and the objective function $1 - R$ is obtained. This process is performed until the objective function is minimised, obtaining an optimised $D_{y_{max}}$ value and the corresponding predicted concentration map generated by the optimised $D_{y_{max}}$ ("$D_{y_{max}}\ Opt$" and "$Optimised\ Conc\ Map$" respectively) for each injection. **Figure 6.25** shows the variation in optimised $D_{y_{max}}$ results for the same test configuration but different injection positions (blue dots), for the vegetation density $\emptyset = 0.025$ and each water depth. This variability is produced because for each case the mixing characteristics for the full channel width cannot be obtained as the dye only spreads over a section of the channel. Hence, a general visualization of global

Santiago Rojas Arques
Department of Civil and Structural Engineering

transverse mixing processes cannot be obtained using individual concentration maps produced from each test.

In order to reduce variability and to obtain a unique $D_{y_{max}}$ value for each water depth and vegetation density, all different injections for the same test configuration were analysed and introduced into the model to obtain one single transverse mixing profile as shown **Figure 6.24**. In this case, a unique $D_{y_{max}}$ value generates the predicted concentration maps for each injection for a given water depth and vegetation density, obtaining 10 predicted concentration maps with a dimension of 122×448 pixels. Then, all predicted concentration maps are merged into one matrix, with a dimension of 1220×448 pixels. In addition, the corresponding 10 observed concentration maps are merged in the same way, obtaining an observed concentration matrix of 1220×448 pixels. Then, the objective function $1 - R$ is calculated, but now R is the Pearson correlation obtained between these two combined matrices. This process is performed until the objective function $1 - R$ is minimised. Resulting from this optimization routine, a unique optimised $D_{y_{max}}$ value is obtained for each water depth and vegetation density, which represents a general transverse mixing process behaviour affecting all different injection cases (represented in **Figure 6.25** as the black line).
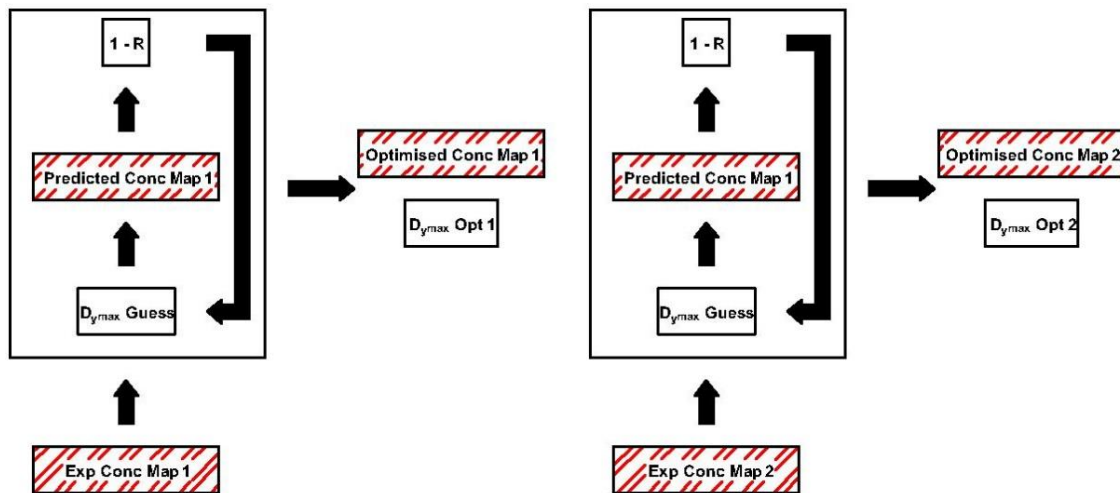
Figure 6.23. Scheme of optimization routine using each concentration map individually.

Santiago Rojas Arques
Department of Civil and Structural Engineering
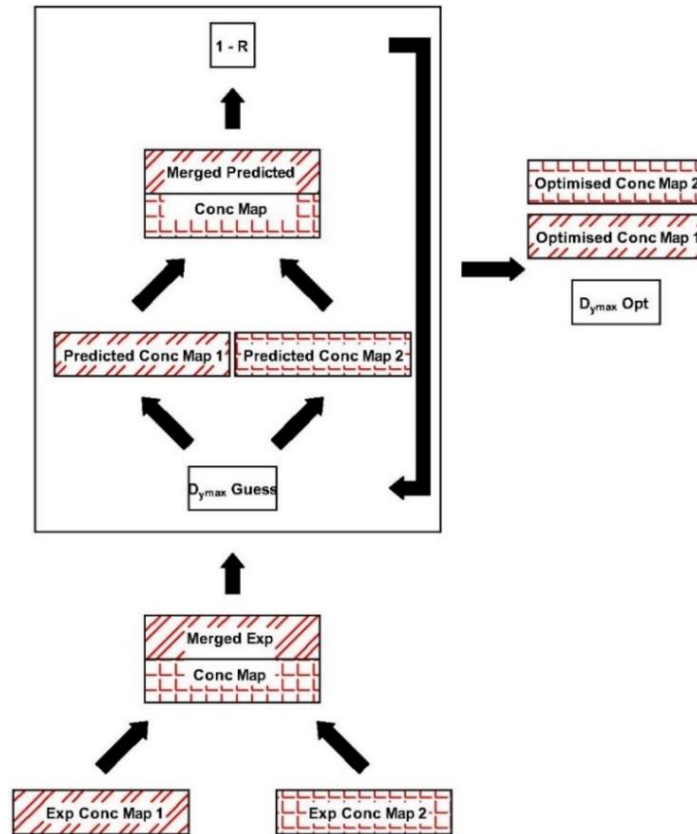
Figure 6.24. Scheme of optimization routine using all concentration maps together.
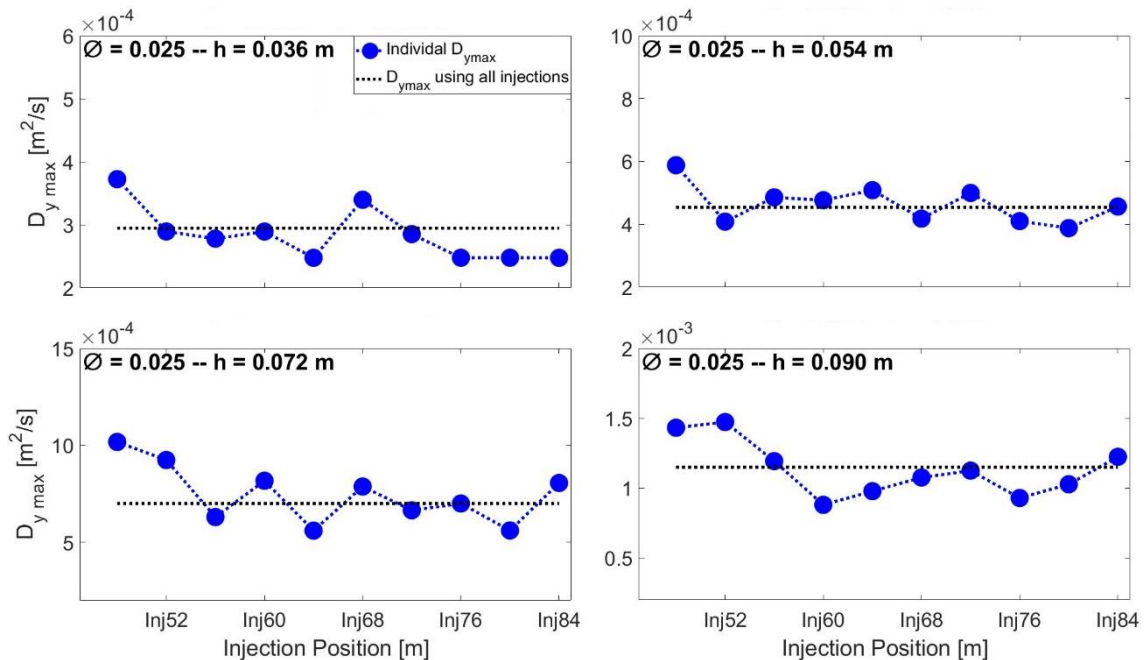
Figure 6.25. Comparison of $D_{y_{max}}$ using individual concentration maps for $\emptyset = 0.025$.

The correlations between each concentration map and those produced by the optimization routine, which optimised all injection tests together (i.e. producing a single $D_{y_{max}}$ for each condition), are plotted in **Figure 6.26** (circles). In addition, the correlation between all experimental and optimised concentration maps that was used as objective function during the

Santiago Rojas Arques
Department of Civil and Structural Engineering

optimization routine $(1 - R)$ are plotted for each water depth and vegetation density (diamonds). **Figure 6.26** shows high correlations obtained for each pair of concentration maps, being higher for the lowest water depths. However, lower correlations were obtained for those injections close to the vegetated boundary, this decrease is more appreciated for denser vegetation.

In addition, **Figure 6.27, Figure 6.28** and **Figure 6.29** show comparisons between experimental concentration profiles and those obtained by the optimization routine for same water depth and vegetation density ($h = 0.054\,\text{m} - \emptyset = 0.006$) but for different injection positions. These optimised profiles were obtained by using the routine explained in **Figure 6.24**.
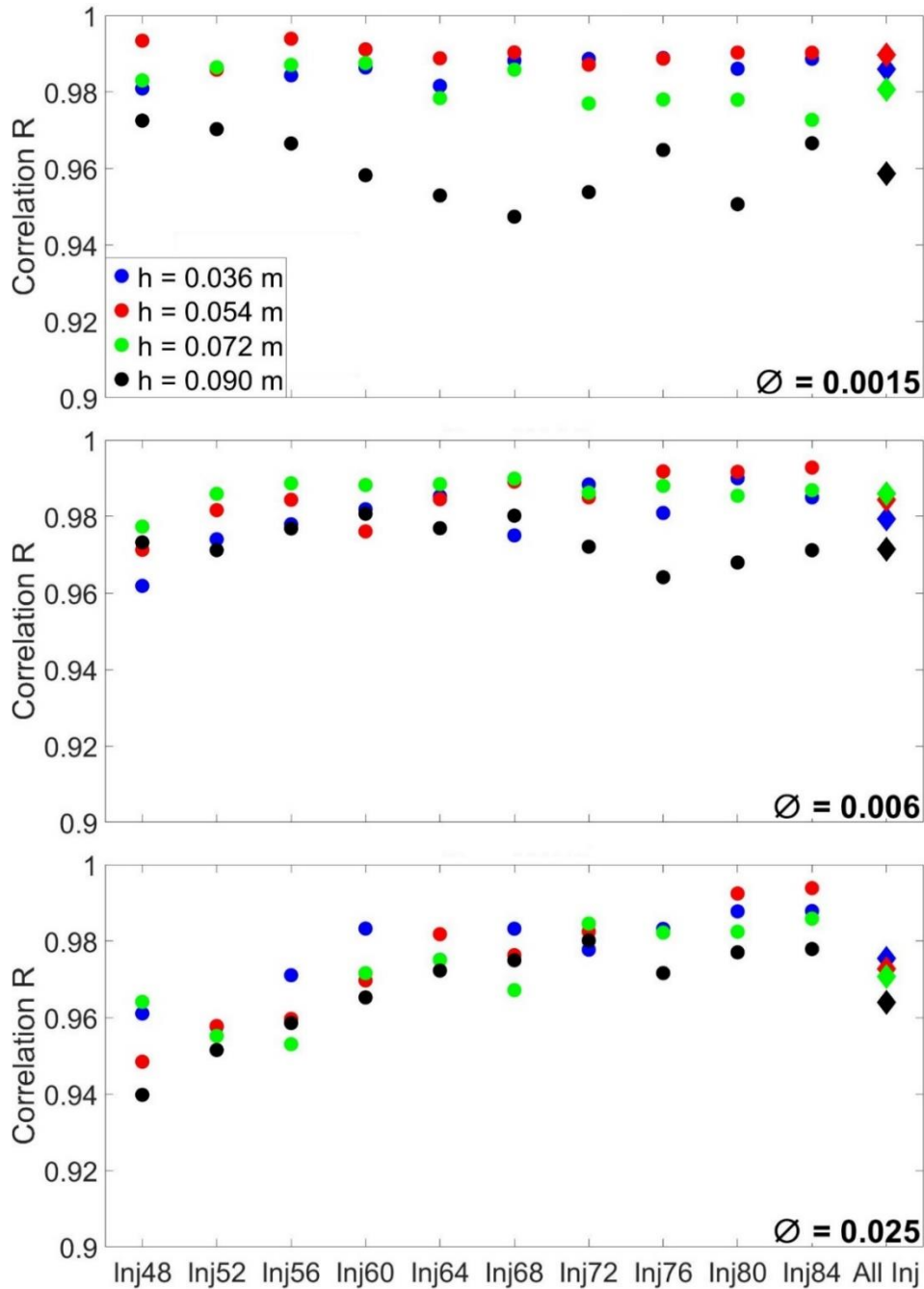
Figure 6.26. 2D correlations between experimental concentration maps and those obtained by the optimization routine based on a single $D_{y_{max}}$ for each flow and vegetation condition.

Santiago Rojas Arques
Department of Civil and Structural Engineering
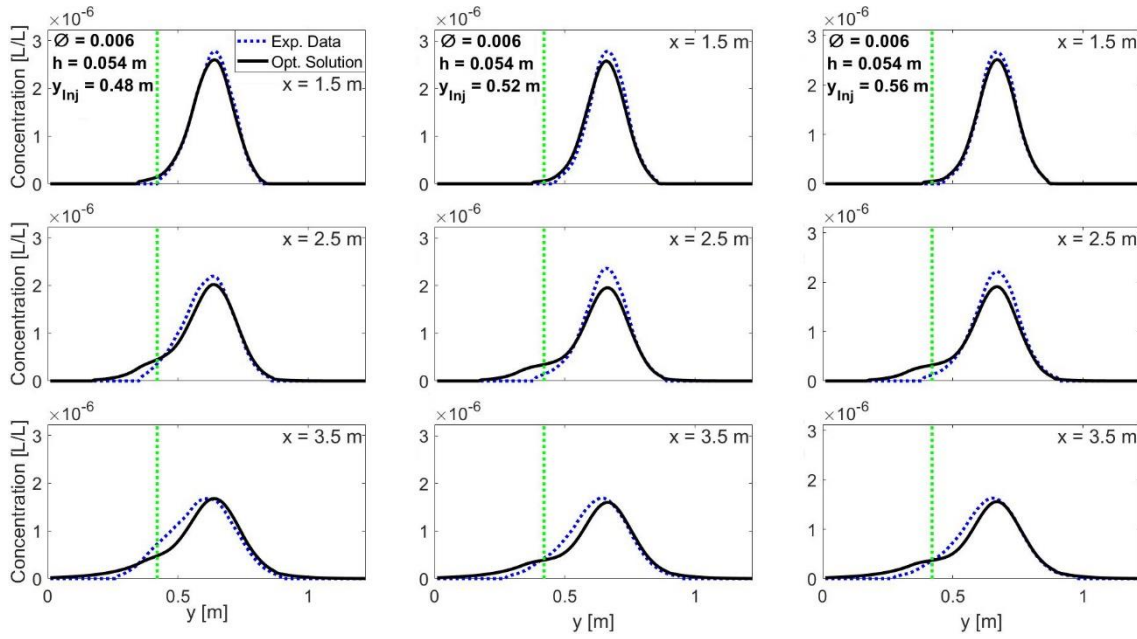
Figure 6.27. Comparison between experimental and optimised concentration profiles for tests $h = 0.054$ m – $\emptyset = 0.006$ from injection $y_{Inj} = 0.48$ m to injection $y_{Inj} = 0.56$ m .
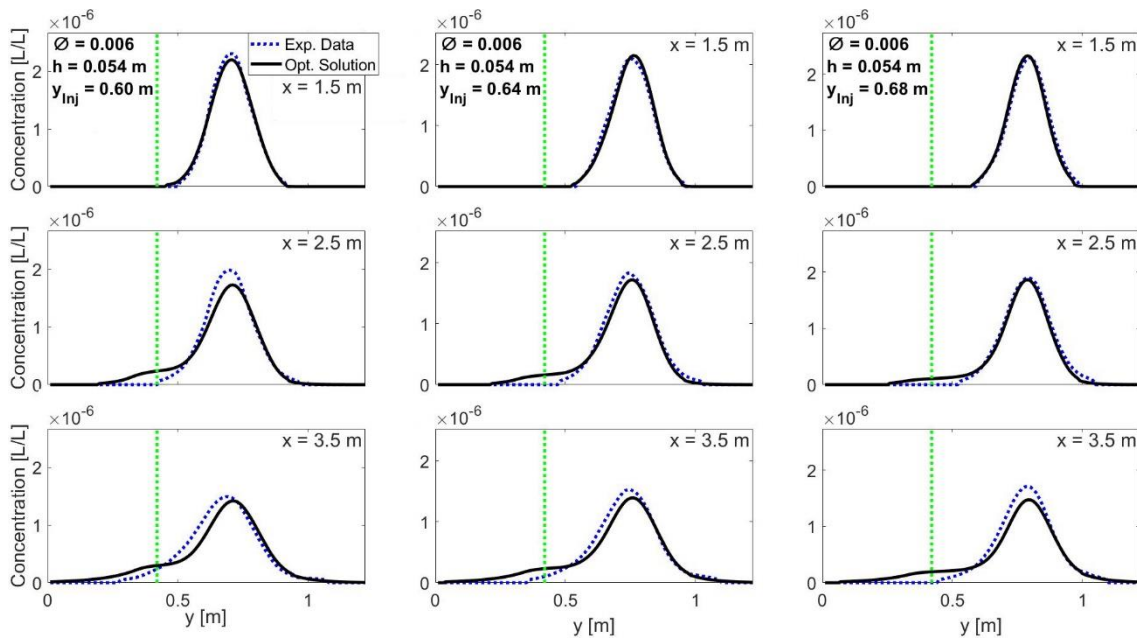
Figure 6.28. Comparison between experimental and optimised concentration profiles for tests $h = 0.054$ m – $\emptyset = 0.006$ from injection $y_{Inj} = 0.60$ m to injection $y_{Inj} = 0.68$ m.

Santiago Rojas Arques
Department of Civil and Structural Engineering
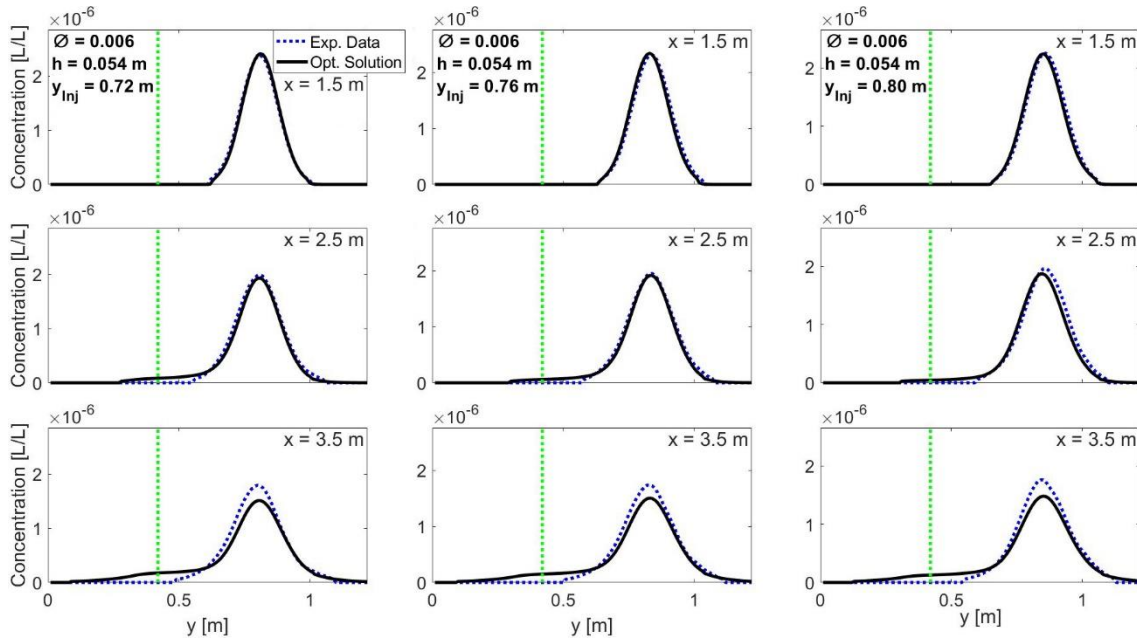
Figure 6.29. Comparison between experimental and optimised concentration profiles for tests $h = 0.054$ m – $\emptyset = 0.006$ from injection $y_{Inj} = 0.72$ m to injection $y_{Inj} = 0.80$ m .

Figure 6.27, **Figure 6.28** and **Figure 6.29** show a comparison between concentration profiles of both experimental and optimised results for same water depth and vegetation density but different injection positions. These optimised profiles were obtained by using the optimization routine that analyses all concentration maps together for a given flow condition (**Figure 6.24**). Results suggest an overall close match between experimental and optimised concentration profiles for all different injections within the spanwise position. Some mismatching is found for those injections located close the vegetated boundary. For these cases, the mean concentration mass of experimental data looks to be displaced to the vegetated boundary and the optimization fails to predict this behaviour. This agrees with the diminution of the correlations plotted in **Figure 6.26.** However, both correlations and visual comparison between experimental and optimised concentration results suggest a good fit.

Optimal transverse mixing coefficient profiles generated by the F.D.M. considering at the same time all different injection positions for each test configuration were plotted in **Figure 6.30** and optimised $D_{y_{max}}$ values are shown in **Table 6.10.**

Santiago Rojas Arques
Department of Civil and Structural Engineering
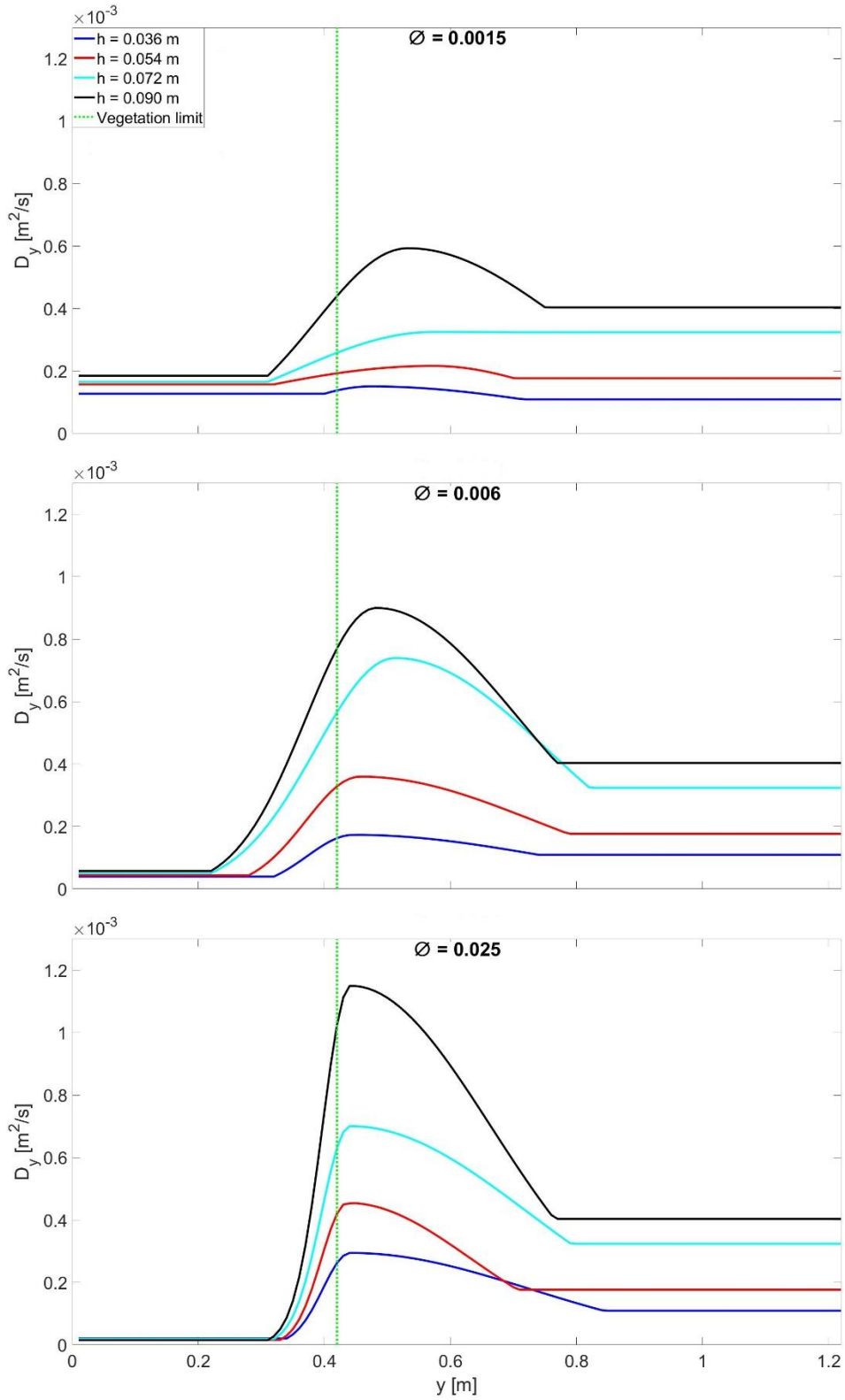
Figure 6.30. Variable transverse mixing coefficients resulting from optimization.

Santiago Rojas Arques
Department of Civil and Structural Engineering

Table 6.10. Maximum transverse mixing coefficient solutions.

a [1/m]	h[m]	U_{free} [m/s]	U_{veg} [m/s]	ΔU [m/s]	$D_{y_{free}}$ [m^2/s]	$D_{y_{veg}}$ [m^2/s]	$D_{y_{max}}$ [m^2/s]
0.397	0.036	0.241	0.129	0.112	$1.056\ 10^{-4}$	$1.290\ 10^{-4}$	$1.506\ 10^{-4}$
0.3967	0.054	0.351	0.156	0.195	$1.771\ 10^{-4}$	$1.560\ 10^{-4}$	$2.163\ 10^{-4}$
0.396	0.072	0.391	0.166	0.225	$3.361\ 10^{-4}$	$1.662\ 10^{-4}$	$3.361\ 10^{-4}$
0.3967	0.090	0.427	0.180	0.247	$4.049\ 10^{-4}$	$1.797\ 10^{-4}$	$5.931\ 10^{-4}$
1.587	0.036	0.261	0.038	0.223	$1.056\ 10^{-4}$	$3.841\ 10^{-5}$	$2.243\ 10^{-4}$
1.587	0.054	0.377	0.048	0.329	$1.771\ 10^{-4}$	$4.844\ 10^{-5}$	$3.691\ 10^{-4}$
1.587	0.072	0.438	0.051	0.387	$3.361\ 10^{-4}$	$5.089\ 10^{-5}$	$6.359\ 10^{-4}$
1.587	0.090	0.482	0.064	0.418	$4.049\ 10^{-4}$	$6.354\ 10^{-5}$	$8.894\ 10^{-4}$
6.349	0.036	0.322	0.016	0.306	$1.056\ 10^{-4}$	$1.595\ 10^{-5}$	$2.945\ 10^{-4}$
6.349	0.054	0.412	0.017	0.395	$1.771\ 10^{-4}$	$1.698\ 10^{-5}$	$4.538\ 10^{-4}$
6.349	0.072	0.500	0.017	0.483	$3.361\ 10^{-4}$	$1.700\ 10^{-5}$	$7.005\ 10^{-4}$
6.349	0.090	0.529	0.020	0.509	$4.049\ 10^{-4}$	$2.020\ 10^{-5}$	$1.150\ 10^{-3}$

Figure 6.30 shows an increase of maximum transverse mixing coefficient when water depth increases for the same vegetation density. In addition, a consistent dependence between $D_{y_{max}}$ and longitudinal velocity difference ΔU is observed in **Figure 6.31**. This relationship agrees with results obtained by **Ghisalberti and Nepf (2005)**, whose experimental results suggest the relationship $D_{z_{max}} \approx 0.3\ \Delta U \delta_{V.S.L.}$
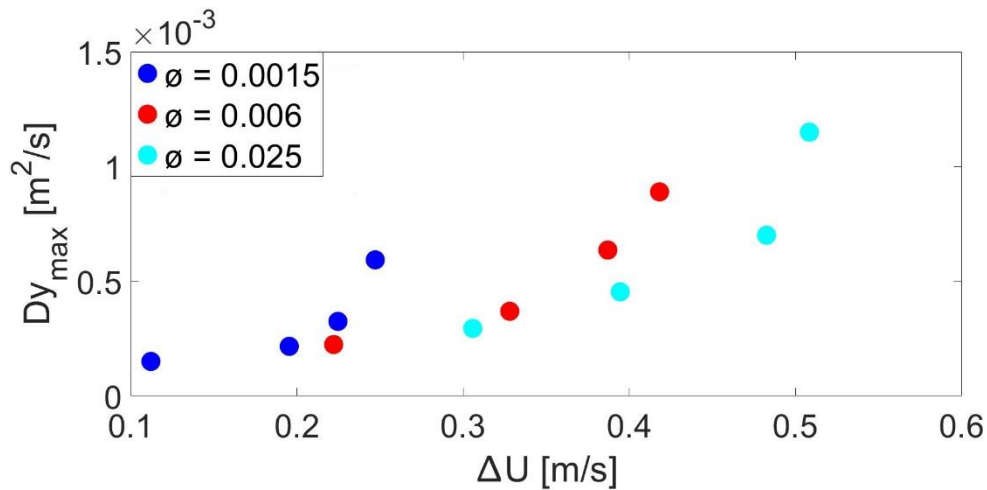
Figure 6.31. Relationship between maximum transverse mixing coefficient and longitudinal velocity difference.

Based on the previous relationship proposed by **Ghisalberti and Nepf (2005)**, the relationship between the maximum transverse mixing coefficient $D_{y_{max}}$ and the product of the longitudinal velocity difference ΔU and the total length of the shear layer ($\delta_{Outer} + \delta_{Inner}$) was studied as shown **Figure 6.32** (right). In addition, **Figure 6.32** (left) shows the relationship between $D_{y_{max}}$ and the product of ΔU and the vegetation density a.

Santiago Rojas Arques
Department of Civil and Structural Engineering
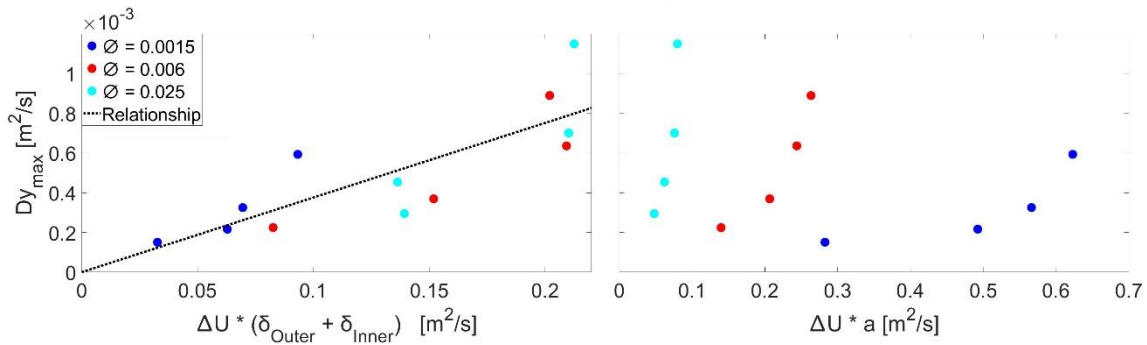
Figure 6.32. Relationship between maximum transverse mixing coefficient and the product of velocity difference and the shear layer length (right), and the product of velocity difference and vegetation density (left).

A relationship of $D_{y_{max}} = 0.038 \, \Delta U (\delta_{Outer} + \delta_{Inner})$ was found for the data shown in **Figure 6.32** (right). However, a low Pearson correlation was obtained for this relationship ($R = 0.81$). Moreover, a lack of any clear relationship was found for data plotted in **Figure 6.32** (left). In addition, an empirical relationship between maximum transverse mixing coefficient and velocity difference (ΔU) and water depth was also studied. This approach is similar to that proposed previously by **Ghisalberti and Nepf (2005)** for vertical mixing within vertical aligned shear layers in submerged vegetated flows. A linear relationship was proposed with these two parameters and the water depth as **Figure 6.33** shows, obtaining a higher Pearson correlation ($R = 0.9810$).

$$D_{y_{max}} = 0.02329 \, (\Delta U \, h) \qquad\qquad eq. 6.23$$
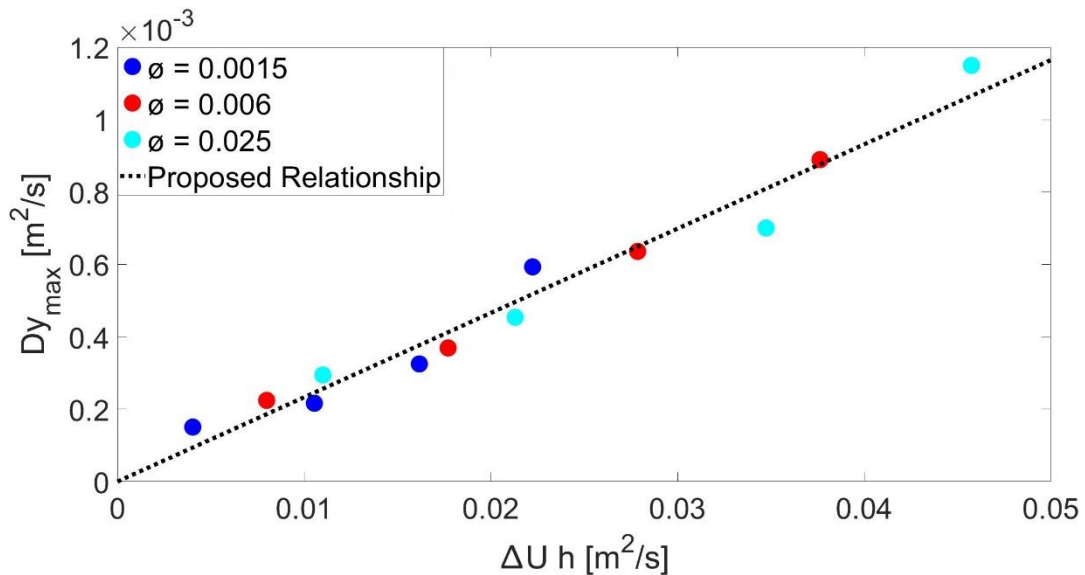
Figure 6.33. Relationship between maximum transverse mixing coefficient and the product of velocity difference and water depth.

Finally, the relationship proposed in **eq. 6.23** and expression introduced in **Section 6.2.1** were applied to predict concentration profiles based on the F.D.M. with $D_{y_{max}}$ given by **eq. 6.23** and the variables defined in the equations listed in the chapter (**eq. 6.19** and **eq. 6.20**), with the assumptions proposed in **eq. 6.21** and **eq. 6.22.** Results were compared with experimental data and plotted in **Figure 6.34** and **Figure 6.35**.

- 132 -
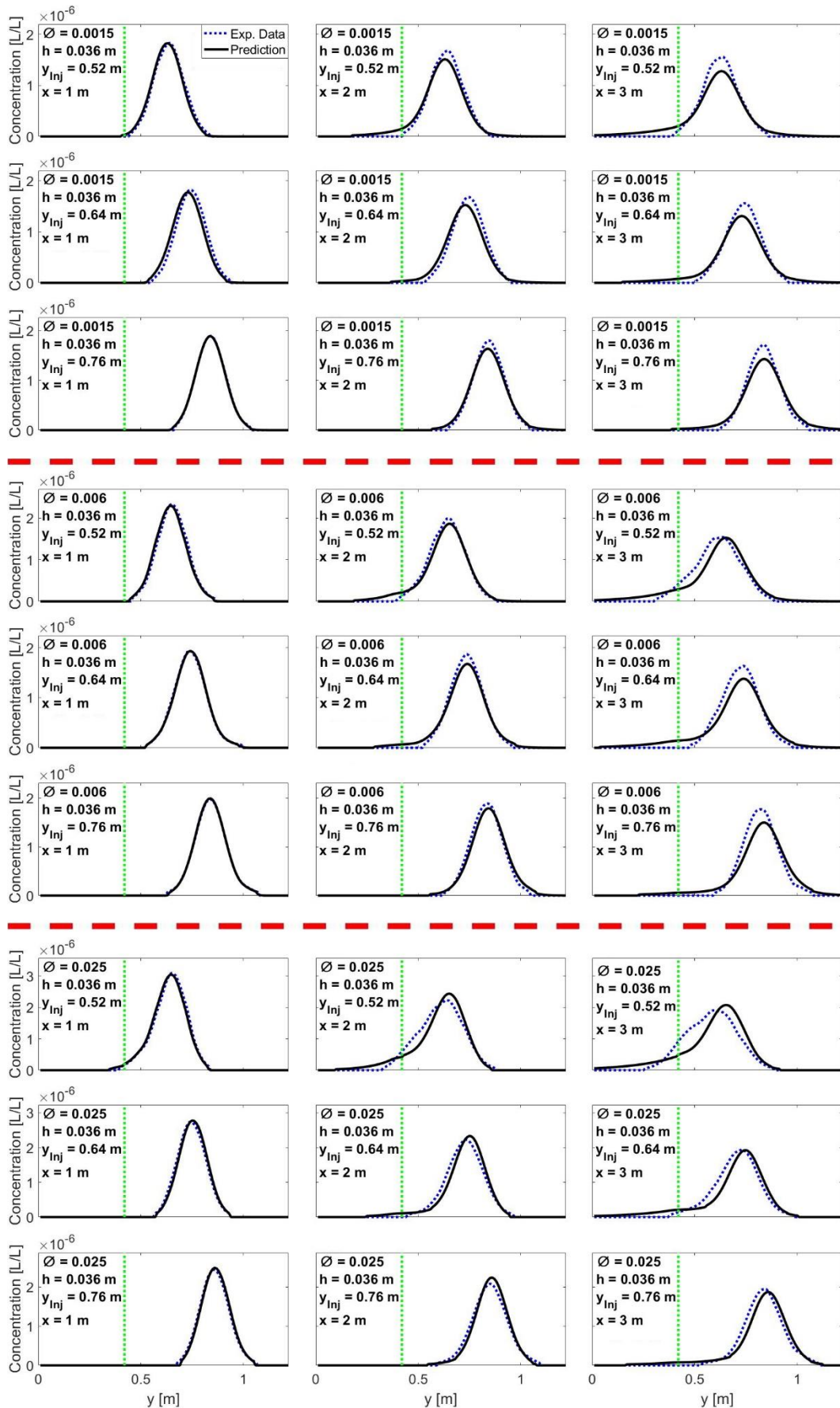
Figure 6.34. Comparison between experimental concentration profiles and predictions for h = 0.036 m.

Santiago Rojas Arques
Department of Civil and Structural Engineering
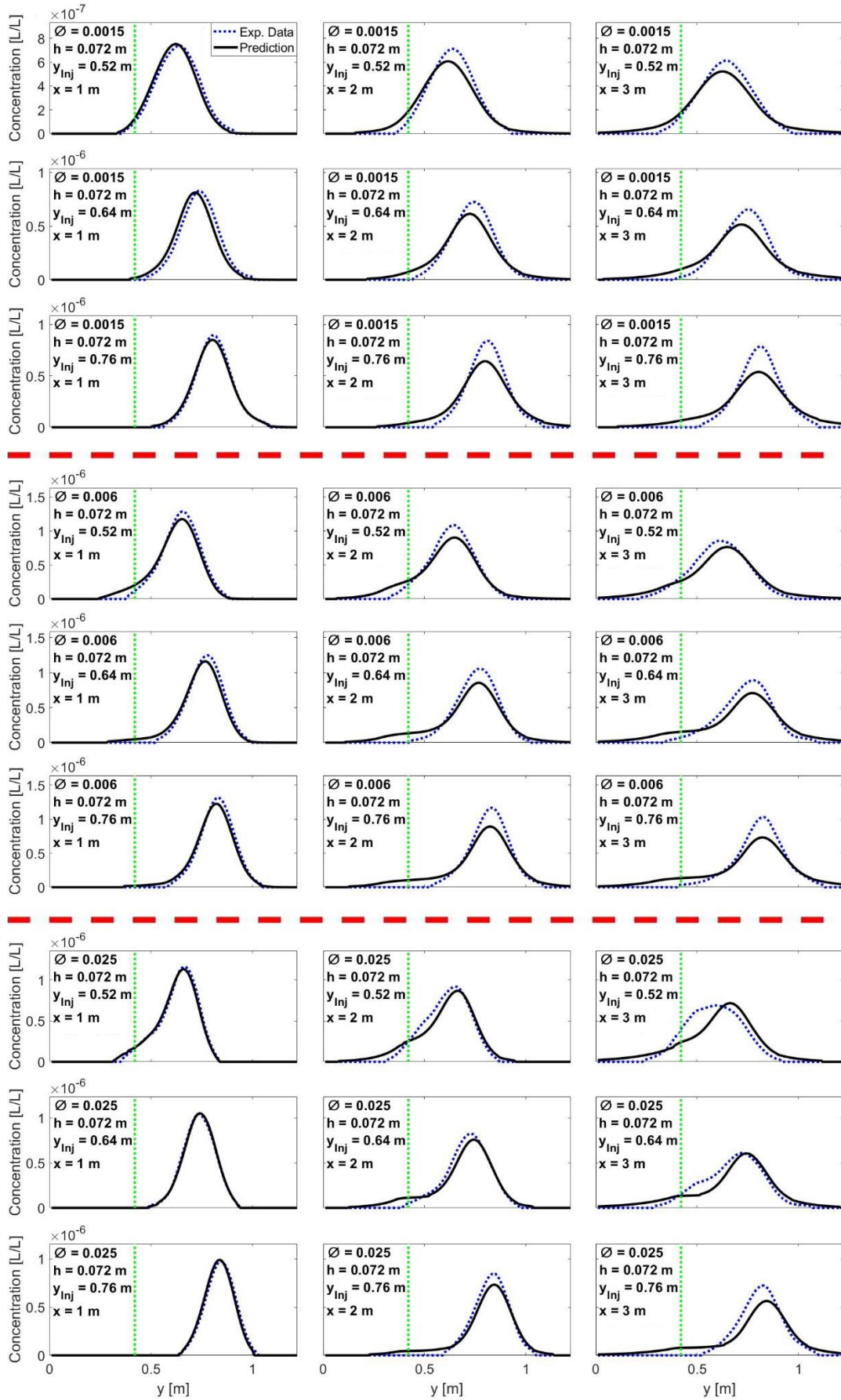
Figure 6.35. Comparison between experimental concentration profiles and predictions for h = 0.072 m.

Santiago Rojas Arques
Department of Civil and Structural Engineering

Figure 6.34 and **Figure 6.35** show concentration profiles from experimental and predicted data by the relationships proposed in **Section 6.2.1** and **Section 6.2.2.** Most of plots suggest a good fit between experimental data and predictions but $\emptyset = 0.025$ profiles show a movement of the main body of profiles of $y_{Inj} = 0.52$ m to the vegetation that the model cannot predict. This displacement is probably produced by secondary currents along the water depth generated by the velocity gradient. This transversal component would produce a translation of the concentration mass to vegetation boundary. Comparison between different densities suggests that this movement of mass mostly affected the test with the densest vegetation ($\emptyset = 0.025$) and is reduced when vegetation density decreases. In addition, a higher effect is appreciated for higher depths, suggesting that this effect is dependent of velocity difference between vegetated patch and free open layer (ΔU).

Correlations between experimental data and predicted profiles were obtained considering only the region of the channel where there were concentration values present (i.e. in the region the dye was present). In addition, considering profiles were quasi-unimodal; absolute relative differences were calculated considering two regions defined as $\bar{C}_{x,y} \pm 1 * std(C_{x,y})$ and $\bar{C}_{x,y} \pm 2 * std(C_{x,y})$. These regions represents the 66 % and the 95 % of total values for a normal distribution, so in these tests would represent differences within the central profile section and within most of the profile respectively.

Table 6.11. Correlations and mean absolute relative differences between experimental data and predicted concentration profiles.

$\emptyset = 0.0015$	R	Rel. Diff. $[\bar{C}_{x,y} \pm 1 * std(C_{x,y})]$	Rel. Diff. $[\bar{C}_{x,y} \pm 2 * std(C_{x,y})]$
$h = 0.036$ m	0.987	11.79%	12.77%
$h = 0.054$ m	0.991	8.91%	13.11%
$h = 0.072$ m	0.982	14.19%	15.70%
$h = 0.090$ m	0.962	20.18%	20.24%

$\emptyset = 0.006$	R	Rel. Diff. $[\bar{C}_{x,y} \pm 1 * std(C_{x,y})]$	Rel. Diff. $[\bar{C}_{x,y} \pm 2 * std(C_{x,y})]$
$h = 0.036$ m	0.979	14.23%	17.31%
$h = 0.054$ m	0.983	12.94%	14.15%
$h = 0.072$ m	0.982	12.49%	14.33%
$h = 0.090$ m	0.970	15.81%	18.13%

$\emptyset = 0.025$	R	Rel. Diff. $[\bar{C}_{x,y} \pm 1 * std(C_{x,y})]$	Rel. Diff. $[\bar{C}_{x,y} \pm 2 * std(C_{x,y})]$
$h = 0.036$ m	0.974	13.87%	18.45%
$h = 0.054$ m	0.959	18.40%	21.77%
$h = 0.072$ m	0.971	14.81%	18.80%
$h = 0.090$ m	0.963	15.47%	21.07%

Results present in **Table 6.11** suggest a good fit between experimental concentration data and predicted profiles. In addition, results show a slightly increase of differences for $\emptyset = 0.025$ tests, which agrees with the extra displacement recorded for injections close vegetated bank discussed in **Figure 6.34** and **Figure 6.35**.

Santiago Rojas Arques
Department of Civil and Structural Engineering

6.3. Two Vegetated Banks Tests Results

Once the prediction of the longitudinal velocity shear layer produced by a vegetated bank was proposed in **Section 6.2,** as well as its effects on the variable transverse mixing profile, a last set of experiments were designed to compare the experimental data against those predictions obtained by the relationships proposed in **Section 6.2.1** and **Section 6.2.2.** For each test, both time-averaged concentration maps and longitudinal velocity data were obtained in the same way as previous experiments.

Tests described in **Section 4.5.3** were analysed using same techniques as described in **Section 5.1** and **Section 5.6** for velocity and concentration data respectively. In these tests, a vegetated bank was installed at each side of the channel and the free flow width between vegetated banks was changed to reproduce an overlapping shear layers resulting from the resistant from each bank.

First, the width of the vegetated banks was designed based on the inner layer lengths (δ_{Inner}) obtained in **Section 6.2.1** by designing a vegetated bank wide enough to allow the development of the inner layer. For one vegetated bank tests, a maximum $\delta_{Inner} = 0.14$ m was obtained (see **Table 6.7**). Based on these results, a vegetated bank width of 0.21 m was installed at each side for each water depth and vegetation density. Moreover, this width represents half of the width used in the previous set of experiments. Therefore, the same amount of vegetation as in previous Section was used, keeping a constant relationship between the water depth and the flow resistance as it was discussed in **Section 4.5.3**. In the same way, the designed width of the free layer between the vegetated banks was designed based on the lengths of outer layer (δ_{Outer}) obtained in **Section 6.2.1**. These tests were designed to reproduce an overlapping of both shear layers produced by each vegetated bank, thus a first free open flow width between both banks was designed as the double of the expected outer length. With this configuration, two full developed shear layers should be produced. Maximum outer layer lengths obtained in previous tests were $\delta_{Outer} = 0.38, 0.36, 0.39$ and 0.34 m for $h = 0.036, 0.054, 0.072$ and 0.090 m respectively (see **Table 6.6**). Based on these results, a first free open width between vegetated banks of $W_{Free} = 0.7$ m was considered.

For the following tests, the free open width between vegetated banks was reduced to reproduce overlapping between both shear layers. These experiments were designed to present a first approach to a scenario where the presence of vegetation at each side of the channel affects the development of the shear layer and its effect of the transverse mixing. Therefore, **Table 6.12** presented free open flow between vegetated banks used for experiments:

Table 6.12. Designed free open flow widths.

$Test$	W_{Free}
$W_{Free\,1}$	0.7 m
$W_{Free\,2}$	0.6 m
$W_{Free\,3}$	0.5 m
$W_{Free\,4}$	0.4 m
$W_{Free\,5}$	0.3 m

Santiago Rojas Arques
Department of Civil and Structural Engineering

6.3.1. Flow Resistance Validation

As explained in **Section 4.5.3,** vegetated bank widths remained constant for all different tests to not to significantly increase channel resistance. Therefore, plastic walls were installed just behind each vegetated bank to isolate central studied region as explained in **Section 4.5.3**. For each test, flow rate was measured as explained in **Section 4.2.1** and results were compared against flow rates obtained for the one vegetated bank tests as shown in **Figure 6.36**.
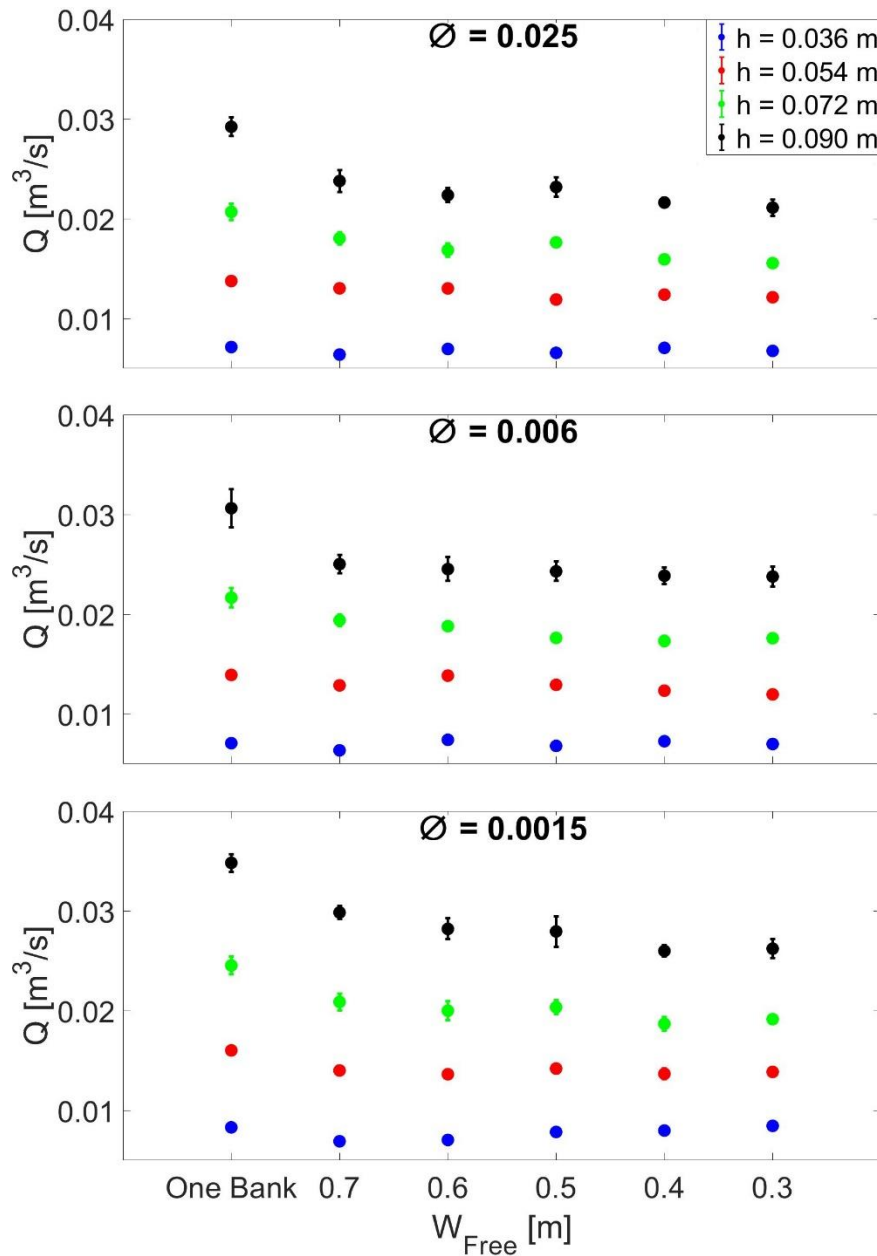
Figure 6.36. Measured flow rates for different W_{Free} and those measured for one vegetated bank tests.

The results plotted in **Figure 6.36** show that flow rates recorded for two vegetated bank tests are lower than those recorded for one vegetated bank tests, although same amount of vegetation was used. This decrease is more appreciable for higher flow depths. These differences may be produced because, although the same vegetated width is installed, for tests with two vegetated banks two shear layers are generated instead of one as in previous

- 137 -

experiments. Therefore, for tests with $W_{Free} = 0.7$ m, two shear layer zones are produced with similar lengths than those produced in previous experiments. As a result, a wider overall shear layer zone is obtained in these new tests, producing a lower overall longitudinal velocity and thus a lower flow rate. In addition, **Figure 6.36** shows a variation of flow rates for tests with the same vegetation density and water depth, but different W_{Free}, although these differences are lower than those appreciated between the one and two vegetated banks tests. These variations may be due to the interaction between the shear layers generated by each bank, producing a reconfiguration of the longitudinal velocity profiles.

6.3.2. Velocity Results

Time-averaged longitudinal velocity maps were obtained using the method explained in **Section 5.1.** Results regarding to $\emptyset = 0.025$ were plotted in **Figure 6.37** with vegetation edge also represented white dots and the area outside walls showed as a white region.
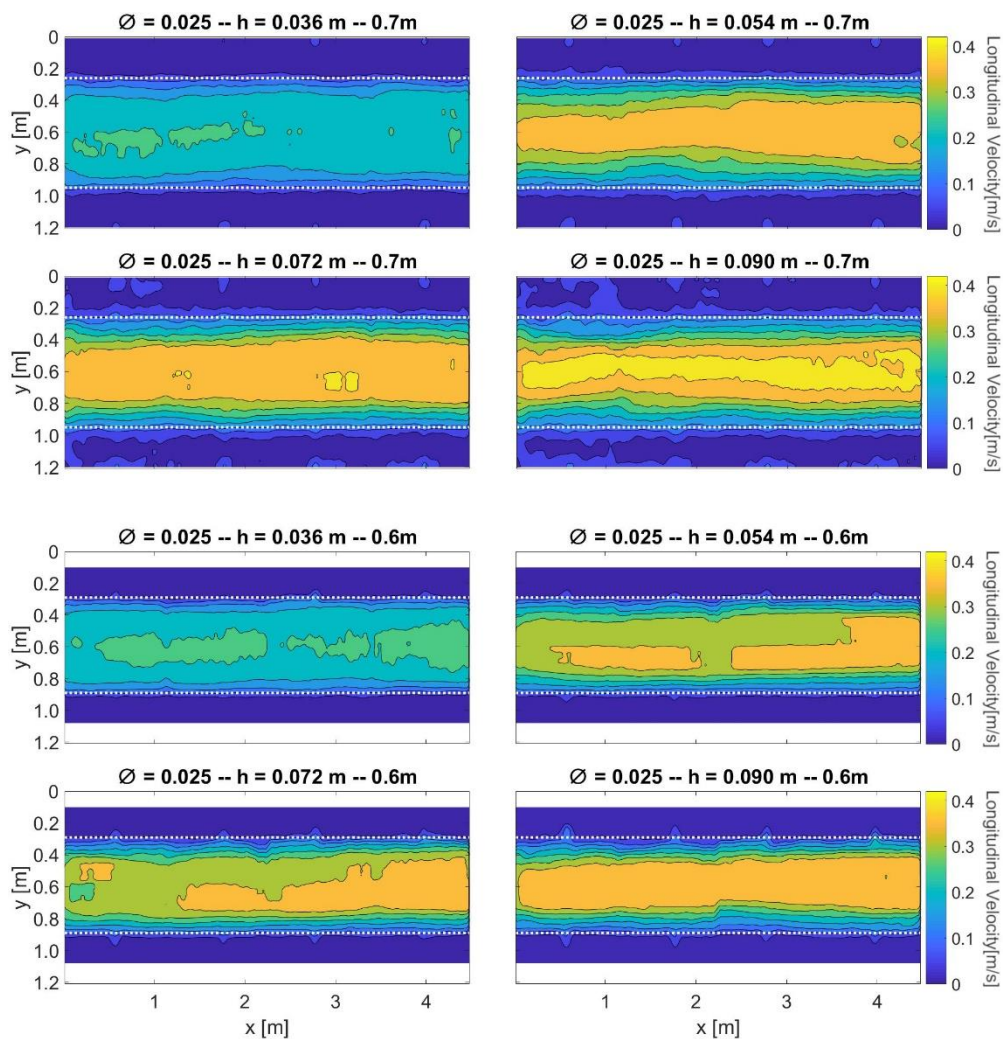
Figure 6.37 (a). Time-averaged longitudinal flow velocity maps for different both sides vegetation conditions for density $\emptyset = 0.025$ with vegetation edge as white dots.

Santiago Rojas Arques
Department of Civil and Structural Engineering
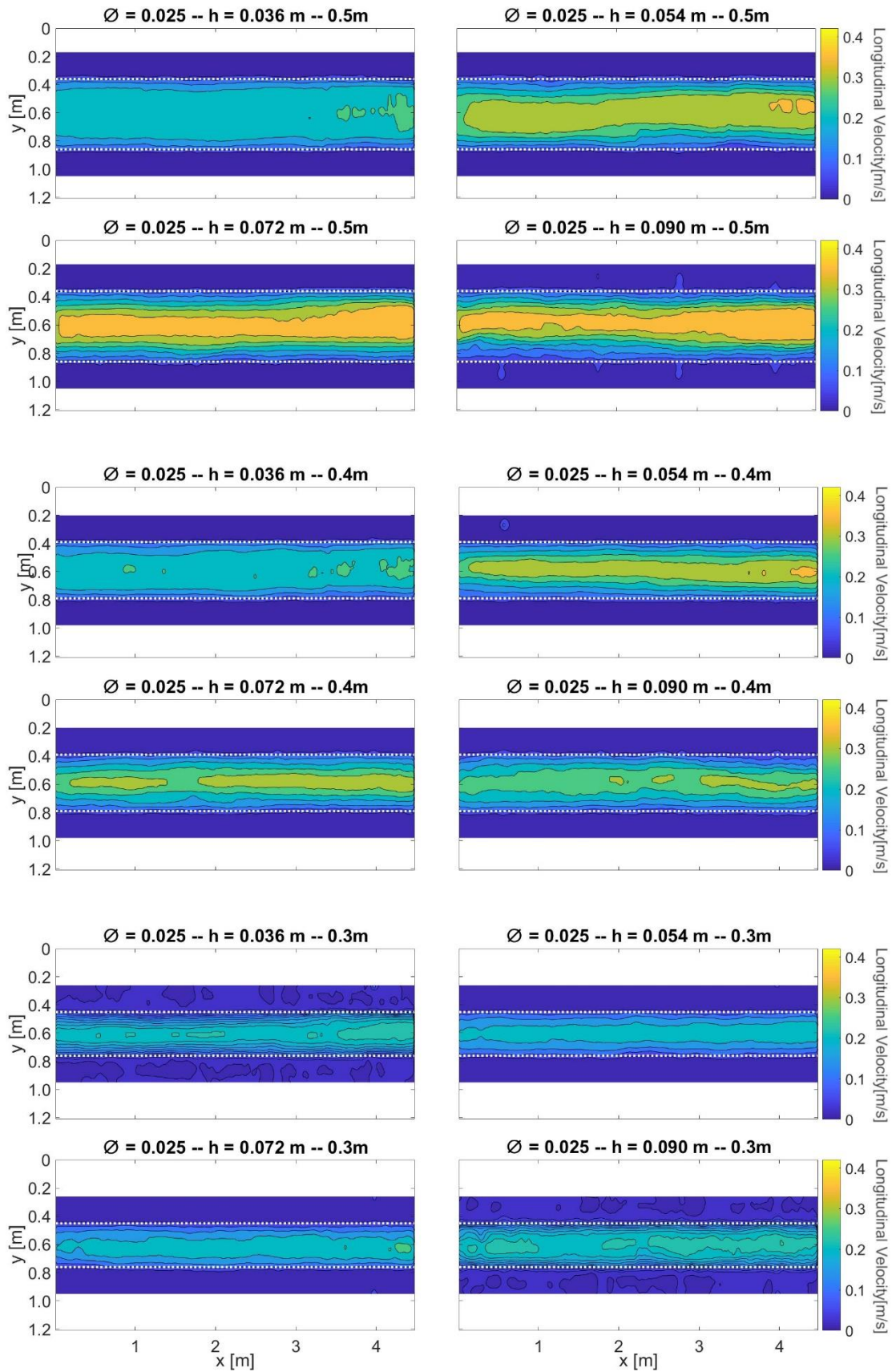
Figure 6.37 (b). Time-averaged longitudinal flow velocity maps for different both sides vegetation conditions for density $\emptyset = 0.025$ with vegetation edge as white dots.

Santiago Rojas Arques
Department of Civil and Structural Engineering

Figure 6.37 suggests a decrease of longitudinal velocity within the non-vegetated region when the distance between vegetated banks decreases. This effect is produced because of the overlapping of both shear layers created by each vegetated region. In addition, **Figure 6.37** shows some flow conditions in which a variation of the longitudinal velocity in free flow region along the length is observed. This variation was also discussed for longitudinal velocities shown in **Fig 6.8** and **Fig 6.9,** and it may be produced because a non-homogeneous PIV tracer distribution was recorded for these tests, producing a variation in the time-averaged longitudinal velocity along the flume length. The lengthwise spatial and time-averaged longitudinal velocity profiles were obtained in the same way as in **Section 6.2.1** and they are shown in **Figure 6.38**.
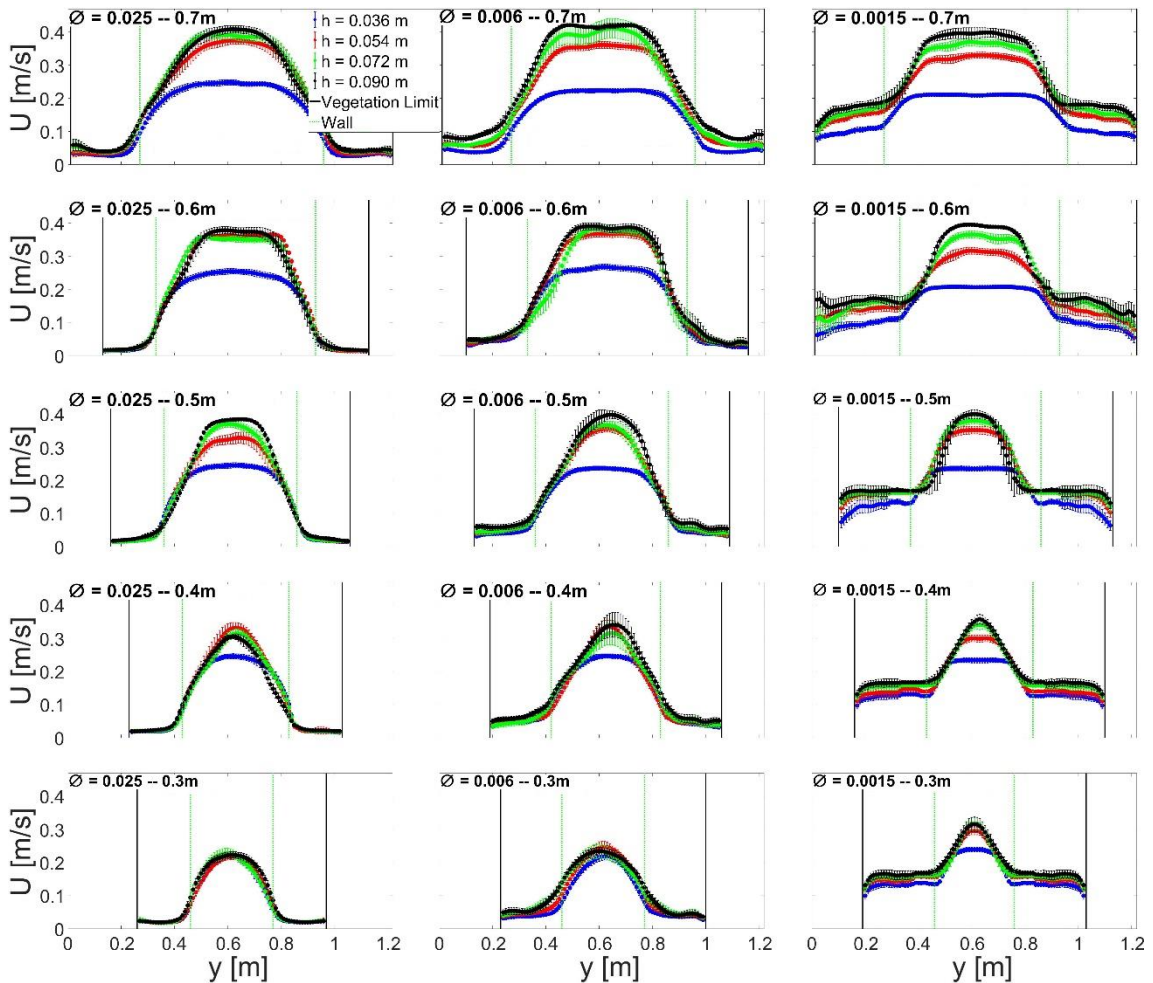
Figure 6.38. Lengthwise and time-averaged longitudinal flow profiles for all free open flow widths.

Time-averaged streamwise-mean longitudinal velocity profiles shown in **Figure 6.38** suggest a change in the development of the shear layers produced by both vegetated banks. In addition, the absolute velocity gradient of the longitudinal velocity profiles was calculate for each test. This absolute velocity gradients were obtained as $\left|\partial U/\partial y\right| = abs(\Delta U/\Delta Y)$. **Figure 6.39** shows the absolute velocity gradients for test configurations $\emptyset = 0.006 - h = 0.090$ m.

Santiago Rojas Arques
Department of Civil and Structural Engineering
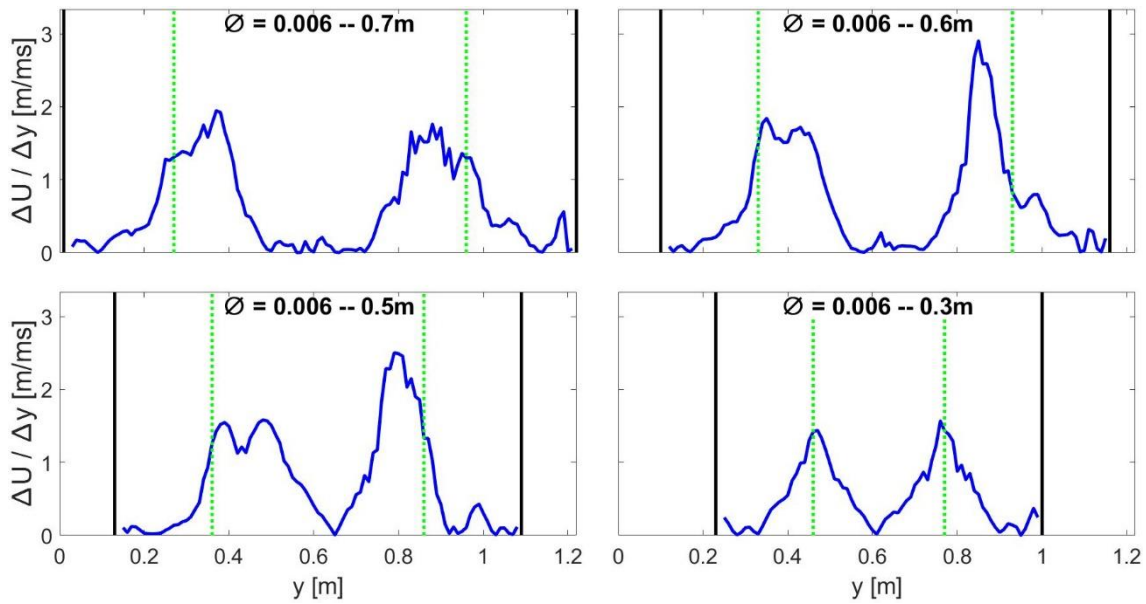
Figure 6.39. Absolute velocity gradients from time-averaged mean longitudinal velocity profiles for test configurations $\emptyset = 0.006 - \text{h} = 0.090$ m.

In **Figure 6.38** it is appreciated that for maximum free open flow width ($W_{Free} = 0.7$ m) full shear layers and a quasi-constant free velocity region between both are shown. This behaviour can be observed in **Figure 6.39**, where a quasi-zero region of absolute velocity gradients for the widest free open flow widths ($W_{Free} = 0.7$ and 0.6 m) is shown.

However, for the other two cases no zero gradient region is observed in the centre of the studied region but both absolute velocity gradients converge in the centre of the studied region. This change in the transverse profile of longitudinal velocity suggests an overlapping of both shear layers when free flow region between vegetated banks becomes narrow enough. Only for test $\emptyset = 0.0015 - h = 0.036$ m a quasi-constant free open flow region is appreciated for all different W_{Free} values in **Figure 6.38**. This behaviour can be explained because this combination of water depth and vegetation density produces the smaller velocity gradient and thus there is enough space for both full developed shear layers even for the narrowest W_{Free}.

In addition, the maximum velocity recorded in the centre of the free flow region shown in **Figure 6.38** was obtained (U_{max}), as well as the longitudinal velocity within each vegetated bank and the flow rate from profiles. **Figure 6.40** presents both maximum longitudinal free flow velocity recorded in the centre of the free flow region (U_{max}) (left) and longitudinal velocity within vegetation (right) for each W_{free} value and vegetation density. Note that the U_{veg} represented in **Figure 6.40** (right) is the mean longitudinal velocity within vegetation considering the mean value of both banks. Another effect derived from the overlapping of shear layers is a decrease in the maximum longitudinal velocity observed in the centre of the free open flow region. **Figure 6.40** (left) shows a clear increase of maximum longitudinal free flow velocity with water depth for $W_{Free} = 0.7$ m. However, for the narrowest cases ($W_{Free} = 0.3$ m), all velocity profiles converge to the same values, except for $\emptyset = 0.0015 - h = 0.036$ m.

Santiago Rojas Arques
Department of Civil and Structural Engineering
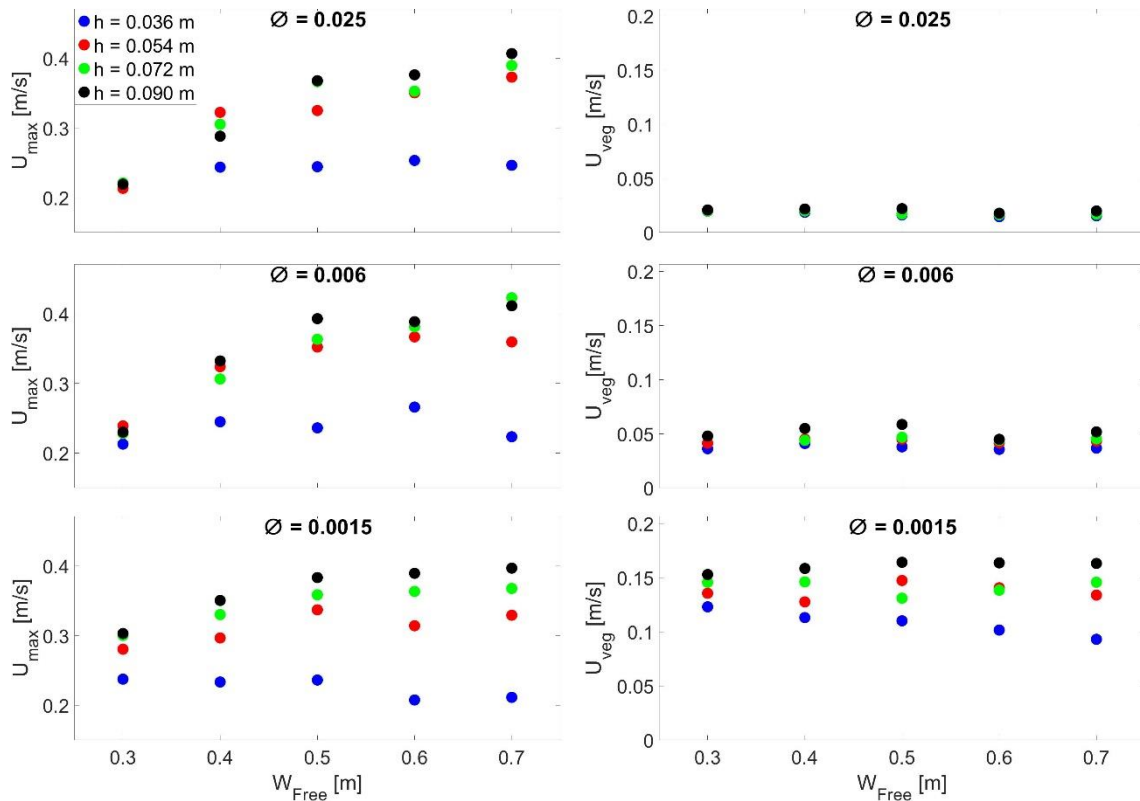
Figure 6.40. Maximum free longitudinal velocity (right) and longitudinal velocity within vegetation (left) for all different test configurations.

For each vegetation density, a decrease of maximum longitudinal velocity is produced for narrower scenarios, obtaining similar velocity values for all different water depths for $W_{Free} = 0.3$ m. This suggests that there is insufficient distance between both vegetated banks to achieve the same maximum free longitudinal velocity obtained for $W_{Free} = 0.7$ m. The right plot of **Figure 6.40** shows mean longitudinal velocity within vegetation (U_{Veg}) for each test configuration, where no significant trend is observed between these results and W_{Free} values. Therefore, for further analysis explained below in this section, a mean longitudinal velocity value within vegetation was obtained for each water depth and vegetation density by considering all values shown in **Figure 6.40** for the different values of W_{Free} and the same vegetation density and water depth. Results are shown in **Table 6.13.**

Table 6.13. Mean longitudinal velocity within vegetation by considering values for all W_{Free} for each water depth and vegetation density.

$Mean\ U_{Veg}$ [m/s]	$h = 0.036$ m	$h = 0.054$ m	$h = 0.072$ m	$h = 0.090$ m
$\emptyset = 0.0015$	0.108	0.137	0.141	0.160
$\emptyset = 0.006$	0.038	0.043	0.046	0.052
$\emptyset = 0.025$	0.017	0.018	0.018	0.020

Based on **Figure 6.40**, a relationship to described the variation of U_{max} based on W_{Free} is proposed. To quantify this variation, a ratio between the maximum longitudinal velocity recorded (U_{max}) and the theoretical free longitudinal velocity value expected for an open channel without vegetation (U_{Free}) was obtained. This U_{Free} was considered as the mean

Santiago Rojas Arques
Department of Civil and Structural Engineering

longitudinal velocity obtained in tests with no vegetation (**Section 6.1**). In addition, the ratio between the free flow width (W_{Free}) and the width needed for a full development of both shear layers ($2\,\delta_{Outer}$) was defined. The outer length δ_{Outer} was obtained using the longitudinal velocity model proposed in **Section 6.2.1**. Therefore, the relationship between U_{max} and W_{Free} was expressed as:

$$\frac{W_{Free}}{2\,\delta_{Outer}} = f\left(\frac{U_{max}}{U_{Free}}\right) \qquad\qquad eq.\,6.24$$

If right term of **eq. 6.24** is higher than 1 ($W_{Free}/2\,\delta_{Outer} > 1$), this means that the free open flow region between both vegetated banks is width enough to allow the full-development of both shear layers. Otherwise, if $W_{Free}/2\,\delta_{Outer} < 1$, an overlapping between both shear layers is produced. In addition, if left term of **eq. 6.24** is smaller than 1 ($U_{max}/U_{Free} < 1$), a decrease of theoretical free longitudinal velocity is produced due to the overlapping of the shear layers. For each vegetation density, the relationship between these calculated ratios is represented in **Figure 6.41**.

Santiago Rojas Arques
Department of Civil and Structural Engineering
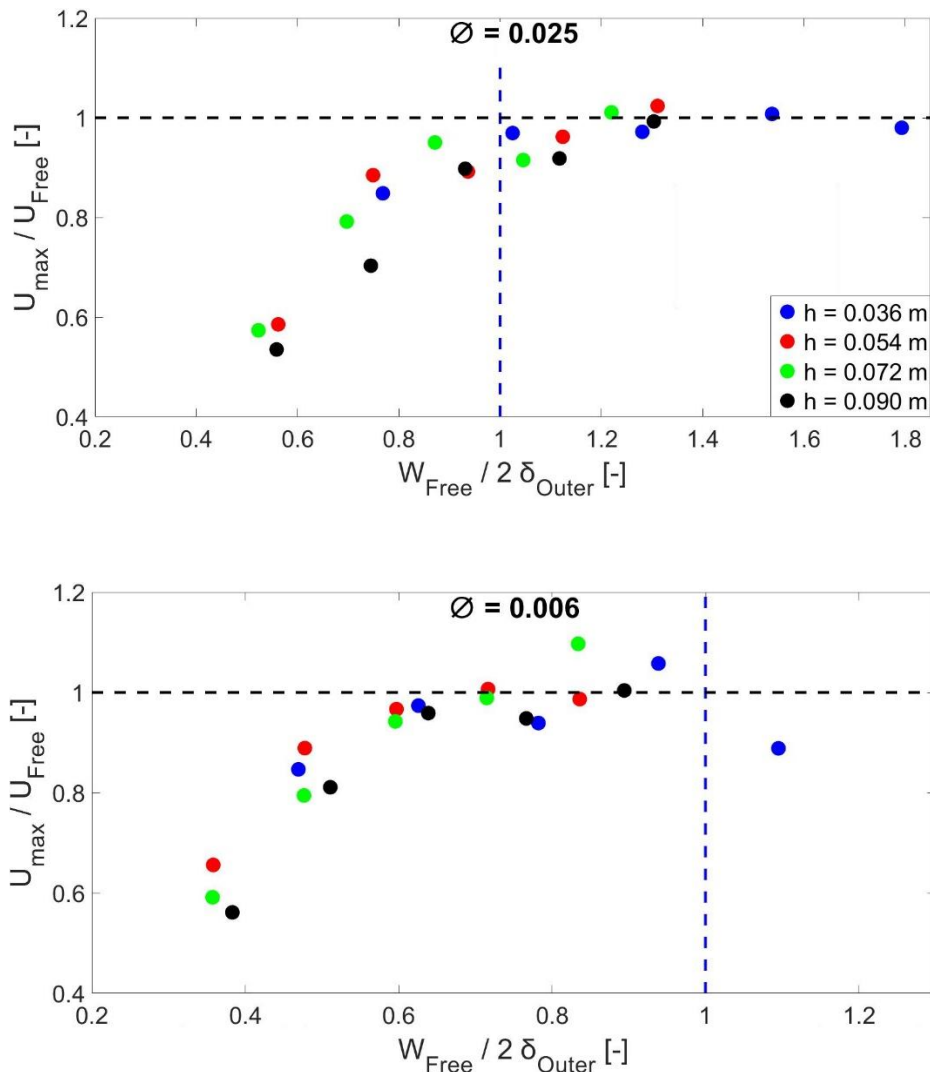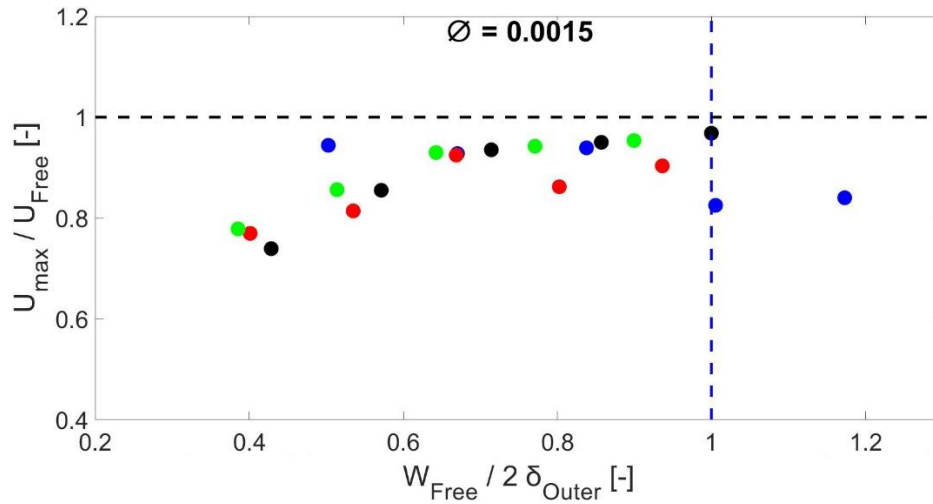
Figure 6.41. Relationship between free region width ratio and maximum longitudinal velocity ratio.

Figure 6.41 shows a reduction of velocity ratio (U_{max}/U_{Free}) when $W_{Free}/2\,\delta_{Outer}$ decreases. This velocity reduction is more significant in $\emptyset = 0.025$ and $\emptyset = 0.006$ than in $\emptyset = 0.0015$ tests, which suggests that this relationship could also depend on vegetation density. Based on this, a new relationship between both velocity and width ratios is proposed by including a parameter based on vegetation density:

$$1 - \frac{U_{max}}{U_{Free}} = A_\emptyset \exp\left[\left(1 - \frac{W_{Free}}{2\,\delta_{Outer}}\right)^2\right] - A_\emptyset \qquad eq.\,6.25$$

Where $A_\emptyset$ is an empirical coefficient:

$$A_\emptyset = \frac{52.14}{100}\,(1 - \emptyset)^{-52.14} \qquad eq.\,6.26$$

Where $\emptyset$ is the solid volume fraction and 52.14 is a coefficient obtained empirically from the fitting the equation to the experimental results shown in **Figure 6.41**. The relationship proposed in **eq. 6.25** was defined based on the assumption that there should be a horizontal asymptote for $W_{Free}/2\,\delta_{Outer} > 1$ as these scenarios allow the development of the full shear layer, and therefore a velocity $U_{max} = U_{Free}$ is achieved. Then, final expressions were obtained by fitting experimental data. In **Figure 6.42** is showed both experimental ratios plotted previously in **Figure 6.41** with relationship proposed in **eq. 6.25** and **eq. 6.26.**

Santiago Rojas Arques
Department of Civil and Structural Engineering
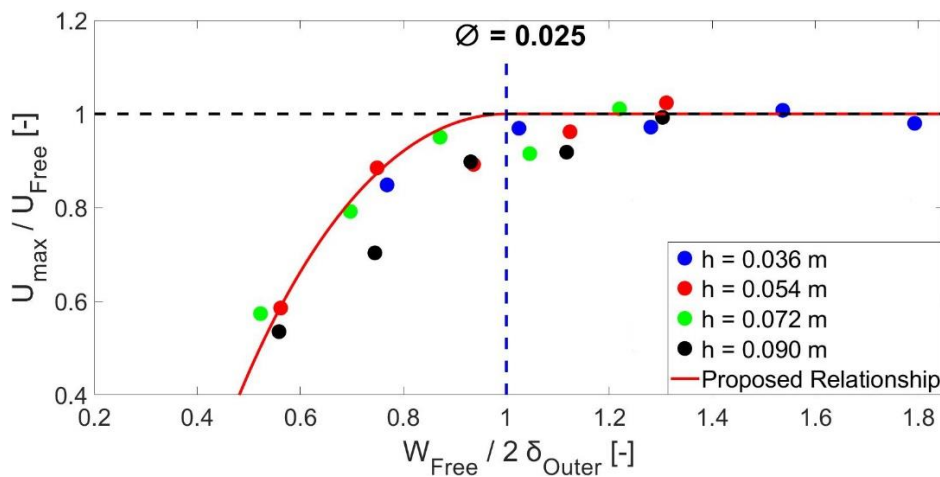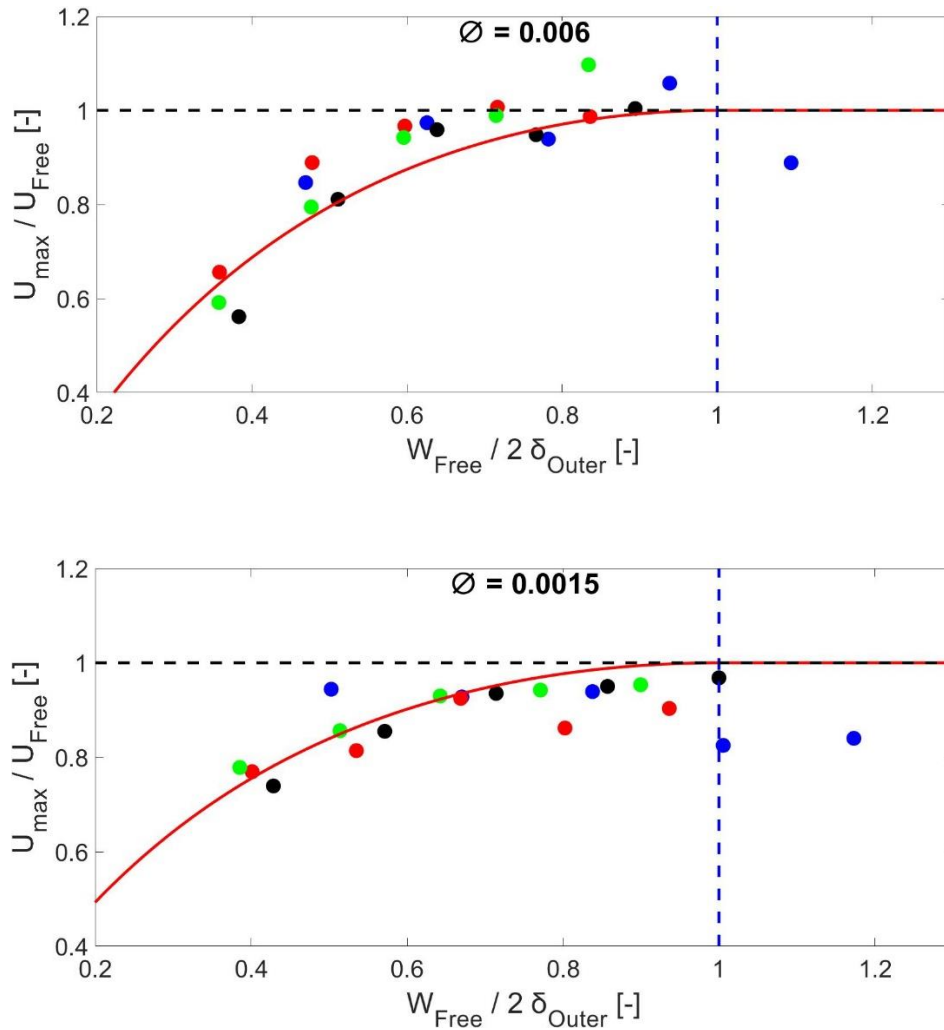
Figure 6.42. Relationship between free region width ratio and maximum longitudinal velocity ratio and proposed predicted relationship (**eq. 6.25**).

The Pearson correlation R between experimental data and results obtained with **eq. 6.25** and **eq. 6.26** as well as absolute relative differences between U_{max} predicted by equations **eq. 6.25** and **eq. 6.26**, and experimental velocities are presented in **Table 6.14.**

Table 6.14. Pearson correlation and mean absolute relative differences between maximum experimental longitudinal velocities and results obtained with proposed relationships.

Density	Correlation $R\ [-]$	Mean Rel. Diff. [%]
$\emptyset = 0.025$	0.94	4.70 %
$\emptyset = 0.006$	0.90	5.56 %
$\emptyset = 0.0015$	0.73	5.06 %

Once a relationship to obtain maximum longitudinal free velocity is defined, the proposed velocity model introduced in **Section 6.2.1** can be modified by adding **eq. 6.25** and **eq. 6.26** to predict time-averaged mean longitudinal velocity profiles with two vegetated banks.

Santiago Rojas Arques
Department of Civil and Structural Engineering

First, the length of outer layer (δ_{Outer}) was obtained by considering the free longitudinal velocity as the mean longitudinal velocity obtained for no-vegetated tests in **Section 6.1** (see **Table 6.1**) and the longitudinal velocity within vegetation as the one showed in **Table 6.13**. As a result, a first outer length approximation is obtained for each water depth and vegetation density by using the relationship proposed in **Section 6.2.1 (eq. 6.7)**.

Then, ratio between the free flow region for each test (W_{Free}) and the double of the outer length previously obtained was calculated, obtaining $W_{Free}/2\,\delta_{Outer}$. Two different scenarios were considered depending on the ratio obtained.

If $W_{Free}/2\,\delta_{Outer} \geq 1$, the free flow region between vegetated banks is wide enough to allow the full-development of both shear layers. Therefore, equations proposed in **Section 6.2.1** are applied and longitudinal free velocity considered is equal to that obtained in no-vegetated tests in **Section 6.1** ($U_{max} = U_{Free}$).

Otherwise, if $W_{Free}/2\,\delta_{Outer} < 1$, the free flow region between vegetated banks is not wide enough to allow the full-development of both shear layers and an overlapping between both shear layers is produced. Therefore, the maximum longitudinal free velocity in the centre of the channel was predicted by using **eq. 6.25** and **eq. 6.26**. In order to predict velocity profiles when both outer layers overlapped, a parabolic expression was proposed to connect both outer layer velocity profiles. This proposed parabolic profile has a maximum velocity value in the centre of the channel that is equal to U_{max} and the profile is matched with both inner layers (δ_{Inner}) generated at each vegetated bank, which are obtained by using the relationship proposed in **Section 6.2.1**. Thus, longitudinal velocity profile within outer region for $W_{Free}/2\,\delta_{Outer} < 1$ is expressed as:

$$U_{Outer} = C_{1b}y^2 + C_{2b}y + C_{3b} \qquad\qquad eq.\,6.27$$

Where:

$$C_{1b} = \frac{U(y_0) - U_{max}}{(y_0 - y_{Centre})^2} \qquad\qquad eq.\,6.28$$

$$C_{2b} = -2C_{1b}y_{Centre} \qquad\qquad eq.\,6.29$$

$$C_{3b} = U_{max} + C_{1b}y_{Centre}^2 \qquad\qquad eq.\,6.30$$

Where y_{Centre} is the position of the centre of the channel; U_{max} is the maximum free longitudinal velocity considered for each configuration and y_0 is the position of the inflection point. **Figure 6.43** shows predicted time-averaged mean longitudinal velocity profiles and their corresponding experimental data for water depth $h = 0.054$ m.

Santiago Rojas Arques
Department of Civil and Structural Engineering
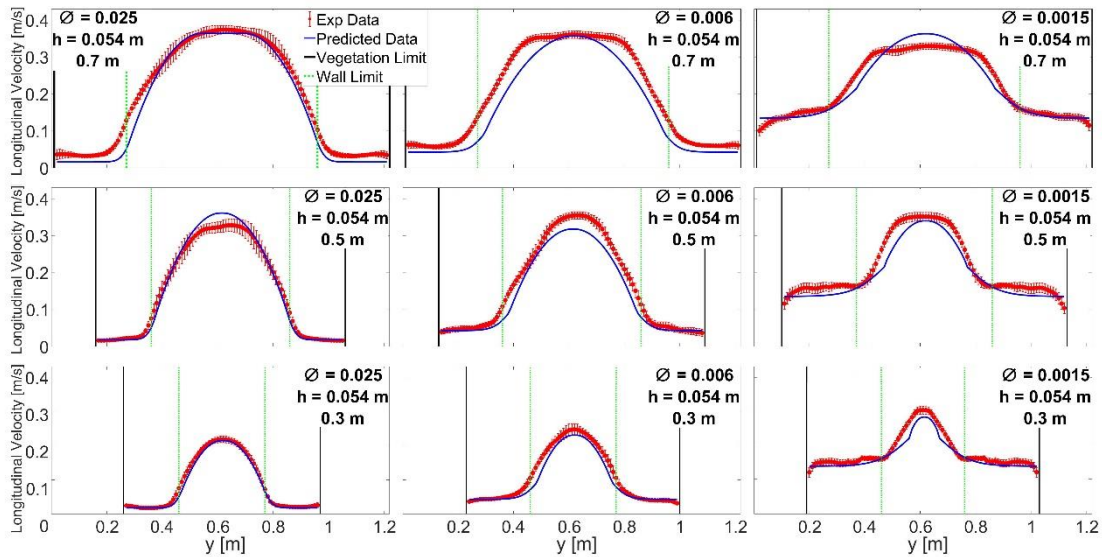
Figure 6.43. Experimental and predicted time-averaged mean longitudinal velocity profiles for h = 0.054 m tests.

Figure 6.43 shows a generally good fit between experimental and predicted data as in shown below in **Figure 6.44** and **Figure 6.45**. Results for $\emptyset = 0.025$ test conditions show a very close agreement between predicted and experimental data. Differences obtained in the centre of the free flow region for $W_{Free} = 0.5$ m are possibly due to differences in the prediction of U_{max}, and differences in $W_{Free} = 0.7$ m are due to a mismatch with the velocity within vegetation. An increased of differences between predicted and experimental longitudinal velocity profiles seems to be produced when vegetation density decreases. These differences can be produced as an accumulation of small errors produced in the prediction of δ_{Outer} and U_{max}, which produce some mismatching in the prediction

The largest differences are found for tests $\emptyset = 0.0015$, in which most of experimental data show a constant free velocity region even when predicted ratio $W_{Free}/2\,\delta_{Outer} \ll 1$. This effect can be produced because of an internal re-adjustment of the longitudinal velocity profile due to the low density considered. This re-adjustment would produce a constant slope with an inflection point closer to vegetation edge, producing a mismatch between the predicted results and the experimental data.

The Pearson correlation R was calculated for each test condition between predicted and experimental velocity profile. First, the correlation was obtained by considering the full velocity profile. In addition, another Pearson correlation was calculated by considering only the free open flow region between both vegetated banks. This second correlation was calculated to neglect constant velocity within vegetation that could increase the correlation even though a bad fitting of free longitudinal velocity was obtained. Both correlation results are shown in **Figure 6.44**.

Santiago Rojas Arques
Department of Civil and Structural Engineering
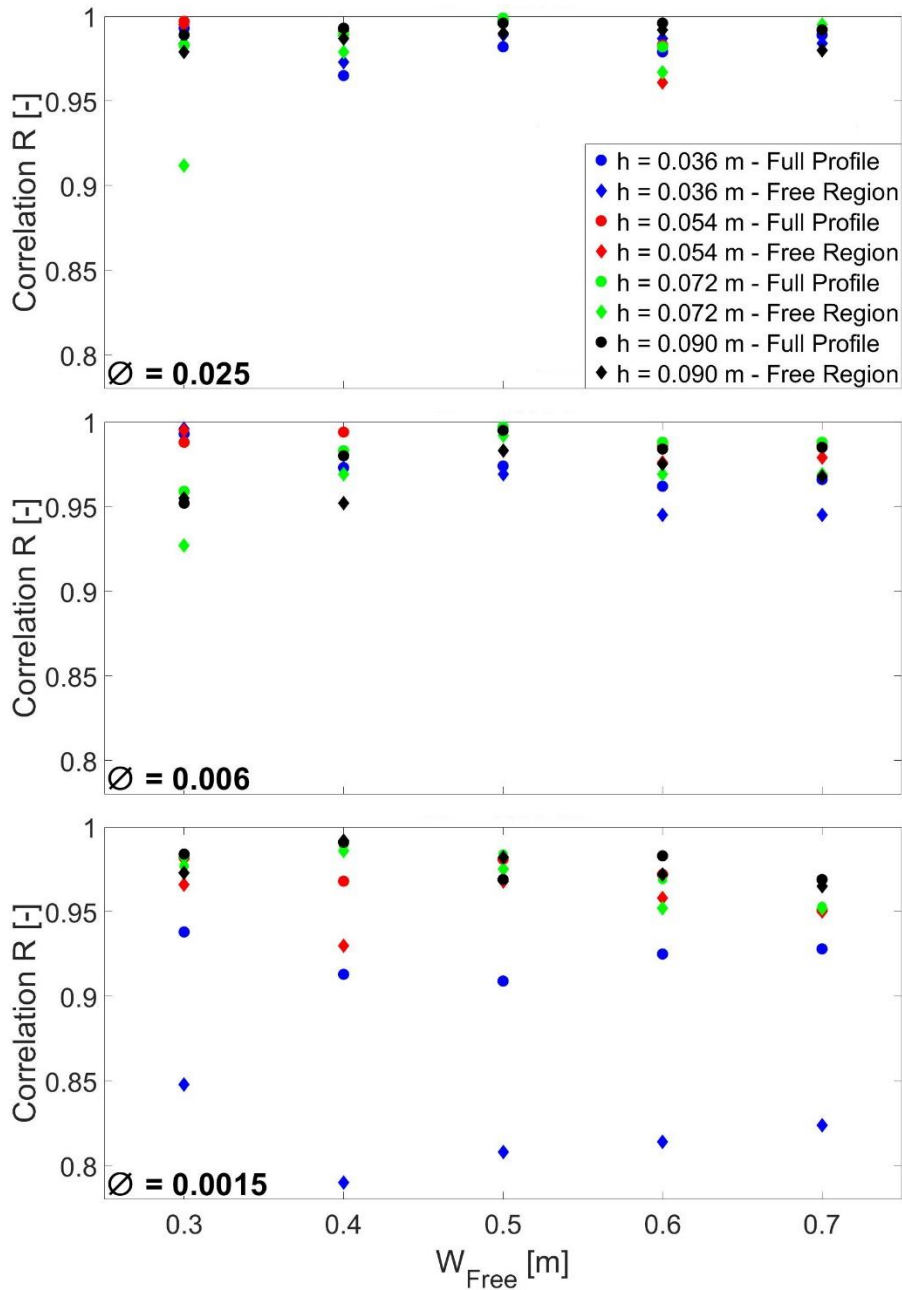
Figure 6.44. Pearson correlation between predicted and experimental velocity profiles.

Figure 6.44 shows Pearson correlation R obtained between experimental and predicted data considering both regions. Results suggest a good fit of predicted data for most cases. However, plots suggest a decrease of correlation for sparser vegetation densities. Moreover, some low results are obtained for $\emptyset = 0.0015$ tests, where correlations around 0.8 are obtained for $h = 0.036$ m. These differences would be produced because the re-adjustment of longitudinal velocity profiles for this specific density described previously.

Santiago Rojas Arques
Department of Civil and Structural Engineering

Finally, mean absolute relative differences between experimental and predicted data considering same two regions as considered for Pearson correlation plotted in **Figure 6.45**.
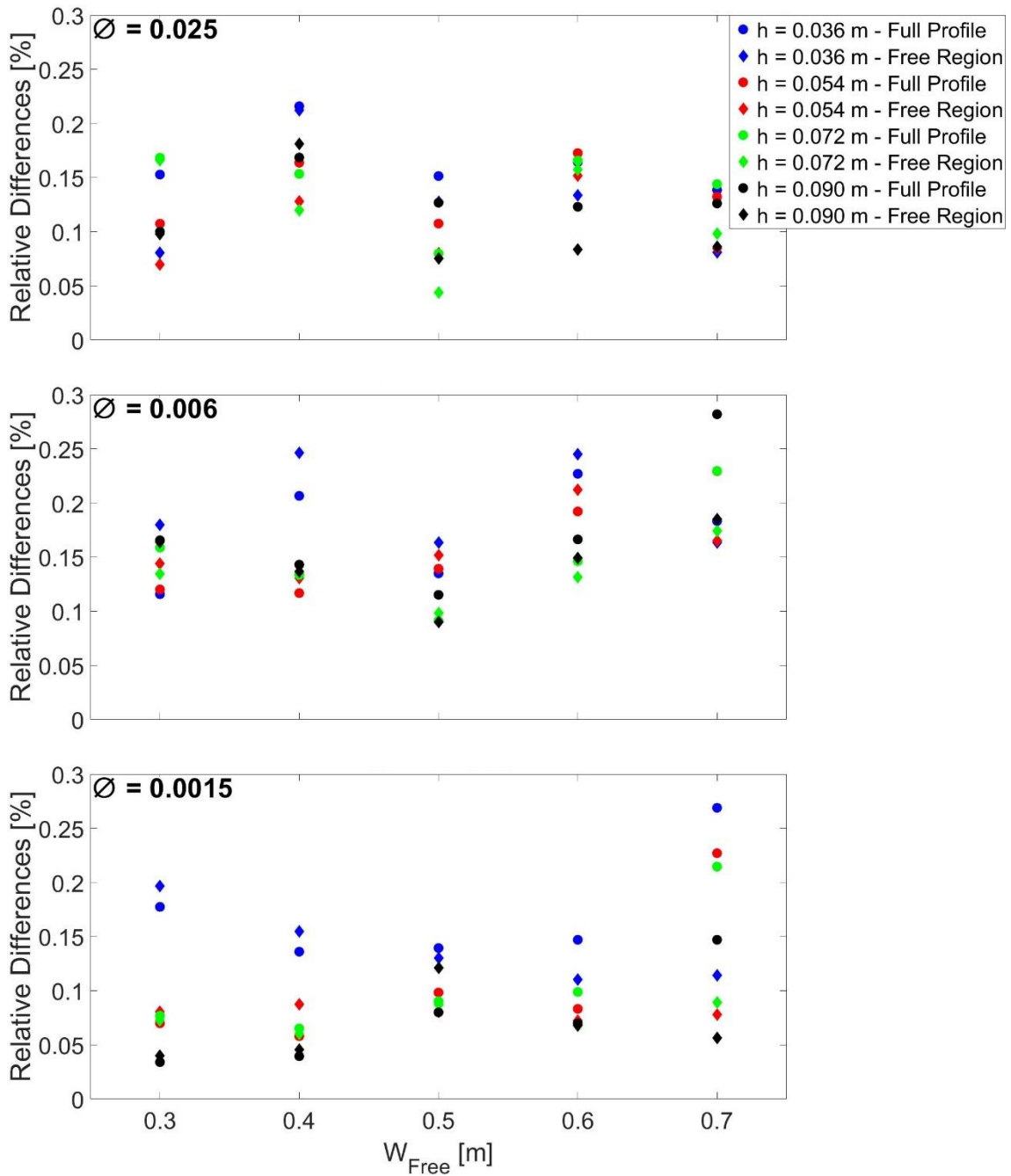
Figure 6.45. Relative differences between predicted and experimental velocity profiles.

Figure 6.45 shows mean absolute relative differences between experimental and predicted data considering the same profile regions as during correlation study. Results suggest smaller differences between profiles around the free region than differences obtained for the full profile. In addition, these results agree with correlation data and suggest a reasonably good fit of proposed model to observed velocity profiles.

Santiago Rojas Arques
Department of Civil and Structural Engineering

6.3.3. Solute Transport Results

A vertical well-mixed injection was released in the centre of the free flow region for each W_{Free} as described in **Section 4.5.3.** As it was explained previously, for these tests four free vegetated transversal sections located just under each camera were designed to record full concentration profiles for tests with the narrowest free regions. These profiles were analysed using same filtering technique as proposed in **Section 5.6.** Finally, a mean concentration profile was obtained for each free vegetated gap, obtaining four different concentration profiles along the length of the recorded area for each test configuration as shown **Figure 6.46** and **Figure 6.47**. **Figure 6.46** shows experimental concentration profiles for test configuration $h = 0.036\,\text{m} - \emptyset = 0.0015$ for all W_{Free} values and **Figure 6.47** shows experimental concentration profiles for test configuration $h = 0.036\,\text{m} - \emptyset = 0.025$.
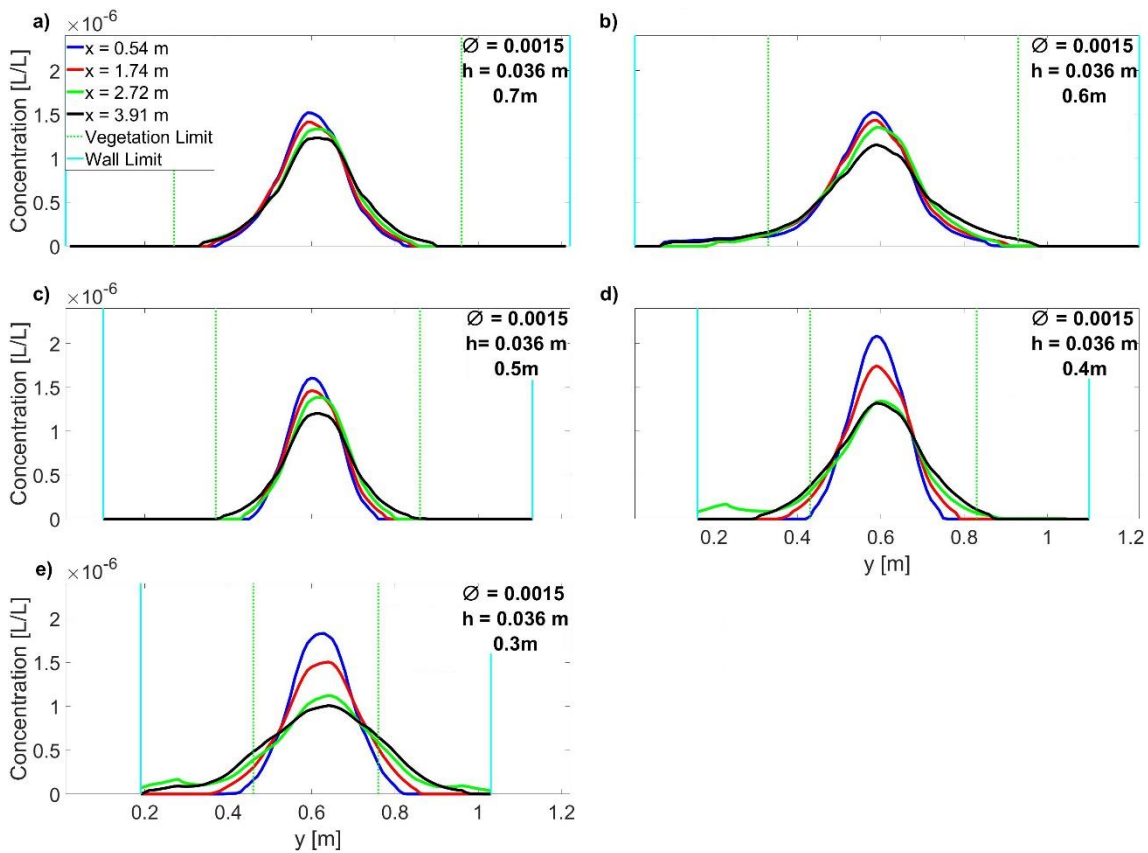
Figure 6.46. Experimental concentration profiles obtained for $h = 0.036\,\text{m} - \emptyset = 0.0015$ test configuration for a) $W_{Free} = 0.7\,\text{m}$, b) $W_{Free} = 0.6\,\text{m}$, c) $W_{Free} = 0.5\,\text{m}$, d) $W_{Free} = 0.4\,\text{m}$ and e) $W_{Free} = 0.3\,\text{m}$.

Santiago Rojas Arques
Department of Civil and Structural Engineering
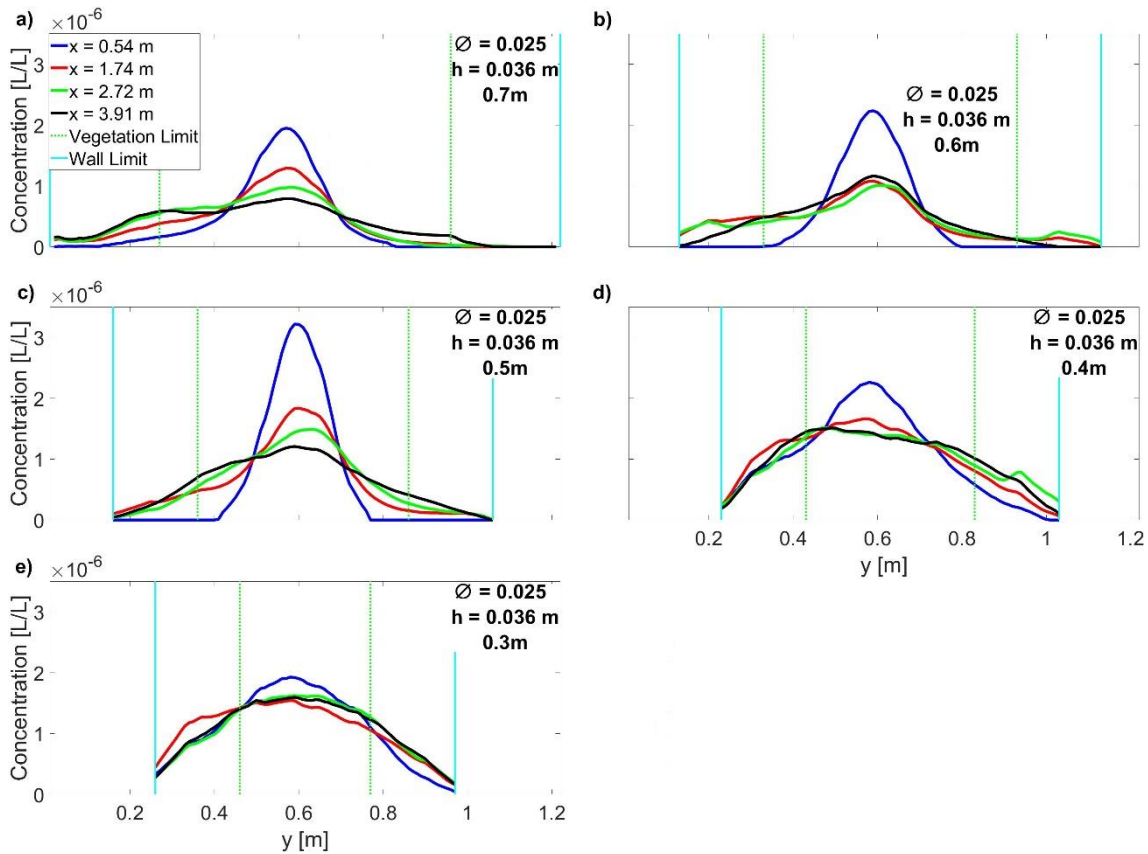
Figure 6.47. Experimental concentration profiles obtained for $h = 0.036\ \text{m} - \varnothing = 0.025$ test configuration for a) $W_{Free} = 0.7$ m, b) $W_{Free} = 0.6$ m, c) $W_{Free} = 0.5$ m, d) $W_{Free} = 0.4$ m and e) $W_{Free} = 0.3$ m.

As shown **Figure 6.46** and **Figure 6.47**, an increase of tracer spreading is observed when W_{Free} decreases for same water depth and vegetation density. This behaviour can be explained by the reduction of free flow region (W_{Free}) between both vegetated banks and the consequent encroachment of shear layers. In addition, an increase in mixing is also appreciated for same W_{Free} value but denser vegetation. **Figure 6.46** and **Figure 6.47** show that for higher vegetation density there is an increase of mixing. This increase is produced because of the increase of velocity gradient produced by vegetated patch (the increase of vegetation density produces a decrease of flow velocity within the vegetated bank, increasing the velocity gradient between the vegetated banks and the free flow region in the centre).

The experimental concentration data obtained for this set of experiments was compared with concentration profiles calculated by proposed empirical model explained in **Section 6.2** for same flow conditions (vegetation density, water depth and W_{Free}).

Transversal profiles of transverse mixing coefficients were obtained by applying the transverse mixing model proposed in **Section 6.2.2 (eq. 6.19** to **eq. 6.22**). For each test condition, U_{max} and U_{Veg} predicted by the velocity model in **Section 6.3.2** (**eq. 6.25** and **eq. 6.26**) were used to predict $D_{y_{max}}$ using **eq. 6.23**. The lengths of variable transverse mixing profiles were obtained by matching them with the length of the shear layers of predicted longitudinal velocity profiles (**eq. 6.9** to **eq. 6.18** or **eq. 6.27** to **eq. 6.30**), and position of $D_{y_{max}}$ was considered equal to the position of the inflection point y_o using **eq. 6.6**. For those tests in which W_{Free} was wide enough to allow a constant free open flow region in the centre of the channel, $D_{y_{free}}$ was

Santiago Rojas Arques
Department of Civil and Structural Engineering

considered equal to the one considered in **Section 6.2.2.** Finally, $D_{y_{Veg}}$ was obtained by using expression proposed by **Nepf (2012)**.

As a result, a transversal profile of transverse mixing coefficient was predicted for each test condition. The transverse profile of longitudinal velocity, the value and position of $D_{y_{max}}$ and the length of region with a variable $D_y(y)$ and the resulting profile of mixing coefficient depend on the vegetation density, the water depth and the width of free flow region W_{Free}. In **Figure 6.48** transverse mixing coefficient profiles for $W_{Free} = 0.7$ and 0.3 m for each vegetation density are plotted.
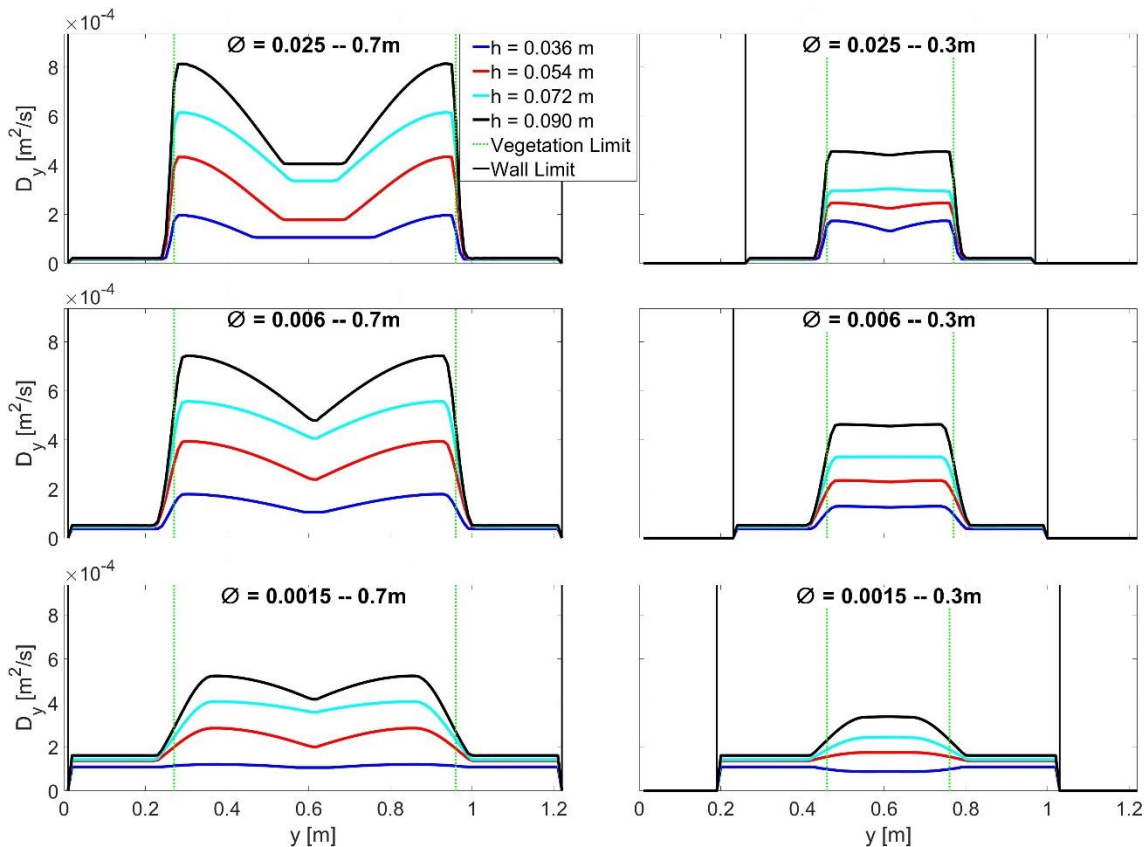
Figure 6.48. Predicted transverse mixing coefficient profiles for vegetation at both sides with a free distance of 0.7 m and 0.3 m.

Figure 6.48 shows the predicted variable transverse mixing coefficient profiles for two different free region widths ($W_{Free} = 0.7$ and 0.3 m) for all different vegetation densities. The prediction shows a decrease of $D_{y_{max}}$ for narrower W_{Free}. This decrease is produced as the value of U_{max} predicted in the centre of the free flow region decreases as it was shown in **Section 6.3.2**. A variation in the variable region of $D_y(y)$ is also observed because of the variation of the shear layer length for each test condition. For those test configurations in which W_{Free} is narrow enough to produce an overlapping of both shear layers, no constant $D_{y_{free}}$ region is produced.

In **Figure 6.48** it is also observed that for test condition $\emptyset = 0.0015 - W_{Free} = 0.3$ m predicted transverse mixing coefficient values in the central free region are smaller than the coefficients predicted within vegetation. In this sparse scenario, the longitudinal velocity within the vegetation is higher than those obtained for denser tests and it is closer the non-vegetated

velocity. Therefore, the $D_{y_{veg}}$ value predicted by **Nepf (2012)** expression is higher than in denser scenarios. In addition, the expression proposed by **Nepf (2012)** produce a large variability for the prediction of transverse mixing within vegetation (**Sonnenwald et al., 2017**). As a result, the resulting transverse mixing profile shows an unrealistic scenario in which the mixing is higher within the vegetation than in the non-vegetated region.

For each test configuration, a prediction of the downstream transversal concentration profiles was obtained using the F.D.M. methodology described in **Section 6.2.2**. The recorded upstream concentration profile was introduced into the F.D.M. as well as the predicted $D_y(y)$ and the longitudinal velocity profile obtained in **Section 6.3.2** for each test configuration. The predicted transversal concentration profiles were compared with corresponding experimentally observed values at $x = 3.9$ m (**Figure 6.49**, **Figure 6.50** and **Figure 6.51** for each vegetation density respectively).

Santiago Rojas Arques
Department of Civil and Structural Engineering
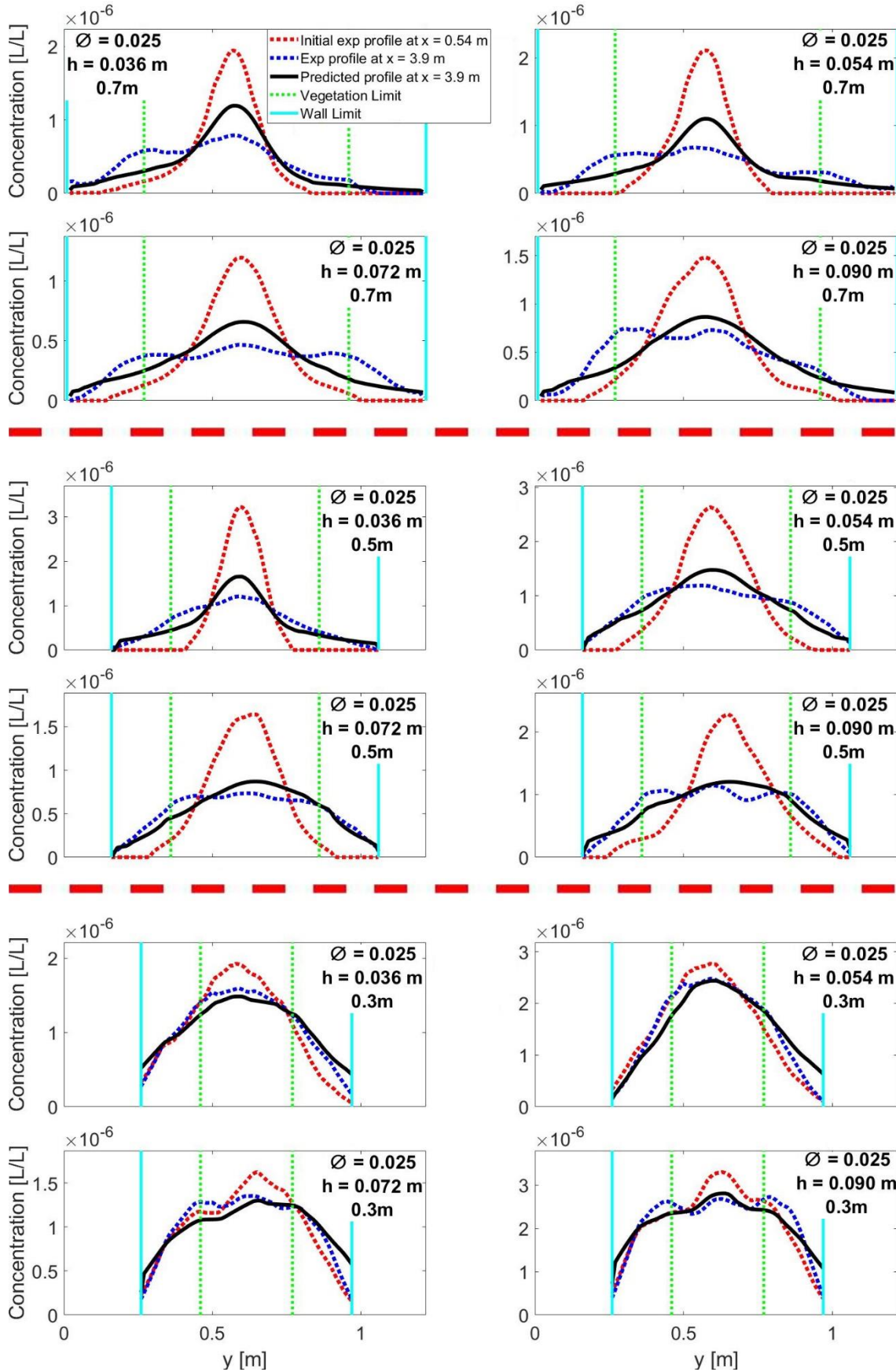
Figure 6.49. Predicted and experimental transversal concentration profiles for both sides vegetation tests for $\emptyset = 0.025$.

Santiago Rojas Arques
Department of Civil and Structural Engineering

Figures 6.49 shows two measured experimental concentration profiles located at $x = 0.54$ m and $x = 3.9$ m respectively, and the predicted profile for each vegetation density at $x = 3.9$ m using the proposed model. In addition, this figure is related to experimental and estimated concentration data for each water depth and the vegetation density $\emptyset = 0.025$. The predicted concentration profiles show a similar behaviour to the experimental ones. This similarity is more observable for the narrower tests ($W_{Free} = 0.5$ m and $W_{Free} = 0.3$ m). In addition, experimental results show that the concentration profiles recorded at $x = 3.9$ m are almost fully-mixed over the transverse direction. This behaviour is appreciated even for the tests with the widest free flow region ($W_{Free} = 0.7$ m) and suggests that the presence of the two vegetated banks enhances the transverse mixing processes compared with those obtained for one vegetated bank. Moreover, it is important to note that, for the narrowest free flow gap ($W_{Free} = 0.3$ m), the differences between the upstream and the downstream concentration profiles are noticeably small in all cases. This similarity suggests that the increase of the turbulence generated in the centre of the free flow region, coupled with the narrow width allowed for these scenarios; produces that the concentration profiles are almost fully-mixed in a short length. However, predicted profiles for $h = 0.036$ m – 0.7 m and $h = 0.054$ m – 0.7 m present a lower mixing rate than that observed in the experimental profiles. In addition, for all water depth tests regarding to $W_{Free} = 0.7$ m, a peak of concentration close the vegetation edge is observed in the downstream experimental profile, being more significant for deeper scenarios. This increment of concentration suggests a displacement of the concentration mass due to secondary currents; in agreement with the translation of mass to the vegetation boundary described previously in **Section 6.2.2.** This displacement seems to decrease for narrower W_{Free}, suggesting that the decrease of the size of the non-vegetated region can cause a reduction of this effect.

Santiago Rojas Arques
Department of Civil and Structural Engineering
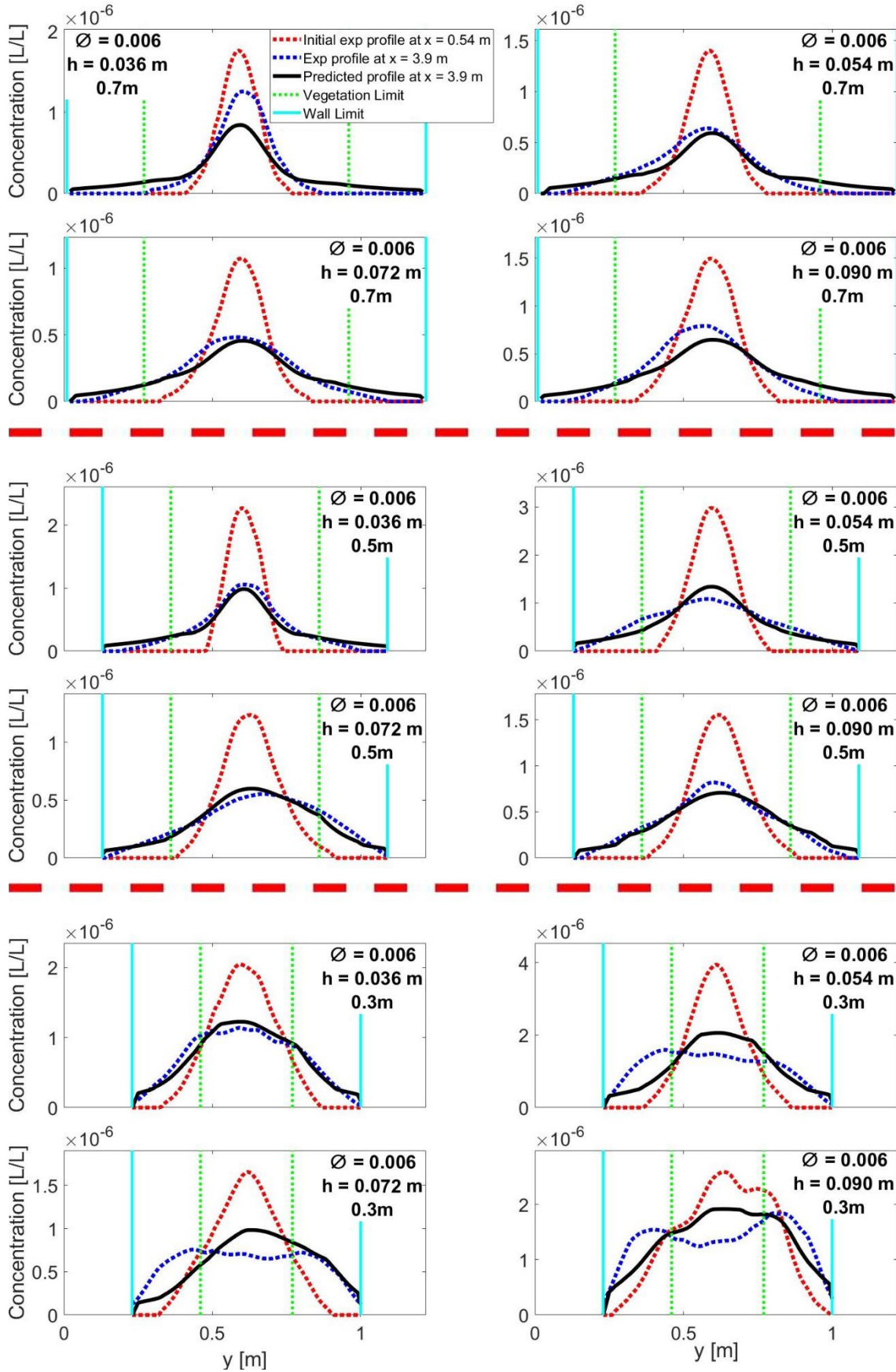
Figure 6.50. Predicted and experimental transversal concentration profiles for both sides vegetation tests for $\emptyset = 0.006$.

Santiago Rojas Arques
Department of Civil and Structural Engineering

Figure 6.50 shows the experimental and predicted concentration profiles for the same free flow gaps and water depths than **Fig 6.49**, but for the vegetation density $\emptyset = 0.006$. In this figure, similar mixing rates are observed between the experimental concentration profiles and those predicted by the proposed model. Moreover, the differences in mixing observed in $\emptyset = 0.025 - W_{Free} = 0.7$ m are reduced in $\emptyset = 0.006$. However, an over predicted -mixing rate is observed for $h = 0.036$ m – 0.7 m. In addition, the displacement of mass close to the vegetation edge discussed for $\emptyset = 0.025$ is reduced, suggesting a diminution of secondary effects, probably as a result of the decrease of the vegetation density.

For the experimental concentration profiles recorded at $x = 3.9$ m, a maximum concentration peak is appreciated for the free flow gap $W_{Free} = 0.7$ m, in opposition to the concentration profiles show in **Figure 6.49**, where the downstream concentration profiles seems almost fully mixed within the free gap. This peak is also recorded for the free flow gap $W_{Free} = 0.5$ m, although is less appreciated for deeper flow conditions. The presence of this maximum concentration value in the centre of the free flow suggests a decrease of the overall transverse mixing compared with the densest scenario. Moreover, results plotted in **Figure 6.50** suggests that narrower free flow gaps and deeper flow conditions increase the overall transverse mixing. In addition, downstream concentration profiles for the narrowest free flow gap ($W_{Free} = 0.3$ m) show almost full-mixed concentration profiles.

Results plotted in **Figure 6.50** agree with the previous one shown for denser vegetated banks, and suggest an increase of the overall transverse mixing compared with those results obtained for one vegetated bank flow tests. In addition, a comparison between these concentration profiles and those plotted in **Figure 6.49** suggests that a decrease of the vegetation density or the water depth produced a decrease of the overall transverse mixing. Moreover, the reduction of the free flow gap allowed between banks enhances the transverse mixing. Finally, results suggest a decrease of the secondary currents that may produce the movement of the main concentration mass.

Santiago Rojas Arques
Department of Civil and Structural Engineering
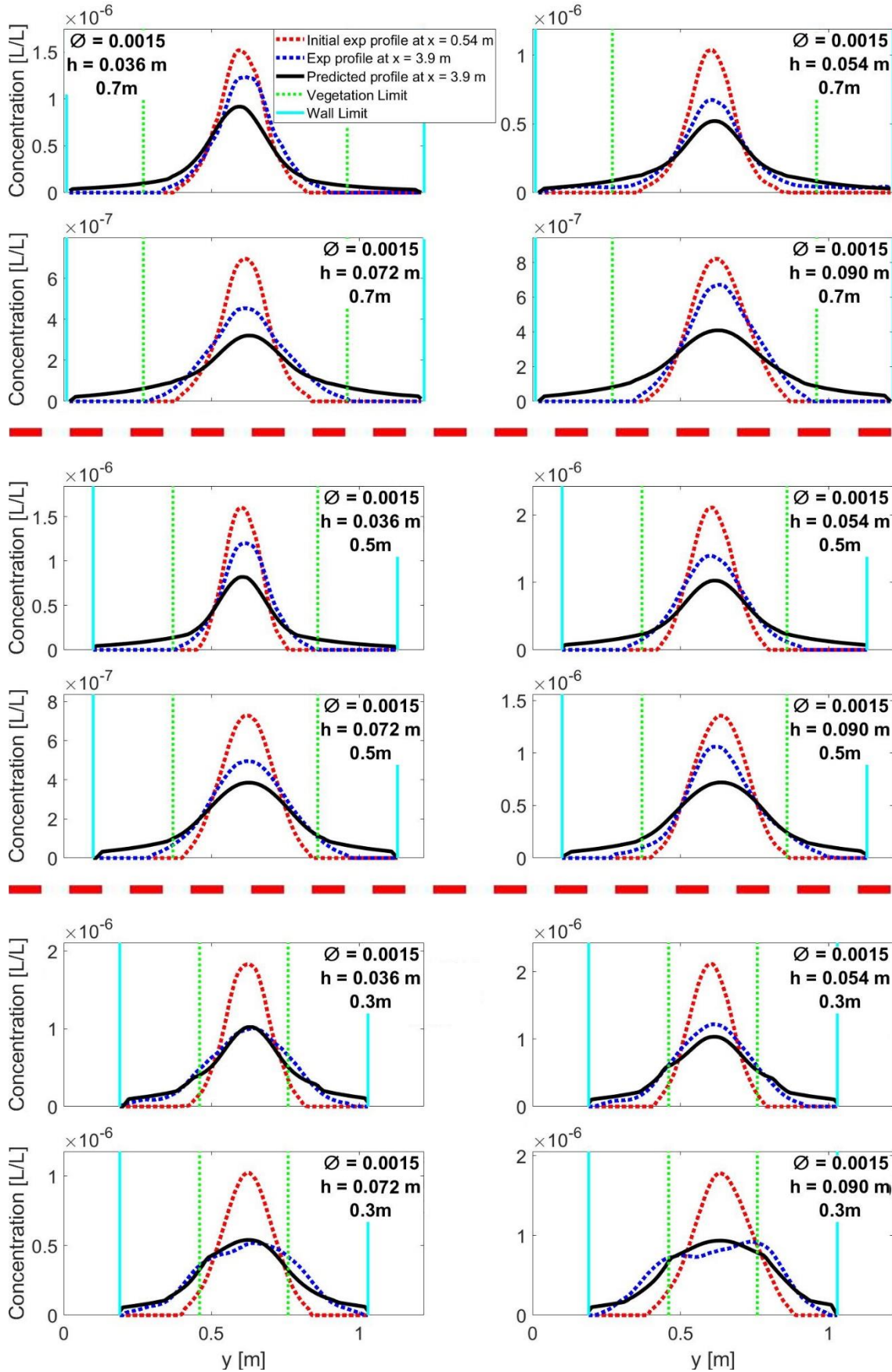
Figure 6.51. Predicted and experimental transversal concentration profiles for both sides vegetation tests for $\emptyset = 0.0015$.

Santiago Rojas Arques
Department of Civil and Structural Engineering

Finally, **Figure 6.51** shows the same experimental and predicted concentration profiles than previous figures, but for the vegetation density $\emptyset = 0.0015$. In this figure, a general over-mixing estimation is observed. For all different free flow gaps and water depths, the results obtained from the proposed model present a higher transverse mixing than that observed from experimental data. This difference may be related with the behaviour of the longitudinal velocity profiles recorded for this vegetation density and discussed in **Figure 6.38**. For these velocity profiles, a constant longitudinal velocity region was observed within the free flow gap even for narrower cases ($W_{Free} = 0.5$ m), in which an overlapping of the shear layers could be expected, and thus a parabolic shape similar to those recorded for denser scenarios. This flat region suggests narrower shear layers for this vegetation density, which would be related with a decrease of the turbulence achieved within the free flow gap and thus a lower transverse mixing process as shown in **Figure 6.51.** However, the scenario with the narrowest free flow gap ($W_{Free} = 0.3$ m) shows that both predicted and experimental concentration profiles present the same mixing rate. These results suggest that for this scenario, the overlapping of the shear layers predicted by the model is similar to that produced in the experiments. This agrees with velocity profiles show in **Figure 6.38**, where an overlapping of the shear layers is appreciated for the two narrowest free flow gaps ($W_{Free} = 0.4$ m and $W_{Free} = 0.3$ m).

Finally, experimental results plotted in **Figure 6.51** show a decrease of the overall transverse mixing compared with those results plotted in **Figure 6.49** and **Figure 6.50**, and agree with the idea that a decrease of the vegetation density produce a decrease of the transverse mixing in this type of flows.

In addition, the Pearson correlation between the predicted and experimental data was obtained in order to visualize the quality of the prediction. Pearson correlation results are plotted in **Figure 6.52**.

Santiago Rojas Arques
Department of Civil and Structural Engineering
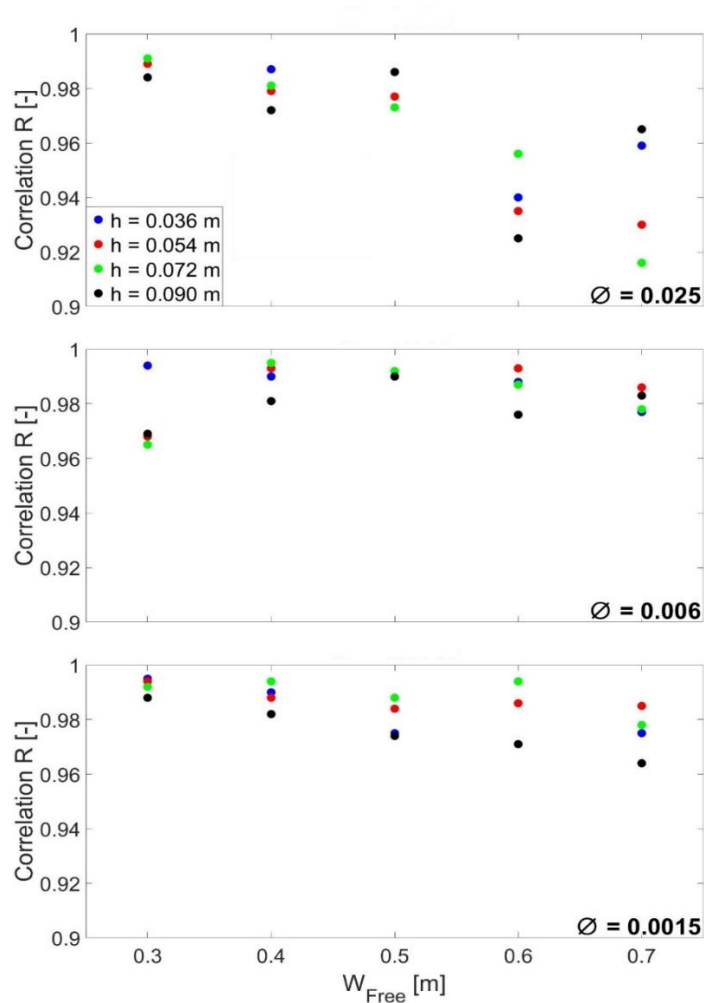
Figure 6.52. Pearson correlation between predicted concentration profiles and experimental one.

Pearson correlations shown in **Figure 6.52** suggest a general good prediction of concentration profiles for all different configurations. Highest differences are observed for a W_{Free} of 0.7 m and 0.6 m, especially for $\emptyset = 0.025$. These higher differences are produced by the displacement of mass concentration discussed in previous paragraph produced by the presence of secondary currents. In addition, lower correlations were obtained for wider scenarios ($W_{Free} = 0.7$ m and 0.6 m) for the vegetation density $\emptyset = 0.0015$. These results agree with previous visual comparisons and are produced due to the over-mixing estimation of these scenarios. However, an increase of the Pearson correlation is observed for narrower flows in agreement with the increase of fitting between the estimated and experimental concentration profiles observed in **Figure 6.51**.

Moreover, relative differences between predicted and experimental concentration profiles using same regions as considered in **Section 6.2.2** and results are shown in **Figure 6.53** and **Figure 6.54**.

- 160 -
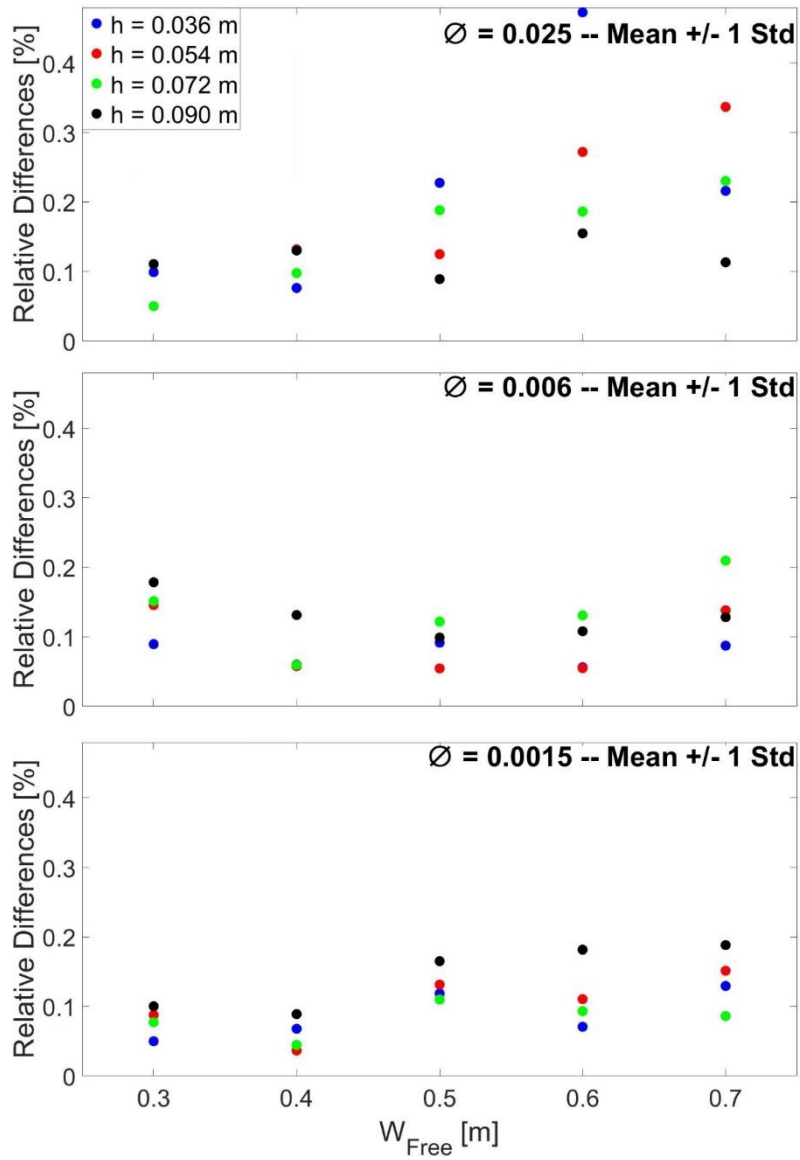
Figure 6.53. Mean absolute relative differences between predicted and experimental concentration profiles considering a region of $\mu \pm 1$ std.
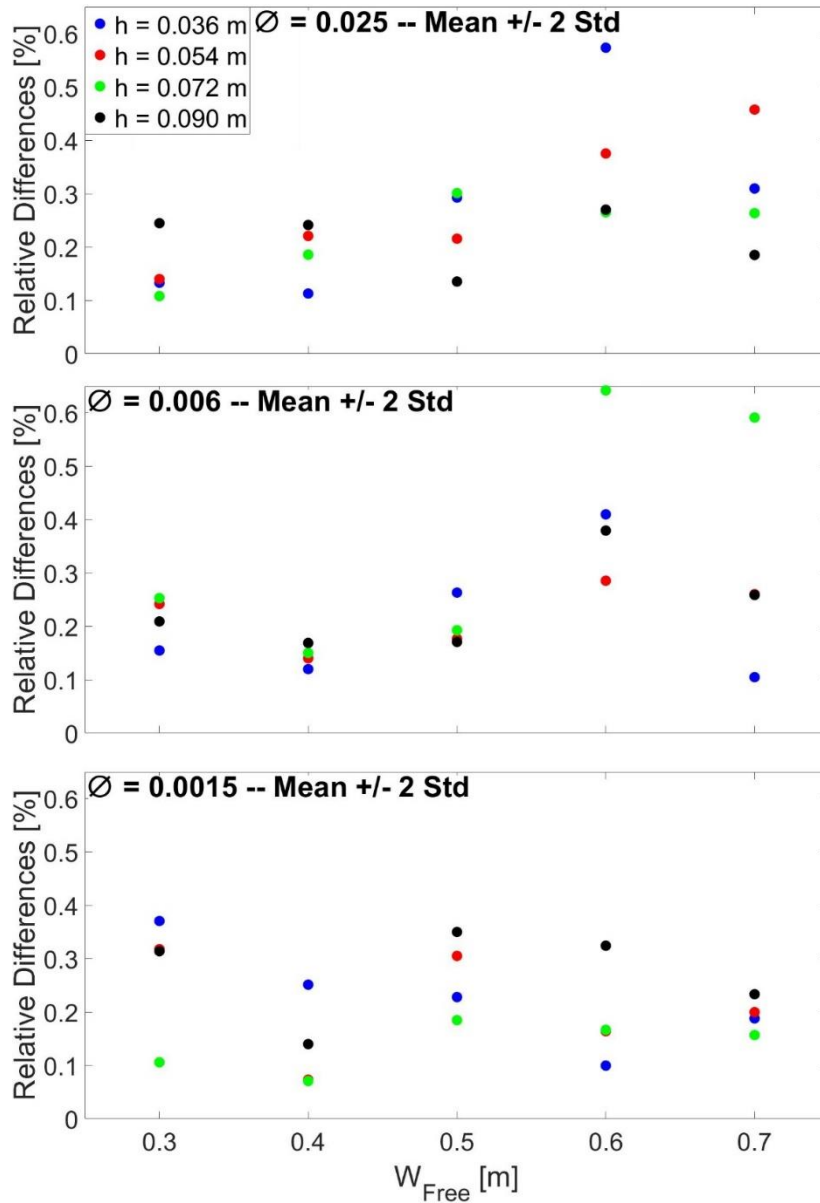
Figure 6.54. Mean absolute relative differences between predicted and experimental concentration profiles considering a region of $\mu \pm 2$ std.

Results shown in **Figure 6.53** and **Figure 6.54** show higher absolute relative differences for $\emptyset = 0.025 - 0.7$ m and 0.6 m tests. In addition, results suggest a decrease of differences when free gap between vegetated banks W_{Free} decrease, in agreement with correlation results.

Santiago Rojas Arques
Department of Civil and Structural Engineering

6.4. Results Summary

In this chapter, the new cost-effective measurement technique developed in **Section 4** and validated in **Section 5** is used to record time-averaged surface velocity fields and time-average vertically well mixed continuous injections to analyse the effects of artificial vegetated banks on longitudinal velocity shear layers and the variation of transverse mixing.

Results from experimental data recorded for one artificial vegetated bank tests, and those obtained from previous works (**White and Nepf, 2008** and **West, 2016**); are used to propose a new model to predict time-averaged longitudinal velocity profiles and variable transverse mixing profiles within a transversally orientated shear layer.

The length of the different parts of the shear layer and the position of the inflection point are predicted based on the vegetation density and the velocity difference between the vegetated and non-vegetated regions. Longitudinal velocity profiles predicted by the proposed model give good results, with Pearson correlations between them and experimental data no lower than 0.938 for $\emptyset = 0.0015$, 0.944 for $\emptyset = 0.006$ and 0.981 for $\emptyset = 0.025$ respectively.

Moreover, the new model predicted the variable transverse mixing coefficient profile within the shear layer, in which a skewed Gaussian shape is proposed and the maximum transverse mixing coefficient is predicted based on the velocity differences between the vegetated and non-vegetated regions and the water depth. The rest of parameters needed to define this profile are obtained based on the shear layer profile. Predicted concentration profiles are compared against experimental data, obtaining a Pearson correlation no lower than 0.962 for $\emptyset = 0.0015$, 0.970 for $\emptyset = 0.006$ and 0.958 for $\emptyset = 0.025$ respectively. In addition, absolute relative differences obtained from this comparison are around 15 %. However, the model cannot predict some mass displacements into the vegetation boundary for densest scenarios recorded in experimental data. This displacement may be produced by secondary currents, which seem to depend on the velocity difference between the vegetated and non-vegetated regions as higher effects are observed in densest and deeper tests. Nevertheless, the results show an accurate prediction of concentration profiles along the shear layer produced by an artificial vegetated bank.

The results obtained in **Section 6.2** show the differential velocity created by the presence of a vegetated bank produces an increase in the transverse mixing within the shear layer, producing a variable transverse mixing profile along the channel width. In addition, results suggest that a skewed Gaussian is a good approximation to define this variable profile. This increase of mixing seems to be related directly with the shape of the shear layer, and with the velocity difference between the vegetated and non-vegetated region and the water depth.

Then, experimental time-averaged longitudinal velocity and concentration profiles are recorded from tests in which two artificial vegetated banks are considered, reducing the non-vegetation region between them in **Section 6.3**. These experiments present a first approach to understand how the shear layers created by each vegetated bank interact when the distance between vegetation boundaries decreases. In addition, the proposed model explained in **Section 6.2** is validated against this new dataset.

The newly proposed model produces a good prediction of longitudinal velocity profiles compared with experimental data for those scenarios where the non-vegetation region between both banks is wide enough to allow a full development of both shear layers. For narrower non-vegetation regions, experimental results show a decrease of maximum longitudinal velocity

Santiago Rojas Arques
Department of Civil and Structural Engineering

achieved in the centre of the non-vegetated region, which depends on the vegetation density and the width ratio $W_{Free}/2\,\delta_{Outer}$. In addition, the shape of velocity profiles approaches to a parable.

In addition, the variable transverse mixing coefficient profiles are predicted and concentration profiles generated by them are compared against experimental data. Predicted transverse mixing profiles suggest that the decrease of the non-vegetated width, and thus the overlapping of both shear layers, produces a decrease of the maximum transverse mixing coefficient achieved, but an overall increase of the mixing rate within this region compared with one artificial vegetated bank scenarios. Predicted concentration profiles are compared against experimental data. Results from $\emptyset = 0.025$ show the same displacement of concentration mass to the vegetation boundaries as that observed for one vegetated bank. This effect is more significant for the widest non-vegetation region and deepest flow, and decreases once the vegetated banks become closer. Therefore, Pearson correlation for these tests show values around 0.91 and relative differences around 20 to 35 % for those scenarios where this displacement is observed. However, once the vegetated banks become closer and these secondary currents seem to be reduced, Pearson correlations no lower than 0.97 and absolute relative differences around 10 to 20 % are achieved.

For $\emptyset = 0.006$ concentration profiles, this displacement is minimal and Pearson correlation no lower than 0.96 are achieved for all scenarios. In addition, absolute relative differences obtained are around 5 to 20 %, confirming an accurate prediction of concentration profiles by the proposed model. Finally, $\emptyset = 0.0015$ results comparison show a high goodness in the prediction, although a general over-mixing of predicted concentration profiles is observed.

Therefore, a new model is proposed to predict both longitudinal velocity and variable transverse mixing coefficient profiles within the shear layer produced by artificial vegetated banks, based on simple analytical expressions and for a range of vegetation density of $\emptyset = 0.0015 - 0.025$. The model only requires information about the mean longitudinal velocity within the vegetated and non-vegetated regions, the vegetation density and the water depth. Predicted results show a good accuracy compared with experimental data, although mismatching is observed for the densest scenarios, where some secondary currents produce a displacement of the mass concentration to the vegetated boundary.

Santiago Rojas Arques
Department of Civil and Structural Engineering

7. Application of the Model

In this section, proposed predictions of mixing processes in channels with vegetated banks introduced in **Section 6.2** and **Section 6.3** are applied to a hypothetical scenario. The aim of this section is to study if the increased mixing caused by vegetated banks is of sufficient scale to have a notable and considerable impact on the mixing of a soluble material over and above that of a non-vegetated channel. In that case, such a vegetated system might have a role to play in mitigating river impacts from events such as CSO spills.

7.1. River Conditions

The scenario to be tested is based on the river characteristics of the Upper Narew River in the northeast of Poland. This river was chosen because its characteristics were well-defined by **Rowiński et al., (2008)** and it represents a good example of a natural river with a relatively small slope, similar to the laboratory experiments reported in this thesis. In addition, this river presents shallow flow conditions ($W_d/h \geq 10 - 20$), which agrees with flow conditions used during tests described previously in this thesis. Based on the real river characteristics (**Rowiński i et al., 2008**), a straight channel is assumed with a constant rectangular section along the studied length. In addition, a basin non-dimensional constant transverse mixing coefficient is assumed for a non-vegetated flow based on results obtained in **Section 6.1.2**. The channel is defined with the following parameters:

- Flow rate $Q = 0.75 \ \text{m}^3/\text{s}$
- Channel slope $S_o = 0.002$
- Channel width $W_d = 6 \ \text{m}$
- Manning's coefficient $n = 0.02$
- Non-dimensional transverse mixing coefficient $D_y/hu^* = 0.13$

An initial analysis is conducted assuming no vegetation is present. Based on the measured characteristics above, a uniform water depth and constant longitudinal flow velocity are obtained by Manning's equation introduced in **Section 2.1 (eq. 2.9.)**, obtaining $h = 0.18 \ \text{m}$ ($W/h = 33.33$) and $U = 0.69 \ \text{m/s}$. In addition, a constant spill of a non-reactive pollutant is introduced into the system and its evolution is studied downstream of the injection source (**Figure 7.1** and **Figure 7.2**). The pollutant is represented as a Gaussian shape in the cross section, assumed steady in time and vertically well-mixed, so only transversal mixing processes are considered.

The water depth, the longitudinal velocity and the transverse mixing coefficient are considered constant along the spanwise direction. A steady state, vertically well-mixed injection located in the centre of the spanwise ($y_{Centre} = 3 \ \text{m}$) was considered. The F.D.M. proposed in **Section 6.1.2** is applied to predict pollutant concentration downstream over $100 \ \text{m}$ of the injection point as shown in **Figure 7.2**

Santiago Rojas Arques
Department of Civil and Structural Engineering
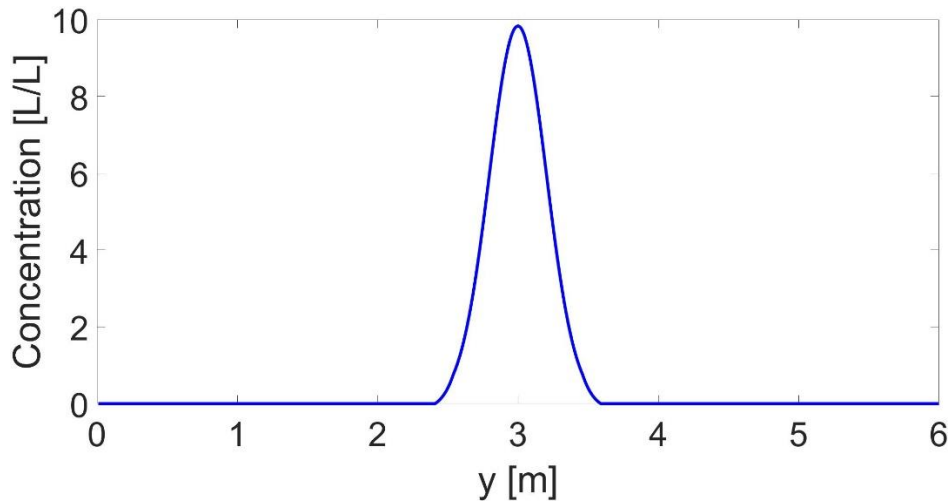
Figure 7.1. Upstream boundary condition of injected pollutant.
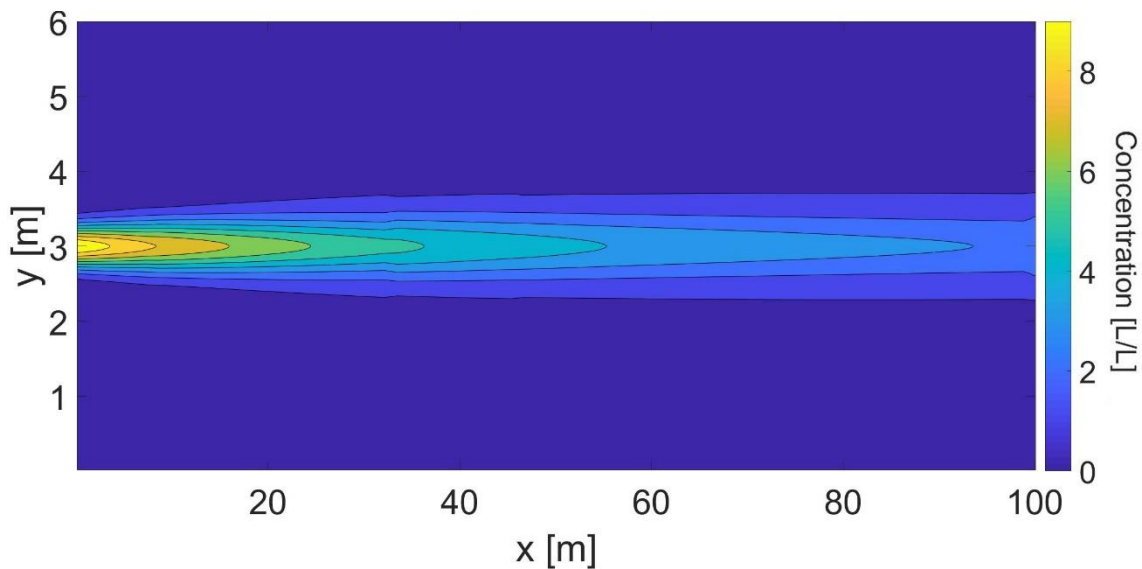
Figure 7.2. Prediction of concentration along 100 m downstream of the injection point for a spill located at $y = 3$ m.

The decrease of the maximum concentration value along the downstream direction is considered as the studied parameter for all scenarios proposed in this section to analyse the effects on the watercourse by the pollutant spill. **Figure 7.3** shows the decrease of maximum concentration value (C_{Max}) along the channel length, normalised by the maximum concentration at the injection point $(C_{Max-Spill})$.

The parameter L_{50} is obtained as the length downstream from the injection point needed to decrease the maximum concentration value by 50 %. This parameter is $L_{50} = 37.7$ m for the injection located at y_{Centre} with no vegetation.

Santiago Rojas Arques
Department of Civil and Structural Engineering
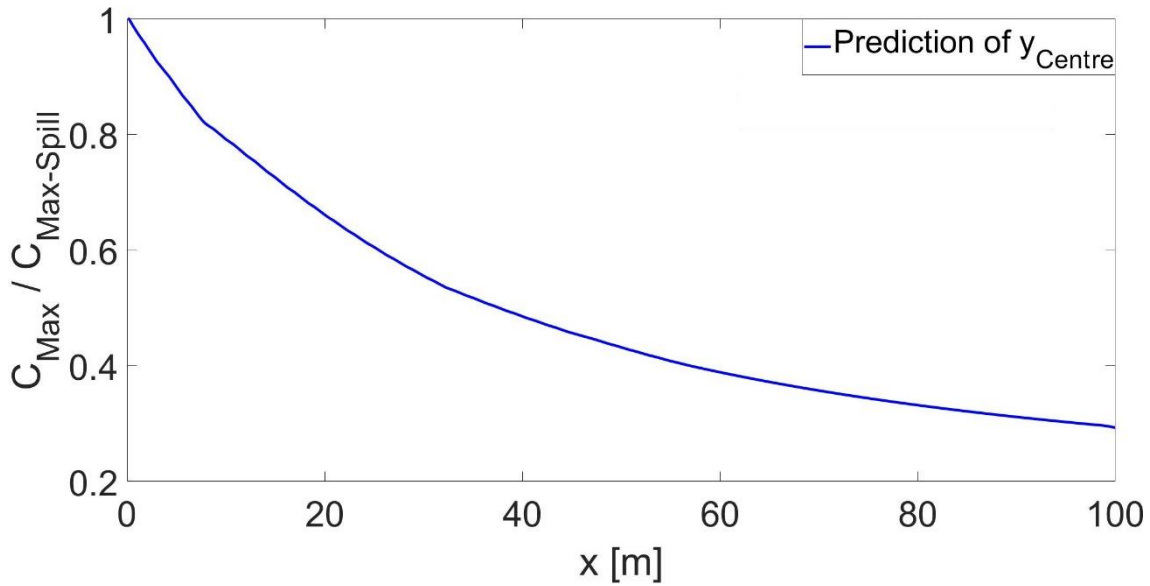
Figure 7.3. Normalised maximum concentration values for predicted concentration profiles along the channel length.

7.2. Single Vegetated Bank Condition

In this section, a single vegetated bank is introduced into the channel and the predicted effects on mixing processes and water depth (linked to flood potential) are compared with the previous non-vegetated scenario. Vegetated characteristics are based on common reeds (*Phagmites Australis*). This species is usually found in the U.K. and Europe and is observed in river banks with channel slopes between $S_o = 0.01 - 0.001$ (**Haslam, 1934**). Several researchers have studied flow resistance in laboratory channels using this type of vegetation instead of artificial vegetation (**James et al., 2004**, **Jordanova et al., 2006**, **Shucksmith et al., 2010**), with typical mean stem diameters of approximately $d = 0.007$ m.

Jordanova et al. (2006) applied the simulation model proposed by **James et al (2004)** to study drag coefficient produced by this type of vegetation for stem scale Reynolds number $Re_{stem} = 246 - 5838$. They proposed a relationship to obtain the effective drag coefficient (C_{D_e}) as a function of the stem scale Reynolds number.

$$C_{D_e} = \alpha_{C_D} Re_{stem}^{\beta_{C_D}} \qquad eq.\,7.1$$

Where α_{C_D} and β_{C_D} are empirical coefficients that depend on the foliage of the vegetation as shown **Table 7.1.**

Table 7.1 Values proposed by **Jordanova et al. (2006)** for parameters α_{C_D} and β_{C_D}.

Description	α_{C_D}	β_{C_D}
Stem only	30.3	-0.38
$3 - 6$ leaves	999.58	-0.80
Full foliage	209.9	-0.58
Upper limit	1241.2	-0.79
Lower limit	10.35	-0.28
Average	114.79	-0.62

- 167 -

Based on these results, a vegetated bank is now considered with a constant vegetated width $W_{Veg} = 2$ m along the full channel length. The same flow rate and channel parameters as in the non-vegetated scenario are considered and different vegetation densities are analysed in the range of $\emptyset = 0.001 - 0.15$. A mean stem diameter $d = 0.007$ m is considered based on stem diameters recorded by previous researchers (**James et al., 2004**, **Jordanova et al., 2006**, **Shucksmith et al., 2010**).

Water depth and longitudinal velocity profile along the spanwise direction for each vegetation density are calculated. A simple optimization routine is developed using Matlab function *fmincon* to find an optimum water depth h that produces a flow rate equal to $Q = 0.75$ m^3/s following the procedure:

- For a given water depth h_i, an initial flow velocity within vegetation is considered U_{veg0}.
- Based on this vegetated velocity, the average value of stem scale Reynolds number and drag coefficient are obtained within the vegetated bank using the expression and coefficients proposed by **Jordanova et al (2006)** (**eq. 7.1 and Table 7.1**).
- Longitudinal velocity within the vegetation is now obtained using the expression introduced in **Section 2.2.3** (**White and Nepf, 2008**) in **eq. 2.26**.
- This procedure is performed for different U_{veg0} values until **eq. 7.2** is satisfied, obtaining U_{Veg}.

$$\frac{abs\left(U_{veg0} - U_{Veg\ Result}\right)}{U_{Veg\ Result}} < 0.1\ \% \qquad\qquad eq.7.2$$

- Longitudinal free flow velocity (U_{free}) is obtained using Manning's equation for the given h_i.
- Longitudinal velocity profile along the spanwise direction is obtained using the proposed method introduced in **Section 6.2.1** (**eq. 6.9** to **eq. 6.12**) by using the free flow velocity (U_{free}) and the longitudinal velocity within the vegetation ($U_{Veg\ Result}$) obtained in previous steps. The flow rate is calculated ($Q_{Solution}$) by integrating the longitudinal velocity over the width.

The full procedure described is run until the objective function $abs(Q_{Solution} - Q)$ is minimised, where Q is set at 0.75 m^3/s, obtaining a water depth and a longitudinal velocity profile along the spanwise direction for each vegetation density. However, in **Table 7.1** it is shown that vegetated parameters proposed by **Jordanova et al. (2006)** depend on plant state (i.e. the amount of foliage and its distribution). Thus, for each vegetation density (represented with the solid volume fraction $S.V.F. = \emptyset$) three different water depths and velocity profiles are calculated by considering average, upper and lower limit values proposed in **Table 7.1**. The water depth results are plotted in **Figure 7.4** and example transversal profiles of longitudinal velocity flow are plotted in **Figure 7.5**.

Santiago Rojas Arques
Department of Civil and Structural Engineering
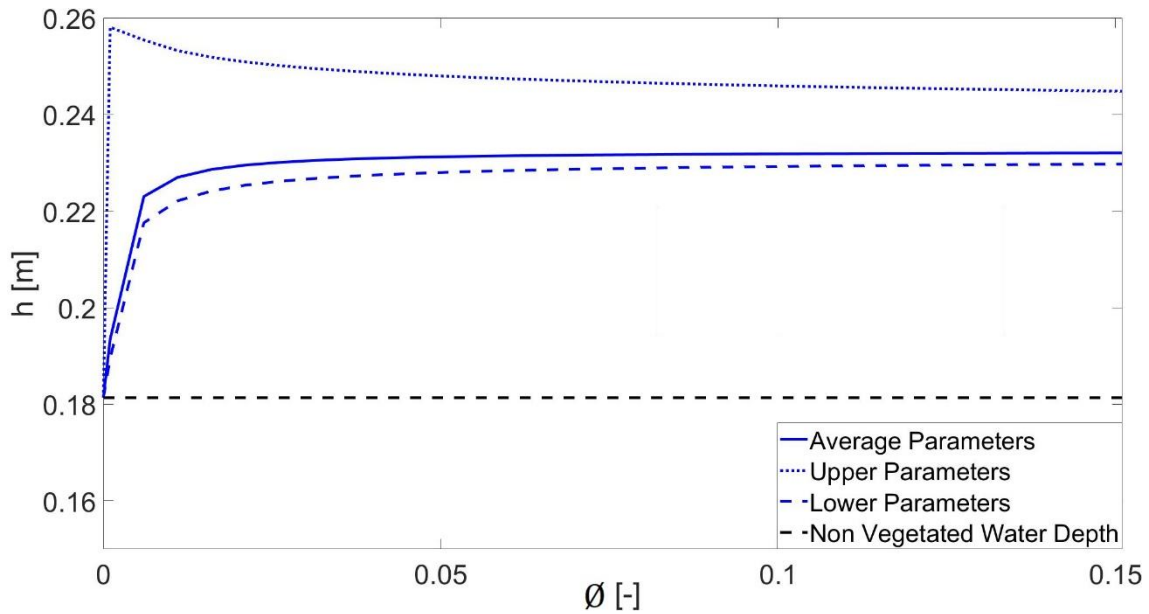
Figure 7.4. Variation of water depth for different vegetation densities.
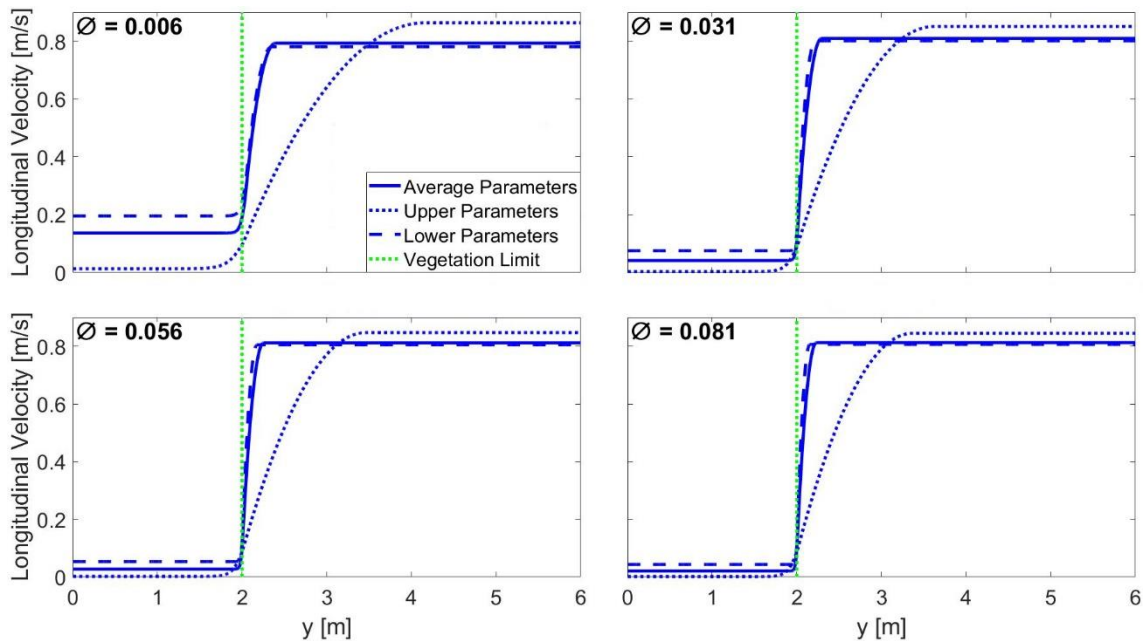
Figure 7.5. Prediction of transversal profiles of longitudinal velocity for different vegetation densities.

Figure 7.4 shows the increase of water depth related with the increase of vegetation density for a fixed vegetated bank width. In addition, **Figure 7.5** shows some examples of predicted transversal profiles of longitudinal velocity for selected vegetation densities. The results plotted in each figure are obtained by considering the average, upper and lower limit values for parameters shown in **Table 7.1.** Results show a wide variability in results, suggesting a strong dependence on drag coefficient. In addition, results in **Figure 7.4** show a different behaviour of the upper parameters results from the rest. This difference may be produced by the prediction of the drag coefficient, which affects the resulting U_{Veg} and therefore the full longitudinal velocity profile. This effect is higher for sparser vegetation density as can be observed in **Figure 7.5** for $\emptyset = 0.006$, where the predicted U_{Veg} for the upper parameters is lower compared with the other two cases, resulting in a different shape for the longitudinal

- 169 -

velocity profile. Therefore, the drag coefficient seems to be a key parameter that must be accurately defined. Results plotted in **Figure 7.4** suggest that the increase of water depth is highly affected by the presence of a vegetated bank, with a maximum increase of 42% above non-vegetated conditions. However, as the vegetation density increases above $\emptyset = 0.04$ the water depth is not significantly increased further.

Predicted longitudinal velocity profiles are then used to predict transverse mixing coefficient profiles along the spanwise direction for each density using the procedure explained in **Section 6.2.2.** Example profiles are plotted in **Figure 7.6**
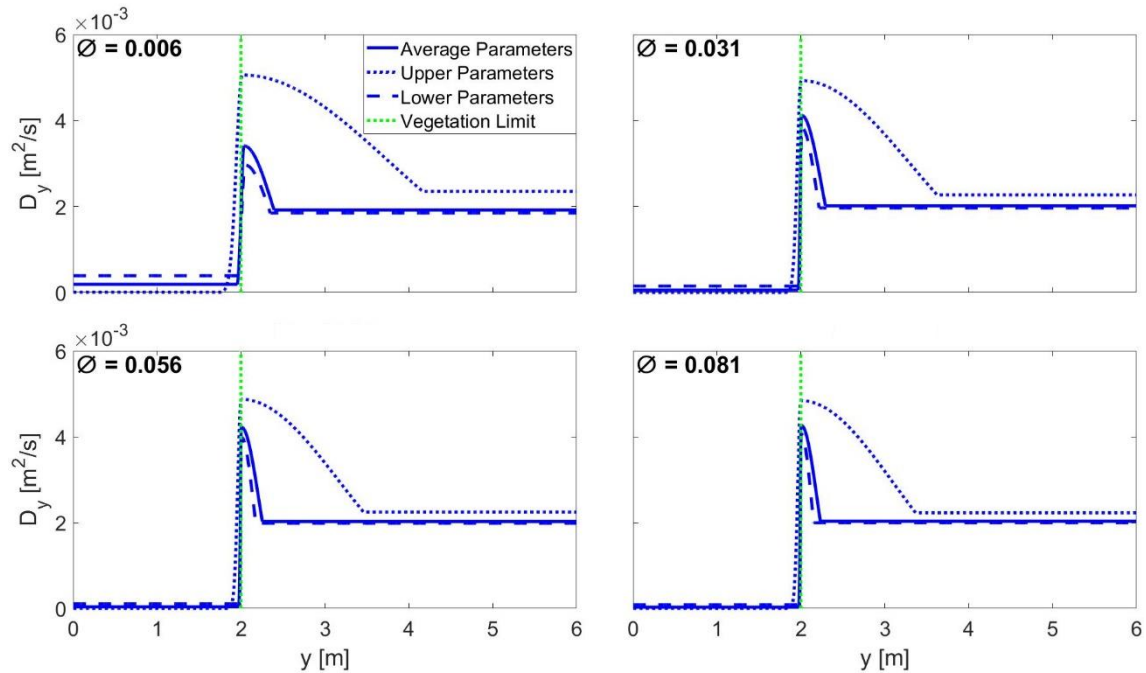
Figure 7.6. Prediction of transversal profiles of transverse mixing coefficients for different vegetation densities and foliage characteristics.

Non-dimensional mixing coefficient D_y/hu^* is assumed to remain constant over the width in the free flow region away from the vegetated bank as the main channel characteristics remain constant. **Figure 7.6** shows a high variability between foliage characteristics in the value of predicted $D_{y_{max}}$ and the length of the variable transverse mixing profile. This variability suggests that the effect of vegetated banks are sensitive to the type and characteristics of the vegetation.

Finally, predicted values of longitudinal velocity, transverse mixing coefficient and water depth obtained for each vegetation density scenario are introduced into the F.D.M. and concentration profiles are predicted $100\,\text{m}$ downstream of the initial concentration profile (**Figure 7.7**). For each vegetation density, three different spill locations are considered along the spanwise direction. As in the non-vegetated flow prediction, a first injection is considered at $y_{Centre} = 3\,\text{m}$. Then, one injection position is considered within the shear layer at $y_{Shear} = 2.5\,\text{m}$ and a last one within the vegetated bank at $y_{Bank} = 1\,\text{m}$. Each predicted concentration distribution is obtained considering both the average, upper and lower foliage parameters obtained previously.

Santiago Rojas Arques
Department of Civil and Structural Engineering

Figure 7.7 shows concentration map distributions predicted for each injection position for a vegetation density $\emptyset = 0.056$. The vegetated edge is represented by white dots.
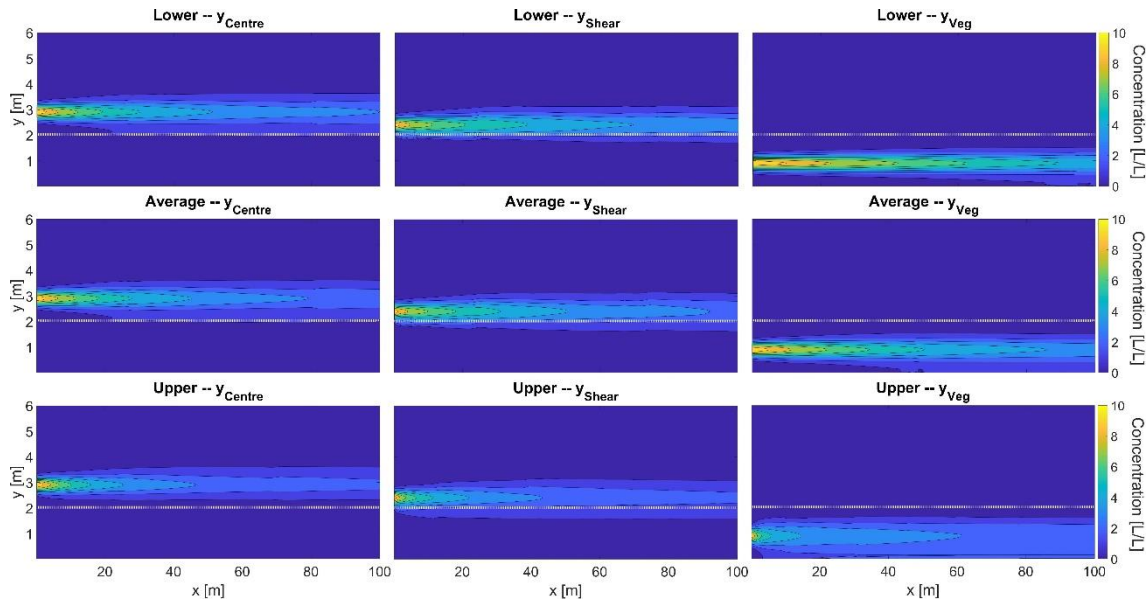
Figure 7.7. Predicted concentration maps for an injection located at the centreline of the channel (left), within the shear layer (centre) and inside vegetated bank (right) for a $\emptyset = 0.056$.

Results plotted in **Figure 7.7** show differences between concentration distributions for the same injection position but different input parameters (upper, average or lower parameters obtained by considering different α_{C_D} and β_{C_D} values). These differences are higher for the injection within the vegetated bank. In addition, concentration maps show the spreading of the plume is lower for the injection located within the vegetated bank, and similar results for different foliage parameters are obtained for those injections located in the centre of the channel and within the shear layer.

The decrease of predicted maximum concentration normalised by the maximum concentration at the source along the channel length is plotted in **Figure 7.8** for the same vegetation density $\emptyset = 0.056$.

Santiago Rojas Arques
Department of Civil and Structural Engineering
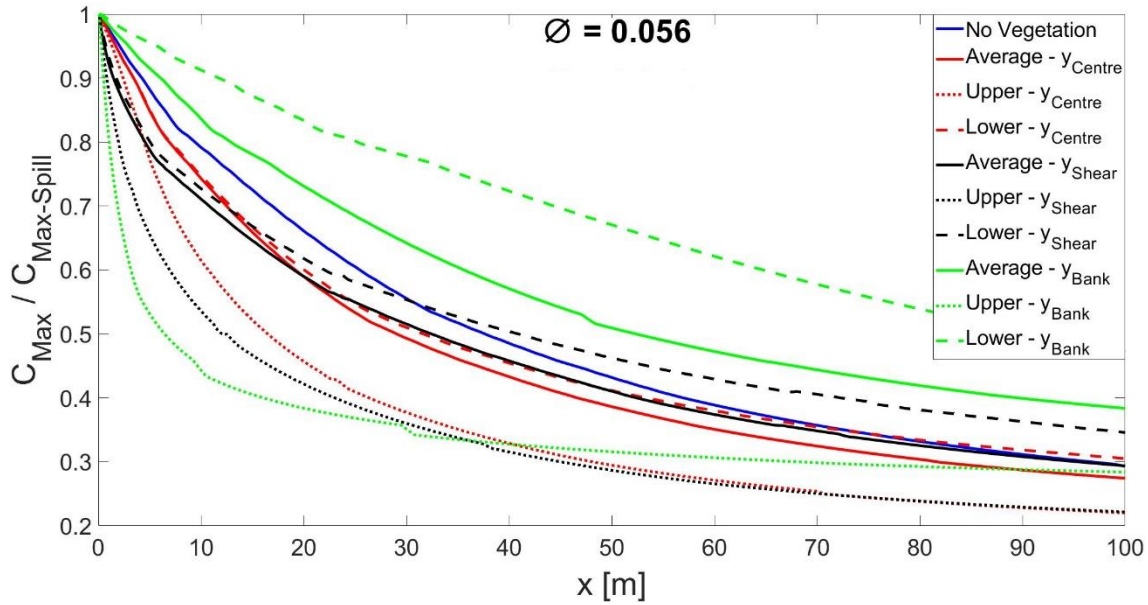
Figure 7.8. Decrease of normalised maximum concentration values along the channel length for different injection points and a fixed vegetation density.

In **Figure 7.8**, the decrease of normalised maximum concentration values is plotted for each spill position for the same vegetation density. The results are obtained by considering average, upper and lower limit foliage parameters from previous steps. In addition, the results obtained for an injection in the centre of the channel with no vegetation are plotted.

Results suggest a higher decrease of maximum concentration value for those injections located at y_{Centre} and y_{Shear}. However, a high variability between foliage characteristics is also obtained for these results, which seems to increase for those injections closer to the vegetated bank. In addition, a lower decrease of maximum concentration values is observed for the injection within vegetation compared with the non-vegetated scenario. Results suggest that the presence of a vegetated bank increases the decay of maximum concentration value if the spill is not produced within vegetation. However, the results seem to be quite sensitive to the drag coefficient considered in the first step, and thus, to the type and state vegetation considered.

In addition, **Figure 7.9** shows the decrease of predicted maximum concentration normalised by the maximum concentration at the source along the channel length for different vegetation densities and with the injector located at y_{Shear}. In this figure it is observed that, although there is a high variability in results for different foliage parameters, results do not change significantly for an increase of vegetation density.

Santiago Rojas Arques
Department of Civil and Structural Engineering
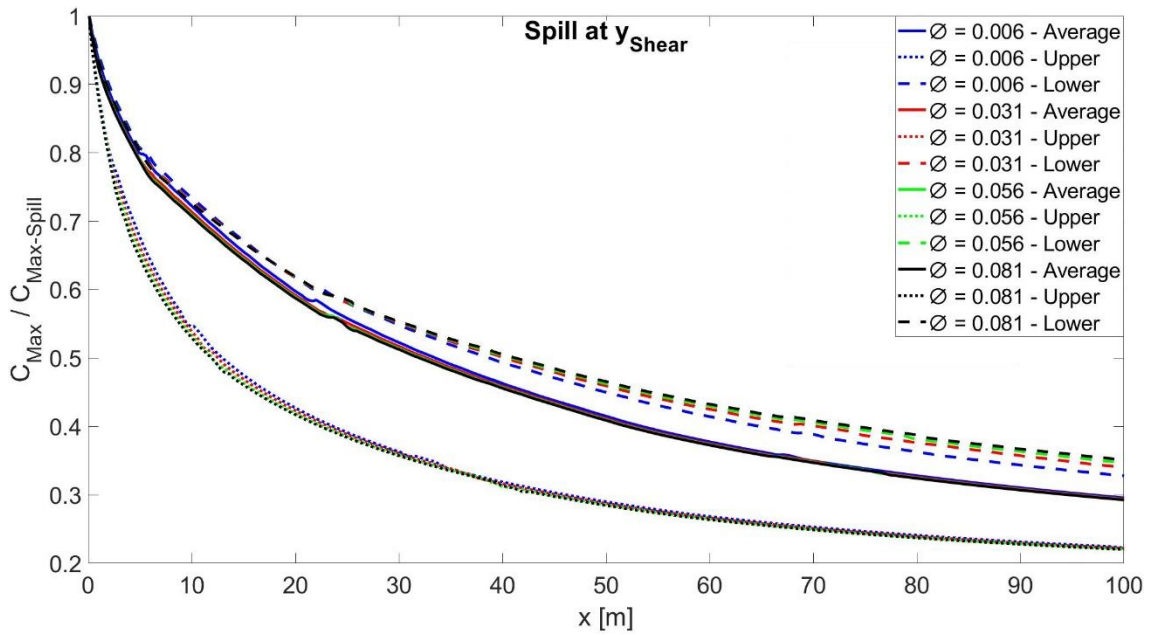
Figure 7.9. Decrease of normalised maximum concentration values along the channel length for a fixed injection point and different vegetation densities.

Finally, for the y_{Centre} and the y_{Shear} scenario, the lengths needed to achieve a maximum concentration value smaller than the 50 % (L_{50}) are obtained for each vegetation density (**Figure 7.10**). The results obtained for non-vegetated conditions are also presented for comparison.
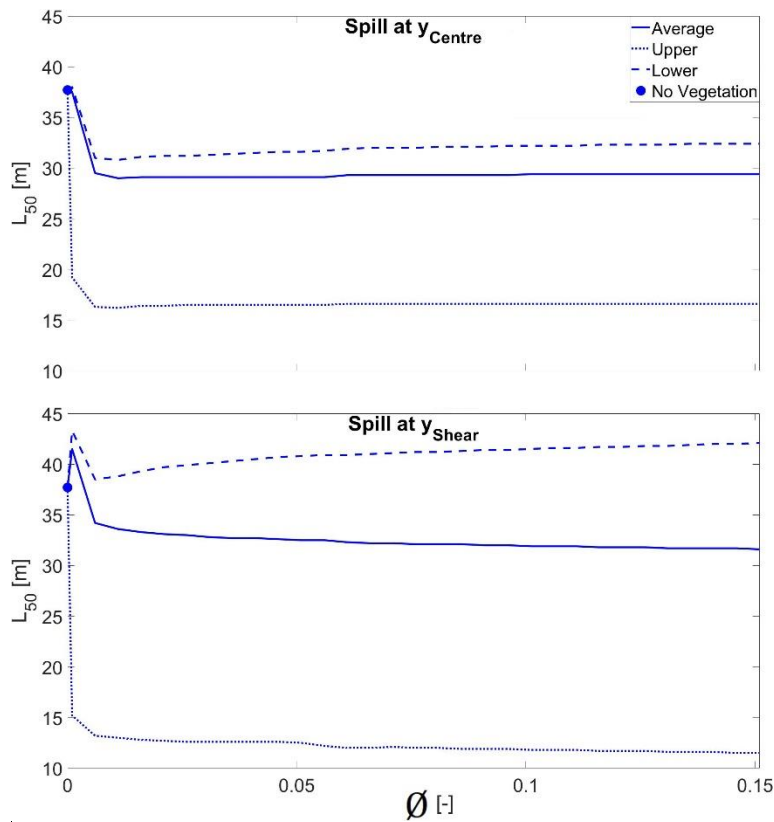
Figure 7.10. Predicted L_{50} for a spill located in the centre of the channel (up) and within the shear layer (down) for different vegetation densities.

Santiago Rojas Arques
Department of Civil and Structural Engineering

Figure 7.10 shows the lengths needed to achieve a maximum concentration value smaller than the 50 % (L_{50}) for the injection positions at the centre of the channel and within the shear layer plotted in **Figure 7.8** for different vegetation densities. Continuous, dots and dashed lines represent the results by considering average, upper and lower values for drag coefficient values showed in **Table 7.1** respectively. In addition, the blue circle plotted at $\emptyset = 0$ represents the L_{50} value for no vegetation conditions obtained in **Section 7.1.**

Results suggest that, for a given river under some assumptions (straight channel and constant transversal section and slope), the presence of a vegetated bank seems to increase transverse mixing processes. **Figure 7.10** suggests that, once a high enough density is achieved ($\emptyset = 0.031$), there is not a significant further increase of solute spreading for denser vegetation. In addition, **Figure 7.10** shows a sudden increase of the value L_{50} for the injection point y_{Shear} at $\emptyset = 0.001$. This increase is only observed for this specific case, and may be produced because of the prediction of the U_{Veg} for this sparse case, which could produce a sudden decrease of variable $D_{y_{Veg}}$, affecting the result. In addition, the prediction of the drag coefficient seems to play a key role in the prediction of mixing processes, demonstrating the importance of the type and state of vegetation considered.

7.3. Summary

A scenario based on a real river is tested under the assumption of one constant vegetated bank along the channel length. The proposed model introduced in **Section 6** is applied to predict transverse profiles of both longitudinal flow velocity and variable transverse mixing coefficients. Finally, the decay of maximum concentration along $100 \, \text{m}$ downstream for different injection positions is studied.

Results show that the presence of one vegetated bank induced an increase of transverse mixing for an injection located around the shear layer compared with the no vegetation condition, reducing the maximum concentration values and the ecological impact of a pollutant spill. However, the spreading of the solute injected within the vegetated bank decreased compared with the non-vegetated condition as the longitudinal velocity and the transverse mixing coefficient is reduced within the vegetated bank. In addition, results suggest that this increase of spreading does not depend on vegetation density once it achieved a certain value ($\emptyset = 0.031$); for denser vegetated banks an increase of the spreading is not observed. In addition, results seem to depend strongly on the drag coefficient considered at the first step, and hence on the type of plant present on the river. Results obtained show that the distance L_{50} can be reduced (by between 22 to 68 %) due to the presence of a vegetated bank, suggesting that this configuration could be useful to mitigate impacts from CSO spills.

Santiago Rojas Arques
Department of Civil and Structural Engineering

8. Discussion

A critical evaluation of the cost-effective method and the proposed model is discussed in this section. Moreover, the limitations and uncertainties that determine the applicability and the reliability of the results are discussed, as well as the implications that these relationships may have in future research.

This thesis has presented the development of a new measurement technique, which allows the recording of 2D surface velocity fields and depth-averaged concentration distributions in shallow water flows. The main goal of this technique is to provide a cost-effective method to study the coupled hydrodynamic and mixing processes in this work and future research using a combination of PIV and PCA techniques.

The PIV technique is based on the identification of tracers flowing within a fixed recorded area in consecutive frames to obtain an instantaneous velocity vector that represents the flow at number of small areas. This technique has been used in previous work (**Weitbrecht et al., 2002; Muste et al., 2004; Novak et al., 2017; Beg et al., 2020**) and it allows the characterisation of the surface flow in large recorded areas, requiring less time than other techniques such as those that use ADV probes. However, this technique only allows the obtaining of surface velocity, and thus no information of the velocity in the vertical direction or the lateral velocity below the surface can be obtained. Moreover, the resolution of the results depends on the resolution of the cameras. In addition, objects in the flow can produce some blind spots in which the cameras cannot record the tracers. This effect is more pronounced when the objects are not located just below the cameras, but on the edges of the recorded frames. This effect can be produced in very dense vegetated areas on the banks. To solve this effect, it would be required the installation of parallel arrays of cameras over the cross-section, or by using transparent vegetation. The technique has been used in this thesis to obtain the mean longitudinal velocity for different vegetated scenarios, providing suitable results to study the influence of vegetated banks on the flow in the central, non-vegetated section. In addition, further investigations can be carried out in order to study the instantaneous velocity (rather than time-averaging as in this thesis) in both directions to improve the understanding of these scenarios. These deeper works may be accompanied with a study of how the different steps taken in the analysis of recorded frames (see **Section 5.1**) could affect the instantaneous velocity results.

The PCA technique is based on the absorbance of a specific range of the light spectrum by a tracer released in the flow. In this thesis, the tracer used is Rhodamine WT, but the technique allows the use of other substances with similar properties, which increases the versatility of the system. Note that the light system used depends on the type of tracer discharged, and thus the dye calibration may vary from one substance to another. The PCA technique allows the recording of steady-state injections and pulse injections, increasing the type of research that can be carried out. Moreover, the technique presents a rapid way to obtain the concentration data compared with other methods such as fluorometer devices (**Pilechi et al., 2016; Seo et al., 2016**) or conductance meters (**Colombani et al., 2015**). In addition, larger areas can be recorded than those methods that require the use of lasers (**Nepf et al., 1997; Hilderman an Wilson, 2006**). This thesis shows that one of the most important factors to record accurate concentration data is the light system, which should provide a homogenous intensity distribution avoiding the presence of strong reflections. These reflections are produced on the surface of the flow, and may be increased by the presence of strong turbulences in the flow.

Santiago Rojas Arques
Department of Civil and Structural Engineering

Therefore, future works should be carried out to study if the increase of turbulence, and hence the increase of flow irregularities on the water surface, may have a significant impact on the quality of recorded data. Moreover, the PCA technique assumes a depth-averaged concentration distribution, and thus it is suitable for shallow water flows. However, the technique may be not suitable for those scenarios in which a strong concentration gradient within the water depth is produced. Moreover, same problem as the PIV technique may be produced with blind spots, requiring the use of parallel arrays of cameras or transparent vegetation.

This measurement technique has been validated against measurements recorded using different methods, confirming the suitability of the technique to obtain velocity and concentration distribution information in shallow water flows. This technique provides new tools to study the hydrodynamic and mixing processes in different scenarios for future researchers. Moreover, this technique presents a reduction in the hardware cost compared with other comparable PIV measurement techniques. The proposed measurement system only requires the installation of standard cameras, in this case GoPro cameras; some LEDs light arrays and a reflective and dispersive material to improve the light intensity distribution. For the analysis of PIV frames, the commercial software Dynamic Studio was used. However, other cheaper options are available in the market such as PIVlab from Matlab (**Thielicke and Stamhuis, 2014**).

The novel measurement technique is used to obtain the mean longitudinal velocity and the concentration distribution of steady state injections in flows with vegetated banks. Empirical relationships are obtained from the relationships between experimental data and the designed flow conditions (i.e. water depth, vegetation density and velocity increment). Based on these relationships, an analytical model is proposed and validated to predict longitudinal velocity and concentration distributions in rivers for different vegetated conditions. Moreover, the effects of a vegetated bank on the enhancing of transverse mixing processes have been studying considering a hypothetical scenario.

The model proposed in this thesis provides a method to estimate the mean longitudinal flow velocity in rivers with vegetated banks, which also allows the estimation of the vegetated effects on the flow compared with a non-vegetated flow. These effects include the increase of the water depth and the velocity increment between the vegetation and the free open flow region. Previous work has proposed different models to predict the flows under these scenarios. However, these models usually demand the obtaining of empirical coefficients defined experimentally such as the slip position between the inner and the outer layer and its velocity (y_m and U_m respectively) defined by **White and Nepf (2007)**; and which are not usually extrapolated to other scenarios. In this thesis, empirical relationships are proposed to estimate the lengths of the shear layer and the position of the inflection point using own experimental data and those recorded in previous work (**White and Nepf, 2007** and **West, 2016**), and thus allowing the use of these relationships in different scenarios. These relationships only require the estimation of the vegetation density and the mean longitudinal velocity within the vegetated bank and in the free flow region, which can be obtained using expressions proposed in previous work. Then, a proposed expression similar to the broadly used expression proposed by **White and Nepf (2008)** is defined to predict the longitudinal velocity profile in flows with a vegetated bank. This expression is based on the estimated lengths of the shear layer and the position of the inflection point, and provides similar results as those using the **White and Nepf (2008)** expression.

Santiago Rojas Arques
Department of Civil and Structural Engineering

In addition, the effects induced by the vegetated bank on the transverse mixing processes are studied. For each flow condition, different steady-state injections are released within the shear layer and the variable transverse mixing profile is optimised for each flow condition. Experimental results show an overall increase of the transverse mixing compared with the non-vegetated flows. In addition, this increase seems to be higher for denser and deeper flow conditions. This trend agrees with previous work (**Ghisalberti and Nepf, 2005; Rubol et al., 2016; West, 2016; West et al., 2020**) and suggests that the presence of the vegetated bank and the corresponding shear layer increase the turbulence intensity and the Reynolds stress within the shear layer and this increase of turbulence enhance the transverse mixing processes. In addition, results suggest that this increase depends on the vegetation density and the water depth, and thus it may depend on the velocity difference produced between the vegetated and the free flow layers.

A skewed-Gaussian shape is proposed to parameterise the transverse mixing profile. This shape is similar to those proposed in previous works (**West, 2016; Sonnenwald et al, 2017; West et al., 2020**) and it is related with the longitudinal velocity profile obtained for each flow condition. Thus, the length of the variable transverse mixing profile is assumed to fit with the length of the shear layer and the position of its maximum value with the position of the inflection point, where the maximum Reynolds stress is expected. In addition, the constant transverse mixing coefficient within the free flow region is assumed to be equal to that obtained for non-vegetated flow scenarios, and the transverse mixing coefficient within the vegetation is estimated using previous expressions proposed by **Nepf (2012)**. Therefore, only the maximum transverse mixing value needs to be optimised for each flow condition. Optimization results agree with experimental data and suggest an increase of the transverse mixing for denser and deeper flow scenarios. A new relationship is found between the optimised maximum transverse mixing coefficient, and the product of the velocity difference between the two co-flowing streams and the water depth. This relationship shows that, for a higher vegetation density or a higher water flow, a higher velocity difference between the vegetated and the free flow regions is produced. This velocity difference increases the turbulent intensity within the shear layer, which enhances the transverse mixing. This new relationship and the proposed expressions to predict the longitudinal velocity profiles are used to estimate the concentration profiles for each test condition. Results are compared against experimental concentration profiles, showing a generally good fit. Largest deviations are observed in cases where there is a lateral movement of the main mass of concentration profiles (i.e. for injections close the vegetation boundary for the denser vegetation tests). This behaviour suggests the presence of a secondary current producing a translation of the solute mass toward the vegetation. In addition, this movement seems to increase with vegetation density and with water depth, suggesting the dependence of this effect on the velocity difference between the vegetated and non-vegetated regions.

In addition, this thesis presents new dataset concerning the hydraulic interaction of two vegetated banks, specifically how the overlapping of the developed shear layers affects the mean longitudinal velocity and the transverse mixing processes. This type of vegetated flow can be found in narrow rivers with vegetation at each side, but no previous work has been found regarding these scenarios. Experimental longitudinal velocity results show that, for wide enough free flow gaps, the two shear layers regarding each vegetated bank can be developed, and a constant free flow velocity is achieved in the centre of the channel. However, for narrower scenarios, an overlapping of the shear layer is produced. This overlapping produces a decrease of the maximum longitudinal velocity in the centre of the channel, which seems to depend on the free flow gap between banks and on the vegetation density. In addition, the velocity profile

- 177 -

no longer exhibit a constant free flow velocity region in the centre, but a parabolic shape is recorded. Moreover, this overlapping effect seems to increase the overall transverse mixing processes within the free flow gap. By taking into account this reduction of the free flow velocity, the proposed model seems to reproduce the mean longitudinal velocity profile and the concentration distribution as the comparison against experimental data suggests. However, further investigations may be carried out to improve the understanding of this type of vegetated flow, including the study of secondary currents and the characterization of the turbulent structures.

Finally, a study of a hypothetical scenario discussed in **Section 7** suggests that the presence of a vegetated bank can meaningfully increases the transverse mixing for those plumes discharged within the shear layer. This increase of transverse mixing seems to be independent on the vegetation density, and the effect of the vegetated bank remains quasi-constant for an increase of the density once it achieves a certain value. Therefore, this model provides a useful making-decision tool for the management of watercourses. The goal of this model is to provide accurate results without the requirement of collections of experimental data or the use of time-demanding models. The model only needs information regarding the vegetated bank, the channel size and the flow rate or the water depth, as those proposed models for submerged vegetated flows (**Battiato and Rubol, 2014; Rubol et al., 2016**). For future research, the estimations produced by the model may be compared against experimental data recorded from real river scenarios to study the sensitivity and accuracy of the results.

However, due to its simplicity, this model only considers the mean longitudinal velocity component of the flow. Therefore, for those scenarios in where important secondary currents or sinuous meanderings are present, further investigations are needed to quantify the effects of the transverse velocity components. Moreover, the empirical relationships are based on experimental results recorded from flows with artificial vegetation. These cylinders, widely used in previous work to simulate the vegetation (**Nepf, 1999; Stone and Shen, 2002**), represents an idealized vegetated flow scenario, and thus further investigations are needed to compared model results against flow and concentration data recorded in flow with real vegetation. In addition, the model is designed to estimate the dispersion of a steady-state injection, and therefore further investigation must be carried out to see how pulses may be affected by vegetated banks.

Santiago Rojas Arques
Department of Civil and Structural Engineering

9. Conclusion

The main aim of this thesis is to study the influence of vegetated banks on transverse mixing processes to mitigate the impact of pollutant discharges on natural rivers.

Previous researchers have studied the flow influence of a vegetated bank, showing an increase of instabilities in the shear layer generated due to the velocity gradient produced between the vegetation and the free open region. In addition, **West (2016)** showed that these instabilities enhance the transverse mixing within the shear layer. In this thesis, a new approach is developed based on experimental results to relate the variation of transverse mixing within the shear layer and the longitudinal velocity profiles with the main characteristics of the vegetated bank.

A new cost-effective measurement technique was developed to measure both surface 2-D velocity fields and depth-averaged concentration distributions of a solute downstream of an injection point in shallow flows. This new method was validated against traditional point probes (ADV for velocity data and Cyclops for concentration data), showing a good agreement between the new technique and traditional techniques data. This new technique provides both surface velocity and concentration distribution data along a full studied area of 4.48×1.22 m^2, using a non-intrusive, easy to operate technique which allows the simultaneous measurement of both types of data. This enables an increase in the amount of concentration profiles recorded as opposed to previous techniques. Most existing methods are based on lasers, and only obtain concentration information for a limited number of spanwise profiles. In addition, this technique decreases the measurement time, allowing an increase in the number of experiments that can be conducted in a given time frame.

With this new technique, time-averaged longitudinal velocity data and depth-averaged solute concentration distributions downstream of a continuous injection were obtained from flows with a vegetated bank. Based on experimental results and those obtained previously by other studies, a relationship between the shear layer length with the velocity gradient (ΔU) and the vegetation bank density (a) was proposed. The proposed relationship was used to generate longitudinal velocity profiles within a vegetated bank flow with same conditions as previous experiments. In addition, experimental data were fitted using similar expressions to those proposed by **White and Nepf (2008)**. Results from both expressions were compared against experimental data, showing very similar results for both proposed models. Pearson correlations obtained were $R \geq 0.97$ for results fitted with the **White and Nepf (2008)** expression and $R \geq 0.94$ for results obtained from the proposed new relationship.

In addition, variable transverse mixing coefficients were obtained using an optimization routine, fitting the predictive concentration profiles with those recorded experimentally. Results suggest that the skewed Gaussian distribution of transverse mixing coefficient can represent the behaviour of the transverse mixing processes within the vegetated shear layer. In addition, the optimised transverse mixing coefficient profiles reproduced the mixing processes recorded for each test condition. Based on these results, a new relationship between the maximum transverse mixing coefficient ($D_{y_{Max}}$) and the product of the velocity difference and the water depth (ΔUh) was proposed, with the rest of parameters needed to define the transverse mixing coefficient profiles being given by the shear layer parameters. This relationship was used to reproduce concentration distributions and the results were compared with experimental data. Pearson correlations were obtained, with values $R \geq 0.95$ in all cases. In addition, absolute mean relative differences between predicted and experimental concentration distributions

- 179 -

were calculated, obtaining differences smaller than 21 %. These results and a visual comparison between concentration profiles show a good fit between experimental concentration distributions and those obtained with the proposed relationship. However, the experimental concentration profiles recorded close to the vegetation boundary exhibit a movement of the main mass for the densest vegetation tests, probably produced by the presence of secondary currents.

Both relationships were combined to generate a new model that predicted the transverse longitudinal velocity profile and the solute concentration distribution downstream of a continuous injection for a twin vegetated bank flow condition. This model was used to predict results for two vegetated flow conditions with different free gaps (W_{Free}) between both vegetated banks and results were validated against experimental data recorded for same flow conditions. Results show a good correlation between experimental and predicted longitudinal velocity profiles for the denser and medium vegetation density ($\emptyset = 0.025$ and 0.006 respectively), with $R \geq 0.95$. However, some mismatches were obtained for less dense flow conditions ($\emptyset = 0.0015$), with $R \approx 0.82$ for the shallower flow condition. These differences could be produced because the re-adjustment of the longitudinal velocity profile for the sparsest density, which produces a mixing rate lower than that predicted by the model. However, the Pearson correlations and the absolute mean relative differences obtained for the overall set of data suggest a good fit of proposed model to observed velocity profiles. In addition, this section provides a novel dataset describing interacting shear layers between two vegetated banks, which represents a first approach for further works to understand this process and how it affects velocity and mixing.

Concentration profiles were also predicted by the model and results were compared with experimental data in the same way as longitudinal velocity profiles. Pearson correlations obtained between predicted and experimental concentration profiles $R \geq 0.96$ for the sparse and medium vegetation density and $R \geq 0.91$ for the dense vegetation density respectively, suggesting a general good prediction of concentration profiles for all different flow conditions.

In addition, mean, absolute and relative differences were obtained between experimental and predicted concentration profiles. Comparisons show similar mixing behaviour between predicted and experimental concentration profiles. The same mass concentration displacement to the vegetation boundary (as in the one vegetated bank tests) is observed for denser vegetated flows, which is reduced when the vegetation and the water depth decrease. This effect reinforces the hypothesis that some secondary currents were generated for the denser vegetation. However, the results suggest a tolerably good prediction of both longitudinal velocity profiles and concentration distributions predicted by the proposed model. Results show the proposed model can predict longitudinal velocity and transverse mixing coefficient profiles within vegetated shear layers using relatively simple analytical expressions. This model only requires information about the vegetation density, the water depth and the longitudinal velocity within the non-vegetated and vegetated regions, which can be approximated by Manning's equation and from a force balance type equation respectively.

Once the proposed model was validated against experimental data, a scenario based on a real river was tested to study whether the effects of vegetated banks on transverse mixing are notable enough to mitigate pollutant discharge impacts. The drag coefficient induced by the vegetation was obtained by applying the relationship proposed by **Jordanova et al. (2006)** for common reeds. Both the longitudinal velocity and the variable transverse mixing coefficient profiles were predicted for different vegetation densities. Results show that the presence of the

Santiago Rojas Arques
Department of Civil and Structural Engineering

vegetated bank enhances the transverse mixing compared with the non-vegetated condition for those injections located in the free flow region close to the shear layer. This increase seems to be higher if the injection moves far from the vegetation boundary. However, results show that once the vegetation density achieved a certain value, the increase of mixing started to stop and the rate of decay of the maximum concentration value became constant for higher vegetation densities. In addition, results suggest a strong dependence on the drag coefficient, and hence on the type of vegetation and its state of growth.

The last section shows the presence of a vegetated bank induced an increase of transverse mixing for a continuous release located within the vegetated shear layer compared with a non-vegetated flow condition. This increase seems to be independent of the vegetation density once it achieved a certain value ($\emptyset = 0.031$). However, results show a strong dependence of this increase on the type of plant and its state of growth. In addition, the enhancing of mixing rate looks to be higher if the injection point is located close the shear layer but far from the vegetation boundary. Finally, results suggest a mass concentration displacement produced by secondary currents that the model did not predict. Therefore, further studies are required to determine the effect of secondary current on transverse mixing for this type of flow.

Santiago Rojas Arques
Department of Civil and Structural Engineering

References

Adrian, R. (1991) "Particle-imaging techniques for experimental fluid mechanics". *Annual Review Fluid Mechanics,* **23**, 261 – 304.

Andrews, B., Cardenas, M. and Bennett, P. (2011) "Analysis of turbulent nonisothermal mixing between a jet and cooler ambient water using thermal imagery". *Geochemistry, Geophysics, Geosystems*. **12**(7), Q07022.

Arnold, U., Hottges, J. and Rouv, G. (1989) "Turbulence and mixing mechanisms in compound open channel flows". *In Proceedings of the 23th IAHR Congress, Ottawa, ON, Canada.*

Baek, K.O. and Seo, I.W. (2016) "On the methods for determining the transverse dispersion coefficient in river mixing". *Advances in Water Resources*, **90**, 1 – 9.

Bakhmeteff, B.A. (1936) "The mechanics of turbulent flow". *Princeton University Press, Princeton*, 66.

Balachandar, R., Tachi, M.F. and Chu, V.H. (1999) "Concentration profiles in shallow turbulent wakes". *Journal of Fluids Engineering*, **121**(1), 34-43.

Balu, M., Balachandar, R. and Wood, H. (2001) "Concentration estimation in two-dimensional bluff body wakes using image processing and neural networks". *Journal of Flow Visualization and Image Processing*, **8**(2–3), 121–140.

Baptist, M.J. (2003) "A flume experiment on sediment transport with flexible, submerged vegetation". *International Workshop on Riparian Forest Vegetated Channels: Hydraulic, Morphological and Ecological Aspects, RIPFOR, Trento, Italy*.

Battiato, I. and Rubol, S. (2014) "Single-parameter model of vegetated aquatic flows". *Water Resources Research*, **50**, 6358 – 6369.

Beg, M.N.A., Rubinato, M., Carvalho, R.F. and Shucksmith, J.D. (2020) "CFD modelling of the transport of soluble pollutants from sewer networks to surface flows during urban flood events". *Water*, **12**, 2514.

Besio, G., Stocchino, A., Angiolani, S. and Brocchini, .M. (2012) "Transversal and longitudinal mixing in compound channels". *Water Resources Research*, **48**(12), 1 – 15.

Botev, Z., Grotowski, J. and Kroese, D. (2010) "Kernel density estimation via diffusion". *Ann. Stat*, **38**, 2916–2957.

Boxall, J.B. (2000) "Dispersion of solutes in sinuous open channel flows". *PhD Thesis, University of Sheffield.*

Boxall, J.B., Guymer, I. and Marion, A. (2003) "Transverse mixing in sinuous natural open channel flows". *Journal of Hydraulic Research*, **41**(2), 153-165.

Cardenas, M.B., Neale, C.M.U., Jaworowski, C. and Heasler, H. (2009) "High-resolution mapping of river-hydrothermal water mixing: Yellowstone National Park". *International Journal of Remote Sensing*, **32**(10), 2765 – 2777.

Carmer, C., Rummel, A. and Jirka, G. (2009) "Mass Transport in shallow turbulent wake flow by planar concentration analysis technique". *Journal of Hydraulic Engineering*, **135**(4), 257–270.

Santiago Rojas Arques
Department of Civil and Structural Engineering

Caroppi, G., Gualtieri, P., Fontana, N. and Giugni, M. (2018) "Vegetated channel flows: Turbulence anisotropy at flow-rigid canopy interface". *Geosciences*, **8**, 259.

Cassan, L., Belaud, G., Baume, J.P., Dejean, C. and Moulin, F. (2015) "Velocity profiles in a real vegetated channels". *Environmental Fluid Mechanics*, **15**, 1263 – 1279.

Chau, K.W. (2000) "Transverse mixing coefficient measurements in an open rectangular channel". *Advances in Environmental Research*, **4**, 287–294.

Cheng, G., Huai, W.X., Han, J. and Zhao, M.D. (2010) "Flow structure in partially vegetated rectangular channels". *Journal of Hydrodynamics*, **22,** 590–597.

Chezy, A. (1769) "Developed and verified by experiments made on an earthen channel". *The Courpalet Canal, and on the Seine River*.

Chow, V. (1959) "Open channel hydraulics". *McGraw-Hill, New York*, pp. 4 – 38.

Chu, V.H. and Zhang, J.B. (2004) "Starting jets in a double-tank apparatus shallow flows". *Selected Papers of the International Symposium on Shallow Flows, Balkerna, Leiden, The Netherlands*, 71-78.

Colombani, N., Giambastiani, B.M.S. and Mastrocicco, M. (2015) "Combined used of heat and saline tracer to estimate aquifer properties in a forced gradient test". *Journal of Hydrology*, **525**, 650 – 657.

De Serio, F., Meftah, M.B., Mossa, M. and Termini, D. (2018) "Experimental investigation on dispersion mechanisms in rigid and flexible vegetated beds". *Advances in Water Resources*, **120**, 98 – 113.

Dennis, P. (2000) "Longitudinal dispersion due to surcharged manholes". *PhD Thesis, University of Sheffield.*

Djordjevic, S. (1993) "Mathematical model of unsteady transport and its experimental verification in a compound open channel flow". *Journal of Hydraulic Research*, **31**, 229 – 248.

Dupuis, V., Proust, S., Berni, C. and Paquier, A. (2017) "Mixing layer development in compound channel flows with submerged and emergent rigid vegetation over the floodplains" *Exp. Fluids*, **58**, 30.

Durbin, P.A. and Pettersson, B.A. (2001) "Statistical theory and modelling for turbulent flows". *John Wiley and Sons, Ltd.*

European Commission (2000) Directive 2000/60/EC of the European Parliament and of the Council of 23 October 2000 establishing a framework for community action in the field of water policy. *Off. J. Eur. Communities*, **327**, 22/12/2000.

Fischer, H.B. (1967) "The mechanics of dispersion in natural streams". *Journal of the Hydraulic Division*, **93**(6), 187—216.

Ghani, U., Anjum, N., Pasha, G.A. and Ahmad, M. (2019) "Numerical investigation of the flow characteristics through discontinuous and layered vegetation patches of finite width in an open channel". *Environmental Fluid Mechanics*, **19**, 1469 – 1495.

Ghisalberti, M. and Nepf, M.H. (2002) "Mixing layers and coherent structures in vegetated aquatic flows". *Journal of Geophysical Research*, **107**(C2), 3011.

Santiago Rojas Arques
Department of Civil and Structural Engineering

Ghisalberti, M. and Nepf, H.M. (2004) "The limited growth of vegetated shear layers". *Water Resources Research*, **40**(7), W07502.

Ghisalberti, M. and Nepf, H. (2005) "Mass transport in vegetated shear flows". *Environmental Fluid Mechanics*, **5**, 527–551.

Ghisalberti, M. and Nepf, H. (2009) "Shallow flows over a permeable medium: The hydrodynamics of submerged aquatic canopies". *Transp. Porous Med*, **78**, 385–402.

Green, J.C. (2005) "Modelling flow resistance in vegetated stream: Review and development of new theory". *Hydrological Processes*, **19**(6), 1245–1259.

Gualtieri, C., Angeloudis, A., Bombardelli, F., Jha, S. and Stoesser, T. (2017) "On the values for the turbulent Schmidt number in environmental flows". Fluids, **2**(2), 17.

Gualtieri, P., De Felice, S., Pasquino, V. and Doria, G.P. (2018) "Use of conventional flow resistance equations and a model for the Nikuradse roughness in vegetated flows at high submergence". *Journal of Hydrology and Hydromechanics*, **66**(1), 107 – 120.

Guo, J. and Zhang, J. (2016) "Velocity distributions in laminar and turbulent vegetated flows". *Journal of Hydraulic Research*, **54**(2), 117 – 130.

Guymer, I. and Spence, K. (2009) "Laboratory study of transverse solute mixing during over-bank flows". *In Proc. Of 33rd IAHR Congress: Water Engineering for Sustainable Environment, Ottawa, Canada.*

Haslam, S.M. (1978) "River plants: the macrophytic vegetation of watercourse". *Cambridge University Press.*

Hilderman, T. and Wilson, D.J. (2006) " Predicting plume meandering and averaging time effects on mean and fluctuating concentrations in atmospheric dispersion simulated in a water channel". *Boundary-Layer Meteorology*, **122**, 535 – 575.

Hinze, J.O. (1964) "Turbulent pipe flow. The Mechanics of Turbulence". *Gordon Breach, New York*, pp. 129-165.

Hirschowitz, P.M. and James, C.S. (2008) "Transverse velocity distributions in channels with emergent bank vegetation". *River Research and Applications*, **25**(9), 1177 – 1192.

Hoffman, M.R. (2004) "Application of a simple space-time averaged porous media model to flow in densely vegetated channels". *Journal of Porous Media*, **7**(3), 183 – 191.

Holley, E.R., Siemons, J. and Abraham, G. (1972) "Some aspects of analysing transverse diffusion in rivers". *Journal of Hydraulic Research*, **10**(1), 27—57.

Huai, W.X., Zeng, Y.H., Xu, Z.G. and Yang, Z.H. (2008) "Three-layer model for vertical velocity distribution in open channel flow with submerged rigid vegetation". *Advances in Water Resources*, **32**(4), 487 – 492.

Huang, Y.H., Saiers, J.E., Harvey, J.W. and Noe, G.B. (2008) "Advection, dispersion and filtration of fine particles within emergent vegetation of the Florida Everglades". *Water Resources Research*, **44**(4), W04408.

Ikeda, S. and Kanazawa, M. (1996) "Three-dimensional organised vortices above flexible water plants". *Journal of Hydraulic Engineering*, **122**(11): 634 – 640.

Santiago Rojas Arques
Department of Civil and Structural Engineering

Islam, M. and Zhu, D. (2013) "A kernel density based algorithm to despike ADV data". *Journal of Hydraulic Engineering*, **139**(7), 785 – 793.

James, C.S., Birkhead, A.L., Jordanova, A.A. and O'Sullivan, J.J. (2004) "Flow resistance of emergent vegetation". *Journal of Hydraulic Research*, **42**(4), 390 – 398.

Järvela, J. (2002) "Flow resistance of flexible and stiff vegetation: A flume study with natural plants". *Journal of Hydrology*, **269**(1-2), 44 – 54.

Järvela, J. (2004) "Determination of flow resistance caused by non-submerged woody vegetation". *International Journal of River Basin Management*, **2**(1), 61 – 70.

Jasim, S.Y., Irabelli, A., Yang, P., Ahmed, S. and Schweitzer, L. (2006) "Presence of pharmaceuticals and pesticides in Detroit river water and the effect of ozone on removal", *Ozone: Science and Engineering*, **28**: 415 – 423.

Jobson, H.E. and Sayre, W.W. (1970) "Vertical transfer in open channel flow". *ASCE*, **96**(HY3), 703-724.

Jordanova, A.A., James, C.S. and Birkhead, A.L. (2006) "Practical estimation of flow resistance through emergent vegetation". *Water Management*, **159**(3), 173.

Juez, C., Jenny, C.S., Schleiss, A.J. and Franca, M.J. (2019) "Floodplain land cover and flow hydrodynamic control of overbank sedimentation in compound channel flows". *Water Resources Research*, **55**(11), 9072 – 9091.

Kadlec, R. and Knight, R. (1996) "Treatment Wetlands". *Lewis Publishers, Boca Raton, FL,* 893.

Kim, S.J. and Stoesser, T. (2011) "Closure modelling and direct simulation of vegetation drag in flow through emergent vegetation". *Water Resources Research*, **47**(W10511), 1–15.

Knight, D.W. and Shiono, K. (1996) "River channel and floodplain hydraulics in floodplain processes", *John Wiley & Sons Ltd*.

Kouwen, N., Unny, T.E. and Hill, H.M. (1969) "Flow retardance in vegetated channels*". Journal of the Irrigation and Drainage Division*, **95**(IR2), 329.

Kubrak, E., Kubrak, J. and Rowiński, P.M. (2008) "Vertical velocity distributions through and above submerged, flexible vegetation". *Hydrological Sciences Journal*, **53**(4), 905–920.

Lau, Y.L. and Krishnappan, B.G. (1977) "Transverse dispersion in rectangular channels". *Journal of the Hydraulics Division*, **103**(HY10), 1173-1189.

Lee, W.T. (2011) "Tridiagonal matrices: Thomas algorithm". http://www3.ul.ie/wlee/ms6021–thomas.pdf, Scientific Computation, University of Limerick.

Li, R.M. and Shen, H.W. (1973) "Effect of tall vegetations on flow and sediment*". Journal of the Hydraulic Division*, **99**(HY5), 814.

Lightbody, A.F. and Nepf, H.M. (2006) "Prediction of near-field shear dispersion in an emergent canopy with heterogeneous morphology". *Environmental Fluid Mechanics*, **6**(5), 477.

Lin, B. and Shiono, K. (1995) "Numerical modelling of solute transport in compound channel flows". *Journal of Hydraulic Research,* **33**, 773 – 788.

Santiago Rojas Arques
Department of Civil and Structural Engineering

Lindner, K. (1982) "Der Stromungswidestand von Pflanzenbestanden". *Mitteilung des Leichtweiss-Institutes fur Wasserbau der TU Braunschweig, Heft 75*.

Liu, D., Diplas, P., Fairbanks, J.D. and Hodges, C.C. (2008) "An experimental study of flow through rigid vegetation". *Journal of Geophysical Research Earth Surface*, **113**, 1 – 16.

Lopez, F. and Garcia, M. (1998) "Open-channel flow through simulated vegetation: Suspended sediment, transport modelling" *Water Resources Research*, **34**(9), 2341 – 2352.

Martins, R., Rubinato, M., Kesserwani, J., Djordjevic, S. and Shucksmith, J.D. (2018) "On the characteristics of velocities fields in the vicinity of manhole inlet grates during flood events". *Water Resources Research*, **54**(9), 6408 – 6422.

Meftah, M.B. and Mossa, M. (2013) "Prediction of channel flow characteristics through square arrays of emergent cylinders". Physics of Fluids, **25**(4), 047, 102.

Meftah, M.B. and Mossa, M. (2016a) "A modified log-law of flow velocity distribution in partly obstructed open channels". *Environmental Fluid Mechanics*, **16**, 453 – 479.

Meftah, M.B. and Mossa, M. (2016b) "Partially obstructed channel: Contraction ratio effect on the flow hydrodynamic structure and prediction of the transversal mean velocity profile". *Journal of Hydrology*, **542**, 87 – 100.

Melton, L.A. and Lipp, C.W. (2003) "Criteria for quantitative PLIF experiments using high-power lasers". *Experiments in Fluids*, **35**(4), 310-316.

Middleton, G. and Southard, J.B. (1978) "The mechanics of sediment movement". *Society of Economic Palaeontologists and Mineralogists*, 401.

Muste, M., Hauet, A., Fujita, I., Legout, C. and Ho, H.C. (2014) "Capabilities of large-scale Particle Image Velocimetry to characterize shallow free-surface flows". *Advances in Water Resources*, **70**, 160 – 171.

Nepf, H.M. (1999) "Drag, turbulence and diffusion in flow through emergent vegetation". *Water Resources Research*, **35**(2), 479.

Nepf, H.M. (2004) "Vegetated flow dynamics". *S. Fagherazzi, M. Marani, L. Blum (Eds.), Ecogeomorphology of Tidal Marshes, Coastal and Estuarine Studies*, **59,** 137 – 164.

Nepf, H.M. (2012) "Flow and transport in regions with aquatic vegetation". *Annual Review Fluid Mechanics*, **44**, 123 – 142.

Nepf, H., Sullivan, J. and Zavistoski, R. (1997) "A model for diffusion within emergent vegetation". *Limnology and Oceanography*, **42**(8), 1735 – 1745.

Nepf, H.M. and Vivoni, E.R. (2000) "Flow structure in depth-limited vegetated flow". *Journal of Geophysical Research*, **105**(C12): 5258 – 547.

Nezu, I., and Onitsuka, K. (2002) "Turbulent structures in partly vegetated open-channel flows with LDA and PIV measurements". *Journal of Hydraulic Research*, **39**(6), 629 – 642.

Nikora, N., Nikora, V. and O'Donoghue, T. (2013) "Velocity profiles in vegetated open-channel flows: Combined effect of multiple mechanisms". *Journal of Hydraulic Engineering*, **119**(10), 1021 – 1032.

Santiago Rojas Arques
Department of Civil and Structural Engineering

Nikuradse, J. (1933) "Strömungsgesetze in rauhen Rohren". *Forschungsheft 361. Ausgabe B. Band 4*, **361**(b), Berlin: VDI.

Novak, G., Rak, G., Preseren, T. and Bajcar, T. (2017) "Non-intrusive measurements of shallow water discharge". *Flow Measurement and Instrumentation*, **56**, 14 – 17.

Oki, T. and Kanae, S. (2006) "Global hydrological cycles and world water resources". Science, 313(5790), 1068 – 1072.

Palmer, M., Nepf, H., Petterson, T. and Ackerman, J. (2004) "Observations of particle capture on a cylindrical collector: Implications for particle accumulation and removal in aquatic systems". Limnology and Oceanography, **49**, 76 – 85.

Petryk, S. and Bosmajian, G. (1975) "Analysis of flow through vegetation". *Journal of the Hydraulics Division*, **101**(7), 884.

Piasecki, M. and Katopodes, N.D. (1999) "Identification of stream dispersion coefficients by adjoint sensitivity method". *Journal of Hydraulic Engineering*, **125**(7), 714 – 724.

Pilechi, A.M., Mohammadian, A., Rennie, C.D. and Zhu, D.Z. (2016) "Efficient method for coupling field data and numerical modelling for the estimation of transverse mixing coefficients in meandering rivers". *Journal of Hydraulic Engineering*, **142**(6), 04016009.

Poggi, D., Porporato, A., Ridolfi, L., Albertson, J.D. and Katul, G.G. (2004) "The effect of vegetation density on canopy sub-layer turbulence". *Boundary-Layer Meteorology*, **11**(3), 565.

Pope, S. (2000) "Turbulent flows". *Cambridge University Press*.

Raupach, M.R., Finnigan, J.J. and Brunet, Y. (1996) "Coherent eddies and turbulence in vegetation canopies: The mixing layer analogy". *Boundary-Layer Meteorology*, **78**(3-4), 351.

Reynolds, O. (1883) "III. An experimental investigation of the circumstances which determine whether the motion of water shall be direct or sinuous, and of the law of resistance in parallel channels". *Proceedings of the Royal Society of London*, **35**, 84 – 99.

Righetti, M. (2008) "Flow analysis in a channel with flexible vegetation using double-averaging method". *Acta Geophysica*, **56**, 801.

Robert, A. (2003) "River processes: An introduction to fluvial hydraulics". *Arnold*.

Rojas-Arques, S., Rubinato, M., Nichols, A. and Shucksmith, J.D.(2018) "Cost effective measuring technique to simultaneously quantify 2D velocity fields and depth-averaged solute concentrations in shallow water flows*" Journal of Flow Measurement and Instrumentation*, **64**, 213—223.

Rosgen, D.L. (1994) "A classification of natural rivers". *Catena,* pp. 169 – 199.

Rowiński, P. M., Czernuszenko, W., Koziol, A., Kuśmierezuk, K. and Kubrak, J. (1998) "Longitudinal turbulence characteristics in a compound channel under various roughness conditions". *Proc. Third Int. Conf. on Hydroscience and Engineering, (Cottbus/Berlin, Germany).*

Rowiński, P.M., Guymer, I. and Kwiatkowski, K. (2008) "Response to the slug injection of a tracer – A large-scale experiment in a natural river". *Hydrological Sciences Journal*, **53**(6), 1300 – 1309.

Rubol, S., Battiato, I. and de Barros, P.J. (2016) "Vertical dispersion in vegetated shear flows". *Water Resources Research*, **52**, 8066 – 8080.

Santiago Rojas Arques
Department of Civil and Structural Engineering

Rubol, S., Ling, B. and Battiato, I. (2018) "Universal scaling-law for flow resistance over canopies with complex morphology". *Scientific Reports*, **8**, 4430.

Rummel, A.C., Carmer, C. and Jirka, G.H. (2002) "Combined planar measurements of flow velocity and mass concentration in shallow turbulent flows part 1: Development of a Planar Concentration Analysis (PCA) system". *Proceedings of Hydraulic Measurement and Experimental Methods Specialty Conference (HMEM)*.

Rutherford, J.C. (1994) "River mixing". *J. Wiley and Sons LTD, New York.*

Sayre, W.W., Chang, F.M. (1968) "A laboratory investigation of open-channel dispersion processes for dissolved, suspended and floating dispersant". *US Geol Suev Prof Pap.*, **433** – E.

Seo, I.W., Lee, M.E. and Baerk, K.O. (1994) "2D modelling of heterogeneous dispersion in meandering channels". *Journal of Hydraulic Engineering*, **134**(2), 196 – 204.

Seo, I.W., Chou, H.J., Kim, Y.D. and Han, E.J. (2016) "Analysis of two-dimensional mixing in natural streams based on transient tracer tests". *Journal of Hydraulic Engineering*, **142**(8), 04016020.

Serra, T., Fernando, H.J. and Rodriguez, R.V. (2004) "Effects of emergent vegetation on lateral diffusion in wetlands". *Water Resources*, **38**(1), 139 – 147.

Shi, Z., Pethick, J.S. and Pye, K. (1995) "Flow structure in and above the various heights of a saltmarsh canopy: A laboratory flume study". *Journal of Coastal Research*, **11**, 1204 – 1209.

Shiono, K. and Feng, T. (2003) "Turbulence measurements of dye concentration and effects of secondary flow on distribution in open channel flows". *Journal of Hydraulic Engineering*, **129**(5), 373 – 384.

Shucksmith, J.D. (2008) "Impact of vegetation in open channels on flow resistance and solute mixing". *PhD Thesis, University of Sheffield*.

Shucksmith, J.D., Boxall, J.B. and Guymer, I. (2010) "Effects of emergent and submerged natural vegetation on longitudinal mixing in open channel flow". *Water Resources Research*, **46**(4), W04504.10.1029/2008WR007657.

Simoes, F.J.M. and Wang, S.S.Y. (1997) "Numerical prediction of three dimensional mixing in a compound channel". *Journal of Hydraulic Research*, **35**, 619 – 642.

Siniscalchi, F., Nikora, V.I. and Aberle, J. (2012) "Plant patch hydrodynamics in streams: Mean flow, turbulence and drag forces". *Water Resources Research*, **48**, W01513.

Smart, P.L. and Laidlaw, I.M.S. (1977) "An evaluation of some fluorescent dyes for water tracing". *Water Resources Research*, **13**, 15 – 33.

Sonnenwald, F., Hart, J.R., West, P., Stovin, V.R. and Guymer, I. (2017) "Transverse and longitudinal mixing in real emergent vegetation at low velocities". *Water Resources Research*, **53**(1), 961 – 978.

Sonnenwald, F., Stovin, V. and Guymer, I. (2018) "Estimating drag coefficient for arrays of rigid cylinders representing emergent vegetation". *Journal of Hydraulic Research*, **59**(4), 591 – 597.

Sonnenwald, F., Guymer, I. and Stovin, V. (2019) "A CFD-Based mixing model for vegetated flows". *Water Resources Research*, **55**(3), 2322 – 2347.

Santiago Rojas Arques
Department of Civil and Structural Engineering

Stephan, U. and Gutknecht, D. (2002) "Hydraulic resistance of submerged flexible vegetation". *Journal of Hydrology*, **269**(1-2), 27.

Stoesser, T., Salvador, G.P., Rodi, W. and Diplas, P. (2009) "Large eddy simulation of turbulent flow through submerged vegetation". *Transport in Porous Media*, **78**, 347 – 365.

Stone, B.M. and Shen, H.T. (2002) "Hydraulic resistance of flow in channels with cylindrical roughness". *Journal of Hydraulic Engineering*, **128**(5), 500.

Sun, X., Shiono, K., Rameshwaran, P. and Chandler, J.H. (2010) "Modelling vegetation effects in irregular meandering river". *Journal of Hydraulic Research*, **48**(6), 775 – 783.

Tabatabei, S.H., Heidarpour, M. Ghasemi, M. and Hoseinipour, E.Z. (2013) "Transverse mixing coefficient on dunes with vegetation on a channel wall". *World Environmental and Water Resources Congress 2013: Showcasing the Future*.

Tang, X., Knight, D.W. and Sterling, M. (2009) "Analytical model for streamwise velocity in vegetated channels". *Engineering and Computational Mechanics*, **164**(2), 91 – 102.

Tanino, Y. and Nepf, H. M. (2008a) "Lateral dispersion in random cylinder arrays at high Reynolds number". *Journal of Fluid Mechanics*, **600**, 339 – 371.

Tanino, Y. and Nepf, H.M. (2008b) "Laboratory investigation of mean drag in a random array of rigid, emergent cylinders". *Journal of Hydraulic Engineering*, **134**(1), 34 – 41.

Taylor, G.I. (1921) "Diffusion by continuous movements". *Proc. London Math. Soc. Ser. 2*. **20**, 196 – 212.

Temple, D.M. (1986) "Velocity distribution coefficients for grass-lined channels". *Journal of Hydraulic Engineering*, **112**(3), 193 – 205.

Termini, D. (2019) "Turbulent mixing and dispersion mechanisms over flexible and dense vegetation". *Acta Geophysica*, **67**, 961 – 970.

Thielicke, W. and Stamhuis, E.J. (2014) "PIVlab – Towards user-friendly, affordable and accurate digital Particle Image Velocimetry in MatLab". *Journal of Open Research Software*, **2**(1), e30.

Trudgill, S.T. (1987) "Soil water tracing, with special reference to the use of Rhodamine WT, Lissamine and Amino G Acid". *Hydrological Processes*, **1**(2), 149 – 170.

Tsakiris, G. and Alexakis, D. (2012) "Water quality models: An overview". *European Water*, **37**, 33 – 46.

Vargas, C.A.A. (2016) "ndnanfilter.m (https://www.mathworks.com/matlabcentral/fileexchange/20417-ndnanfilter-m)", *MATLAB Central File Exchange. Retrieved March 1*.

Velasco, D., Bateman, A. and Medina, V.A. (2008) "A new integrated, hydro-mechanical model applied to flexible vegetation in riverbeds". *Journal of Hydraulic Research*, **46**, 579 – 597.

Vörösmarty, C.J., Pamela, G., Salisbury, J. and Lammers, R.B. (2000) "Global water resources: Vulnerability from climate change and population growth". *Science*, **289**(5477), 284 – 288.

Ward, P.R.B. (1973) "Measurement of dye concentrations by photography". *Journal of the Environmental Engineering Division*, **99**(3), 165 – 175.

Santiago Rojas Arques
Department of Civil and Structural Engineering

Webel, G. and Schatzmann, M. (1984) "Transverse mixing in open channel flow". *Journal of Hydraulic Engineering*, **110**(4), 423 – 435.

Weitbrecht, V., Kühn, G. and Jirka, G.H., (2002) "Large scale PIV-measurements at the surface of shallow water flows". *Journal of Flow Measurement Instrumentation*, **13**(5-6), 237–245.

West, P. (2016) "Quantifying solute mixing across low velocity emergent real vegetation shear layers". *PhD Thesis. University of Warwick, School of Engineering*.

West, P.O., Wallis, S.G., Sonnenwald, F.C., Hart, J.R., Stovin, V.R. and Guymer, I. (2020) "Modelling transverse solute mixing across a vegetation generated shear layer". *Journal of Hydraulic Research*, DOI: 10.1080/00221686.2020.1818307.

White, F.M. (1991) "Viscous fluid flow". *New York: McGraw-Hill*.

White, B.L. and Nepf, H.M. (2007) "Shear instability and coherent structures in shallow flow adjacent to a porous layer". *Journal of Fluid Mechanics*, **593**, 1 – 32.

White, B., L. and Nepf, H., M. (2008) "A vortex-based model of velocity and shear stress in a partially vegetated shallow channel". *Water Resources Research*, **44**(1), W01412.

Wilson, C., Stoesser, T., Bates, P. and Pinzen, A.B. (2003) "Open channel flow through different forms of submerged flexible vegetation". *Journal of Hydraulic Engineering*, **129**, 847 – 853.

Yan, C., Nepf, H.M., Huang, W.X. and Cui, G.X. (2017) "Large eddy simulation of flow and scalar transport in a vegetated channel". *Environmental Fluid Mechanics,* **17**, 497 – 519.

Zeng, Y., Huai, W and Guymer, I. (2008) "Transverse mixing in a trapezoidal compound channel". *Journal of Hydrodynamics*, **20**, 645 – 649.

Zhang, J.B. and Chu, V.H. (2003) "Shallow turbulent flows by video imaging method*". Journal of Engineering Mechanics*, **129**(10), 1164 – 1172.

Santiago Rojas Arques
Department of Civil and Structural Engineering